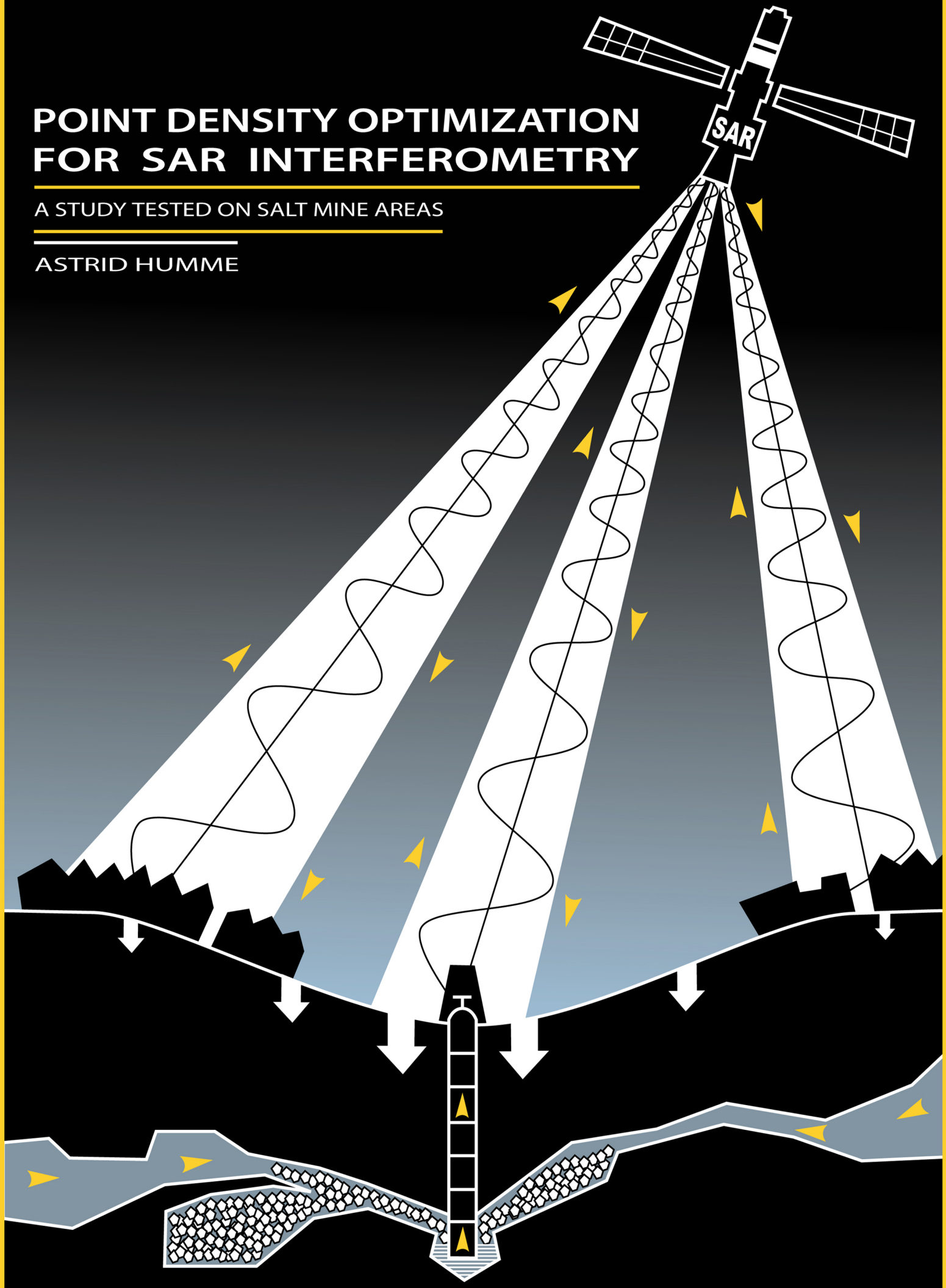


POINT DENSITY OPTIMIZATION FOR SAR INTERFEROMETRY

A STUDY TESTED ON SALT MINE AREAS

ASTRID HUMME



Point density optimization for SAR Interferometry

-A study tested on salt mine areas-

M.Sc. thesis

Astrid J.M. Humme

November 2007

Department of Earth Observation and Space Systems
Faculty of Aerospace Engineering
Delft University of Technology

Contents

Preface	vii
Summary	ix
Nomenclature	xiii
1 Introduction	1
1.1 Motivation	1
1.2 Objectives	3
1.3 Research methodology	4
1.4 Outline	4
2 Solution mining and surface deformation	7
2.1 Surface deformation due to human activities	7
2.1.1 Damage due to mining activities	9
2.2 Solution mining	9
2.3 Surface deformation due to solution mining	11
2.4 Test case Veendam concession	12
2.5 Test case Barradeel concession	13
3 Deformation monitoring with InSAR	15
3.1 Introduction	15
3.2 Principles of InSAR	16
3.3 Principles of Persistent Scatterer Analysis	18
3.3.1 PS processing steps	19
3.3.2 Quality description	24
4 PS identification optimization methods	29
4.1 PS selection optimization	29
4.1.1 Manual PS identification	30
4.2 PS testing optimization	31
4.2.1 Non-linear deformation subtraction	32
4.2.2 Breakpoint model	38
5 Optimized results of the test cases	41
5.1 Introduction	41
5.2 Conventional PS processing results.	44
5.3 Results manual PS identification	49
5.4 Results bilinear interpolation method	54
5.5 Results Gaussian bowl method	60

5.6	Results breakpoint model	65
5.7	Unwrapping errors	73
5.8	Validation PS results	76
5.9	Conclusions	83
6	Physical subsidence modeling	87
6.1	Mogi model	87
6.2	Results Mogi model	90
6.2.1	Results Mogi Model Veendam concession area	90
6.2.2	Results Mogi model Barradeel concession area	94
6.3	Conclusions	97
7	Conclusions and recommendations	101
7.1	Conclusions	101
7.2	Recommendations	104
A	ERS data baseline plots	111
B	Linearized Least Squares system bowl estimation	117
C	Densification results	121
C.1	Track 108	121
C.2	Track 380	127
C.3	Track 487	134
C.4	Track 151	139
C.5	Track 258	146
D	Estimated Mogi parameters	153
D.1	Estimated Mogi parameters Veendam concession	153
D.2	Estimated Mogi parameters Barradeel concession	156

Preface

This thesis has been written as final project for the study Earth Observation, one of the masters present at the faculty Aerospace Engineering of the Delft University of Technology. The research and documentation forfeit around a year. I started working full time in June 2006 and finished end October 2007. The research tries to increase the Persistent Scatterer density and distribution, tested on salt mining areas close to Veendam and Harlingen. Different methods are implemented to reach the goal. With an increase of PS density and distribution the deformation pattern in the areas is aimed to be estimated more accurate and reliable. Hence enabling deformation monitoring and prediction.

I would like to express my gratitude to the people involved with the realization of my research and thesis. First of all, I would like to thank Ramon Hanssen for supervising me during my research. I learned a lot from your vision and knowledge. Also your more philosophical approach to science broadened my field of view. Thank you for that. I would also like to show my gratitude to Freek van Leijen, Petar Marinkovic and Gini Ketelaar. Thank you for the extensive clarifications to my questions on InSAR and the support I received during my research. The visualizations and movies would haven't been as good without Zbigniew Perski, thank you. I also would like to thank the rest of the radar group for their help and sociability. Special acknowledgments go out to the mining companies Frisia Salt B.V. and Nedmag Industries for their support. Meetings and visits clarified the mining process for me. The results of this thesis would not be as grounded without the data the companies Frisia and Nedmag made available. Finally, thanks go to professor Dick Simons and Peter Fokker from TNO Built Environment and Geosciences, who were willing to be members of my graduation committee.

Astrid Humme
Delft, 12 November 2007

Summary

Earth's surface deformation can be monitored with images acquired by Synthetic Aperture Radars (SAR). Interferometric processing of the images, making use of the phase contributions, provides surface deformation with centimeter accuracy. The accuracy of InSAR is limited by temporal decorrelation, atmospheric effects and geometrical decorrelation. To overcome these main errors Persistent Scatterer (PS) analyses are developed. The techniques obtain deformation measurements with millimeter accuracy, which is achieved by the analysis of the interferometric phase of time-coherent scatterers in a stack of tens of differential interferograms.

To be able to estimate an accurate deformation pattern based on PSs in an area of interest, it can be possible that a high density of PSs is required. Investigation of PS analyses performed on the North of the Netherlands indicated low densities of PSs in several areas experiencing large deformation (cm/year) in a relatively small area (tens of km²). To obtain an accurate deformation pattern, the density of PSs has to increase. Possible causes of a low PSs density are:

- the absence of scatterers possessing coherent scattering properties in the areas of interest,
- points possessing coherent scattering properties, but are not identified as PS during their selection, or
- points possessing coherent scattering properties being rejected as PS during the subsequent processing steps.

The first cause is a consequence of scattering properties of objects on the Earth's surface, and since these properties can not be changed, this research concentrates on the last two potential causes. Potential methods to overcome these problems are investigated in this research. The methods are tested on two areas. These are the Veendam concession and Barradeel concession, both situated in the North of the Netherlands and experiencing deformation due to salt mining. Three satellite tracks are used for the Veendam concession and two tracks for the Barradeel concession.

The second cause is overcome making use of manual selection of pixels most likely experiencing a coherent phase in time. These pixels are not subjected to the conventional selection procedure, but immediately proceed to the testing steps. Man-made features show to have a large possibility experiencing a coherent phase of time. The technique increased the density of the PSs in most tracks and estimated deformation and topographic heights are comparable with conventional analyses. Although a large number of unrealistic deforming or incorrect estimated deformation of PSs is present, filtering of these PS still results in an increase of PS. Assuming a bowl shaped deformation pattern present in both test cases, indicated an increase in the accuracy of the estimated deformation pattern.

The third cause is dealt with by deformation subtraction and a functional break-point model. Pixels with non-linear deformation behavior are discarded when they do not fit the linear deformation model within specified boundaries. This linear model is implemented in the conventional method to model deformation. The discarded pixels can be coherent scatterers, containing valuable information on the deformation pattern in an area of interest, hence the pixels should not be rejected.

The implementation of models correcting the differential phase of a pixel for the contribution of non-linear deformation, results in the acceptance of pixels with non-linear deformation. The implemented models are a Gaussian model and a bilinear interpolation based on a Delaunay triangulation, both describing the subsidence pattern. The algorithms estimate a subsidence pattern at every epoch. The pattern is subtracted from the differential phase. Subtraction of estimated deformation is performed to decrease the variance of the phase and therefore obtain a phase that can be described by a linear deformation model more accurately. The usage of these models resulted in most cases in a larger density of identified PSs. Also the accuracy of the estimated deformation pattern increased, assuming a bowl shaped deformation pattern. Estimated deformation surfaces approaching reality are requirement for this statement. When the estimated surfaces do not approach reality, the subtraction of the deformation can add non-linear behavior, hence less PSs are identified. Deformation surfaces based on leveling results are subtracted in the Barradeel test case, which resulted into PSs in the center of the subsidence bowl. These PSs were not identified after subtraction of deformation based on conventional PS results.

Besides deformation subtraction the third cause is dealt with by a functional model describing the temporal behavior of PSs with a break-point model. A break-point model consists out of two connected linear lines experiencing a different slope. This model can occur for instance when no deformation is present at subsequent epochs, followed up by a period of deformation. The implemented break-point model did not increase the density of identified PSs in most cases, but break-point model corrected unwrapping errors introduced by the usage of a linear model describing deformation. The reason why the break-point did not increase the density of PSs is not identified during this research.

The results of the different implemented methods for a track are combined in one dataset to obtain a high PS density. Geocoding the combined PS results enabled comparison between estimated PS deformation and height of different tracks. The results of the three Veendam tracks are comparable, the same holds for the Barradeel tracks. The estimated vertical deformation in the Veendam concession is -155 mm over 11 years starting from 1995. In the Barradeel area the estimated vertical deformation is -334 mm over 13 years, starting from 1992. But since mining activities started in 1996 and before 1996 almost no deformation was present, this total measured deformation approaches the deformation over the timespan starting in 1996 until 2005. The combination of salt mining and gas subtraction introduces a tilt in Franeker of -15.8 mm/km over 13 years.

Validation of the PS results is performed making use of leveling results describing a comparable period in time. The PSs surrounding leveling measurement positions with a distance less than 200 meters are used to calculate the correlation between the datasets. Correlation coefficients are ranging from 0.827 to 0.950 for the Veendam concession. Track 108 experienced the largest correlation coefficients (0.918 to 0.950) and track 487 the smallest (0.827 to 0.891). Between PS results of track 108 and leveling measurements in the Veendam concession a difference of -10 to -15 mm is present for all the investigated time periods, where the PS results are underestimated compared to the leveling results. This can have been introduced by unwrapping errors at the cavern locations. The largest used leveling time period ranges from 1995 until 2004.

In the Barradeel concession the correlation coefficients between the leveling measurements and PS results range from 0.915 to 0.939. The leveling datasets correspond to the PS closest to BAS-1. The West of the subsidence bowl is underestimated. Investigation of the timeseries indicates a break-point around 1997 in this area. Hence this has introduced an underestimation of the deformation after 1997.

Deformation of the Earth's surface due to mining activities is caused by physical processes taking place in the subsurface. Hence measured surface deformation holds information on the physical process introducing this land subsidence. Understanding of the physical process can be used to predict subsidence introduced by arbitrary volume change. The Mogi model describes deformation making use of volume changes, the depth and the location of a point source. The conventional Mogi model is used to estimate the unknown parameters at the Veendam concession area based on the estimated PS deformation. An alternative model is used for the Barradeel concession area, since two subsidence bowls interfere. Salt mining near Harlingen and gas extraction near Franeker cause subsidence in the Barradeel area. The bowls are described by the addition of two Mogi sources with different depths, locations and volume changes.

The estimated parameters in the tracks covering the test areas corresponded, except for xrd coordinates in one track covering Veendam and one track covering the Barradeel concession. These coordinates obtained different estimates due to the distribution of PSs. The lack of PSs in the area of interest had an influence on the final xrd estimates. The other parameters corresponded to each other and to the provided volume changes and known reservoir locations and depths. The correlation factor between the estimated volume changes by Mogi and the provided production volumes in the Barradeel case is 0.989. In the Veendam case the highest correlation coefficient between the estimated volume changes and the provided volumes is 0.955. Best fitting provided volumes are the squeeze volumes and the production volumes. The squeeze volume is the volume of salt crept into the cavern. Creep is introduced due to the low pressure in the cavern, resulting into a pressure difference making the salt flow to the cavern.

Despite the high correlation coefficient between the PS deformation of the Barradeel test case and the estimated Mogi deformation, the residuals between the datasets are large in the salt mining subsidence bowl. Underestimation of the deformation in the center of the bowl by the Mogi model and overestimation of the deformation at the dikes situated in the West of the bowl results into errors of 150 mm over 8 years. Several reasons can have introduced the large residuals.

- The PS deformation can differ from reality. This is emphasized by the leveling measurements which indicated larger deformation at the dike than the PS deformation.
- The looking direction of the satellite can have caused a difference in the measured deformation. Subsidence can be larger on the sea side of a dike than on the land side.
- Mogi assumes a point source, but Frisia Salt makes extensive use of the creep properties of salt, resulting into a different subsidence pattern.

It is not clarified whether the estimated PS deformation is not correct, or whether the deformation can not exactly be modeled by the Mogi source possibly due to the creep phenomenon.

The Mogi model proves to be a feasible model to estimate reservoir parameters from PS deformation. This conclusion is based on the calculated correlation coefficients between provided production volumes and estimated volume changes. Despite high correlation coefficients the deformation pattern calculated with Mogi parameters does not necessary represent the PS deformation.

The research goals are reached. Two of the three implemented optimization models increase the identification success rate of the PSs. These methods are the manual PS identification and deformation subtraction method. The third model, breakpoint model, did not increase the success rate, but eliminated unwrapping errors. Hence this method is an optimization method.

The Mogi model is implemented to model physical processes based on the optimized PS deformation dataset. Validation of the estimated parameters, (x, y) , the depth and volume changes indicated the feasibility of the Mogi model to model the physical processes. It is feasible to model the physical processes with the Mogi model based on PS deformation. But in the Barradeel test case the residuals between the provided volumes and estimated volume changes are high although the correlation between the datasets is large.

Nomenclature

List of Symbols

0	Initialization value
\mathbf{A}	Design matrix
B	Baseline
B_{\perp}	Perpendicular baseline
$D.$	Dispersion operator. second moment
D_a	Amplitude dispersion; Width of the antenna
D_p	Surface displacement in line-of-sight of the satellite
d	Depth of the subsidence bowl; Depth of the cavern
\mathbf{d}_n	Proximity vector
$E.$	Expectation operator
e	Error
H	Height of a point above the Earth's surface
L_a	Length of the antenna
m	Number of observations
N	Nugget value
n	Number of parameters
p	Horizontal observation location
Q	Variance-covariance matrix
R	Distance between the Mogi source and observation location
R_1	Slant range between satellite and resolution cell
r	Radius of the subsidence bowl; Range
T	Temporal baseline
v	Velocity
W	Width of the extraction
\mathbf{w}_n	Weight vector
\mathbf{x}	Vector of parameters
x_s	X-coordinate of the Mogi source
x_c	X-coordinate center subsidence bowl
y_s	Y-coordinate of the Mogi source
y_c	Y-coordinate center subsidence bowl
z	Deformation
z_c	Z-coordinate center subsidence bowl

$\partial\theta$	Angular change in look angle
$\partial\phi$	Unwrapped differential phase
β_r	Angular beam width in range direction
β	Height-to-phase conversion factor
$\hat{\gamma}$	Ensemble coherence
Δ_d	Average displacement rate
Δ_h	Topographic height
ΔV	Volume change of the cavern
ζ	Angle of draw
θ	Look angle
θ_{inc}	Incidence angle
λ	Radar wavelength
ν	Poisson's ratio
σ	Lagrange multiplier; Standard deviation
σ_a	Standard deviation of the amplitude
σ_ϕ	Standard deviation of the phase
ϕ	Phase
ρ	Correlation coefficient

Abbreviations

APS	Atmospheric Phase Screen
BLUE	Best Linear Unbiased Estimation
CSA	Canadian Space Agency
DD	Double-Difference
DBM	Dead Burned Magnesium
ENVISAT	ENVIronmental SATellite
ERS	European Remote Sensing Satellite
ESA	European Space Agency
GPS	Global Positioning System
InSAR	Interferometric Synthetic Aperture Radar
JERS	Japanese Earth Resources Satellite
LAMBDA	Least-squares AMBiguity Decorrelation Adjustment
NASDA	National Aeronautics and Space Development Agency (Japan)
OMT	Overall Model Test
PS	Persistent Scatterer
PSC	Persistent Scatterer Candidate
PSP	Potential Persistent Scatterer
Radar	Radio Detection and Ranging
RD	Rijks Driehoek
SAR	Synthetic Aperture Radar
SLC	Single Look Complex
SNR	Signal-to-Noise Ratio
WGS84	World Geodetic Survey 84

Chapter 1

Introduction

Many measurement techniques are developed to study the Earth's surface deformation. The techniques experience different levels of accuracy and required man-hours. One of the developed techniques is space-borne Synthetic Aperture Radar Interferometry (InSAR). InSAR is based on microwave pulses emitted by a space-borne SAR instrument. These pulses hit the Earth's surface, are scattered back to the satellite, and received by the SAR antenna. After receiving the signal the amplitude, phase, and travel time of the pulse are stored. Usage of phase differences between sensors imaging a resolution cell, enables measuring distance differences between sensors and resolution cell with millimeter accuracy [21]. The obtained parameters enable the measurement of topography and deformation of the area of interest.

Since the 1990's InSAR is successfully applied to measure the Earth's topography and surface deformation, e.g. surface displacements caused by wide scale phenomena like volcanoes [33] [1] and earthquakes [22] [34]. A SAR image covers an area of $100 \times 100 \text{ km}^2$, and obtains potentially a spatial resolution of 4×20 meters, enabling recognition and analysis of wide scale displacements.

In general InSAR experiences three limitations, i.e. atmospheric phase delay, temporal decorrelation and geometric decorrelation. Atmospheric phase delay is mainly caused by the water vapor in the troposphere and can introduce a delay of several centimeters, depending on atmospheric conditions. Temporal decorrelation is caused by physical terrain changes between the images taken at different acquisition times. These changes affect the scattering characteristics of the surface, which result in a loss of coherence between the images. Geometric decorrelation is introduced by different angles of incidence to a resolution cell at different acquisition times. A spectral shift due to this difference is introduced in the data spectrum. Then overlap in data spectrum becomes smaller with increasing difference in angle. Decorrelation occurs when no overlap is present in the data spectrum [48].

Persistent Scatterer techniques are developed to overcome these three main limitations [14]. The techniques search for sub-pixel sized scatterers coherent over time in a stack of tens of SAR interferograms. These Persistent Scatterers (PSs) are used to estimate the atmospheric delay effect and noise, and subsequently subtract these from the initial data. After subtraction, PS deformation and topography independent of atmosphere, geometric and temporal decorrelation rests.

1.1 Motivation

In the North of the Netherlands gas extraction causes land subsidence. The Netherlands is a small, densely populated country where land deformations can affect a large group of people.

Besides land is mainly situated below water level introducing a sensitive water balance which can be affected by the land deformation. Hence, land subsidence caused by human activities needs to be monitored and reported. To minimize the possible damage resulting from mining activities, the government and mining companies agree upon an allowed maximum subsidence.

Deformation monitoring with GPS or leveling techniques are labor-intensive, hence monitoring large areas is time consuming. With the combination of wide scale coverage and high resolution InSAR reduces labor time to measure surface deformation compared to other geodetic techniques [21]. Deformation due to gas subtraction in north of the Netherlands is studied by PS analysis [29]. Estimated deformation is presented in figure 1.1. The PS results indicate several small areas where relatively large deformation occurs and a low density of PSs describes the deformation pattern. This density of PSs is not large enough to capture the full deformation pattern. Interpolation can be used, but does not guarantee an actual deformation pattern. Hence the density of PSs needs to be increased to be able to use PS-InSAR as accurate measurement technique. This research focuses on the improvement of the PS density, to enable deduction of a more accurate deformation pattern.

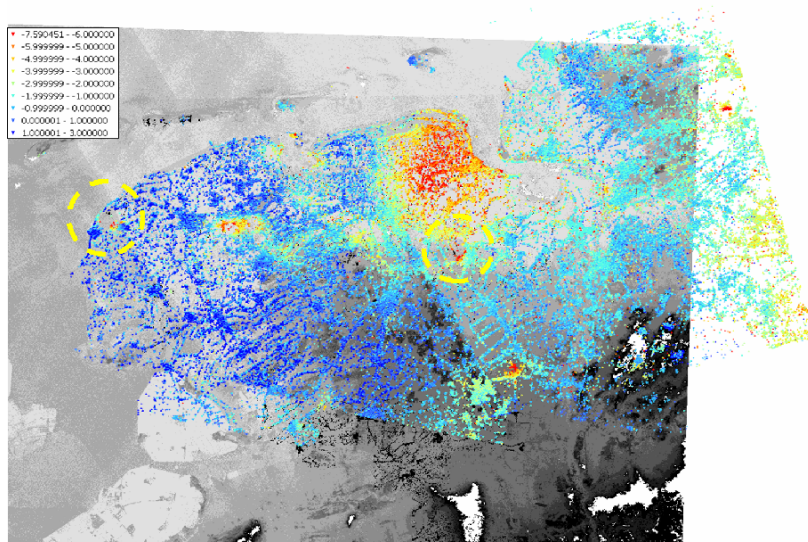


Figure 1.1: The annual deformation of the Persistent Scatterers resulting from Persistent Scatterer Interferometry. The \triangle represent PSs acquired from ascending data. The ∇ represent estimated PSs from the descending tracks. The two test areas are indicated with a yellow dotted circle. In the west the Barradeel concession is situated. The eastern circle encapsulates the Veendam concession [29].

Two areas are used as test sites throughout this thesis. These areas are encircled by the yellow lines in figure 1.1. Deformation in these areas is mainly introduced by salt mining [46]. The area of interest in the southeast is the Veendam concession near Veendam and the area in the northwest is the Barradeel concession near Harlingen.

In the Veendam concession mining started around 1979. In this year Shell-Billiton and NOM, a Dutch investment bank, merged and founded Magin, Magnesia International, to be able to expand the number of gas borings [36]. Instead they discovered a magnesium chloride deposit in the Veendam surroundings. Salt mining started and was passed over to Nedmag Industries in 1994 which continued to mine the area. Currently Nedmag Industries still mines magnesium chlorides from large salt deposits at depths of over the 1500 meters. Gas extraction in the northeast of the Netherlands introduces an extra source of deformation in the Veendam

concession.

In the Barradeel concession near Harlingen, Frisia Salt started mining salt in 1996 from depths of 2800 meters. Due to high pressure differences, between the salt layer and the cavern, and high temperatures present in the salt layers, salt is expected to creep back to the cavity, enabling the usage of the same boring for many years [2]. Extreme creep velocities are present and are exploited throughout the mining process [31]. In the Barradeel concession area salt flows 100 times faster than in most for other salt mining cases. Present subsidence in the surroundings of Harlingen are introduced by salt mining and gas extraction by Vermilion Energy.

1.2 Objectives

The research goal can be divided into two topics. The first topic focuses on optimizing the density of the identified PSs in an area of interest. Throughout this thesis the emphasis is set to this research goal. The second topic models physical subsurface processes based on the acquired deformation pattern obtained with optimization techniques increasing the PS density. The research goal is to:

”present methods optimizing the success rate of identifying Persistent Scatterers, and determine the feasibility of modeling physical subsurface processes from the temporal deformation results obtained from the Persistent Scatter analysis.”

To be able to increase the density of the identified PSs, potential causes for a decreased PS density need to be investigated. These are:

- the absence of scatterers possessing coherent scattering properties in the areas of interest,
- points possessing coherent scattering properties, but are not identified as PS during their selection, or
- points possessing coherent scattering properties being rejected as PS during the subsequent processing steps.

The first cause is a consequence of the scattering properties of objects on the Earth’s surface, and since these properties can not be changed this research concentrates on the last two potential causes. The second cause focuses on the selection of pixels. An image is composed out of millions of pixels. Selection of all these pixels as possible PSs, results in an unacceptably long computation time. To decrease the time, pixels with an assumed coherent temporal phase behavior, derived from temporal amplitude variances, are selected. This results into a subset of selected pixels that contains the most coherent pixels, but likely not all coherent pixels in the image.

The third cause focuses on the rejection of the selected pixels during subsequent processing steps. During these steps the deformation patterns through time of all pixels are acquired. The stored travel time by the satellite equipment is not accurate enough, hence the phase is acquired to measure accurate deformation. Since the number of phase cycles a signal traverses before the last cycle hits the radar device is unknown, the exact distance to a pixel is unknown. To obtain this number of phase cycles, ambiguities, linear temporal deformation behavior is assumed. When the actual deformation does not approach linearity, between specified boundaries, the pixel is rejected as PS. Pixels experiencing prominent non-linear behavior will be rejected by the analysis, but can obtain coherent scattering properties. Potential methods to overcome this problem are investigated in this research.

The second topic in the research goal is modeling physical subsurface processes. If volume changes can be estimated making use of measured deformation, a prediction of deformation can be made based on the volume change. A feasibility study on the derivation of the physical processes based on PS-InSAR, indicates whether PS-InSAR can be used as an useful tool for deformation prediction.

1.3 Research methodology

Several optimization methods for PS selection and PS testing to increase the success rate of identification of PSs are investigated. PS selection is the first step in which pixels are selected based on coherent temporal phase behavior. PS testing are the subsequent steps in which the topography and deformation is estimated and tested. One method is implemented to optimize PS selection, hence implemented to identify pixels with coherent temporal phases. This method selects specified pixels of interest by means of a mask. These pixels are not subjected to the selection procedure, but treated as selected pixels instantly. Hence identification is not based on temporal amplitude variances, but on the knowledge of the type of scatterers frequent identified as PS.

Pixels with non-linear deformation behavior are discarded when they do not fit the linear deformation model within specified boundaries. But they can be coherent scatterers, containing valuable information on the deformation pattern in an area of interest. During this project it is researched whether, to optimize the PS testing steps, the use of models, that correct the differential phase of a pixel for the contribution of non-linear deformation, results in the acceptance of pixels with non-linear deformation. A Gaussian model and bilinear interpolation based on a Delaunay triangulation describing the subsidence pattern are used to estimate non-linear behavior. Also the use of a functional breakpoint model, which describes the deformation with two linear graphs with different slopes, is investigated.

Inverse modeling is performed by means of a Mogi model [38]. The Mogi model describes deformation of the land surface height due to volume changes of a point source located in the subsurface. For the Veendam concession two versions of the model are investigated. These two models are a conventional model and a model which takes the deformation contribution of gas extraction in the north of the Netherlands into account.

1.4 Outline

Chapter 2 treats surface deformation due to mining activities. Emphasize is put on solution mining, which is used in both the Veendam and Barradeel concession. The last two paragraphs of the chapter give an introduction to these test cases.

In chapter 3 a review of the principles of InSAR and the Persistent Scatterer analysis is presented. The short description on InSAR provides the reader with sufficient knowledge to understand the processing steps taken in the Persistent Scatterer analysis, also explained in this chapter. The final section treats a quality description on PS results.

Chapter 4 presents and discusses the optimization methods, implemented to increase the density of PSs for large deforming areas. First a method optimizing the selection of pixels is presented. Subsequently methods influencing the differential phase are discussed.

Results of the implemented optimization methods are covered in chapter 5. The results are analyzed and conclusions are drawn in this chapter. A validation of the PS results is performed on leveling results.

Chapter 6 treats an inverse model from which volume changes and locations of the salt reservoirs are derived. The Mogi model is used to find the relationship between deformation on the Earth's surface and physical processes in the subsurface.

Chapter 2

Solution mining and surface deformation

Land subsidence is the vertical deformation of the Earth's surface. The causes of this phenomenon are divided into natural activities and human activities. The Barradeel and Veendam concessions, experience subsidence mainly due to human activities. In these areas salt is mined using solution mining.

The first three sections of this chapter explain the causes and consequences of surface deformation instigated by human activities with emphasis on the solution mining technique. An introduction to the test sites, the Veendam concession and the Barradeel concession, is given in section four and five.

2.1 Surface deformation due to human activities

The principal causes of subsidence due to human activities are [9]:

- digging out of caverns, subsurface cavities, and possible collapse of them,
- decrease in the pore pressure of the Earth's mass due to the withdrawal of fluid or gas.

Extracting dissolved rock formations like salt and magnesium or digging up non-solvable rock like coals, leaves caverns at the former place of the minerals. The withdrawal of the mineral redistributes the forces on surrounding rock formations of the cavern. Deformation of these formations can occur due to the loss of support of the dissolved or gained mineral. As a result compression or collapse of the cavern can take place. Both a bowl-shaped deformation pattern caused by compaction of the rock formations above the cavern or a sinkhole due to collapse of the cavern can occur on the surface. As can be observed in figure 2.1 the extent of the affected surface is larger than the worked width in the cavern. The spatial limit of the effect on the surface is defined by the angle of draw ζ . It can generally be assumed that a flatlying cavern influences a terrain experiencing even surface topography with a maximum angle of 45° [41]. Thus, assuming the width of the cavern stays constant, when the cavern gets deeper, the wider the area of subsidence will be. When considering a given point P on the surface, see figure 2.1, the area of influence is a circular base of an imaginary cone starting in the cavern and with point P at the cone tip. The diameter of the area is equal to 1.4 times the depth of the cavern. In Europe and Great Britain this value 1.4 is empirically determined. If working outside this area, point P will not be affected. Figure 2.2 presents three different cases [41]:

- sub-critical working, width/depth ration < 1.4

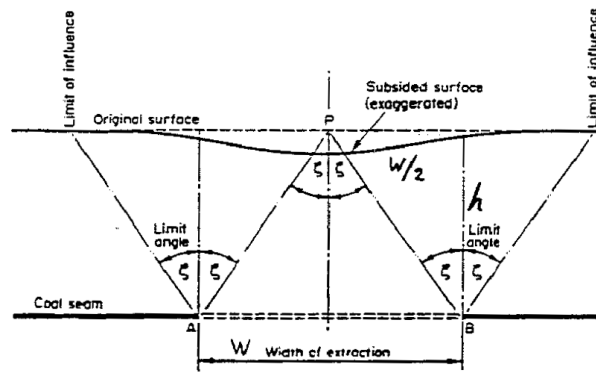


Figure 2.1: Mining configuration where W is the width of the extraction, ζ the maximum angle of draw and h the depth of the cavern [41].

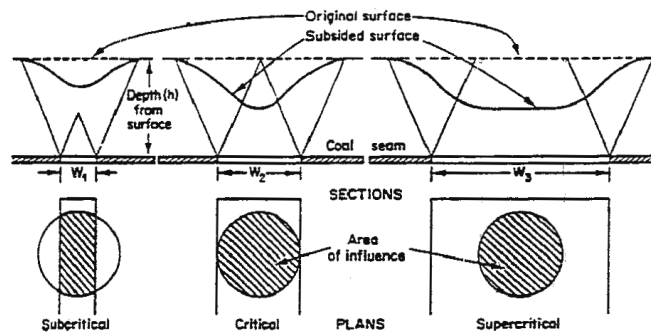


Figure 2.2: Sub-critical, critical and supercritical working is indicated in this figure. Working outside the area of influence (shaded area) does not affect subsidence at the tip of the imaginary cone [41].

- critical working, width/depth ratio = 1.4
- supercritical working, width/depth ratio > 1.4.

The maximum possible subsidence is only achieved when the width of working is critical or supercritical. The same cases hold for a vertical oriented cavern [24].

Horizontal strain is the differential horizontal displacement and is important when observing the damage to surface constructions in subsiding areas. Both compressional and tensional strains are present in these areas. A positive differential horizontal displacement is a tensional strain, and a negative value is compressional strain. In the three indicated critical cases the point of maximum horizontal displacement is free from compressive and tensile strain, since the horizontal displacement is zero at this location [41]. The focus is set on deformation throughout this research. Damage is not investigated, hence strains are not calculated.

Next to the angle of draw, the depth of the cavern, the width/depth ratio and the height of the cavern most influence the surface deformation. This height is directly proportional to the amplitude of the strain curve on the surface [41].

The second principal cause is the decrease in fluid or gas pressure due to the removal of fluid or gas in the rock formations. The space between grains, composing the rock formations, is filled with gas or liquid. Fluid and grain pressure of subsurface layers above a certain point determine

the total subsurface pressure at the specific point. When the fluid or gas is removed from the spaces between the grains, the grain pressure has to increase because the pressure induced by overlaying mass stays the same. The result is compaction of the mineral grains which shows as subsidence on the surface.

2.1.1 Damage due to mining activities

Simultaneous movements in the three directions at the surface are introduced by mining operations. The movements can be expressed as horizontal strain in two directions, vertical strain and differential vertical strain. Horizontal strain is the most common cause of damage. If a structure subsides as a whole, no damage will occur. But when fierce compressional or tensional horizontal strains occur, masonry can be fractured, structural openings can be squeezed or buckling can appear. Hence the amplitude of a movement is of no major importance, but rather the relative movements. The degree of damage is dependent on the characteristics of the structure, e.g. shape, materials used, age. Another cause of severe damage can be the differential vertical strain, more commonly known as tilt. Tilt is the relative vertical strain per unit length horizontally. Structures and piped systems are most affected by this strain [41].

Indirect damage on structures can occur by a change in the ground water table. Consequences can be a decrease in agricultural profit due to drainage, ecological damage due to a change in environment for flora and fauna or a decrease in safety due to the subsidence of dikes [9]. The Netherlands are located below sea level and therefore has a sensitive water balance. The subsidence of the land or rise of the water level can have severe consequences. Deformation on the Earth's surface is accurately observed by law. The mining companies in the Netherlands are obliged to report and measure the effects on the stability of the surface due to their activities. This is supervised by Staatstoezicht op de Mijnen, which is part of the Ministry of Economic Affairs. Another reason to keep an eye on the deformation is the dense population of the Netherlands. When subsidence occurs the probability will be large that this affects a vast group of people. Small deformations can cause noteworthy damage on the water balance or structures.

To prevent damage as much as possible it is necessary to restrict the surface strain and movements, and take precautionary measures based on predictable deformation. Of major importance here is the prediction of deformation and strain. Deformation can be reduced when mining activities are accurately planned. Some characteristics are not to be changed like depth of the cavity or the rock formations overlaying the cavity, but the production volume or drilling locations can influence the subsidence. Usage of a vertical or diagonal shaft influences the effect a boring has on the rock formations. Hence the choice of a location affects the deformation. Measures like backfilling the caverns can be taken to minimize the deformation [41]. When the movements of the Earth's surface can not be influenced any more, for instance structures could be adjusted or the ground water level can be adjusted to prevent damage.

2.2 Solution mining

In both areas of interest solution mining is used for the withdrawal of salt. This technique is based on the addition of a solvent, e.g., water, to the mineral which is to be acquired. Due to this addition the mineral is dissolved and pumped to the surface where the mineral solution is filtered from the solvent. Two possibilities of injecting the solvent can be used [24]. The first possibility is indirect circulation, which makes use of solvent injection from the upper side of the salt layer. Salt close to the roof is dissolved firstly and flows down into the strata where it is collected and pumped to the surface. The second possibility is the injection of the solvent on

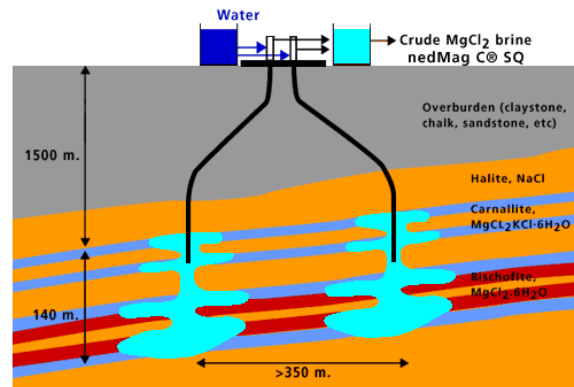


Figure 2.3: The solution mining configuration of Nedmag Industries operating in the Veendam concession area [36]. Indirect circulation and two borings are displayed in this figure.

the lower side of the salt layer where the bottom of the salt layer is dissolved. This technique is called direct circulation. The difference in approach rests in the stability during the solution process. Dissolving from the bottom to the top causes less danger of collapse of the cavern roof compared to dissolving from the top to the bottom. When the overburden introduces a pressure on the cavern and the roof is not able to withstand this pressure due to loss of the support by the removed salt, a roof failure can occur. Solving from the bottom will leave the roof supported by the salt layer and therefore causes less danger of collapse. If the salt is solved from the top a film of oil rests on the solvent to decrease the danger of collapse of the roof due to withstanding the solution of the upper salt layer and therefore increase of the bearable pressure of the overburden by the cavern roof. Figure 2.3 shows the indirect solution mining configuration as used in the Veendam concession area. Another difference in the methods of solution mining is the number of borings used at a location [24]. In some cases one bore hole can be used through which both the solvent is injected and the solution of the mineral is removed. Mostly a single bore hole is used when mining deep salt deposits. Typically two or more borings are used to obtain a higher rate of production.

When high pressure differences and temperatures occur between the salt layer and the cavern, the viscosity of salt decreases. This enables creep, a process in which salt starts flowing to the caverns. High temperatures (377 K [2]) in the 3 kilometer deep Barradeel caverns cause salt to flow with an average speed of 20 meters per year. This is about 100 times faster than measured in other salt caverns experiencing creep [31]. At both test sites use is made of this characteristic of salt. The flow of salt increases the width of the extraction area, which results into a larger than expected subsidence bowl radius on the surface based upon the working width and angle of draw configuration.

Control and stabilization of the cavern are the most troublesome in solution mining [30]. It is difficult to make an accurate prediction of the rate and direction of salt solution and thus it is difficult to accurately predict the shape and size of the cavern [30]. The development of the cavern can be estimated by measuring the salt removed while observing the formation of the cavity using sonar techniques [24]. This information is important for the determination of the subsidence bowl shape and rate. In the Netherlands, Staatstoezicht op de Mijnen determined a minimum distance of 300 meters between different caverns to prevent them to touch and form one large cavern with accompanying risks of collapse [30].

2.3 Surface deformation due to solution mining

Subsidence due to solution mining generally has the shape of a shallow bowl. The deformation pattern depends on the amount of bore holes used [24]. Two (or more) bore holes introduce two (or more) caverns, which eventually will be connected. One bore hole introduces one cavern. The cavern influences the surface deformation, hence with more bore holes lateral caverns with irregular shapes are formed which results in surface deformation differing from surface deformation introduced by one bore hole.

Sinkholes can also occur at the location of the cavern. They are generally formed when not enough attention is paid to the gaining process. As result the cavern can loose stability and collapse. The rate of the sinkhole formation depends on the depth of the cavern and the strength and type of rock formations overlaying the cavern.

The prediction of the subsidence shape and rate is based on the strength and length of the rock formations above the cavern. The composition of these formations is determined by taking samples. Solution mining proposes an extra problem. Because of the addition of a solvent and the extraction of the solution, the rock formation absorbs or loses liquid which influences the strength of the rock over time. Determining the composition of the formation by sampling may not provide enough information, since the reaction of the rock formation to solution mining is not fixed and spatial difference can be present. Another uncertainty in the prediction of the amount and shape of the surface deformation is the unknown size and shape of the cavern. The cavity is obtained by dissolving the salt and therefore the area and volume shape of the pre-dissolved mineral deposit is unclear.

Ground water can also play a major role in the formation of the cavern. When a ground water stream touches the cavern, salt can be washed away and influence the stability of the cavern. This may result in unexpected subsidence or even collapse of the cavern [24].

In the east of the Netherlands salt was found close to the city Hengelo. During the WWII salt was in high demand and as a consequence the government over-produced the salt mines. The stability of the caverns was neglected which resulted in the collapse of some of the caverns and sinkholes appeared on the surface. A study on the Hengelo area [41] showed that some caverns are growing to the surface.

From the study on the Hengelo area, [41], three classes of caverns were formed; zero, one and two. Caverns of class zero possess a thick salt roof which is not able to collapse and expose the upper layers of rock formations, if these upper rock layers are not exposed a sinkhole is unlikely to occur. Class two caverns have a thin top salt layer so that the formation of a sinkhole is likely. As long as the salt layer keeps crumbling these caverns will cause surface deformation, and eventually possibly form a sinkhole. Class one caverns have salt layers experiencing a thickness between the thickness of salt layers in class zero and class two.

The surface deformation evolves in three stages [41]. During stage I the cavern is surrounded by thick salt layers, which are normally stable. No surface subsidence occurs. Caverns of class 0 generally remain in this stage. In stage II salt layers start crumbling and upper rock formations are revealed, deformation on the surface is noticeable. If upper rock formations are sufficiently resilient a cavern will stay in this stage and surface deformation stops. This halted deformation is classified as stage IIb. If the upper rock formation starts cracking, the cavern can work itself up to stage III. This stage eventually results in a sinkhole unless the rock formations stop failing and deformation of the surface stops. This is classified as stage IIIb. Predicting if stage III will occur is impossible. The formation of a sinkhole can take days or hours. Even when prior deformation was minimal, a sinkhole can develop within hours. The recent stage of the cavern can generally be measures with, for instance, the leveling technique.

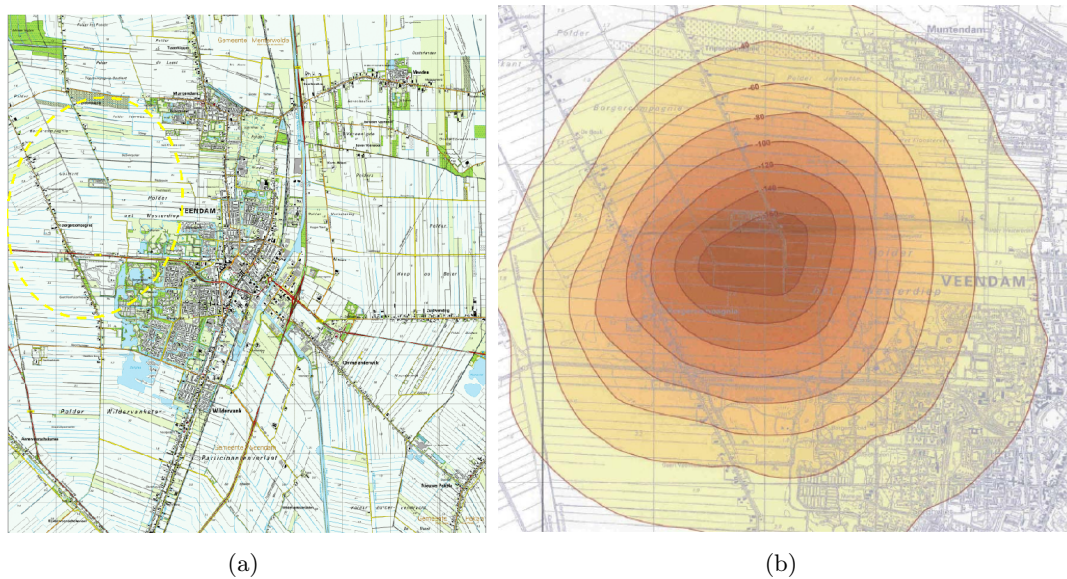


Figure 2.4: (a) The topographic map of the surroundings of Veendam including the concession area indicated by the yellow-dotted line. (b) Subsidence based on leveling measurements over the period 1993-2004 due to salt mining in the Veendam concession. The subsidence is displayed in millimeters. [37]

Currently deformation is monitored using leveling which is a labor-intensive technique. With the use of satellite radar images and interferometry, deformation can be measured in a less labor-intensive manner. An ERS satellite radar image covers an area of $100 \times 100 \text{ km}^2$. These characteristics make radar interferometry an appealing technique. Several parts of the Netherlands are processed using the Persistent Scatterer (PS) processing method. This technique is explained in chapter 3. During analysis of the PS results, small areas highly deforming were poorly or not at all represented by the PS, see figure 1.1. Two of these areas are the Veendam concession where magnesium salt mining is performed by Nedmag Industries and the Barradeel concession where Frisia Salt mines NaCl salt. In this report options to increase the density of the number of indicated Persistent Scatterers (PS) are investigated, tested on these two concession areas.

2.4 Test case Veendam concession

The first test site is situated in the surroundings of Veendam, which is located in the North of the Netherlands at $53^{\circ}06'$ northern latitude and $6^{\circ}52'$ eastern longitude, figure 2.4(a). In 1979 Shell-Billiton and the NOM, a Dutch investment bank, started Magin Magnesia International, which discovered a magnesium chloride deposit in this area [36]. This formed the basis of Magin's Dead Burned Magnesia (DBM) production, which started during 1981. In 1994 the company passed over into the hands of a new consortium of shareholders and was renamed Nedmag Industries Mining and Manufacturing B.V., in which Nedmag stands for Nederlandse Magnesia. Currently Nedmag Industries still mines magnesium chlorides from large salt deposits at depths of over the 1500 meters.

The different products produced by Nedmag are magnesium oxide, magnesium chloride, magnesium hydroxide and calcium chloride [36]. Magnesium oxide is mainly used in the cement and

steel business. With an annual output of more than 165.000 tons, Nedmag is the world's largest producer of synthetic dead burned magnesium oxide (DBM). This production rate is expected to expand to an annual output of 180.000 tons in 2008. Magnesium chloride is used in a wide range of applications, from industrial processes like textile finishing and catalyst production to the manufacture of feed and food additives. Calcium chloride (CaCl_2) can also be used in a wide range of application, e.g., dust control, control fluid in drilling operations and preventing ice bonding to the pavements during winter.

In 1995 salt was mobilized and brought up by means of the squeeze technique. Due to a cavern pressure of 75 bar the viscosity of the solid MgCl_2 salt decreases and enables creep of the salt. Until 1999 a balance was found between the squeeze volume and the withdrawn volume. The cavern volume stayed constant, but deformation occurred due to creeping salt. After 1999 the demand for Magnesium salt increased resulting into greater water injection and loss of the stable cavern volume [35]. Bowl-shaped surface deformation determined by the volume of salt crept to the caverns is assumed, see figure 2.4(b). The subsidence in 2004 relative to the measurement in 1993 are plotted in this figure. Maximum subsidence is located close to the mining location and has a magnitude of approximately 17 cm over the indicated timespan.

The surroundings of Veendam are imaged by the satellites ERS-1 and 2 from 1992 until 2005. Data characteristics of the acquisitions in the two descending and ascending tracks across the mining area are found in appendix A. The deformation area due to salt mining covers about $6 \times 6 \text{ km}^2$ and is mostly agricultural area. The PS analysis is proven to give a coverage over 100 PS/ km^2 [29] in urban area and therefore is assumed to give a respectable representation of large scaled deformation present. The density of PS in agricultural area is usually smaller, because less prominent scatterers are present in agricultural land. If the density of the PS in agricultural can be increased, the deformation patterns can be described better. This is one of the goals of this thesis, see section 1.2.

2.5 Test case Barradeel concession

Frisia Salt B.V. is located in Friesland, one of the northern provinces of the Netherlands. Since 1996 Frisia Salt has mined halite from caverns at 2.8 kilometers depth [12]. The concession is situated at $53^\circ 21'$ northern latitude and $5^\circ 48'$ eastern latitude and covers about $8 \times 8 \text{ km}^2$, see figure 2.5(a). The salt withdrawn from the caverns has a purity of 99.9% making Frisia a production company of international importance. The products vary from industrial salt and salt for the chemical industry to road and consumption salt.

Direct circulation and one bore hole are the typical methods of solution mining used in the Barradeel concession. The first two drilling holes, BAS-1 and BAS-2, were put into production in 1996. BAS-1 is nowadays used as a reserve cavern. In December 2004 BAS-2 was taken out of production, since the by the government permitted volume of salt was reached. These two borings are separated by 500 m. In October 2003 a third production location called BAS-3 started pumping dissolved salt and from April 2006 BAS-4 is used to mine salt. Due to the extraordinary creep characteristics of the salt, larger surface deformation than expected occurred for BAS-1 and 2. The subsidence bowls of BAS-1 and 2 are situated close together and therefore started interfering. BAS-3 and 4 are situated at 3 kilometer distance from each other to prevent the subsidence bowls of the caverns to amplify each other. Oranjewoud B.V. predicted the subsidence in the area due to the mining activities of Frisia based on leveling measurements. Figure 2.5(b) shows the locations of the drilling holes and the deformation based on leveling measure-

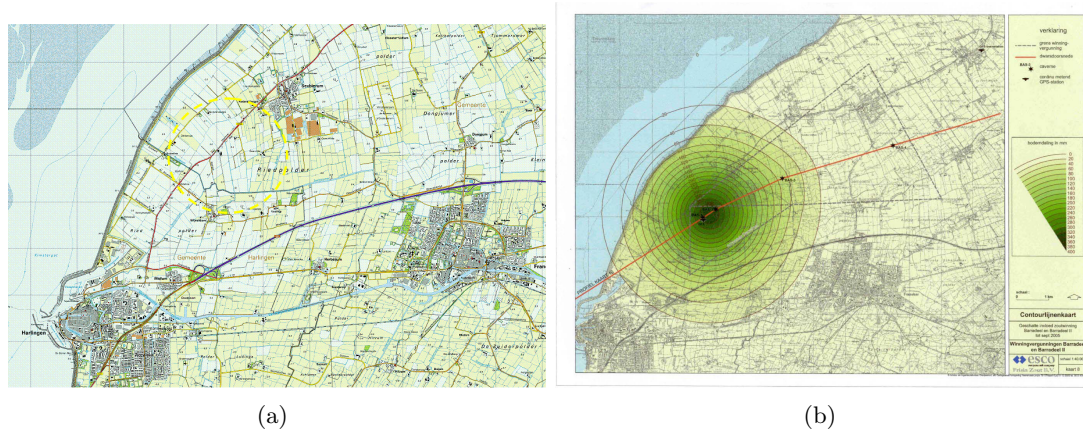


Figure 2.5: (a) A topographic map of the surroundings of Harlingen. The yellow dotted line indicates the position of the Barradeel concession. (b) Interpolated deformation based on leveling measurements caused by salt mining over the period 1995-2005. The original measurement data is corrected for external deformation like deformation due to gas subtraction by Vermilion near Franeker [7].

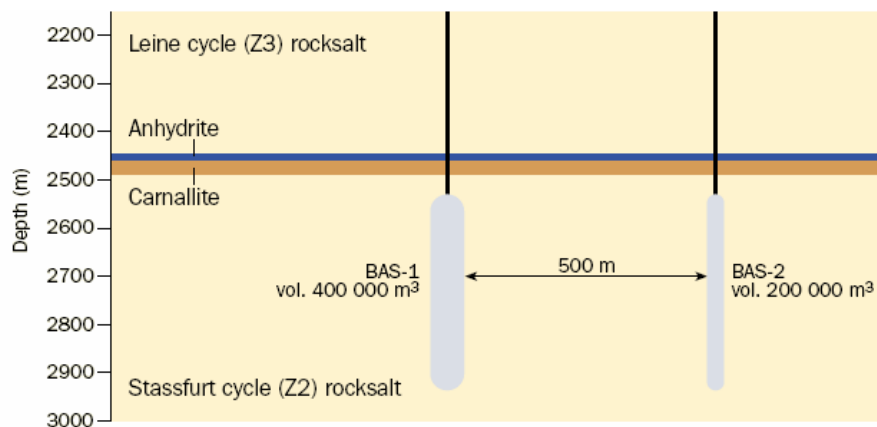


Figure 2.6: Configuration of the caverns BAS-1 and BAS-2 [2]

ments. The location experiencing largest measured deformation is situated close to BAS-1. The total deformation of this measured location amounts 32,7 cm in September 2005 relative to the zero-measurement taken in 1995 [7].

ERS-1 and ERS-2 data available for the Barradeel concession area can be found in appendix A. The data spans a time period from 1992 until 2005. Since BAS-3 began production in 2004, BAS-1 and 2 are of main interest for this test case. A configuration of BAS-1 and 2 can be found in figure 2.6. As with the surroundings of Veendam, the Barradeel area also consists mainly out of non-urbanized land and therefore thwarts a large density of PS.

Chapter 3

Deformation monitoring with InSAR

3.1 Introduction

Radar (RADio Detection And Ranging) introduced many opportunities for detection and ranging of objects, range measuring between the Earth and other planets, mapping of planetary bodies and determining rotation speed of planets with the use of the Doppler effect [23] [3] [18]. Later in the 1990's, using radar interferometry, high-precision measurements of deformation could be made [32] [17].

Imaging of the Earth's surface with satellite space-borne radar began when the ERS-1 was launched in 1991, followed by ERS-2 in 1995 and ENVISAT in 2002. In addition to these ESA satellites the National Space Development Agency of Japan (NASDA) brought the JERS in operation and the Canadian Space Agency (CSA) launched RADARSAT both contributing to the development of radar interferometry. During this period InSAR (Interferometric Synthetic Aperture Radar) started to be recognized as a powerful tool to measure topography and deformation.

InSAR has the advantage of high resolution, 4×20 m, on wide spatial scale, 100×100 m². The main limitations of the technique are temporal and geometrical decorrelation, and phase delay due to atmosphere which is changing in time and space. Temporal decorrelation in the area of interest is caused by physical terrain changes between the images taken at different acquisition times. These changes affect the scattering characteristics of the surface, which results in a loss of coherence [21].

Geometric decorrelation is the introduction of noise due to an increase of the effective distance between two sensors (baseline). The angle of incidence at the Earth's surface between the sensors will generally differ which introduces a spectral shift between the two data spectra. Overlapping parts of the spectra contain useful information and non-overlapping parts contain noise. A shift of the data spectra increasing the non-overlapping sections hence increases noise and therefore decorrelation.

Atmospheric phase delay is mainly caused by the water vapor in the troposphere and can introduce a delay of several centimeters, depending on atmospheric conditions. This delay imposed on an interferogram at a certain epoch is referred to as the Atmospheric Phase Screen (APS).

Persistent Scatterer (PS) techniques have been developed to overcome these three limitations through selection of pixels with coherent scattering properties over time, see section 3.4. Using PS techniques the time span of useful SAR images and their sampling through time, temporal resolution, is greatly increased, but spatial resolution is decreased by selection of inhomogeneously spread pixels with a stable phase behavior out a stack of tens of interferograms.

This chapter treats the basic theory on InSAR and the Persistent Scatterer technique, which can be found in the first and the second section respectively. In the third section a quality description of the PS technique is given.

3.2 Principles of InSAR

The Earth is monitored by satellites which are equipped with radar instruments. The radar emits electromagnetic pulses in radio and microwave frequency band and detects the reflections of the pulses from objects in the line of sight of the radar. The satellites ERS-1 and ERS-2 both emit pulses in the C-band with a wavelength of 5.66 cm. Combining the advantage of an active system with a ground track ensuring global coverage, enables the satellite to monitor the entire Earth as the satellite passes.

Scatterers situated on Earth scatter back the pulses emitted by the side-looking radar device. The intensity of this scattered signal depends on the physical properties of the scatterer. Figure 3.1 shows the imaging geometry. When the pulse is received back at the satellite the two-way travel-time is recorded. Multiplication of this time with the speed of light and dividing by two, results into the range from satellite to scatterer. The data of 100 km wide strips of the Earth are stored. With the use of a synthetic long antenna and the chirp compression technique a resolution of 4 by 20 meters is achieved [21].

Single Look Complex (SLC) images are post-processed images composed out of complex values for every pixel spaced on a regular grid. These complex values, or phasors, contain the amplitude and phase summation of all scattering elements present in the resolution cell. A complex interferogram is created out of the phase differences between two sub-pixel coregistered images obtained at different acquisitions times. The differences between the phases of the pixels are obtained by complex multiplication. After subtraction of the phase introduced by a chosen reference datum, the differential phases visualize topography and deformation of the area imaged, and possibly atmospheric phase delay, orbit errors and noise. A color cycle in the interferogram is called a fringe, representing one phase cycle.

The geometric relationship between differential phases and topography stems from the interferometric configuration, figure 3.2. Two points at the same distance from a sensor can not be distinguished with single distance measurements. Observing angular differences $\partial\theta$ between point P' and P with two sensors separated by the baseline B , enables the calculation of the height of point P , H_P , above a reference surface. The angular difference need to be derived from distance measurements, as the instruments are not capable of directly measuring this difference. Because the stored travel-time does not approach the required millimeter accuracy, the observed phases of the reflected pulse are used.

As the baseline changes, the data spectrum shifts due to a difference in incidence angle. If the baseline increases, the overlapping part in the data spectrum decreases, resulting in decorrelation. The correlation is lost when the baseline reaches the critical baseline. This critical baseline for flat terrain is 1.1 km for ERS satellites.

The phase observation is the contribution of (i) the phase proportional to the range and (ii) the phase due to scattering characteristics of the resolution cell. The last term is assumed to give an identical phase contribution when the phase is measured under the same conditions at a different time. This cancels out the term – the resolution cell is said to be coherent. At the moment the pulse is received the phase can be measured. The number of phase cycles, ambiguities, traversed before the last cycle hits the radar device is unknown. Solving this unknown ambiguity of the

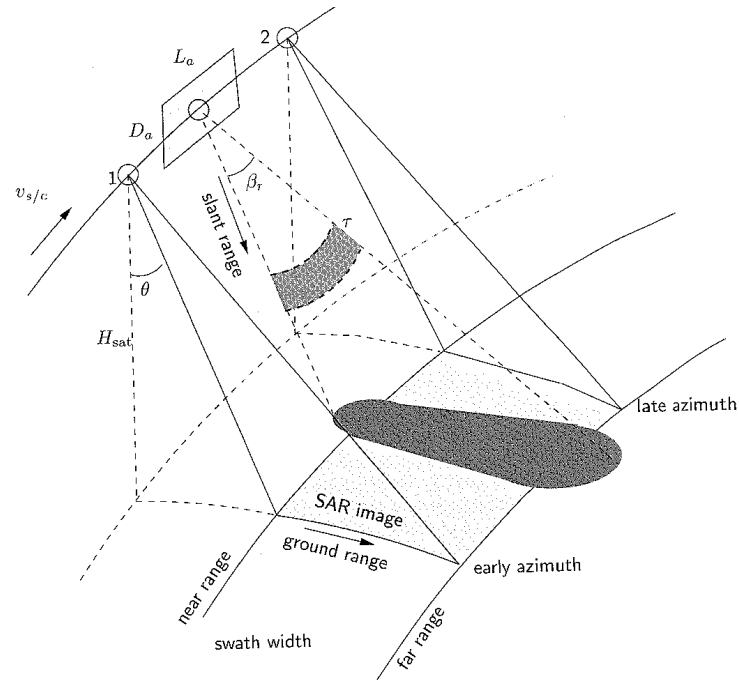


Figure 3.1: Geometry of a SAR acquisition. The dark shaded area indicates the footprint of a single pulse. The light shaded area represents the total SAR image, composed out of the pulses emitted while flying over the area of interest with velocity v_s/c . L_a and D_a are the length respectively the width of the antenna, θ the look angle of the sensor and β_r the angular beam-width in range direction [21].

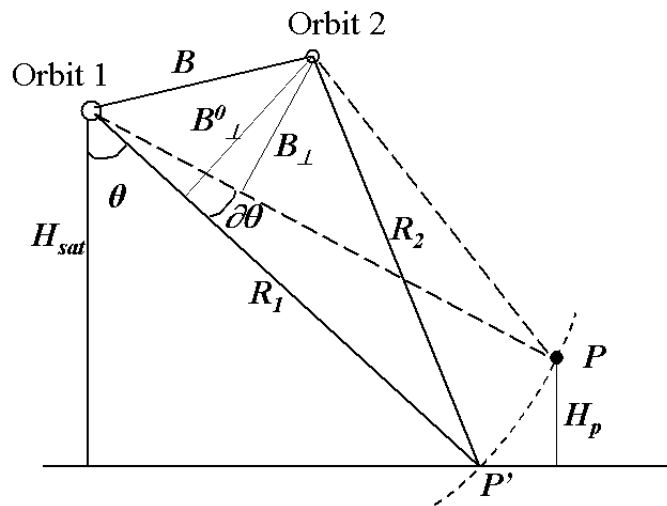


Figure 3.2: Interferometric configuration. Two different acquisitions enable the calculation of the height of point P , H_p . The look angle change, $\partial\theta$ is determined from the phase difference between the acquisitions and can be rewritten into H_p with the use of geometry (Figure based on [21]).

differential phase for is defined as unwrapping. The unwrapped differential phase follows

$$\partial\phi = \phi_{\text{topo}} + \phi_{\text{defo}} + \phi_{\text{atmo}} + \phi_{\text{orbit}} + \phi_{\text{noise}}. \quad (3.1)$$

The parameters comprising this equation are the phases introduced by the topography present in the area imaged ϕ_{topo} , the phase difference due to deformation between the two acquisitions ϕ_{defo} , the atmospheric phase delay ϕ_{atmo} , orbit errors ϕ_{orbit} , and noise ϕ_{noise} . After rewriting the model to the main parameters and neglecting ϕ_{atmo} , ϕ_{orbit} and ϕ_{noise}

$$\partial\phi_P = -\frac{4\pi}{\lambda} \left(D_P + \frac{B_{\perp}^0}{R_1 \sin \theta^0} H_P \right), \quad (3.2)$$

remains [21]. The phase difference of the signals scattered by pixel P at different acquisition moments is $\partial\phi_P$, and λ is the wavelength of the carrier signal. D_p is the surface displacement in the line-of-sight of the satellite, B_{\perp} is the perpendicular baseline, R_1 is the range between satellite and point P on the Earth's surface, θ^0 the initial value of the look angle of the sensor obtained from the reference surface and H_P is the height of point P with respect to the reference surface. The right term in front of H_P is called the height-to-phase conversion factor β

$$\beta = \frac{4\pi}{\lambda} \cdot \frac{B_{\perp}^0}{R_1 \sin \theta^0}. \quad (3.3)$$

The relation between the phase difference, height and displacement of the point P can be found in equation (3.2), after substitution of the phase difference, $\partial\phi_P$, with 2π . The sensitivity of a fringe for topography is based on the effective distance between the sensors. When the baseline increases (with the critical baseline as a limit), the height-to-phase conversion factor increases, see equation (3.2), resulting in a smaller measurable height by one fringe, and the topography can be more accurately measured by the phase. The deformation phase is insensitive for difference in the configurations, but depends on the wavelength of the emitted signal [21]. The sensitivity for deformation is approximately 1000 times larger than that for topography.

3.3 Principles of Persistent Scatterer Analysis

In the late 1990s Persistent Scatterer (PS) techniques were first introduced by [14]. These techniques were developed to overcome three main limitations of Synthetic Aperture Radar Interferometry (InSAR), i.e. temporal decorrelation, geometrical decorrelation and phase delay due to atmosphere. The PS technique uses tens of images to identify pixels with coherent scattering properties over time, which are called Persistent Scatterers. Because a stable phase through time is required, pixels experiencing temporal decorrelation are eliminated. The PSs are inhomogeneously spread over the image and are often reflections of man-made objects [47]. A PS density over 100 PS/km² can be obtained in urban areas [29].

The reflected pulse by corner reflectors, trihedral reflectors, possesses a large amplitude and stable scattering properties, making it an ideal PS. Due to their scattering properties a relatively large spectrum of angle of incidences are scattered by the reflectors and received by the satellite [19]. Hence observing the reflection from different angles of incidence will not result into geometrical deformation. The scattering properties of a frequently occurring double-bounce reflection between the Earth's surface and a wall of a house approaches the scattering properties of a corner reflection [27].

Usage of a large stack of interferograms enables filtering of the atmospheric contribution to the phase. The filter makes us of the spatial correlation and temporal decorrelation to estimate the atmospheric phase screen, see section 3.3.1.

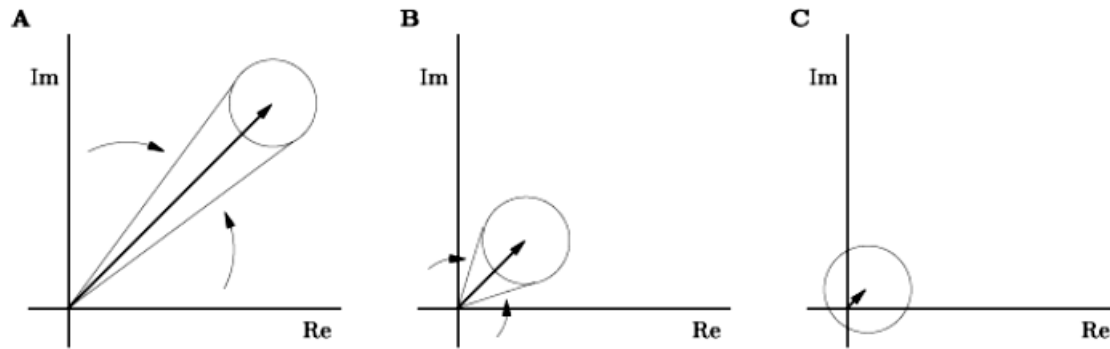


Figure 3.3: Phasor with an error ellipse in the complex plane. The errors are assumed to be equal in imaginary and real situation. The amplitude of the phasor influences the phase variance, the angle between the arrows, as can be derived from figure **A** and **B**. The phase variance in figure **A** is less than in figure **B** due to the difference in amplitude. In Figure **C** the phase variance is large and therefore nearly worthless [21].

3.3.1 PS processing steps

The PS analysis is divided into several steps which are explained in this section. This paragraph gives a short introduction to the processing steps, the subsequent paragraphs will elaborate these steps.

A stack of interferograms compiled out of calibrated scenes, coregistered to a chosen master interferogram is used as input. The master image is selected maximizing the (predicted) total coherence of the interferometric stack, based on the perpendicular baseline, temporal baseline and the mean Doppler centroid frequency difference [25]. The first step of the analysis is a selection of pixels with a low amplitude dispersion, PS Candidates (PSC). As explained in the subsequent paragraph, these pixels are presumably the most coherent pixels. Between these points a network is formed, which enables calculation of the topographic height and displacement of a PS per epoch relative to a chosen reference point. First the parameters of interest and ambiguities are estimated for the arcs using the Integer Least Squares approach [43]. The parameters of interest can spatially be unwrapped, with respect to an arbitrary reference point, if possible in a stable area, and obtained per PSC. PSCs that cannot be tested or experience ambiguities not fitting in the unwrapped network are rejected as PS and not taken into account in further processing steps. A smaller set of PSs remains to which filters are applied for the separation of the atmospheric phase. The atmospheric phase screen (APS) of the interferograms is computed using a geostatistical interpolation method, which is sequentially subtracted from the differential phase of the PSCs. Processing steps starting from forming the network until spatial unwrapping the arcs will be performed again using the phases corrected for the atmosphere. Finally Potential PSs (PSPs) are used to densify the PSs. Since the PSPs do not influence the constructed network, they can be less coherent than PSCs and hence the amplitude dispersion threshold for selection of these pixels is set less strict than for PSCs. The PSPs are connected to the PSCs and parameters will be estimated for these points. PSPs not fitting the network are rejected. A flow diagram of the process can be found in figure 3.4.

PS Selection Based on the amplitude dispersion D_a of a pixel, the PS selection creates a set of Persistent Scatterer Candidates (PSCs) and a set of Potential Persistent Scatterers (PSPs). PSCs are used to form a network from which the unknown parameters topography and deformation are derived.

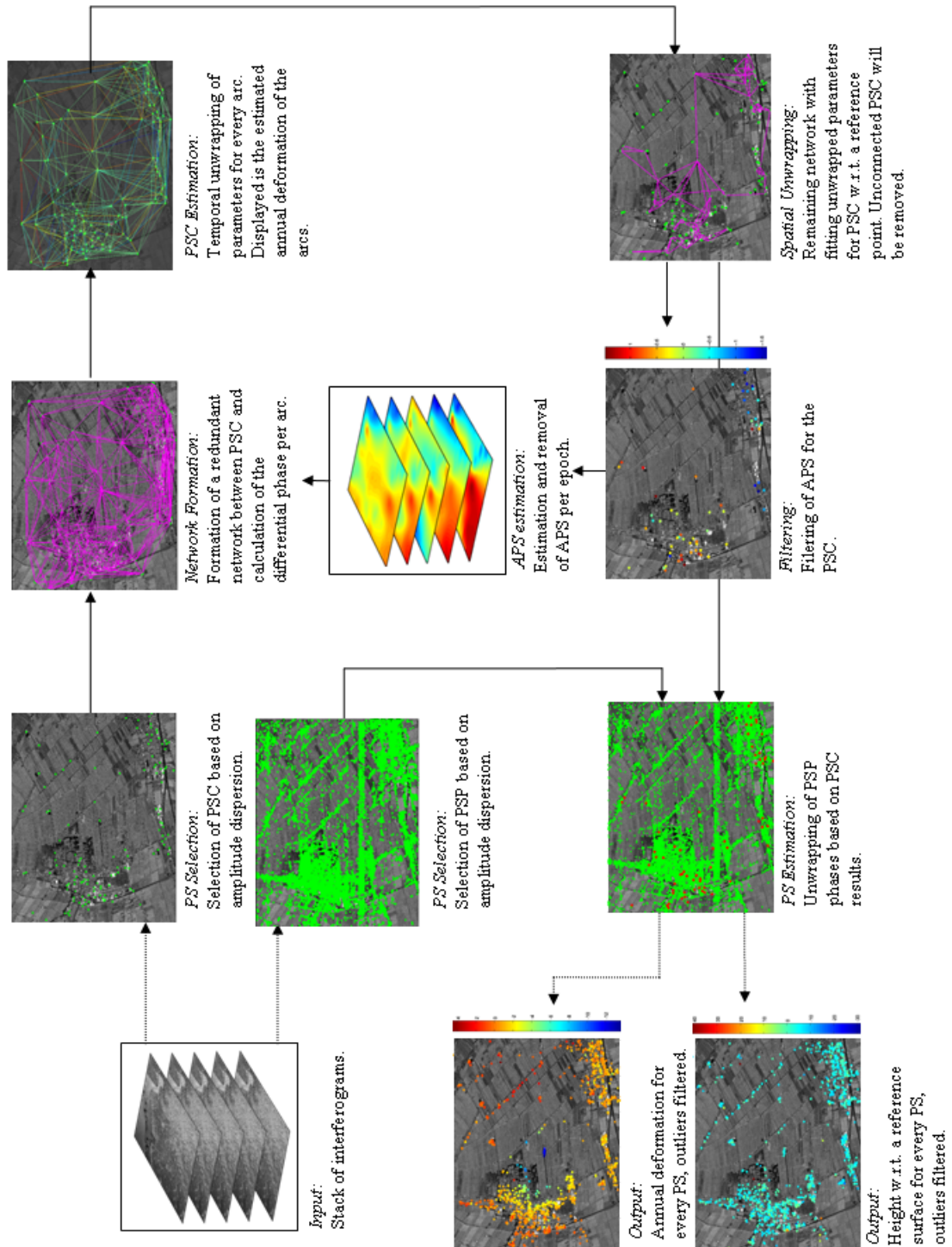


Figure 3.4: Flow diagram of the ps analysis

PSC	Persistent Scatterer Candidate	Construct the initial network
PSP	Potential Persistent Scatterer	Densify the final set of PS
PS	Persistent Scatterer	Group of PSC and PSP which parameters and ambiguities fit the network

Table 3.1: Definitions PSC, PSP and PS

The PSPs are applied to densify the network as is explained later in this section. Since the wrapped phase still contains unknown signal contributions, identifying potentially coherent pixels, potential PSs, without analysis of the phase is not possible at the moment. Figure 3.3 illustrates the relationship between the amplitude magnitude and phase variance. Hence a certain target is a potential PS when its received reflection has a relatively large amplitude and constant phase over time. The relationship between the phase standard deviation σ_ϕ and the amplitude dispersion of a certain pixel is described in [15] as

$$D_a = \frac{\sigma_a}{\bar{a}} \approx \hat{\sigma}_\phi, \quad (3.4)$$

where the ratio of the temporal standard deviation of the amplitude is σ_a , and the temporal mean of the amplitude is \bar{a} . Thus a pixel with a constant, relatively large, amplitude during all acquisitions is expected to have a small phase dispersion. Typical amplitude dispersions set as threshold for PSC selection are between 0.25 and 0.4. In [15] it has been shown that the estimation of the phase stability based on the amplitude dispersion approaches reality very well if $\sigma_\phi < 0.25$ [rad]. Figure 3.5 shows that there is no linear relation between the amplitude dispersion and phase standard deviation for larger values. Low signal-to-noise ratios tend to an amplitude dispersion of 0.5 [rad] [15] [25]. But pixels with a smaller amplitude dispersion are expected to have smaller phase standard deviation. This makes thresholding on the amplitude dispersion a useful tool of selecting pixels with expected small phase variances.

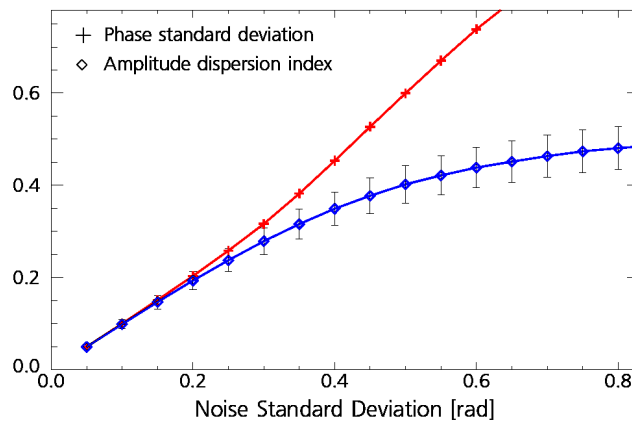


Figure 3.5: Simulation of the amplitude dispersion index. A complex variable $z = s + n$ is simulated at 5000 points. The signal was fixed to $s = 1$, while the noise standard deviation on the real and imaginary parts of n was gradually incremented from 0.05 to 0.8. 33 interferograms are supposed to be available. The mean estimated dispersion D_a (diamonds) and their standard deviations are plotted as function of the noise standard deviation, together with the phase standard deviation σ_ϕ (plus marks). Small values of the amplitude dispersion index are a good estimate for the phase standard deviation. This simulation is performed by [25] based on [15].

A grid is used to achieve a homogeneous distribution of the PSCs over the area. Because

the estimated atmospheric signal will be interpolated over the network composed by the PSCs, a homogeneous distribution is preferred.

For each grid cell the pixel with minimal amplitude dispersion is selected. This value is compared to a certain threshold specified by the user, which serves as selection criteria. Points near to each other with a low amplitude dispersion are not selected as PSC to avoid the selection of side lobes, introduced by strong reflections in the radar data. The selection of point near each other is prevented by a shift of the grid borders of half the grid size in both directions. The point with the smallest amplitude dispersion is selected. This guarantees a minimum distance between PSCs equal to the cell width [26].

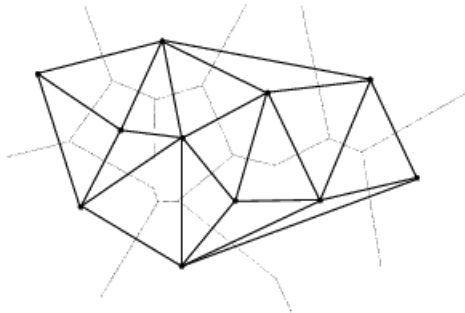


Figure 3.6: Delaunay triangulation based on the Voronoi diagram (shaded lines)

Forming a network The selected PSCs are connected by arcs to form a network. The network enables the formation of relative differential phase observations. This way, influences of error sources such as atmospheric and orbit errors are minimized as differences between nearby points of these error sources are small [14]. The redundant network can be defined by, e.g., Delaunay triangulation, which tries to maximize the minimum angle of all angles in the triangles constructed by the PSCs (figure 3.6). Redundancy is required to detect incorrect estimations of parameters of interest.

PSC parameter estimation After the formation of a network, the unwrapped estimations of the relative deformation and height differences of an arc with respect to the reference surface can be calculated. Algorithms, like the ambiguity function [8] [15], LAMBDA [42] or bootstrapping [44], can be selected as unwrapping algorithms. The ambiguity function treats the observations as equally weighted and does not give the quality of the estimated parameters, in contrast to the LAMBDA and bootstrapping method. A functional model has to be specified in order to estimate the relative deformation and topographic height. A model for the unwrapped differential interferometric phase, $\partial\phi$, can be found in equation (3.1). In this equation the scattering phase term ϕ_{obj} introduced by the path length traveled in the resolution cell to arrive at the object position is not taken into account. This term is introduced since PSs are situated at a sub-pixel positions. When the phase is interpolated at the exact sub-pixel position, ϕ_{obj} vanishes. The sub-pixel position can also be estimated as an extra parameter [25].

The topographic phase ϕ_{topo} has an approximately linear relation with the perpendicular baseline and for a certain pixel in the observed interferogram this can be written as

$$\phi_{topo} = \beta \cdot \Delta_h, \quad (3.5)$$

with β the height-to-phase conversion factor for the target, see equation (3.2), and Δ_h the topographic height, which is the difference between the height of the PSC and the reference

PSC [15]. The displacement of a Persistent Scatterer can be modeled with a linear model in time

$$\phi_{defo} = -\frac{4\pi}{\lambda}T \cdot \Delta_d. \quad (3.6)$$

In which λ is the wavelength of the carrier signal, T the temporal baseline with respect to the master scene and Δ_d the average displacement rate of a pixel. The atmospheric and noise phase are not modeled, but will be estimated from the residues and subsequently filtered. Note that when the deformation behavior differs from the assumed linear behavior in time, it will be included in the noise term. A discussion about non-linear behavior can be found in [14] and [25]. The arcs will be unwrapped based upon minimal residues which is assumed to be the optimal solution of the functional model

$$\partial\phi = \beta \cdot \Delta_h - \frac{4\pi}{\lambda}T \cdot \Delta_d + \phi_{error} + 2k\pi. \quad (3.7)$$

Spatial unwrapping The parameters of interest and interferometric differential phases are now known for every arc. To obtain these at every Persistent Scatterer Candidate the parameters of interest obtained for the arcs need to be integrated with respect to a reference point. Due to noise and model imperfections residues will be present after integration. The unwrapping errors can be identified and rejected using the spatial network. A three-step procedure is used for this. First, arcs with a questionable precision are rejected. This precision can be deduced from, e.g., low temporal ensemble coherence or large least-squares residues. The estimated temporal ensemble coherence is defined as

$$\hat{\gamma}_{x,y} = \frac{1}{K} \sum_{k=1}^K e^{(j \cdot \phi_{error_{x,y}})}, \quad (3.8)$$

where $\hat{\gamma}$ resembles the estimate of the ensemble coherence, K is the total amount of interferograms and j is the imaginary number. The residual, $\phi_{error_{x,y}}$ is the difference between the modeled and observed phase at location (x, y) in the observed interferogram based on equation (3.7).

One arc connected to a PSC can not be tested and two arcs connected can not identify the arc containing errors, hence three arcs are necessary to detect unwrapping errors. In the second step a PSC not connected to at least three arcs is rejected.

The third step is the identification of unwrapping errors. Correcting ambiguities can result into doubtful answers, since over-correction can introduce ambiguities not representing reality. Therefore Persistent Scatterers with arcs obtaining unwrapped parameters not that do not fit in the network are removed. The unwrapped parameters of the arcs and PSCs that remain are assumed to fit in the network without residues and to be unwrapped correctly, hence quality control methods and error propagation algorithms can be used. Finally parameters of interest are estimated again, using the adapted network.

Filtering After spatial unwrapping, the topographic height and relative deformation for every epoch is obtained. When these parameters are correctly estimated, the residual phase will contain mainly atmospheric delay, non-modeled deformation, orbit errors, and noise. Non-modeled deformation is separated from the atmospheric and orbit phase during this step.

The Atmospheric Phase Screen (APS) of the master is estimated by averaging the residual phases over all the interferograms. Non-linear deformation is also present in the residual phase, which contains mainly atmospheric phase. Atmosphere is assumed to be correlated in space, but uncorrelated in time [20]. Hence estimation of atmosphere can be done with a low-pass filter in the spatial domain and a high-pass filter in time-domain. Temporal correlation is assumed for

non-modeled deformation. After applying the filters on the residual phases, the APS for every slave is retrieved [14].

Estimation of the APS The atmospheric phase screen at the PSC locations is assumed to be known after filtering. With this knowledge the APS for the whole image needs to be created, to be able to subtract the APS also at PSP locations. To estimate this atmospheric phase screen, a geostatistical interpolation method (kriging) is used. A covariance function is estimated, which describes the spatial behavior of the atmosphere, to predict the atmospheric contribution for the whole scene. The predictions are performed using block kriging (the division of data in blocks), due to the large amount of data. To avoid large transitions between the blocks, spline smoothing is used on the APS.

The calculated APS is now subtracted from the interferogram. The steps starting from forming a network until estimating the APS, are repeated once more with phases corrected for atmosphere. A network is formed and the PSC estimation is performed once more to estimate the parameters of interest of the initial PSC selection. These parameters are used in the next step.

PS estimation During the first step Potential Persistent Scatterers (PSPs) were selected based on a higher amplitude dispersion threshold than the PSCs. The interferometric phases are unwrapped and the parameters are estimated for these PSPs during this step. Equal as during the PSC estimation step, the PSPs are independently unwrapped relative to the three closest PSCs defined in the previous, estimation of the APS, step. The estimated ambiguities, from which the reliabilities are considerably improved, can be tested again. The PSPs are stored when at least two of the arcs fit to the network of unwrapped PSCs. The parameters, topographic height, deformation parameters and residual phase (assumed to also represent non-modeled deformation) for the PSs are now estimated with respect to a single reference point.

3.3.2 Quality description

Currently the quality of PS-InSAR is still undetermined, introduced by the lack of knowledge of the causes influencing the quality. Under good conditions the precision of the line-of-sight relative deformation can reach the millimeter-range [28]. An example of causes influencing the precision of the measurements are atmospheric effects, functional model imperfections, the number of interferograms, the temporal distribution of the data, and the scattering properties of the target.

Precision and reliability describe the quality of estimated parameters. The variability of observations and estimators of the unknowns are defined by the precision, while the reliability describes the sensitivity of the estimators for model errors [45]. These two terms stand alone. When the observations have a high precision, it is not necessary that the unknown parameters are estimated reliable.

Precision Precision can be divided in internal and external precision. The internal precision describes the dispersion of the estimated measurements $Q_{\hat{y}}$ and external precision is the dispersion of the estimated unknown parameters $Q_{\hat{x}}$. This precision is calculated with the use of the propagation law of variances. Making use of the Best Linear Unbiased Estimator (BLUE) the precision results into [45]:

$$Q_{\hat{y}} = A Q_{\hat{x}} A^T \text{ and} \quad (3.9)$$

$$Q_{\hat{x}} = (A^T Q_y A)^{-1} \quad (3.10)$$

where the double-difference matrix (DD) is described by the first matrix on the right side of equation (3.12).

The covariance matrix of deformation is given in equation (3.15). No correlation is assumed between the locations due to temporal correlation, hence these values are set zero. Correlations between similar locations in different interferograms are present and are therefore present in the covariance matrix of the deformation

$$Q_{defo} = [DD] \begin{bmatrix} C_{defo,i}^{00} & & C_{defo,i}^{10} & \cdots & C_{defo,i}^{k0} & \\ C_{defo,i}^{01} & C_{defo,j}^{00} & C_{defo,i}^{11} & \cdots & C_{defo,i}^{k1} & C_{defo,j}^{k0} \\ C_{defo,i}^{01} & C_{defo,j}^{01} & C_{defo,j}^{11} & \cdots & C_{defo,i}^{k1} & C_{defo,j}^{k1} \\ \vdots & \vdots & \vdots & \vdots & \vdots & \vdots \\ C_{defo,i}^{0k} & & C_{defo,i}^{1k} & \cdots & C_{defo,i}^{kk} & \\ C_{defo,i}^{0k} & C_{defo,j}^{0k} & C_{defo,j}^{1k} & \cdots & C_{defo,i}^{kk} & C_{defo,j}^{kk} \end{bmatrix} [DD]^T. \quad (3.15)$$

The variance-covariance matrices of the different contributions can be composed with these described covariance matrices and results in

$$Q_y = \begin{bmatrix} 4C^{00} & 2C^{01} & \cdots & 2C^{0k} \\ 2C^{10} & 4C^{11} & \cdots & 2C^{1k} \\ \vdots & \vdots & \ddots & \vdots \\ 2C^{k0} & 2C^{k1} & \cdots & 4C^{kk} \end{bmatrix}. \quad (3.16)$$

When k is the number of interferograms, and the size of the matrix is $k \times k$.

Table 3.2 presents the stochastic parameters used for the PS analysis. The values assigned to the parameters are initial estimates. The exact stochastic parameters are not known.

Parameter	Value
σ_{noise}	$\pi^*30/180$
σ_{atmo}	$\pi^*20/180$
r_{atmo}	3000 [m]
σ_{defo}	$\pi^*20/180$
r_{defo}	1 [year]

Table 3.2: Stochastic parameter for PS-InSAR

The estimation of \hat{e} and the specified variance-covariance matrix are used to estimate the variance factor σ^2 of the data. Multiplication of this factor with Q_y results into a new variance-covariance matrix, which more accurately describes the precision of the observations. The precision of the estimated unknown parameters $Q_{\hat{x}}$ is acquired according to equation (5.2) using the new variance-covariance matrix of the observations.

Reliability The internal reliability is a measure of the model error which can be detected with a certain probability. Reliability of the models can be inferred using, e.g., the overall model test (OMT) which tests an alternative hypothesis H_a against the null-hypothesis H_0 . In this test, the number of independent errors q is equal to the difference between the number of observations m and the number of unknowns n [45]. This test statistic is described as

$$\underline{T}_{q=m-n} = \hat{e}^T Q_y^{-1} \hat{e}, \quad (3.17)$$

where $\hat{e} = y - A\hat{x}$ and the test statistics are distributed as

$$H_0 : \underline{T}_q \sim \chi^2(m - n, 0) \text{ and } H_a : \underline{T}_q \sim \chi^2(m - n, \lambda),$$

with λ is the non-centrality parameter [45].

The OMT is implemented in the unwrapping procedure to test the functional model, with different estimates of topographic height and deformation, and the unwrapped phase. The estimated parameters resulting into the smallest OMT are accepted.

The reliability of the PS results is described by the OMT between the estimated linear deformation and the actual estimated deformation of a certain pixel.

Chapter 4

PS identification optimization methods

The two test sites Veendam and Barradeel are introduced in chapter 2. Figure 1.1 shows the annual deformation of the north of the Netherlands obtained from the Persistent Scatterer (PS) analysis, the test sites are encircled. Deformation due to mining activities is present in the concession areas and as shown in figure 1.1 a low density of inhomogeneously spread PSs describes this deformation. In these cases deriving the deformation pattern is difficult due to the low density of PSs. Increasing the number of PSs can increase the reliability of the deduced pattern, from which physical processes in the subsurface can be derived. When the relation between subsurface activities and deformation is known, prediction models can be made to estimate deformation due to these activities.

Persistent scatterers are points with coherent scattering properties over time, recognized as such by the PS analysis. Three possible causes for the low density of PSs can be indicated:

- the absence of coherent scatterers (PSs) in the areas of interest,
- points possessing coherent scattering properties not being identified as PSC/PSP during the selection step, or
- PSC/PSP possessing coherent scattering properties being rejected as PS during the subsequent processing steps.

The first cause is a consequence of the scattering properties of objects on the Earth's surface, and since these properties can not be changed this research concentrates on the last two potential causes. The implemented methods which are suggested to optimize the identification success rate of PSs, are described in this chapter. The results of the methods tested on the test sites are discussed in chapter 5.

The first section describes an optimization method for the PS *selection*. This method is developed to identify points possessing coherent scattering properties, which are not being identified by the conventional amplitude dispersion method. The second section deals with PS *testing* optimization. The methods are suggested to accept the PSCs/PSPs possessing coherent scattering properties, which are rejected as PS during the parameters estimation steps in the conventional PS analysis.

4.1 PS selection optimization

The PS selection method is based on the amplitude dispersion of a pixel, see section 3.3.1. As selection criterion, amplitude dispersion thresholds are set for the selection of PS Candidates

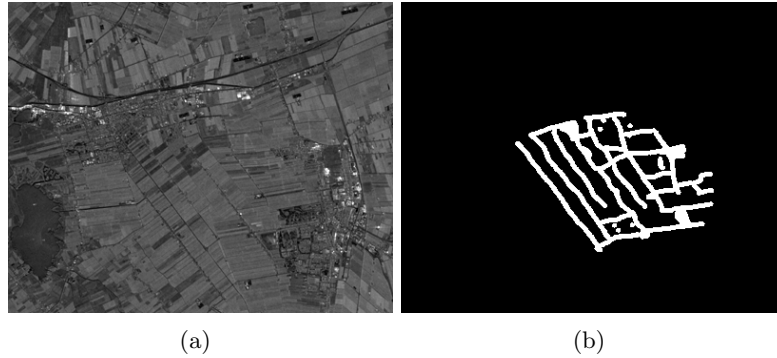


Figure 4.1: (a) Multi reflectivity map of track 380. The map is composed out of averaged amplitudes for every pixel of the interferograms from the stack. (b) Mask of track 380 in which the white pixels correspond with pixels of interest.

(PSCs) and for the selection of the PS Potentials (PSPs). PSCs are points experiencing a low amplitude dispersion and are therefore assumed to have coherent scattering characteristics over time. Since PSPs are connected and tested to the PSCs to increase the density of the PS, the threshold for the PSP selection can be chosen less critical than for the PSC selection. This results in a larger amount of selected PSPs than the amount of selected PSCs.

Selection of all pixels in an image to increase the density of PSs, results into an unacceptable long computation time. The amplitude dispersion is utilized to select the coherent pixels. A larger amplitude dispersion increases the number of selected pixels, but introduces a decrease in the signal-to-noise ratio (see figure 3.4). Although points possessing coherent scattering properties are still present in the subset of pixels with an amplitude dispersion larger than the chosen threshold, they will not be taken into account throughout the process to decrease computation time.

A method to identify points possessing coherent scattering properties, not identified by the amplitude dispersion method, is discussed in this section. The method is based on manual selection of pixels of interest.

4.1.1 Manual PS identification

Man-made constructions such as buildings, bridges and poles tend to be identified as PS due to their scattering properties [47]. Double-bounce reflections often occur on these constructions. The coherence of the reflections of these constructions can approach the coherence of the triple-bounce reflection of a corner reflector, which is a perfect PS [27]. If a pixel experiences an amplitude dispersion above the specified threshold it probably has incoherent temporal phase, see section 3.3.1, but this does not necessary has to be the case. Because pixels containing man-made constructions are likely to be PSs, but can be rejected due to their amplitude dispersion index, a mask is created to select these pixels. They can directly be considered as PSPs by means of the mask, without proceeding through the selection. A matrix with dimensions identical to the interferogram, composed out of ones at locations containing the features of interest and zeros otherwise, is specified as input for the PS analysis.

Creation of the mask is performed with a graphical interface. A multi reflectivity map is composed out of averaged amplitudes for every pixel of the interferograms from the stack. This map is read into the graphical interface. Manually a mask is drawn on the multi reflectivity map. Figure 4.1 shows an example of the mask created for track 380 covering the Veendam concession. The white pattern covers the pixels containing the man-made features in the area experiencing low PS density. The drawn mask is converted to a matrix which is the same size as the image.

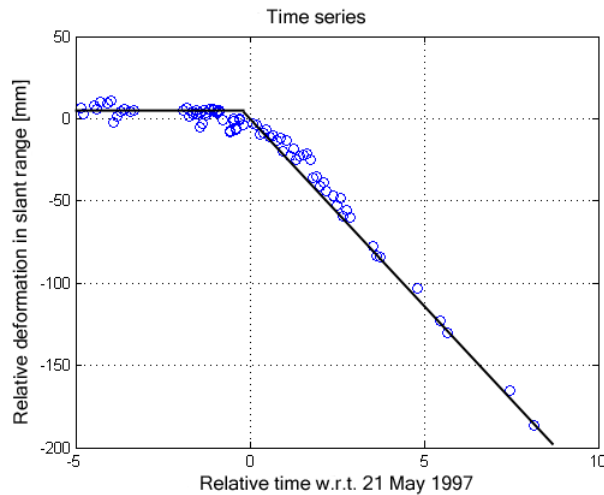


Figure 4.2: Time series of a pixel situated in the subsidence bowl of the Barradeel concession. The circles represent the estimated relative deformation per epoch. According to the horizontal part of the graph subsidence started around 1996 and developed linear over time.

The positions of the ones in the matrix indicate the positions of the pixels in the image which are selected and are not compared to the set amplitude dispersion threshold.

4.2 PS testing optimization

PS processing steps influence the identification of Persistent Scatterers and their estimated topographic height and deformation. This section focuses on the influence of ambiguity resolution. The acceptance of PSs is based on the functional model implemented for ambiguity resolution. The functional model is described by eq. (3.7). The topographic phase ϕ_{topo} has an approximately linear relation with the perpendicular baseline. The displacement of a Persistent Scatterer is modeled with a time-linear model. In certain cases the actual vertical surface movement is non-linear, hence the actual deformation is poorly represented by the best fitting linear model.

A frequently occurring non-linear model is the breakpoint model. This model is shown in figure 4.2. For SLC images acquired a few years in prior to mining activities, no deformation is present in the interferograms during these years. This is represented by the horizontal part of the graph in the figure. When deformation due to mining activities occurs on the Earth's surface, the time series experiences a change in slope described by the second linear part of the graph. Time series of the deformation of PSs situated in the subsidence bowls in the Barradeel and Veendam concession show resemblance with the breakpoint model.

When the linear model, does not fit the temporal non-linear behavior of a PS within specified boundaries by the user, the PS is rejected. Rejection of such a PS is likely because the deformation is approached by a model not describing the actual deformation. This section describes methods influencing the ambiguity resolution step. The first method is subtraction of deformation surfaces estimated for every epoch. These surfaces are estimated with the use of a bowl equation or bilinear interpolation method. After subtraction of estimated wrapped deformation from the differential phase, the residues between the estimated deformation and actual deformation present in the phases are unwrapped. Subtraction of estimated deformation is performed to decrease the variance of the phase and therefore obtain a phase that can be described by a linear deformation model more accurately. The second method is the implementation of the

breakpoint model in the functional model.

4.2.1 Non-linear deformation subtraction

To overcome rejection of PSCs/PSPs deforming non-linear over time, the deformation pattern respectively to the chosen master epoch is estimated for every epoch. The estimated deformation is wrapped and converted into the phase component by means of the conversion factor

$$r2ph = -\frac{4\pi}{\lambda}, \quad (4.1)$$

derived from equation (3.2). The estimated deformation phase component is subtracted from the differential phase. After subtraction of the estimated deformation phase the residual deformation phase, atmospheric phase, topographic component, ambiguity, possible orbit errors and a noise term remains.

Two models are implemented for the estimation of non-linear deformation. These are the subsidence estimation based on linear interpolation of the estimated PSC deformation, and a geometrical subsidence bowl model. With the linear interpolation the deformation based on the PSCs is triangulated and PSPs are projected on the triangle encapsulating the location of the PSPs to obtain the estimated deformation for an epoch. The deformation corresponding to the location of the PSCs/PSPs on the triangle is wrapped and subtracted from the corresponding PSCs/PSPs.

The estimated deformation based on the subsidence bowl method estimates a bowl describing the deformation based on the PS results of the conventional PS analysis (see figure 3.4). The estimation is performed with least-squares [45]. The bowl is described by a Gaussian function.

PSCs are presumably the most coherent pixels of an image, hence the increase in density of the number of PSs, performed with the PSPs, is based on the estimated topographic height and deformation of the PSCs. Estimation of the deformation pattern based on the PSCs is therefore more certain than estimation based on the final PSs. In general an estimation based on the PSs is noisier due to the local deformations and outliers present in the PSs. Outliers are PSs experiencing larger deformations than in reality present in the area of interest or PSs assigned to an unrealistic topographic height. The two methods can be applied to the estimates of the PSCs or PSs. But when describing the deformation based on the PSCs, a very rough deformation pattern is expected, because less PSCs are present than PSs.

Deformation estimation: Bilinear deformation

The Delaunay triangulation of a set of points in a plane, is a triangulation for which none of the points is inside the circumference of any triangles present in the triangulation. The minimum angle of all triangle angles contained by the triangulation is maximized. If no three points are on the same line and no four are on the same circle, for a two dimensional set of points, an unique Delaunay triangulation for set of points exists [11].

To estimate the deformation, a triangulation is made based on the deformations respectively to a reference epoch of the Persistent Scatterer Candidates. Because the convex hull of the PS dataset describes the borders of the triangulation, four extra points are added on the corners (when not present) to triangulate the whole interferogram. These are set at the same deformation as the nearest PSCs, hence deformation outside the original deformation is based on the assumption PSs deform according to the nearest PSs to the corners, which does not necessarily has to be reality. An example of the Delaunay triangulation based on the PSCs is presented in figure 4.3. When the deformation of intermediate locations is desired, the deformation at the intermediate location is retrieved from the deformation of the triangle at that specific location.

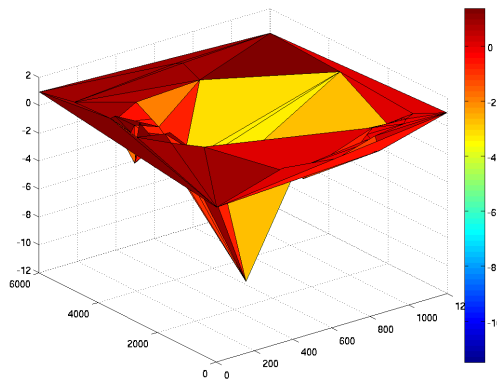


Figure 4.3: An example of a Delaunay triangulation based on the estimated deformation for the PSCs of track 108 covering the Veendam concession.

Definition of the normal vector of the triangular plane enables formulation of the plane equation, with which the deformation at any location on the plane is calculated. The equation of the plane through point $P_0(x_0, y_0, z_0)$ with normal vector $\mathbf{n} \langle a, b, c \rangle$ is

$$a(x - x_0) + b(y - y_0) + c(z - z_0) = 0. \quad (4.2)$$

The normal of a plane is composed out of the cross product of two vectors passing through 2 points situated on the plane. The vectors should not pass through the 2 same points, since this results into a cross product of zero. The vectors taken used in the calculation are the corner points of the triangle. The equation of the triangular plane enables calculation of the deformation of any point situated on the plane when the location (x, y) is known. The estimate of the deformation per epoch of the PSCs and PSPs is wrapped and converted into a phase component by means of the conversion factor (eq. (4.1)). The original differential phase is corrected for this deformation component of the corresponding pixel. After the correction of the PSC and PSP phases for the deformation, the conventional PS analysis is performed to acquire estimated topographic heights and the residuals of relative deformation. During the first unwrapping step a set of PSCs was eliminated, therefore the deformation estimation is based on a subset of the initial indicated PSCs. To get an optimal result, all initial selected PSCs need to be corrected and used for the formation of the new network. Therefore the whole PS analysis needs to be performed again. A flow diagram of this process can be found in figure 4.6.

Deformation estimation: bowl model estimation

Deformation due to salt mining can be described by a bowl. Both Veendam and Barradeel concession experience bowl shaped deformation, which can be modeled with [39]

$$z(x_i, y_i) = d \cdot \exp\left(-\frac{1}{2} \frac{(x_i - x_c)^2 + (y_i - y_c)^2}{r^2}\right) + z_c. \quad (4.3)$$

This equation is based on a Gaussian function describing a symmetrical bowl with smooth deformation behavior at the edges of the bowl, see figure 4.4(a). The d represents the maximum depth of the bowl, r is the radius of the bowl, and (x_c, y_c, z_c) the origin location.

These unknown parameters are to be estimated for every epoch and are based on the estimated PS-InSAR deformations for every PS at every epoch. The parameter vector is estimated

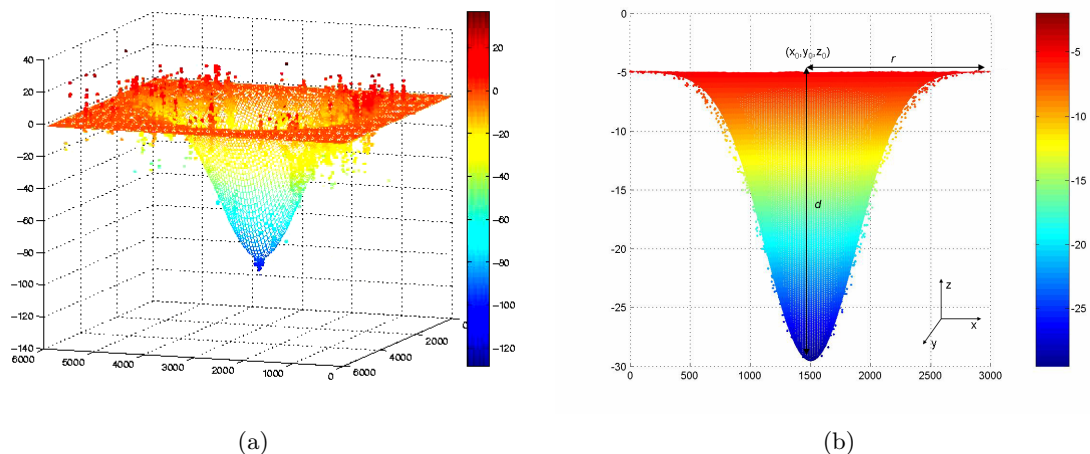


Figure 4.4: Gaussian bowl based on PS data covering Veendam. The surface is the deformation described by the Gaussian function and deformation is presented in millimeters. The center of the bowl is described by (x_0, y_0, z_0) , the depth by d and the radius of the bowl by r .

according to the least-squares technique [45]. Least-squares deals with linear systems of equations. Since the design matrix A of the model is defined by a non-linear Gaussian function, the bowl function has to be linearized. The linearization of the least squares model for a non-linear problem becomes

$$A(x) \approx \begin{bmatrix} a_1(x^0) \\ \vdots \\ a_m(x^0) \end{bmatrix} + \begin{bmatrix} \partial_x^T a_1(x^0) \\ \vdots \\ \partial_x^T a_m(x^0) \end{bmatrix} \cdot \Delta x. \quad (4.4)$$

Subsequently the linearized model of observation equations will be

$$E \{ \Delta y \} = \partial_x^T A(x^0) \Delta x; \quad D \{ \Delta y \} = Q_y \quad (4.5)$$

where $\partial_x^T A(x^0)$ is the gradient vector, $\Delta y = y - A(x^0)$, y is the vector with observations, $\Delta x = x - x^0$, x is the vector of estimated parameters, x^0 is the vector of initial parameters, and Q_y the variance-covariance matrix of the observations. Appendix B contains the linearized design matrix, gradient vector and gradient terms.

Since $A(x)$ is non-linear it cannot be expected that $\hat{x} = x^0 + \Delta \hat{x}^0$, when $\Delta \hat{x}^0$ is the least-squares solution of the system of equations in eq. (4.5). It is assumed that with the use of iteration the estimated parameters approximate \hat{x} well enough to consider them to be identical to \hat{x} [45]. In every iteration cycle the linearized least-squares problem is solved. The initial parameters for the first iteration are derived from apriori knowledge. Succeeding iteration steps apply estimates of the previous step as initial values. The iterative scheme is called the Gauss-Newton method, as displayed in figure 4.5.

A stop value δ is included to terminate the iteration. This term is chosen to be $\|\Delta \hat{x}_k\|_{N(x_k)} \leq \delta$. The value increases with increasing amount of parameters to be estimated. Therefore the amount of epochs must be taken into account and whether the origin is taken fixed or not. The iteration stop criterium for the different models is chosen to be 0.1 meter difference between consecutive estimated source locations

$$\sqrt{(x_{i+1} - x_i)^2 + (y_{i+1} - y_i)^2 + (z_{i+1} - z_i)^2} \leq 0.1[\text{m}],$$

and 1% difference between the estimated depths and radius

$$\frac{\|d_{i+1} - d_i\|}{d_i} \leq 0.01$$

$$\frac{\|r_{i+1} - r_i\|}{r_i} \leq 0.01.$$

If the parameters for every epoch are estimated in one system of equations, the number of parameters is 5 times the number of epochs. The system is overdetermined when estimated deformation, and the (x, y) position, at every epoch for 2 PSs is available. The position and deformation are 3 known variables. Thus when 2 PSs are available, 6 parameters are known. With this number of known parameters, 5 unknown parameters are solvable. Since in general the number of identified PSs by PS-InSAR succeeds 2 PSs, the system is likely to be overdetermined.

The algorithm implemented enables the estimation of the parameters separate for every epoch, or estimation of the parameters for all epochs in one least-squares estimation. These methods are explained in appendix B. Also the origin, depth and/or radius can be specified as given and therefore will not be estimated.

The standard deviation of the estimated PS deformations is set to 4 mm, based on the standard deviation specified in [28]. No inter-correlation is assumed between the PSs and therefore the Q_y matrix will be a diagonal matrix containing the PS variances. Not all PSs should have assigned a similar quality, since many phenomena influence the estimation, like the implemented functional model or the scattering properties of the target. Because an accurate quality description is not available, an uniform standard deviation is assumed.

Also emphasis on the spatial relationship between certain PSs can be introduced due to the use of inter-correlation in the covariance matrix. The least-squares technique inverts the covariance matrix, but due to limitations of the program, matrices succeeding 8000×8000 entries cannot be inverted. Taking into account inter-correlations increases the memory usage, hence even reduces the maximum size of the matrix to be inverted. When inversion of larger matrices

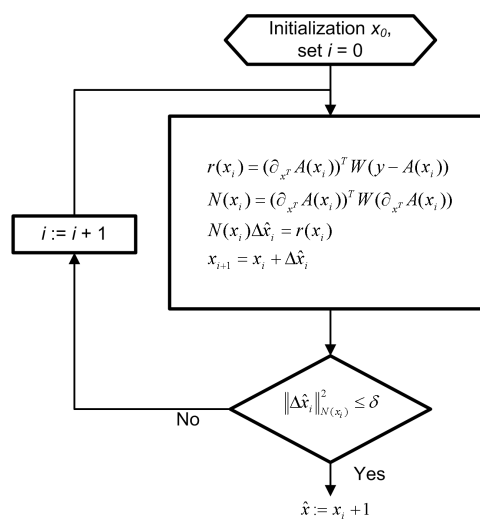


Figure 4.5: The Gauss-Newton iteration [45], where i is the iteration number, x_0 the initial unknown parameters, W is the weight matrix and $\partial_{x,r} A(x_i)$ is the gradient vector. With this system iteratively a least squares problem can be solved.

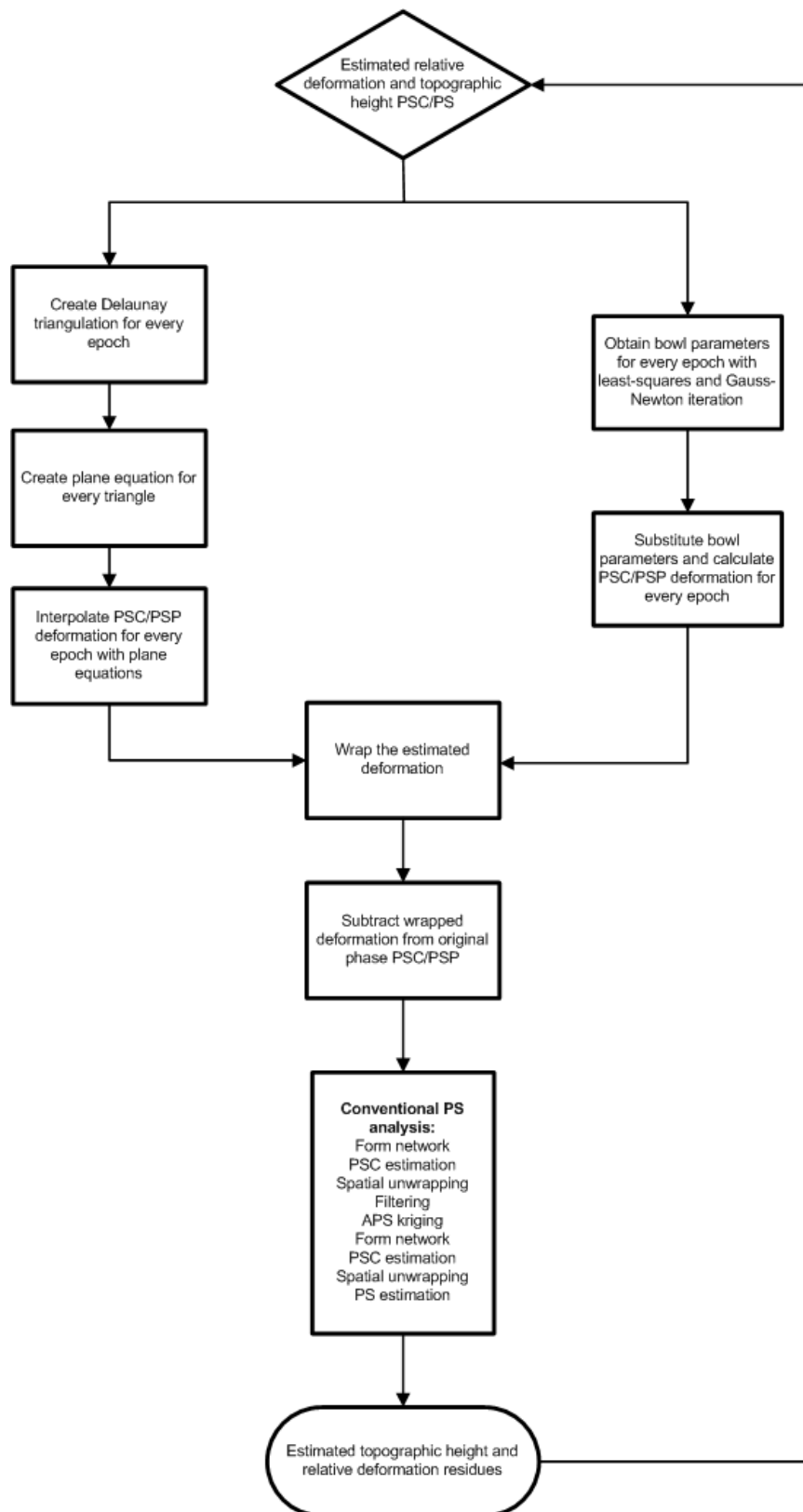


Figure 4.6: Flow diagram of the non-linear deformation elimination with bilinear interpolation or bowl estimation.

is desired, block inversion can be used. This is not implemented in this study, a diagonal covariance matrix is applied.

When the unknowns are estimated, the subsidence enables calculation of the deformation on any point as described in equation (4.3). After selection of the PSCs and PSPs the phases of these pixels are corrected for the estimated deformation. Deformation on the location of interest is calculated in slant range and wrapped making use of the conversion factor (see equation (4.1)). The wrapped phase is subtracted from the corresponding pixel phase. A flow diagram for this process is found in figure 4.6.

For the estimation of a bowl model the wide-scale deformation pattern is of importance. Fine-scale behavior of individual Persistent Scatterers through time may negatively influence the estimated parameters, when this behavior differs significantly from the wide-scale behavior. Thus local deformation due to, for instance, foundation failure is not of interest. When the number of local deforming PSs approaches the number of PSs deforming according to the wide-scale deformation, the influence of the local deforming PSs is significant on the estimated bowl parameters. These PSs need to be filtered to prevent this.

The w-test can be used to check an observation for a significant error with respect to a chosen model [45]. When observing a single observation error the random variable w-test statistic \underline{w} is one-dimensional resulting into

$$\underline{w} = \frac{c_y^T Q_y^{-1} \hat{e}_0}{\sqrt{c_y^T Q_y^{-1} Q_{\hat{e}_0 \hat{e}_0} Q_y^{-1} c_y}} \quad (4.6)$$

Assuming \underline{w} is normal distributed the test is two sided and therefore the null hypothesis H_0 is rejected if

$$w < -\sqrt{k_\alpha} \text{ or } w > \sqrt{k_\alpha}$$

where k_α is the critical value. The PS deformation velocities are tested against the mean of the velocities and α is taken to 0.0250. Due to the subsidence bowl the actual deformation at all the locations cannot be approximated by a flat plane, hence the spatial distribution is taken into account. The deformation velocity of a rejected PS is compared with the deformation velocity of 15 nearest rejected PSs. When the deformation velocity of these PSs differs with not more than the standard deviation of the PSs accepted by the null hypothesis, the PSs are accepted. The standard deviation of the PSs accepted by the horizontal plane is used as selection criterion assuming this is a good representation of the variability of the PS deformation rate.

Inversion of the covariance matrix of the measurements can be performed by the computation program until a matrix size of 8000×8000 entries. This restricts the calculation of the w-test statistic for large PS datasets. Datasets resulting from the PS analysis easily consist out of over 8000 PSs. The quadtree approach is used to group PSs until the covariance matrix of the PSs reaches the size that can be inverted. A quadtree partitions (most often) a two dimensional space by recursively subdividing it into four regions [16]. Common characteristics of all forms of quadtrees are that they decompose the space into adaptable cells, with a maximum capacity for every cell, here the amount of PSs, and the tree directory follows the spatial decomposition of the quadtree. The toolbox of Kirill K. Pankratov is used for the quadtree partition in this study [40]. This toolbox performs a recursive division of a 2-dimensional set. The plotted results of the toolbox based on PS-InSAR results of track 108 is shown in figure 4.7.

The PS dataset is reduced using the size of the blocks. The program grouping PSs searches for the smallest block and assigns one PS describing the mean deformation and topographic height of most PSs situated in the block. This is an iterative process and terminates when the dataset reaches the maximum number of PSs, set by the user. When the deformation rate of a

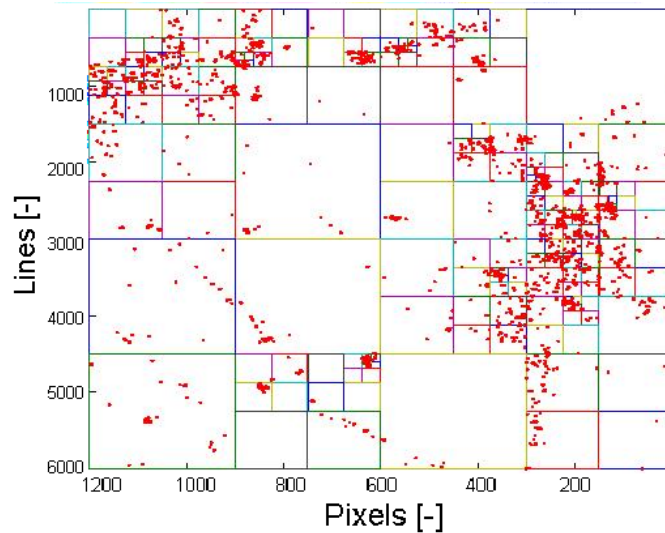


Figure 4.7: Quadtree division of the PS-InSAR result of track 108. The capacity of a block is set to 100.

certain PS and the mean of the PSs in the block differ more than once the standard deviation of the PSs in the block, the point is not taken into account. The PSs that are not averaged, will be eliminated during the w-test.

4.2.2 Breakpoint model

During the unwrapping step, see section 3.3.1, PSCs and PSPs are unwrapped according to the functional model, see eq. (3.7). Possible values for height, deformation and ambiguity are searched through with bootstrapping and the values corresponding to the smallest error term are taken as estimates. When searching through an infinite search space, best fitting solutions could be unrealistic. To restrict the search space to a physically realistic output the space is constrained with the standard deviations for the topography and deformation. Periodogram estimation sets boundaries to the estimates of twice the standard deviation in positive and negative direction. Bootstrapping and LAMBDA estimation consider the given standard deviations as pseudo observations constraining the boundaries of the search space [42] [44].

Under the null-hypothesis a linear deformation model is used, but at locations situated in the subsidence bowl of Veendam or Barradeel a breakpoint model may give a better fit, see figure 4.2. The breakpoint model is composed out of two linear functions connected to each other. The functional model in eq. (3.7) changes under consideration of the breakpoint model in

$$\beta \cdot \Delta_h - \frac{4\pi}{\lambda} T_1 \cdot \Delta_{d_1} - \frac{4\pi}{\lambda} T_2 \cdot \Delta_{d_2} + \phi_{error} = \phi - 2k\pi, \quad (4.7)$$

where T_1 and T_2 denote the temporal baselines corresponding to the time period covered by the rate displacements Δ_{d_1} and Δ_{d_2} in the first and second linear model respectively. The breakpoint model is implemented in the PS analysis in such a manner that a PSC or PSP is tested both against the linear and the breakpoint models, resulting into the estimated parameters belonging to the model experiencing the smallest Overall Model Test.

The rates of displacements Δ_{d_1} and Δ_{d_2} are calculated using the Best Linear Unbiased Estimation (BLUE), where the vector of the estimated parameters are the rates of displacements Δ_{d_1} and Δ_{d_2} and the topographic height, and the vector of observations contains the differential

phases for every epoch. The deformation contribution estimation when the breakpoint takes place after the date of the master image, for k epochs is written as

$$\begin{pmatrix} \phi_{\text{defo}}^1 \\ \vdots \\ \phi_{\text{defo}}^n \\ \phi_{\text{defo}}^{n+1} \\ \vdots \\ \phi_{\text{defo}}^k \end{pmatrix} = \text{h2ph} \begin{pmatrix} T^1 & 0 \\ \vdots & \vdots \\ T^n & 0 \\ T^n & T^{n+1} - T^n \\ \vdots & \vdots \\ T^n & T^k - T^n \end{pmatrix} \begin{pmatrix} \Delta_{d_1} \\ \Delta_{d_2} \end{pmatrix}. \quad (4.8)$$

where the breakpoint occurs at the n^{th} epoch and r2ph denotes the range-to-phase conversion factor as given in (4.1). This system of equations is implemented in equation 4.7. Because the deformation phase has to be zero when the temporal baseline is zero, due to the reference image, a second system of equations is implemented for breakpoints taken before the date of the master image, the system of equation follows

$$\begin{pmatrix} \phi_{\text{defo}}^1 \\ \vdots \\ \phi_{\text{defo}}^{n-1} \\ \phi_{\text{defo}}^n \\ \vdots \\ \phi_{\text{defo}}^k \end{pmatrix} = \text{h2ph} \begin{pmatrix} T^1 - T^n & T^n \\ \vdots & \vdots \\ T^{n-1} - T^n & T^n \\ 0 & T^{n+1} \\ \vdots & \vdots \\ 0 & T^k \end{pmatrix} \begin{pmatrix} \Delta_{d_1} \\ \Delta_{d_2} \end{pmatrix}. \quad (4.9)$$

With this model the linear graphs are connected. This is because in the system of equations (4.8) after the breakpoint epoch, the phase contribution due to deformation is based on the final value of the first linear graph plus the contribution of Δ_{d_2} times the temporal baseline measured from the breakpoint epoch. In the system of equations (4.9) the same approach is used, but now based on Δ_{d_2} .

The model is part of the functional model, which is compared to the unwrapped phase. The residues are applied in the OMT, as explained in section 3.3.2, to find the best fitting parameters.

Chapter 5

Optimized results of the test cases

5.1 Introduction

The results of a Persistent Scatterer (PS) analysis performed on the ERS images covering the north of the Netherlands are presented in figure 1.1 [29]. Two areas are visualized which experience noteworthy deformation due to salt mining and which are represented by a low density of PSs. The area of interest in the northwest contains the Barradeel concession and the area of interest in the southeast contains the Veendam concession. Three possible causes can have introduced the low density of PSs in the areas of interest. These causes are the absence of scatterers behaving like PSs in the areas, points possessing scattering properties of PSs not being identified as PSC/PSP during the selection step, or PSC/PSP possessing scattering properties of PSs being rejected as PS during the succeeding processing steps. The latter two causes are treated in this thesis to increase the density of the number of PSs. Increasing the density is performed to be able to estimate the deformation pattern more accurately. The algorithms explained in chapter 4 are implemented to improve the results of the PS analysis. These algorithms are the:

- manual PS identification,
- deformation subtraction estimated by bilinear interpolation,
- deformation subtraction estimated by a Gaussian bowl model,
- and the breakpoint model.

The algorithms are tested on the test cases Barradeel and Veendam. PS results based on these implemented algorithms are presented and discussed in this chapter. The annual velocities presented throughout this chapter are in slant range, unless otherwise stated. Slant range is in the line of sight of the satellite.

The Veendam concession area is imaged by the ERS-1 and 2 satellites. The images of the descending tracks 108 and 380 and ascending track 487 are used to compose interferograms. Figure 5.1 shows the configuration of the tracks. Two types of interferograms need to be omitted, since they deteriorate the results of the PS analysis. These are misaligned interferograms and high Doppler frequency interferograms.

The PS analysis analyzes phase differences on pixel level, meaning pixels covering corresponding locations on Earth's ought to be aligned. When errors in the alignment occur, a loss of coherence is introduced. Physical correspondence between a scatterer in the images is lost due to misalignment. This causes complete decorrelation, making a PS analysis meaningless. Hence misaligned interferograms are eliminated from the interferogram stack.

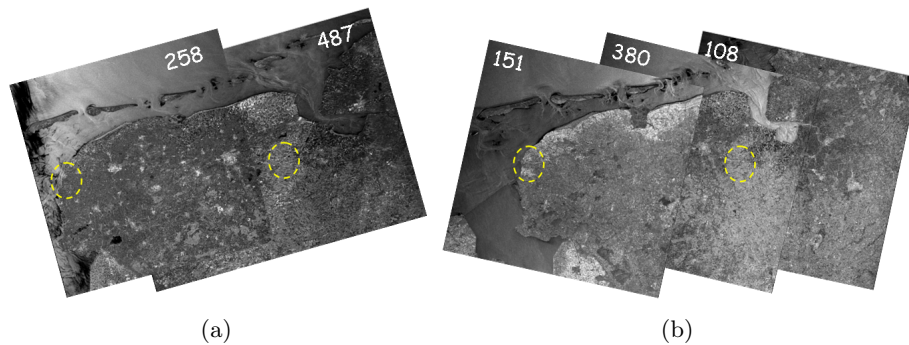


Figure 5.1: The tracks covering Veendam and Barradeel concession. The ascending tracks are presented in (a) and descending tracks in (b). The areas of interest are encircled.

The Doppler centroid frequency is the center frequency of the passage of a point scatterer through the antenna beam. A difference in the centroid frequency causes a shift in the data spectrum introducing noise. Because SLC images are processed at a fixed Doppler centroid frequency, adjusting the frequency for an interferogram is not possible [21]. Since Veendam and Barradeel are both situated in rural area, a small number of PSCs constructs the network. Due to the small number of PSCs the distance between PSPs and PSCs is relatively large, resulting in a relatively weak network. When interferograms experience a large Doppler frequency difference, arcs are rejected due to the estimated noise, resulting in more rejected arcs. To prevent arcs to be rejected due to the Doppler difference, these images are deleted. A typical Doppler bandwidth for ERS is 1377 Hz. Therefore interferograms experiencing a frequency difference with a master interferogram over 500-600 Hz are omitted. The final subset of images used for interferogram processing are as presented in appendix A. The PS analysis is performed on the resulting interferograms.

Characteristics on the different tracks covering the Veendam concession are presented in table 5.1. The selection of the master image is based on maximizing the (expected) total coherence of the interferometric stack, which causes visual interpretation of the interferograms and aids quality assessment as explained in [25].

Track	N^0 images	Master image	First image	Last image
108	68	11986 05-AUG-1997	04261 09-MAY-1992	54571 27-SEP-2005
380	75	11757 20-JUL-1997	05034 02-JUL-1992	45324 21-DEC-2003
487	31	21884 27-JUN-1999	09149 15-APR-1993	38918 29-SEP-2002

Table 5.1: Interferogram stack characteristics Veendam concession.

Deformations in the Barradeel concession area are imaged by ERS-1 and 2 satellites. The descending track 151 and ascending track 258 both cover this area of interest, which can be found in figure 5.1. Table 5.2 contains the characteristics on the tracks. And the images from which interferograms are processed are presented in appendix A. These interferograms are used as input stack for the PS analysis. Again images are filtered on coregistration and Doppler centroid frequency difference.

Making use of the optimization algorithms leaves after PS processing an optimized dataset. Because deformation due to salt mining is assumed to be shaped like a bowl and the quality of a PS still rest undetermined, a Gaussian model is applied to calculate internal and external precision. Based upon the acquired dataset, unknown parameters describing the bowl are

Track	N ⁰ images	Master image	First image	Last image
151	75	11134 21-MAY-1997	04304 12-MAY-1992	52610 13-MAY-2005
258	37	10025 06-JUN-1997	08920 30-MAR-1993	44835 10-FEB-2000

Table 5.2: Interferogram stack characteristics Barradeel concession.

Parameter	Track 151	Track 258	Track 108
x_c [pixels]	1216	404	600
y_c [lines]	3562	3600	2960
z_c [mm]	0	0	0.31]
<i>radius</i> [lines]	550	550	1012
<i>depth</i> [mm]	-104	-79	-45

Table 5.3: Bowl parameters used for precision estimate of track 151 and track 258.

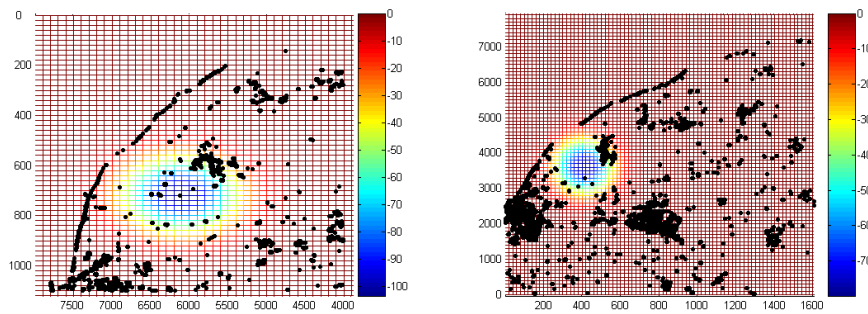
estimated applying the least-squares method. The system of equations for this model is equal to the system applied in the bowl method, with the estimation of parameters for one epoch as explained in appendix B. To be able to determine whether the optimization methods increase the precision of the estimated deformation, the conventional internal precision is compared to the internal precision of the specific optimization method. With $Q_y = \sigma^2 I$, where the standard deviation σ is set to 5 mm and I describes the identity matrix with the number of PS entries, the $Q_{\hat{x}}$ and $Q_{\hat{y}}$ for non-linear systems are calculated with BLUE as:

$$Q_{\hat{y}} = (\partial_{x^T} A(x^0)) Q_{\hat{x}} (\partial_{x^T} A(x^0))^T \text{ and} \quad (5.1)$$

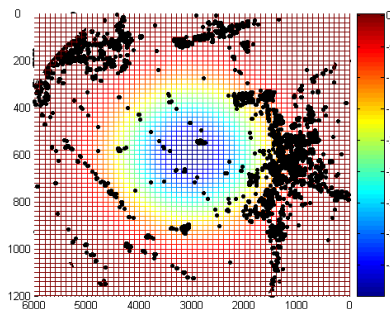
$$Q_{\hat{x}} = \sigma^2 [(\partial_{x^T} A(x^0))^T (\partial_{x^T} A(x^0))]^{-1}. \quad (5.2)$$

In the Barradeel case two subsidence bowls are present. These are introduced due to gas subtraction and salt mining. This presence of two bowls makes estimation of the bowl parameters difficult, impossible or unreliable. Therefore bowl parameters based on leveling results are used, and the internal and external precision are calculated based on these parameters. Hence no estimation of the parameters is performed. The parameters are based on leveling results of epoch 65 for track 151 and of epoch 30 for track 258. The parameters used are found in table 5.3 and plots of the bowls for both tracks are presented in figure 5.2. Also for track 108 the estimation of a bowl is difficult or impossible with the implemented algorithm, because the deformation pattern is not a perfect spherical bowl. Therefore the parameters of the bowl are set fixed and the precision is investigated according to these parameters. The parameters are based on leveling results for epoch 60 and can be found in table 5.3. A plot of the bowl is presented in figure 5.2. For the other two tracks covering Veendam the estimation of the bowl parameters posed no problems, hence here estimation of the parameters is performed based on the PSs identified by the method of interest.

In the first section of this chapter conventional PS results are discussed. The relevance of the gridcell size and PSP selection threshold is treated. The succeeding four sections deal with the results of the different algorithms implemented to increase the PS density. These sections discuss the results of a single track for Veendam and a single track for Barradeel. The selection of tracks is based on a maximum difference between conventional and optimized results. The results of all tracks are presented in appendix C. A difference in PS distribution between conventional and optimized results is discussed and quality of the PS estimates is treated. The sixth section handles unwrapping errors present. These are mainly the consequence of the implemented functional model. The subsequential section validates the results making use of leveling



(a) Subsidence bowl estimated track 151 (b) Subsidence bowl estimated track 258



(c) Subsidence bowl estimated track 108

Figure 5.2: Plot of the subsidence bowls composed with the parameters as found in table 5.3 for track 151, track 258 and track 108. The PSs identified by the bowl method are displayed in black. Presented subsidence velocities are in [mm/year].

data provided by the mining companies Nedmag Industries and Frisia Salt and the final section presents conclusions and a discussion on the results.

5.2 Conventional PS processing results.

This section presents the PS results of the conventional algorithm. A flow diagram of the conventional analysis is found in figure 3.4. The functional model, equation (3.7), implemented in the process describes linear deformation and pixel selection is based on the amplitude dispersion, equation (3.4). Processing parameters as set throughout the analysis are found in table 5.4. The method bootstrapping is chosen as unwrapping algorithm, since a quality description is taken into account unlike for the ambiguity function, and the processing time is significantly less than for LAMBDA. The ensemble coherence, equation (3.8), threshold is typically set to 0.75 and the PSC amplitude dispersion threshold to 0.25 as explained in [15], but since it is expected that the deformation in the subsidence bowls in our test sites can not accurately be described by a linear function, the threshold for the ensemble coherence is set at 0.6, to prevent the PSs situated in the bowls to be rejected. The amplitude dispersion threshold for PSCs is kept at 0.25. The maximum arc length is taken beyond the distance over which atmosphere is assumed constant. Before the first unwrapping step of the PSCs the atmosphere is not yet filtered. When the error between the model and actual phase is large due to the atmospheric influence, the arcs will be rejected, hence the same result is obtained as when thresholding on arc length. The network is chosen to be a more redundant network, with 8 arcs connecting a PSC to neighboring PSCs. The influence of the gridcell size and PSP threshold of the amplitude dispersion are discussed

Parameter	Value
Method to solve ambiguities	Bootstrapping method
Ensemble coherence threshold	0.6
Gridcell size	50, 200 or 300 [m]
PSC threshold	0.25
Maximum arc length	20e3 [m]
Network	More redundant
Number of arcs per PSC	8
PSP threshold	0.4 or 0.45

Table 5.4: Input parameters for the PS analysis

in this section.

Gridcell size Variation of the gridcell size results into a difference in the initial network, composed out of selected PSCs. This effect is shown in figure 5.3. A pixel is assigned as PSC to a gridcell, depending on the amplitude dispersion. For every gridcell the amplitude dispersions of the pixels are investigated. The pixel experiencing the smallest amplitude dispersion below a specified threshold is selected as PSC. If the amplitude dispersion of none of the pixels crosses the set threshold, none of the PSCs is assigned to the specific gridcell. An initial network between the resulting PSCs is formed and the differential phases of the arcs composing the network are unwrapped. If the unwrapped deformation and topographic height do not fit the formed network the arc is rejected. The arcs do not fit the network when addition of the heights of three adjacent arcs forming a closed triangle does not count up to zero. After unwrapping and testing the network, PSCs not connected to any arcs are removed. This results in an adjusted initial network on which further processing is performed. Initial and adjusted initial networks of track 380 with gridcell size 200 or 300 meters are found in figure 5.3.

Note that some PSCs contained in an initial network are not contained in the other network, while that is expected. This depends on the calibration implemented. The calibration corrects the amplitudes changes through time, for instance, due to different sensor characteristics. PSCs contained in one initial network experience an amplitude dispersion approaching the threshold. Due to calibration the same PSCs in the other initial network possesses an amplitude dispersion larger than the threshold, hence the PSC is rejected.

Figures 5.3(e) and 5.3(f) display the final PS annual deformation velocity based on a timespan of 11 years. As can be seen the distribution of PSs differs between the two images, especially in the northeast of the mining location, which is located in the west of Veendam. When a gridcell size of 300 meters is chosen a PSC at the mining location is accepted, resulting into acceptance of PSPs in the northeast of the mining location. Because the PSPs are tested against the three closest PSCs, which includes the mining location, the estimated topographic height and deformation of the PSPs fits the network.

Investigation of the initial network is necessary before proceeding to the methods subtracting deformation. Both the subsidence bowl model and Delaunay triangulation are based on the PS results. Every epoch an estimation is made of the subsidence calculated by the models. Subtraction of the deformation contribution to the phase, estimated by the models, should be able to remove deformation. This decreases the variability of the phase, which should result into a better approximation of the linear functional model, hence introducing a larger identification success rate of PSs. The Delaunay triangulation is based on the PSCs composing the network after unwrapping. When this network does not contain a PSC in the subsiding area, an approx-

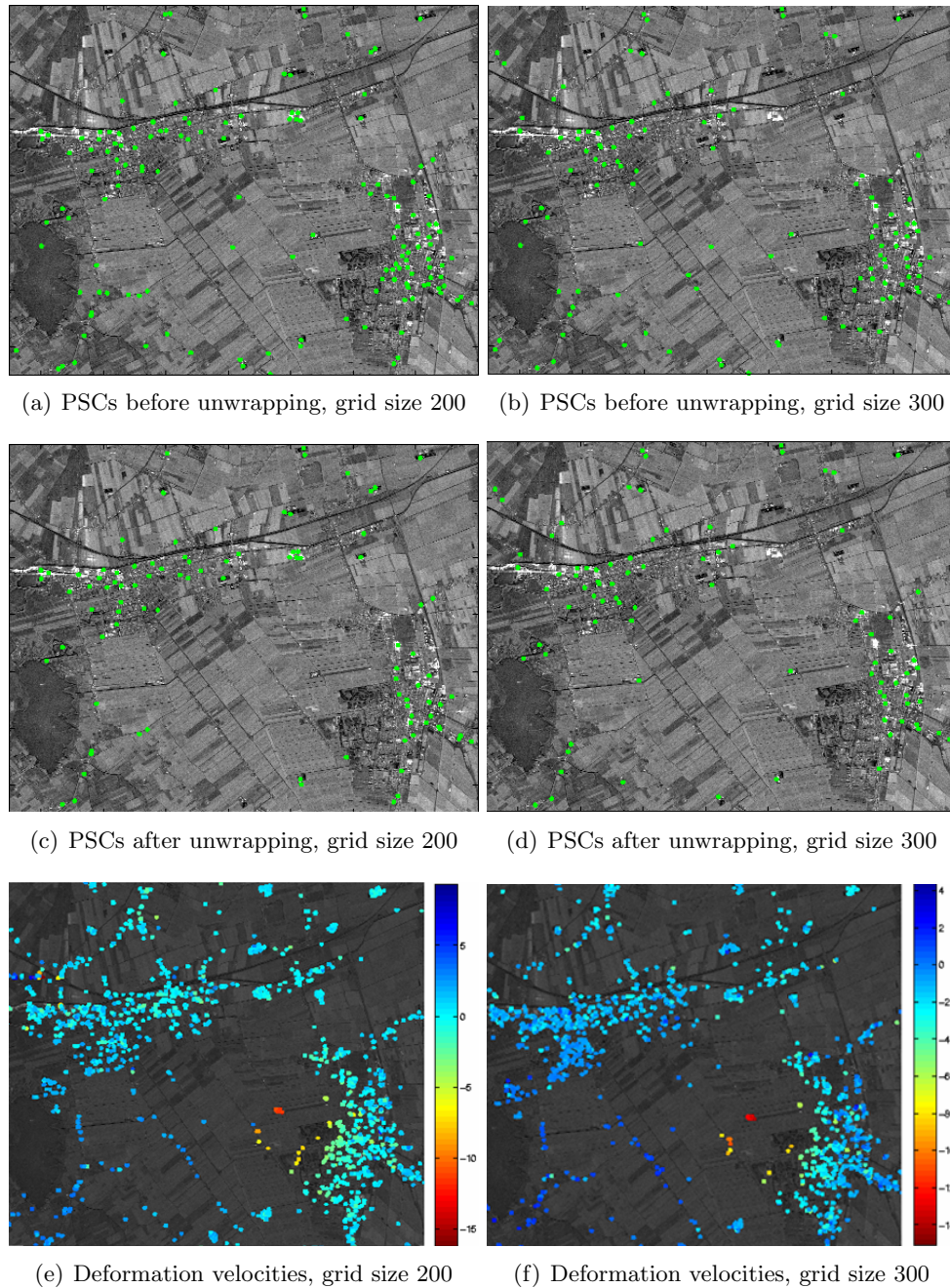


Figure 5.3: The influence of the initial network. Figure (a) and (b) present the PSCs of track 380 with an amplitude threshold of 0.25 and gridcell size of 200 respectively 300 meters. The PSCs remaining after unwrapping the networks are presented in figures (c) and (d). Usage of a different gridcell size results in a different initial network. Figure (e) and (f) present the annual PS deformation velocities [mm/year]. Northwest of the mining location in figure (f) PSs are found, in contradiction to figure (e). The presence of the PSC at the mining location has resulted into an increase of PS density in this area.

imate flat terrain is estimated, see figure 5.11. Subtraction of this estimate does not result into subtraction of deformation at the area of interest, and therefore the variability in general rests unchanged.

Throughout this research subsidence bowl estimation is based on the final Persistent Scat-

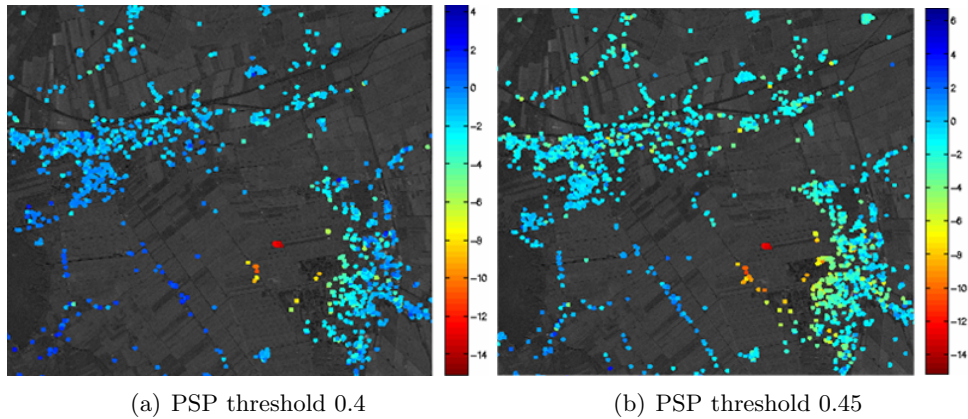


Figure 5.4: Influence of the PSP threshold. Figure (a) and (b) present annual PS deformation velocities [mm/year] of track 380 with an gridcell size of 300 meters and a PSP threshold of 0.4 respectively 0.45. The density of PSs has increased with decreasing amplitude dispersion threshold.

ters. An error in unwrapped parameters of the initial network influences the deformation estimation. An example of the influence in the unwrapped PS parameters can be found in appendix C. For track 108 gridcell sizes of 200, 300 and 50 meters are applied. The initial network based on a gridcell size of 50 meters contains a PSC in the southwest subsiding with the same rate as the mining location. This PSC influences the acquired PS deformation in its surroundings, resulting in a different deformation pattern compared to the deformation pattern acquired with gridcell size 200 or 300 meters, see figure C.1(c).

PSP amplitude dispersion threshold Amplitude dispersion thresholds for PSC and PSP selection are specified by the user. Increasing the amplitude dispersion index applied as threshold results in an larger number of selected pixels. The signal-to-noise ratio increases with increasing amplitude dispersion index, hence a larger number of phase instable pixels is selected as explained in section 3.3.1. A larger number of pixels introduces more identified PSs, but also longer computation time. Hence a trade-off between these has to be made by the user. Figure 5.4 presents the results of the conventional PS analysis performed with a threshold of 0.4 and 0.45. As seen the density of PSs can significantly differ.

Aliasing of the estimated deformation model can occur when a small amount of interferograms is present over a relatively large timespan. This takes place with ascending track 487. Over a timespan of 9 years, 31 interferograms are available. The deformation pattern of a pixel is less constraint through time in this case, resulting in a larger variability of possible linear models which fit the differential phase of a pixel, including deformation models not describing the actual behavior. A high dispersion threshold will select many pixels, including pixels accepted as PS described by a linear model which does not represent actual behavior due to aliasing. Hence thresholding on a lower amplitude dispersion will reduce the amount of outliers.

Quality description Annual velocities and the Overall Model Test for track 108 covering the Veendam concession area and track 151 covering the Barradeel concession area are found in figure 5.5. The conventional results of all tracks are presented in appendix C. These datasets are filtered as explained in section 4.2.1. The maximum deformation velocity found in the Veendam area with the conventional dataset for track 108 is -12 mm/year and for Barradeel track 151 this velocity is -19 mm/year. These velocities are relative to a chosen reference point. Hence when the reference point also experiences deformation, as is the case in the Veendam area due to gas

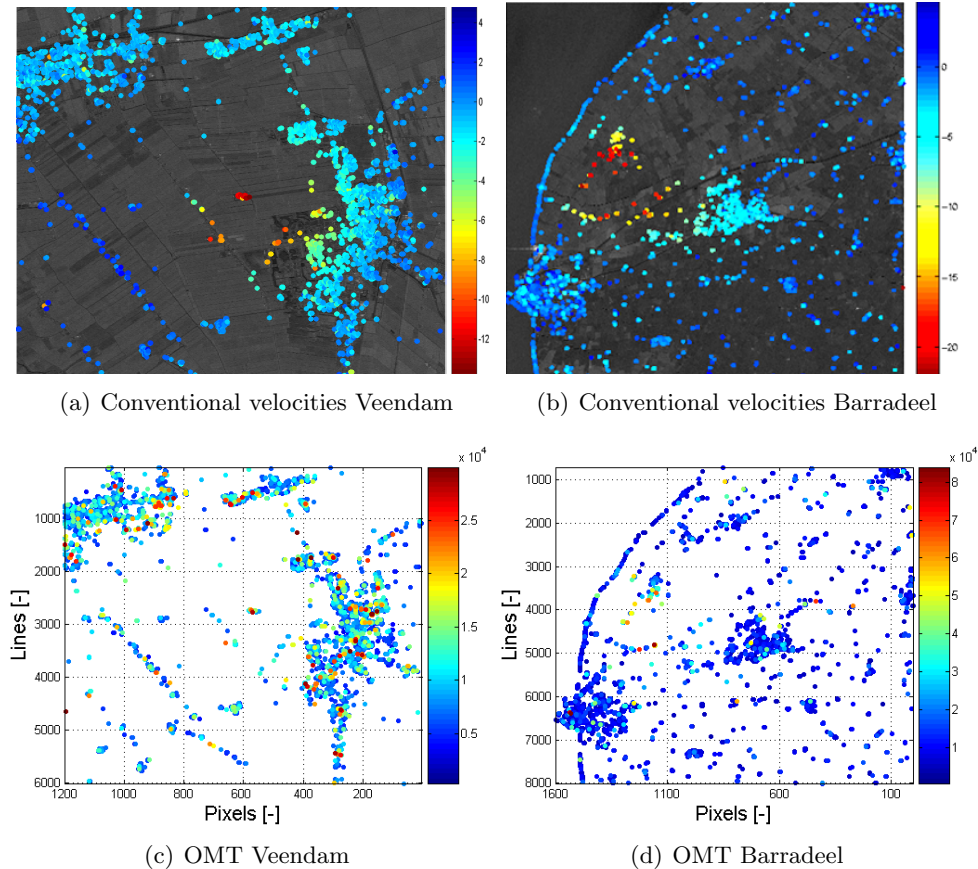


Figure 5.5: (a) Annual PS deformation of track 108 with an gridcell size of 300 meters and a PSP threshold of 0.45. (b) Annual PS deformation [mm/year] of track 151 with an gridcell size of 200 meters and a PSP threshold of 0.45. (c) + (d) The Overall Model Test between the linear model and the estimated deformation for every epoch for track 108 respectively 151.

subtraction in the north of Groningen, the velocities differ when observed from a non-deforming area. This can introduce a smaller deformation rate than in reality present. In the Veendam case we are interested in the deformation due to Salt mining and therefore the contribution of gas subtraction can be (partially) eliminated when choosing a reference coordinate experiencing deformation due to gas subtraction, but not due to salt subtraction.

The OMT describes the differences between the linear subsidence function applied for unwrapping and the estimated deformation for every epoch. In the Barradeel subsiding area the OMT values are larger than PSs experiencing no subsidence due to salt mining, hence the linear deformation function at these locations approximates the estimated deformation less reliable than PSs situated outside the subsidence bowl. This was expected since it is known that Frisia started mining in 1996, therefore the area did not experience deformation in the earliest interferograms. A breakpoint model should represent the deformation more accurate (see section 5.6). In the Veendam concession this mentioned breakpoint model is less obvious, hence the deformation approaches the linear model more accurate and are the high OMT values randomly distributed over the whole crop area.

The internal and external precision is determined making use of a Gaussian bowl. In subsequent sections the obtained precisions between conventional and optimized methods are discussed to indicate whether the implemented methods optimize the PS dataset.

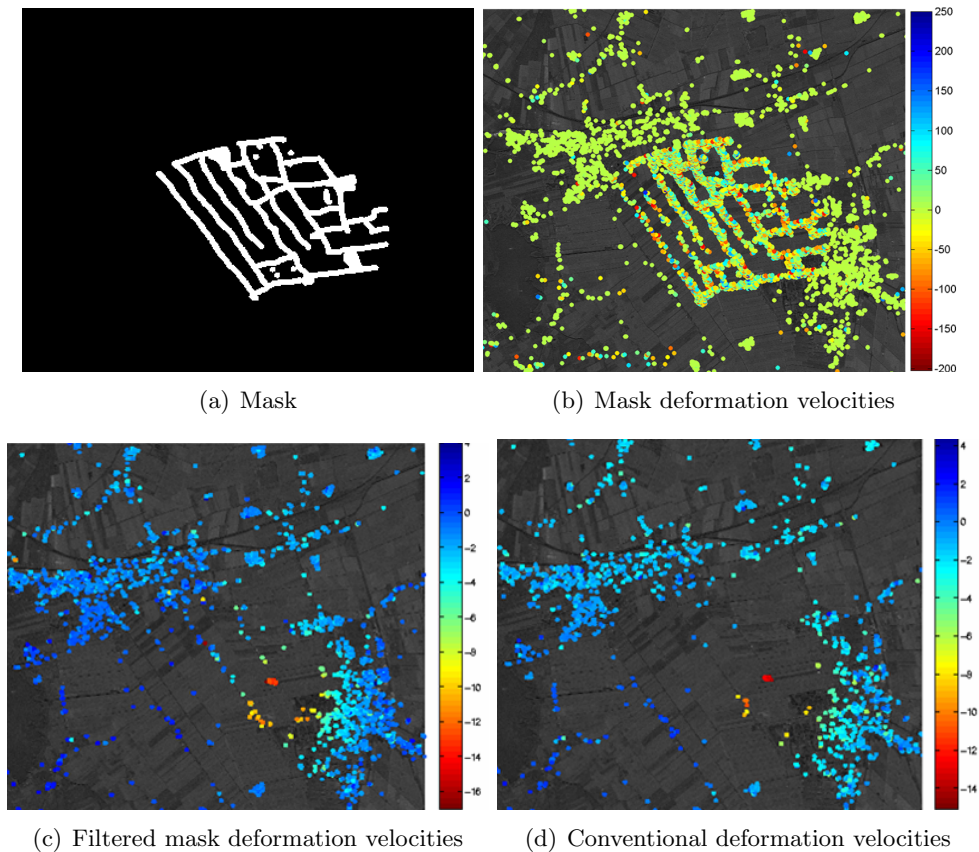


Figure 5.6: Filtered PS deformation velocities [mm/year] obtained with manual PS identification. Created mask for track 380 in which the white pixels correspond with pixels of interest is displayed in (a). The deformation velocities and filtered deformation velocities [mm/year] of the PS analysis or shown is figure (b) and (c). Comparing the filtered PSs with the conventional PSs (d), shows an increase of PS density.

5.3 Results manual PS identification

A multi reflectivity map is composed out of averaged amplitudes for every pixel of the interferograms from the stack. This map is used to draw a mask containing the pixels of interest, which do not proceed through the selection process but are considered to be PSPs immediately. The selection procedure is performed since thresholding on amplitude dispersion can reject pixels behaving as good PSs. Man-made features in the area of interest are likely to be PSs due to their scattering properties (see section 4.1.1), hence pixels containing these features are manually selected in a graphical interface. A black-white figure is composed, in which white pixels belong to locations of interest. An example of this figure can be found in figure 5.6. Converting this figure into a matrix containing ones at the locations of the pixel of interest and otherwise zeros, results in a mask used as input file for the PS analysis.

Figure 5.6(b) contains the results after PS processing, with the masked area taken into account. Many PSs are present in this plot experiencing an unrealistic deformation rate or topographic height. These outliers need to be filtered to obtain the large scale deformation pattern. Because a large number of outliers is present, spatial correlation can not be used as filtering criterion. New criteria are the maximum and minimum estimated topography and deformation velocity. The topography of a PS is unlikely to be lower then -10 meter and higher then 15 meter (assuming no towering flats are present in the subsidence area). This is based

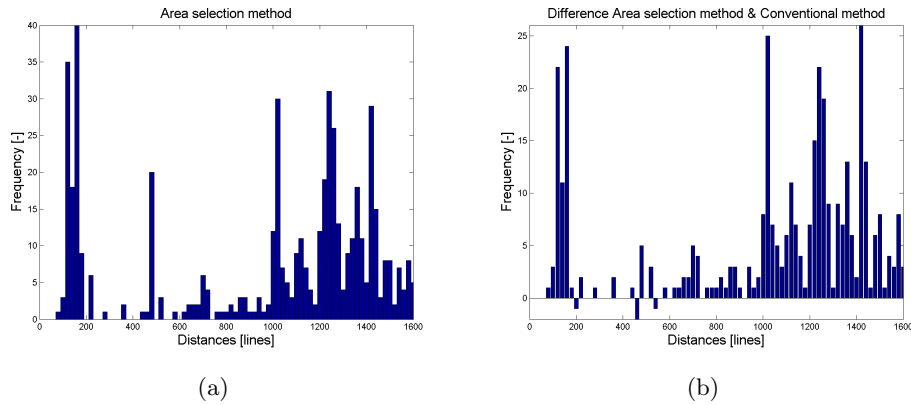


Figure 5.7: (a) Histogram of the distances between the central point in the subsidence bowl to neighboring PSs obtained with the manual PS identification method performed on track 380. Figure (b) represents the difference between the distances in the conventional case and histogram (a). An increase in the PS frequency of a bin and spatial distribution is present.

on a reference coordinate positioned at the same height as the Earth's surface. If the reference coordinate is situated on e.g. a building, a correction has to be made. The required correction can be checked with the histogram of the estimated topography of all the PSs. Assuming most PSs are located on the surface, the peak in the histogram displays the surface. Hence the difference between the peak of the histogram and the topography of the reference point, always set at zero, represent the height of the reference point above Earth's surface.

When the PS results still contain outliers the deformation velocity can be used as filter. An approximation of the minimum and maximum subsidence is applied as threshold. PSs deforming outside these boundaries can be assumed to be unrealistic and are eliminated.

Ensemble coherence can not be used as filter in the two test cases. Most PSs situated in the subsidence bowl experience a low ensemble coherence since the deformation for an epoch deviates significant from the deformation obtained with a linear model. Thresholding on ensemble coherence can filter these crucial PSs, which is not desired.

To quantify the density improvement, a crop is made of the specific area of interest, which is the area experiencing subsidence due to salt mining. The distances between the center of the crop and the PSs present in the crop are calculated. These distances are plotted in a histogram which is shown in figure 5.7(a). Comparing the distances with the distances in the conventional case, results in histogram 5.7(b). Positive bars indicate a increase of the number of PSs at that specific distance bin. Using the expression 'an increase of the density of PSs in the area of interest' does not give insight whether the PSs are cluttered together or are homogeneous distributed. Therefore the expressions density and distribution are separately investigated. The difference in density is derived from the local density of the area covered by a bin. An increase in the number of PSs contained by this bin, is an increase in the local density. When during this section the expression 'an increase in density' is used, the average density of the bins is positive. The distribution is used in the global sense. This enables the usage of density and distribution simultaneously. As can be seen in figure 5.6(c) the density of PSs has improved. An increase in the number of PSs for most bins is present and therefore in general the density of PSs increased. Also the position of the bins is of importance. As shown the number of PSs with a short distance increased, which implies that the gaps between the mining area and the city decreased.

Investigation of the PS results of Barradeel concession acquired with the manual PS identi-

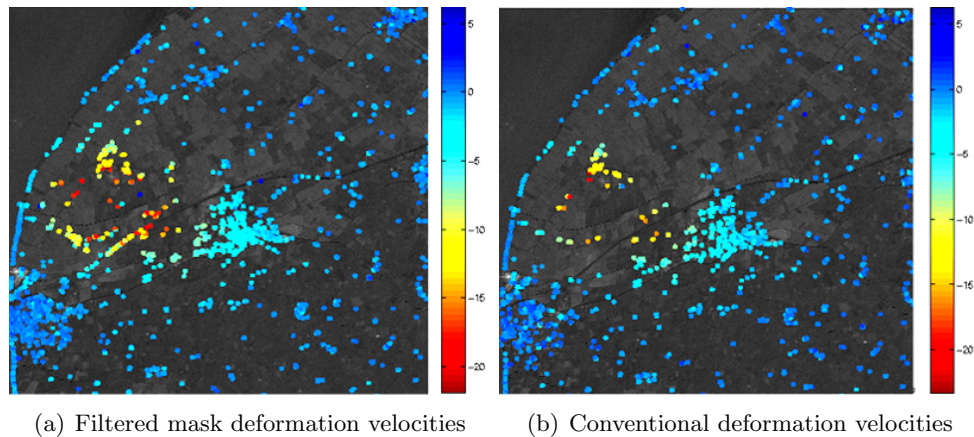


Figure 5.8: Comparing the annual deformation velocity [mm/year] of the manual PS identification method with gridcell size of 300 meters and PSP threshold of 0.4 for track 151, figure (a), with the conventional velocities experiencing same PSP threshold and gridcell size, figure (b), results into an increase of PS density. But it is doubtful whether all outliers are filtered out.

fication method resulted also in an increase in PS density and distribution. Investigation is performed in the same manner as for track 380, with the distances from PSs to a central point in the subsidence bowl. But it is doubtful whether all identified PSs represent reality (see figure 5.8). The two PSs experiencing uplift close to the center of the bowl can be eliminated, because their behavior is not of interest when considering large scale deformation. Southeast to the center of the subsidence bowl two roads can be distinguished. Both roads deform, but the results impute a subsidence approaching the subsidence of the center of the bowl, which is not expected. There are too many PSs situated close to each other and deforming at the same rate to assume this deformation does not represent reality. Hence they can not be removed. Obtaining extra PSs in this area with different methods could give a decisive answer to this problem.

Discussion on all tracks Plots of the annual deformation velocities for all the tracks are found in appendix C. The density and distribution of the PSs increased for all tracks in the manual PS identification case, except for the ascending track 487 covering the Veendam concession. The increase in density of PSs indicates that indeed, as expected, pixels obtaining PS properties are rejected since their amplitude dispersion is above the set threshold. In the manual PS identification results of track 487 the density and distribution of PSs stayed equal to the conventional method. This could be due to the fact that most of the PSs identified by the manual PS identification method are also identified in the conventional case. This would mean that all identified PSs by the manual PS identification mask experienced an amplitude dispersion below the set PSP threshold and therefore selection of pixels above this threshold did not result into extra identified PSs. Note that, as discussed for track 151 covering the Barradeel concession, for most manual PS identification results some doubtful PS velocities are present. When the variance of the PS velocities in a small area is large and at random, it is doubtful whether all the velocities are correct. Due to the large variance and dense distribution it is difficult to filter uncorrect PSs, since it is unclear which velocity represents the reality. This holds especially for the manual PS identification results in track 258.

The deformation patterns and velocities acquired for the different tracks are compared to the conventional cases of corresponding tracks. The deformation patterns are comparable between the manual PS identification methods and the conventional cases for all tracks, not taking into account certain outliers. The bowls are shaped in the same way as conventional results.

Track	Velocity manual PS identification [mm/year]	Velocity conventional [mm/year]
108	-12.1	-12.2
380	-13.0	-13.2
487	-13.1	-13.1
151	-19.9	-18.8
258	-19.8	-19.6

Table 5.5: Annual velocities investigated for all tracks in the manual PS identification case.

The annual velocities of the different tracks are presented in table 5.5. Note that the annual velocities between tracks can not be compared since the images cover a different timespan and the possibility is present that tracks covering the same area are based on different reference coordinates. A comparison of the annual velocities between tracks is made in section 5.8. Except for track 151, also the velocities are comparable between the manual PS identification method and the conventional cases for all tracks. In the Veendam cases these are the velocities of the center of the bowl. In the Barradeel case there are no PSs identified in the center of the bowl and therefore different areas are chosen to investigate whether the velocities are equal. For track 151 this is the closest area containing PSs to the west of the subsidence bowl center. The area has the size of $2 \times 1 \text{ km}^2$. In the Veendam concession the annual velocity based on track 380 is -13 mm/year . And for the Barradeel test site the annual velocity close to the center of the subsidence bowl for track 151 obtained with the manual PS identification method is -20 mm/year compared to -19 mm/year of the conventional case. This PS is uncorrect unwrapped as can be seen in figure 5.3. More on unwrapping can be read in section 5.7. The assumed realistic deformation behavior experiences larger deformation at the final epochs, and therefore this annual velocity is lower than the other PS. This velocity influences the mean annual velocity resulting into a conventional annual velocity smaller than the annual velocity estimated with the manual PS identification method.

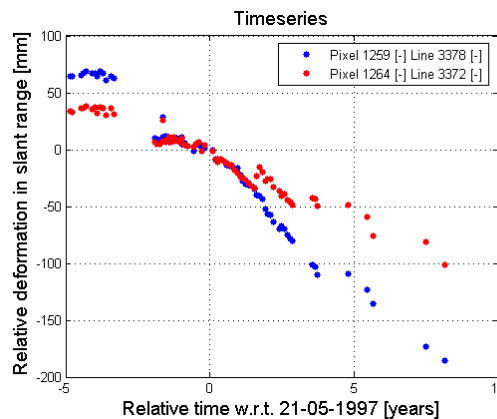


Figure 5.9: Time series track 151 of pixels close to the center of the subsidence bowl obtained with the conventional method experiencing PSP threshold 0.4 and gridcell size 200 meters. Unwrapping errors in the deformation behavior of the pixel represented by the red curve, results into a lower average annual velocity. Most PSs present in the area deform like the pixel represented by the blue curve.

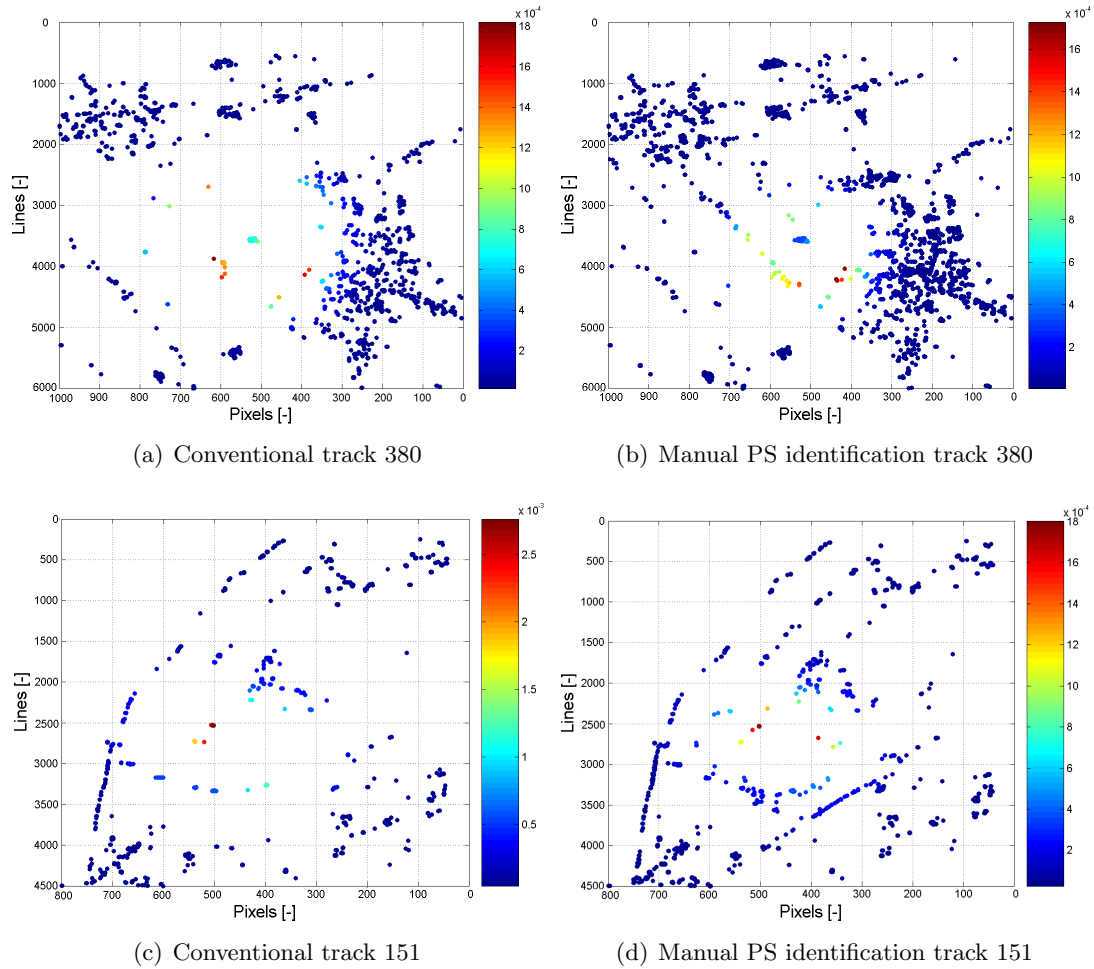


Figure 5.10: (a) Internal precision of track 380 making use of the conventional method (a) and the manual PS identification method (b). Figure (c) and (d) present the internal precision of the conventional respectively the manual PS identification method of track 151. Plotted are the entries on the diagonal matrix of the $Q_{\hat{y}}$ matrices.

Quality description In this case the Overall Model Test investigates the difference between linear model and the unwrapped time series. For the test cases Veendam and Barradeel the OMT is comparable between the manual PS identification method and the conventional methods. Hence in the Veendam area the large OMT values are randomly spread over the area and in the Barradeel area they are located in the subsidence bowl, see figure 5.5. This implies that the model used to estimate deformation for the subsidence area in Barradeel approaches the estimated deformation less reliable than in the subsidence area of Veendam. Since the manual PS identification does not influence the functional model, it is expected that the OMT values are distributed accordingly to the conventional method.

The external and internal precision are acquired for both test sites in the manual PS identification case making use of a Gaussian function, describing the subsidence bowl. These precisions are compared to the precisions of the conventional results. Table 5.6 presents the ratio between the manual PS identification cases and the reference case. Every covariance coefficient on the diagonal of the $Q_{\hat{x}}$ matrix is divided by the corresponding coefficient of the conventional $Q_{\hat{x}}$ matrix. The mean of these ratios is presented in the table. The external precision for track 487 has not increased since the same number of PSs are identified, but more incorrect PSs are

present in the dataset, which influences the precision. In the other cases the external precision had increased, despite the incorrect unwrapped or accepted PSs.

Whether the internal precision, $Q_{\hat{y}}$, increased or decreased compared to the conventional method with same gridcell size and PSP threshold, can be found in the same table 5.6 This is based on the diagonal values in the matrix. Again all tracks experienced an increase compared to the conventional model except for track 487. This is due to the same reason as the internal precision. Figure 5.10 presents the plots displaying the diagonal entries of the $Q_{\hat{y}}$ matrix for track 380 and 151. The diagonal entries of the conventional case and the manual PS identification case are both present in the figure. As can be seen in both cases the precision becomes better in the manual PS identification case. The spatial behavior of the precisions also stays alike, expect for the center and the western area of the subsidence bowl in the manual PS identification case of track 380. The precision becomes better in this area due to the estimation of the bowl parameters used to derive the precision. The radius and the depth of the estimated bowl is larger in the manual PS identification case then the conventional case, resulting into a better fit. The difference in estimated parameters is introduced by the difference in density of PSs in the center and the west of the bowl.

Track	$Q_{\hat{x}}/Q_{\hat{x},conv}$	$Q_{\hat{y}}/Q_{\hat{y},conv}$
108	0.79	precision increase
380	0.48	precision increase
487	1.12	precision decrease
151	0.51	precision increase
258	0.65	precision increase

Table 5.6: Internal and external precision investigated for the manual PS identification cases of all tracks.

5.4 Results bilinear interpolation method

The bilinear interpolation is used to estimate the deformation of a pixel for every epoch. Subtraction of this estimated deformation is assumed to reduce the variability of the phase, and therefore increasing the success rate of identified PSs. The triangulation is based on the PSCs constructing the final initial network of the conventional method. At least one PSC should be present in the main subsiding area else a deformation estimation based on a bilinear interpolation does not result into subtraction of deformation present in the subsidence bowl. Figure 5.11 shows two cases of the Barradeel concession area covered by track 151. The first case is based on an initial network which does not contain a PSC in the subsidence bowl and the second case is based on an initial network which contains a PSC in the subsidence bowl. Note that the displayed deformation velocities are the estimated deformation velocity added to the subtracted deformation, hence resulting into the subsidence bowl. Figure 5.11 also shows Delaunay triangulations based on the annual PSC deformation velocities.

Clearly the PS analysis presented in figure 5.11(c) did not result in an increase of the PS density. Whether the identified PSs, making use of the bilinear interpolation method and a gridcell size of 300 meters, increased the density is investigated with distance measurements. According to section 5.3 the distances from the PSs located in the subsidence bowl and a central position of the investigated PSs are calculated. A histogram of the distances is found in figure 5.12(a). Comparing these to the conventional PS distribution, results into histogram 5.12(b). An increase of the number of PSs is concluded from this figure and a more homogeneous distribution

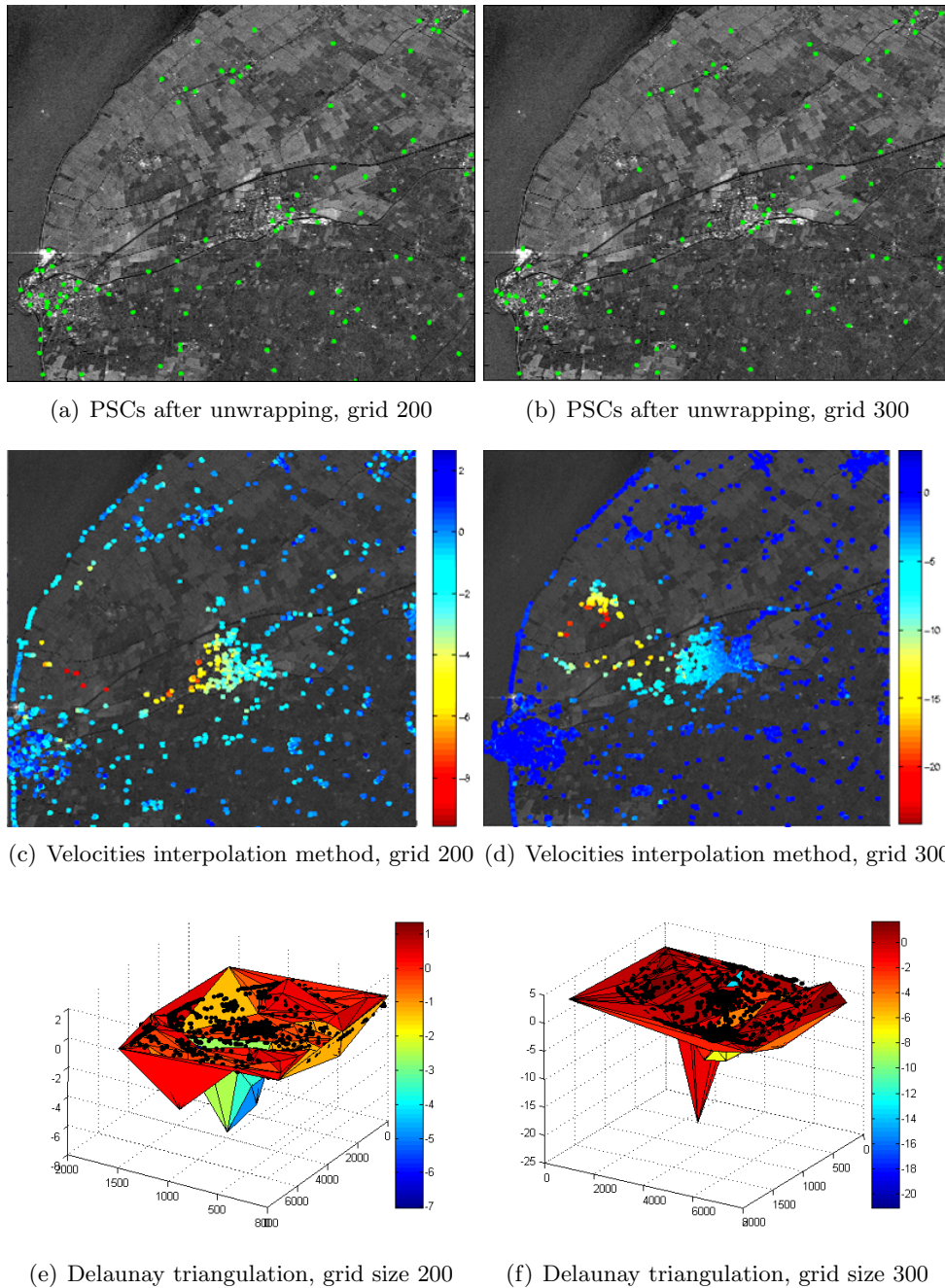


Figure 5.11: (a) PSCs composing the final initial network for track 151 with a gridcell size of 200 meters and (b) with a gridcell size of 300 meters. Figures (c) and (d) present the deformation rate of track 151 with a gridcell size of 200 meters respectively 300 meters. Delaunay triangulations based on the PSCs for the two cases are shown in (e) and (f). The maximum velocity in triangulation (e) is -7 mm and the maximum velocity in triangulation (f) is -21 mm. Note that the annual velocities displayed in the figures are the velocities resulting from the PS analysis plus the subtracted velocities based on the deformation estimation method.

of PSs is acquired.

In figure 5.13 the annual PS velocities of the identified PSs with the interpolation method for track 380 covering the Veendam concession can be found. Comparing these to the conventional

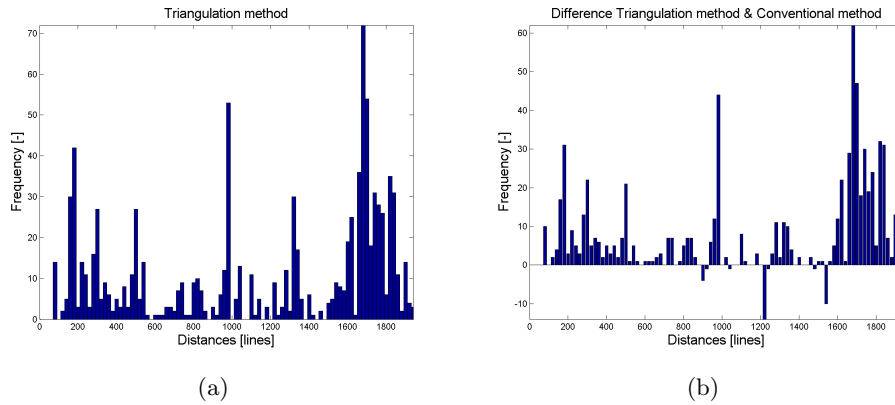


Figure 5.12: (a) Histogram of the distances in track 151 between the central point in the subsidence bowl to neighboring PSs obtained with the bilinear interpolation method. Figure (b) represents the difference between the conventional distances and histogram (a). An increase in PS density and spatial distribution is present.

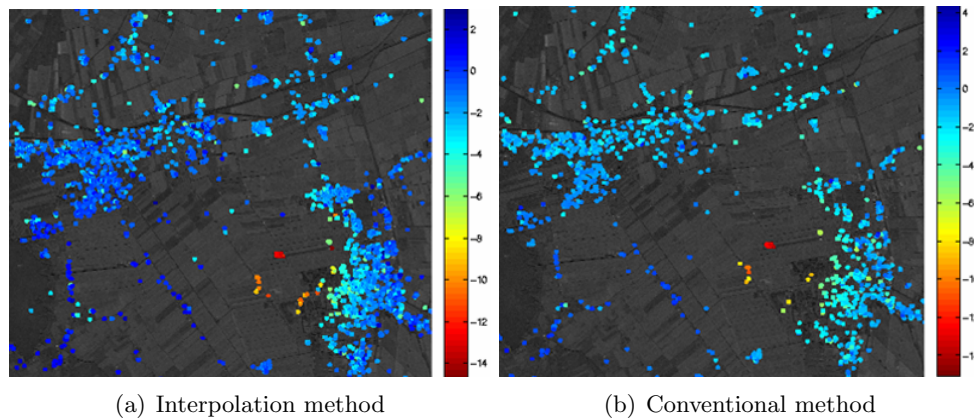


Figure 5.13: The annual velocities track 380 of the interpolation method (a) and the conventional method (b) with corresponding PSP threshold and gridcell size. Note that the annual velocities displayed in the figures are the velocities resulting from the PS analysis plus the subtracted velocities based on the deformation estimation method.

PS velocities indicates an increase in density and a more homogeneous distribution of PSs. This has been investigated in the same manner as for track 151, where the distances from the center of the subsidence bowl to the PSs are obtained and compared to the distances in the conventional results. In the bilinear interpolation results the distribution of PSs is a bit denser in the southern area of the bowl, but also the variation of velocities is rather large, hence it is doubtful if the results present the reality. The overall deformation pattern is comparable to the conventional method though.

Discussion on all tracks Plots of the annual deformation velocities for all the tracks are found in appendix C. The density and distribution of the PSs increased for all tracks in the bilinear interpolation case. But note that for some tracks the variance of the PS velocities in a small area is large and at random. Therefore it is doubtful whether all the velocities are correct. Due to the large variance and dense distribution it is difficult to filter uncorrect PSs, since it is unclear which velocity represents the reality.

The velocities and deformation patterns acquired for the different tracks are compared to the

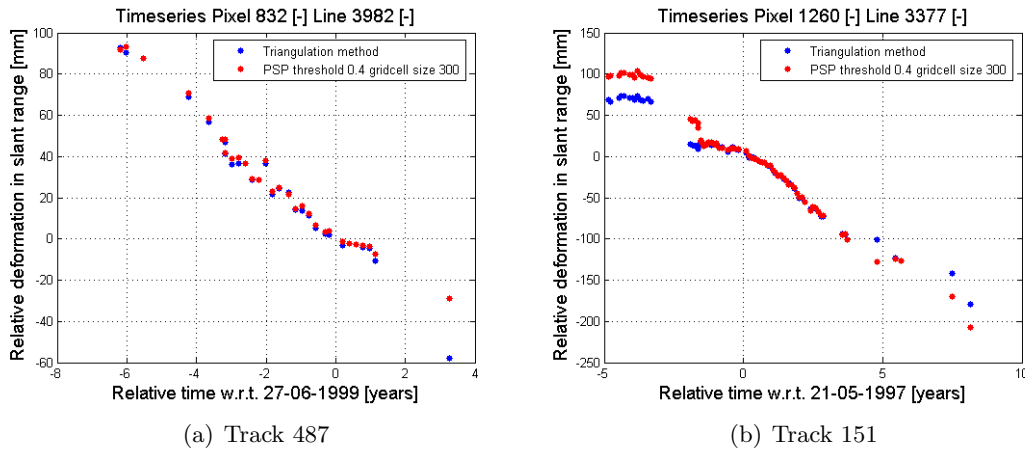


Figure 5.14: (a) Time series of a PS in the center of the subsidence bowl experiencing unwrapping differences between the conventional and interpolation method for track 487. (b) Time series of a PS close to the center of the subsidence bowl experiencing unwrapping differences between the conventional and interpolation method for track 151. Hence in both cases different annual velocities are the result.

conventional cases of corresponding tracks. The deformation patterns are comparable between the bilinear interpolation methods and the conventional cases for all tracks, not taking into account certain outliers. The bowls are shaped in the same way as conventional results. This also assumes that the unwrapping errors especially present in the Barradeel test cases, are not eliminated with the interpolation method. This is because the subtracted deformation is based on the PSs experiencing the unwrapping errors, this addition from the removed deformation signal, results into addition of the unwrapping errors again. More on unwrapping errors can be found in section 5.7.

The annual velocities of the different tracks are presented in table 5.7. As in the manual PS identification case the velocities of the center of the bowl in the Veendam cases are averaged to acquire an annual velocity at the center of the bowl. And in the Barradeel case the same area ($2 \times 1 \text{ km}^2$) as in the manual PS identification case close to the center of the bowl is chosen to investigate whether the velocities between the conventional and optimization method are equal. The estimated velocity of the maximum subsiding PSs for the Veendam test site track 380 -13 mm and for the Barradeel test site track 151 is -20 mm. The conventional method to which the interpolation method is compared, obtains the same PSP threshold and same gridcell size as the interpolation method. Because the threshold and gridcell size chosen for the manual PS identification method can differ from the interpolation method, this explains the difference in the velocities of the conventional methods in tables 5.5 and 5.7. In the Veendam test case the deformation velocity estimated with the interpolation method approximates the conventional deformation velocity. For the tracks 487, 151 and 258 there is a difference in the conventional velocity and the new acquired velocity. These differences can be explained.

The interpolation method performed on track 487 corrected unwrapping errors, which introduced a higher velocity than in the conventional case. For certain points unwrapping errors for the last epoch are eliminated, resulting into a larger annual velocity for those specific PSs. Figure 5.14(a) shows for one PS the correction of unwrapping errors. The difference in annual velocity for track 151 is also due to unwrapping differences. As can be seen in figure 5.14(b), a PS experiencing an unwrapping error seems to subside faster than actual, since the unwrapping errors show deformation at the period before mining started. Investigation of the PSs present in this area showed an unwrapping error of 4 fringes until 1996, where in the other cases this

Track	Velocity interpolation method [mm/year]	Velocity conventional [mm/year]
108	-11.5	-11.5
380	-13.2	-13.2
487	-14.0	-13.1
151	-19.9	-23.7
258	-18.7	-17.4

Table 5.7: Annual velocities investigated for all tracks in the bilinear interpolation case.

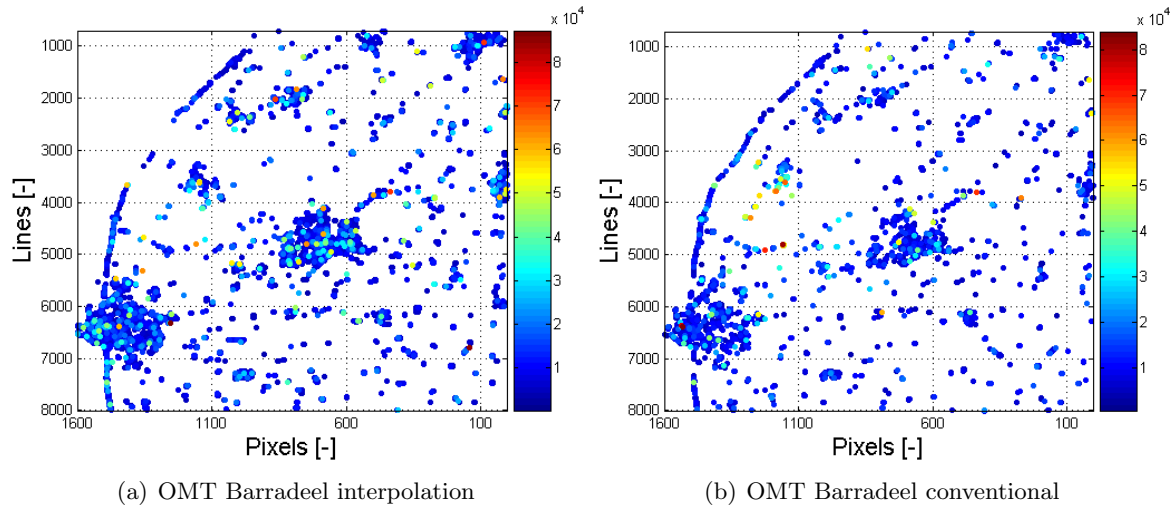


Figure 5.15: (a) The Overall Model Test between the linear model and the estimated deformation for every epoch for track 151 in the interpolation case. Deformation is subtracted with a bilinear interpolation. (b) The Overall Model Test between the linear model and the estimated deformation for every epoch for track 151 in the conventional case.

unwrapping error is 2 fringes. This difference in error causes the difference in velocity. The difference in velocity for track 258 is introduced by a different chosen reference coordinate. The reference coordinate experienced deformation compared to the reference coordinate of the bilinear interpolation, and hence a different annual velocity for the center of the bowl is achieved. The PS chosen as reference coordinate in the conventional method is also identified in the interpolation method. Addition of the deformation found in the interpolation dataset for the reference coordinate of the conventional dataset to the deformation of all PSs in the conventional dataset, results into comparable velocities. An example of this can be found in section C.3.

Quality description The OMT values of the PSs identified with the use of the interpolation method for track 151 based on a gridcell size of 300 meter, are presented in figure 5.15. The OMT at the subsidence area significantly decreased in comparison to the conventional results, hence the estimated parameters describe the differential phase of these PSs more reliable than for the conventional results and the deformation model approximates the deformation contribution to the residual phase. This result was expected, when assuming that the subtracted deformation has a better fit to the conventional dataset, then the linear model estimated in the case. Therefore the residuals will be smaller between the estimated linear model in the interpolation case then the residuals in the conventional case.

The external and internal precision are acquired for both test sites in the manual PS identi-

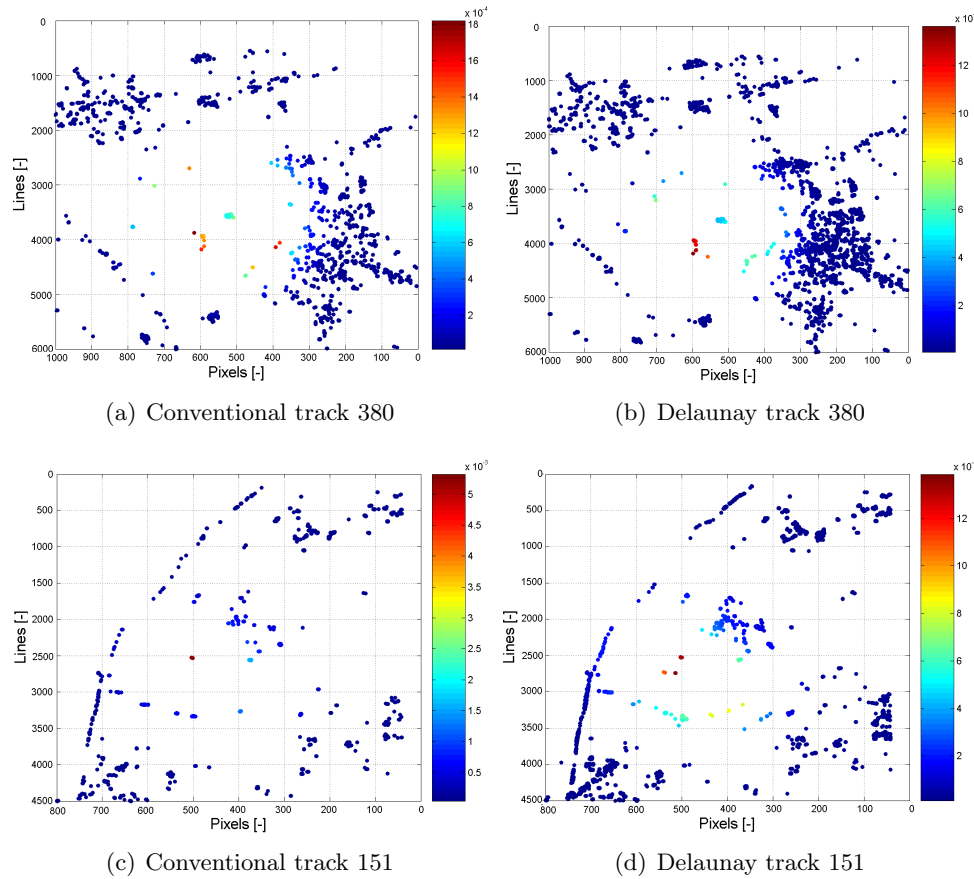


Figure 5.16: (a) Internal precision of track 380 making use of the conventional method (a) and the bilinear interpolation method (b). Figure (c) and (d) present the internal precision of the conventional respectively the bilinear interpolation method of track 151. Plotted are the entries on the diagonal matrix of the $Q_{\hat{y}}$ matrices.

cation case making use of a Gaussian function, describing the subsidence bowl. These precisions are compared to the precisions of the conventional results. Table 5.8 presents the ratio between the interpolation cases and the reference case. Every covariance coefficient on the diagonal of the $Q_{\hat{x}}$ matrix is divided by the corresponding coefficient of the conventional $Q_{\hat{x}}$ matrix. The mean of these ratios is presented in the table. The external precision for all the tracks increased compared to the conventional method. Thus the model parameters can be estimated more precise with these PS dataset than with the conventional PS datasets.

Whether the internal precision, $Q_{\hat{y}}$, increased or decreased compared to the conventional method with same gridcell size and PSP threshold, can be found in the same table 5.8. This is based on the diagonal values in the matrix. Only the internal precision for track 258 decreased compared to the conventional method. The interpolation case does not contain a much denser distribution of PSs, but a more homogeneous distribution. Since the number of PSs in the Sexbierum area, north of the subsidence bowl, decreased compared to the conventional results and some errors are present in the PS set the internal precision also decreased. The figure 5.16 presents the plots displaying the diagonal entries of the $Q_{\hat{y}}$ matrix for track 380 and 151. The diagonal entries of the conventional case and the bilinear interpolation case are both present in the figure.

Track	$Q_{\hat{x}}/Q_{\hat{x},conv}$	$Q_{\hat{y}}/Q_{\hat{y},conv}$
108	0.71	precision increase
380	0.45	precision increase
487	0.81	precision increase
151	0.61	precision increase
258	0.89	precision decrease

Table 5.8: Internal and external precision investigated for the interpolation cases of all tracks.

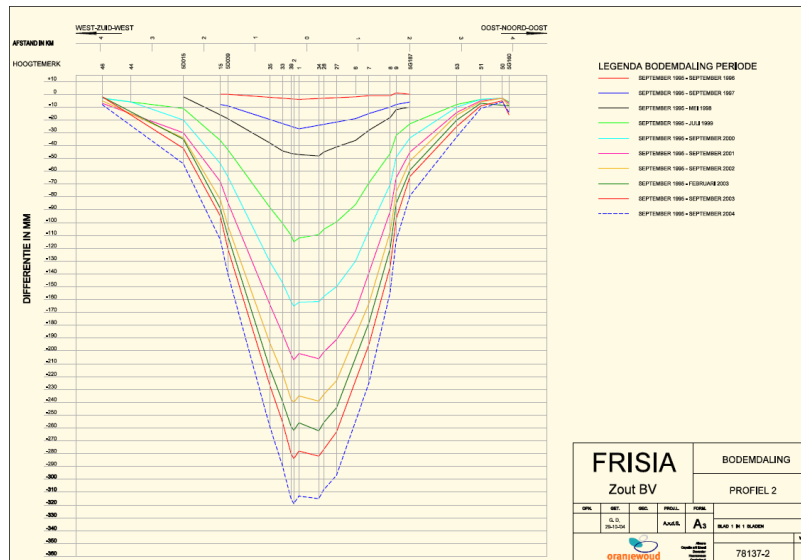


Figure 5.17: Measured propagation of the subsidence bowl [4].

5.5 Results Gaussian bowl method

With the Gaussian bowl method deformation surfaces are estimated for every epoch. The phase contribution of these surface is removed from the differential phase. Equal as for the bilinear interpolation, the elimination of the deformation is assumed to reduce the variability of the phase, resulting into a higher success rate of indicated PSs. The unknown parameters of the bowl for an epoch are estimated with the use of least-squares, which makes use of initial parameters. These are acquired from the conventional PS estimations. The initial values of the origin of the bowl (x^0, y^0) are based on the cavern locations. For the Veendam concession it is assumed that the cavern is located at the mining site, which is the subsiding area in the center of the bowl, and for the Barradeel concession the location of BAS-1 is applied. The initial z^0 -coordinate of the origin is set to deformation most frequent occurring. Assumed is that this is the offset between the Earth's surface and the deformation of the reference point. The depth d^0 is the deformation of the PSs present in the neighborhood of the initial origin of the bowls, and the radius r^0 is roughly estimated based on the radius of the PS deformation describing the bowls. Since the number of initial parameters is at least $2 \times \text{Number of Epochs} + 3$ for every track, the initial parameters are not presented in this thesis.

Different least-squares models are applied to obtain the parameters, (x_c, y_c, z_c) , d , r . These models are:

- The estimation of the parameters for all epochs at once, with or without a stable origin through time. Without a stable origin through time the number of estimated parameters is $5 \times \text{Number of Epochs}$.

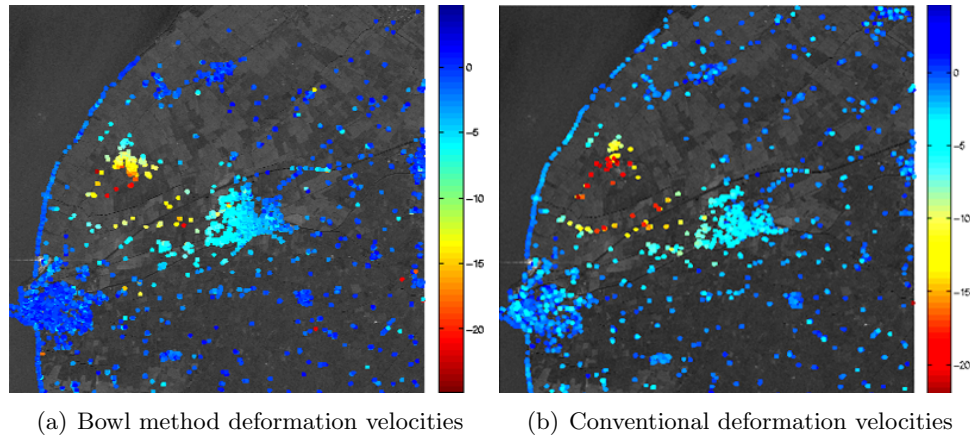


Figure 5.18: (a) Annual deformation velocities of the Gaussian bowl method applied to track 151. (b) Conventional estimated deformation with PSP threshold 0.45 and gridcell size 200 meters. Note that the annual velocities displayed in the figures are the velocities resulting from the PS analysis plus the subtracted velocities based on the deformation estimation method.

- The estimation of parameters based on one epoch for an estimation with or without a stable origin through time. Without a stable origin through time the number of estimated parameters is 5×1 Epoch.
- And the estimates with or without stable origin through time based on subsets of the epochs. With n the number of Epochs in the subset and without a stable origin through time, the number of estimated parameters is $5 \times n$ Epochs.

In these three cases for every epoch parameters are determined. Thus the number of calculations made in case 1 is 1 calculation, in case 2 *Number of epochs* calculations and in case 3 this is *Number of subsets* calculations. The system of equations are described in appendix B. Estimated parameters experiencing the smallest Overall Model Test are applied to estimate the deformation surfaces.

Estimated parameters tend to iterate to infinity, when the subsidence bowl deformation approaches the variation of deformation in the PS dataset. Hence estimation of subsidence surfaces at epochs approaching the date of the master interferogram is most of the time not possible. Estimation of the parameters for every epoch at once, tends to iterate to infinity due to the presence of images experiencing deformation comparable to the variation of the deformation in the PS dataset. This is due to the fact that no deformation bowl is measurable, hence also no origin, range and depth can be indicated. Considering estimation of the parameters for one specific epoch at the time, overcomes the mentioned problem. The parameters for the epochs approaching the master date are not estimated, since the deformation is comparable to the variation of the deformation in the PS dataset. This results in differential phases which are not corrected for epochs close to the master acquisition time. Also the division of the epochs in subsets, instead of treating the parameters for every epoch, overcomes the estimation problem.

For the tracks covering the Veendam concession the best estimated parameters were obtained with the iteration system considering the parameters for one specific epoch. The estimation of the parameters in the Barradeel test case for both the tracks, iterated for most least-squares models to infinity. This is due to the difference between the symmetrical subsidence bowl and the deformation present in the Barradeel concession. Two subsidence bowls interfere in this area, a bowl due to salt mining and a bowl due to gas extraction. The estimates of the bowl which did

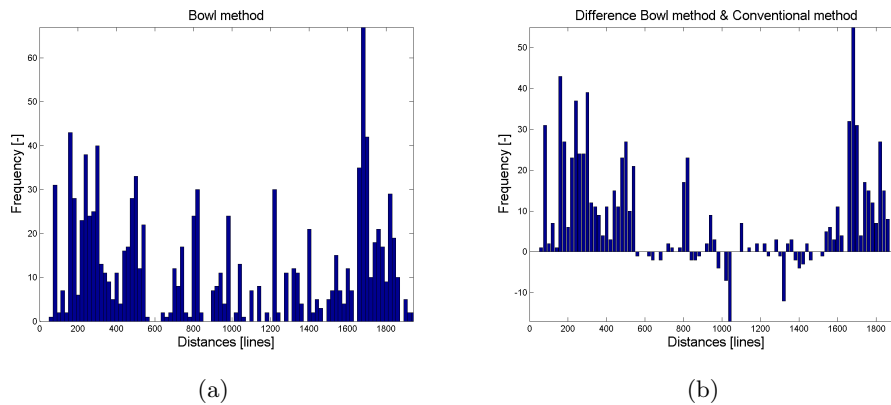


Figure 5.19: (a) Histogram of the distances in track 151 between the central point in the subsidence bowl to neighboring PSs obtained with the Gaussian bowl method. Figure (b) represents the difference between the conventional distances and histogram (a). An increase in PS density and spatial distribution is present.

not iterate until infinity did not describe the bowl due to salt mining, but was situated between the two present subsidence areas. Leveling measurements are linearly interpolated over time to acquire deformations at the SAR image acquisition dates, to be able to estimate the deformation surface at different epochs. The graphs on which the model is based is shown in figure 5.17 and is acquired from [4]. The deformation for every epoch is calculated with the bowl method where the parameters are extracted from the leveling measurements, subsequently the deformation contribution is subtracted from the differential phase. The results of the deformation pattern estimated with the use of bowl estimation as well as conventional results are presented in figure 5.18. A PS at the maximum subsiding position is indicated by the PS analysis. Because the surface estimation now is based on a-priori values obtained from leveling a different deformation pattern is estimated. This deformation pattern approaches reality better, since the breakpoint behavior is taken into account. Therefore the annual velocities in the subsidence bowl are lower than for the conventional method. More about this is explained in section 5.7

The density and distribution of the PSs obtained with the bowl estimation is presented in the histogram 5.19(a). A crop is made of the PSs in the subsidence bowl and distances are measured between the PSs in the crop and the central position. The distances display the density (y-axis) and distribution (x-axis) of the PSs. The difference between the conventional PS distribution and this method is displayed in histogram 5.19(b). The density of PSs has increased and the distribution of the PSs improved. Hence the bowl method succeeded into a increasing the success rate of identified PSs.

Also for the Veendam concession the bowl method is applied. Since the shape of the bowl in this case is more obvious, the parameters can be estimated instead of derived from leveling results. Figure 5.20 displays the bowl method results and the conventional results in the case the same PSP threshold and gridcell size is taken. As can be seen, and as has been investigated with the distances from PSs to a central point in the subsidence bowl, the density and distribution of PSs increased.

Discussion on all tracks Plots of the annual deformation velocities for all the tracks are found in appendix C. The density and distribution of the PSs increased for all tracks in the bowl estimation case, except for track 258. The density decreased, but the distribution became more homogeneous. A possible reason for this decrease in density could be the application of

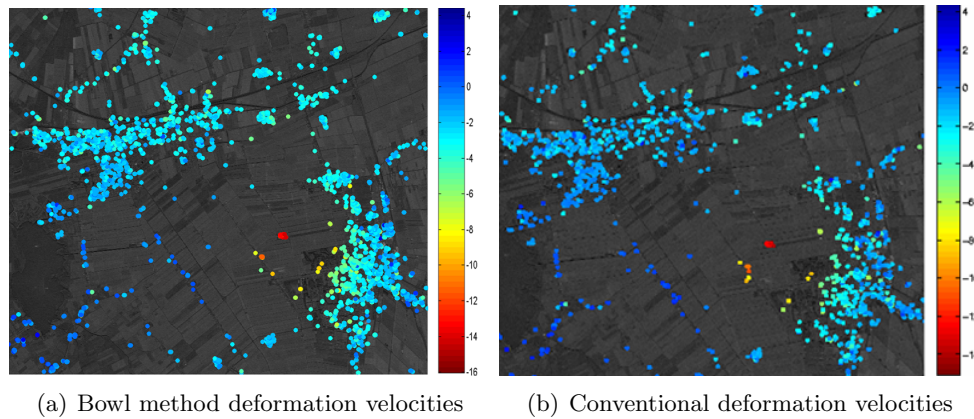


Figure 5.20: (a) Annual deformation velocities of the Gaussian bowl method applied to track 380. (b) Conventional estimated deformation with PSP threshold 0.4 and gridcell size 300 meters. Note that the annual velocities displayed in the figures are the velocities resulting from the PS analysis plus the subtracted velocities based on the deformation estimation method.

uncorrect estimated parameters. This will increase the variability of the phase, resulting into less identified PSs. For track 380 also a Gaussian bowl based on the PSCs is used for subtraction of the deformation. This case is discussed in section C.2. Since no PSC was present at the center of the subsidence bowl, the estimated deformation approached a flat terrain. Subtraction of this flat terrain did not decrease the variability of the phase enough to be able to identify more PSs.

The velocities and deformation patterns acquired for the different tracks are compared to the conventional cases of corresponding tracks. For the Veendam test site the deformation patterns between the bowl method and conventional method are comparable. This is expected since the subtracted deformation is based on the conventional PS results and therefore adding the subtracted deformation and the PS bowl results will approach the annual velocities of the conventional method. For the Barradeel test site the estimated bowl surfaces are based on leveling results, hence a difference between the conventional method deformation pattern and the bowl method deformation pattern is expected. This pattern is shown in figure 5.21(a) and is mainly caused by unwrapping variabilities in the period before starting mining and the last two epochs as presented in figure 5.21(b).

The annual velocities of the different tracks are presented in table 5.9. In the Veendam cases these are the velocities of the center of the bowl and, like in the previous cases, in the Barradeel case track 151 this is the closest area containing PSs to the west of the subsidence bowl center. Except for track 151 and 108, the velocities are comparable between the bowl methods and the conventional methods for all tracks. In the Veendam concession the annual velocity based on track 380 is -13 mm/year. And for the Barradeel test site the annual velocity in the subsidence bowl for track 151 is -18 mm/year compared to -19 mm/year of the reference case.

The difference in velocity for the bowl estimation method in track 108 is introduced by uncorrect unwrapped time series. For this track the deformation estimation was uncorrect at two epochs, resulting in unwrapping errors. The calculated velocity became larger than in reality. This resulted in a smaller annual velocity for the bowl estimation method. Next to the unwrapping errors 3 PSs experiencing no deformation over time are identified. This also reduces the annual deformation. The time series are presented in figure C.3.

In the bowl case for track 151 the density of PSs in the area is larger than in the conventional case and consists out of two groups. One group deforming as the conventional PSs and one group deforming with -16 mm/year. Hence the mean results into a number in between the

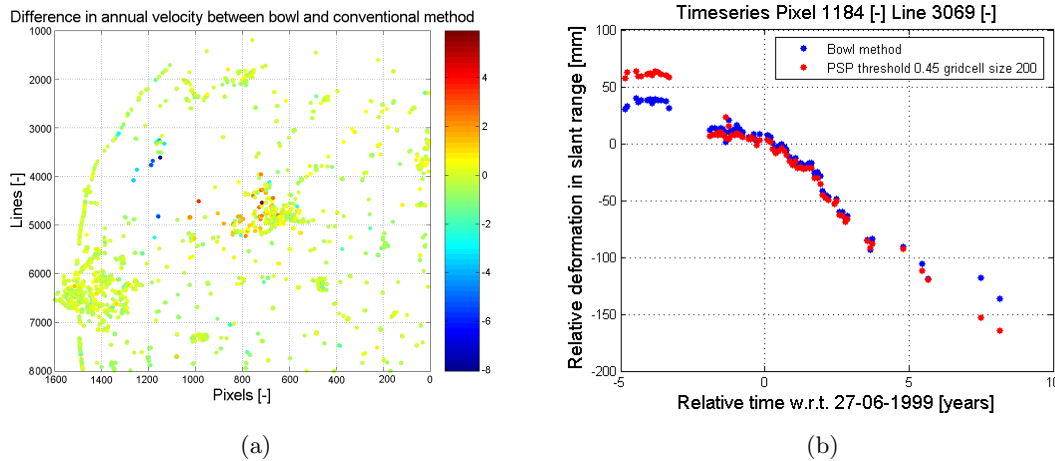


Figure 5.21: (a) The difference in annual velocity between corresponding PSs identified in the bowl method or conventional method of track 151. (b) Timeseries of a PS situated close to the center of the bowl. The blue graph indicates the timeseries of the bowl method and the red graph indicates the timeseries of the conventional method. Due to unwrapping differences a decrease in the annual velocity for the bowl method is present.

group velocities. The difference in subsidence velocity is caused by the unwrapping errors after 2000. For the group subsiding -16 mm/year the data experiences an unwrapping error of at least 2 fringes, and therefore seems to subside slower than in reality, as can be seen in figure 5.21(b). This figure does not represent a PS in the center of the bowl, but experiences the same unwrapping error after 2000. These errors are introduced by the estimated parameters. The range of the bowl was estimated to small, resulting into a smaller subsidence away from the center of the bowl. Interesting to see is that in the bowl method the same PSs are identified as for the conventional case, but only one of the eight PSs present in that area experiences an unwrapping error at the last two epochs. The other identified PSs by the bowl method do experience the unwrapping errors at the last epochs. This is probably a reason why the PSs are not identified with the conventional method.

Track	Velocity bowl method [mm/year]	Velocity conventional [mm/year]
108	-10.5	-12.3
380	-13.8	-13.2
487	-13.0	-13.1
151	-17.8	-18.8
258	-18.9	-18.7

Table 5.9: Annual velocities investigated for all tracks in the bowl estimation case.

Quality description The OMT and the estimated variance for the Barradeel case are displayed in figure 5.22. The OMT has decreased for the PSs in the subsidence bowl. The two PSs close to the center of the subsidence bowl experience a larger OMT value compared to the neighboring PSs, but compared to the conventional OMT values, the reliability of the model became larger.

The external and internal precision are acquired for both test sites in the bowl method making use of a Gaussian function, describing the subsidence bowl. Table 5.10 presents the ratio between

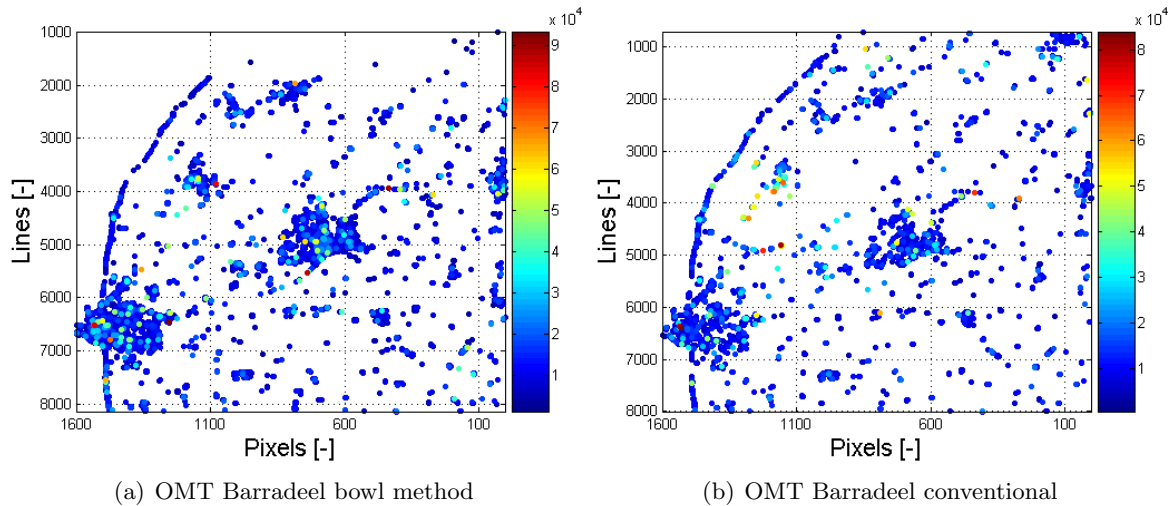


Figure 5.22: (a) The Overall Model Test between the linear model and the estimated deformation for every epoch for track 151 in the bowl case. Deformation is subtracted with a bilinear interpolation. (b) The Overall Model Test between the linear model and the estimated deformation for every epoch for track 151 in the conventional case.

the bowl cases and the conventional case. The bowl case for track 258 experienced a decrease in external precision compared to the conventional case. This is introduced by less PSs in the northern area, Sexbierum, of the subsidence bowl compared to the conventional case, and a few PSs which are clearly unrealistic, but still present in the dataset.

Whether the internal precision, $Q_{\hat{y}}$, increased or decreased compared to the conventional method with same gridcell size and PSP threshold, can be found in the same table 5.10. This is based on the diagonal values in the matrix. Again all tracks experienced an increase compared to the conventional model except for track 258. This is due to the same reason as the internal precision. The figure 5.23 presents the plots displaying the diagonal entries of the $Q_{\hat{y}}$ matrix for track 380 and 151.

Comparison of the conventional method and the bowl method of track 380, results into different spatial patterns of the precisions. Observing the bowl method precisions shows that the precision of the PSs in the west and the center of the bowl increase compared to the conventional method. But the precision of the PSs in the south east stays behind. The distribution and density is leading for the precision in these cases. This is caused by the parameters estimated to calculate the precision. Since more PSs are present in the south and the center of the bowl in the bowl method and in the conventional method in the west more PSs are present, the estimated radius and depth, used to calculate the precisions, differ between those cases. Hence the density of PSs indirectly influences the precision in these cases. But nevertheless this way of calculating the precision is assumed good enough to show the difference in precisions.

As can be seen in both cases the precision becomes better with the bowl method. As expected the spatial pattern of the precision for track 151 compared to the conventional method differs. This is introduced by change of time series for certain PSs as shown in figure 5.21(a).

5.6 Results breakpoint model

The breakpoint model first tests the phase to the linear model and when the OMT exceeds specified bounds, the breakpoint model is applied. The model consists out of two linear functions connected at the end respectively the begin of the graphs. Two different approaches of this model

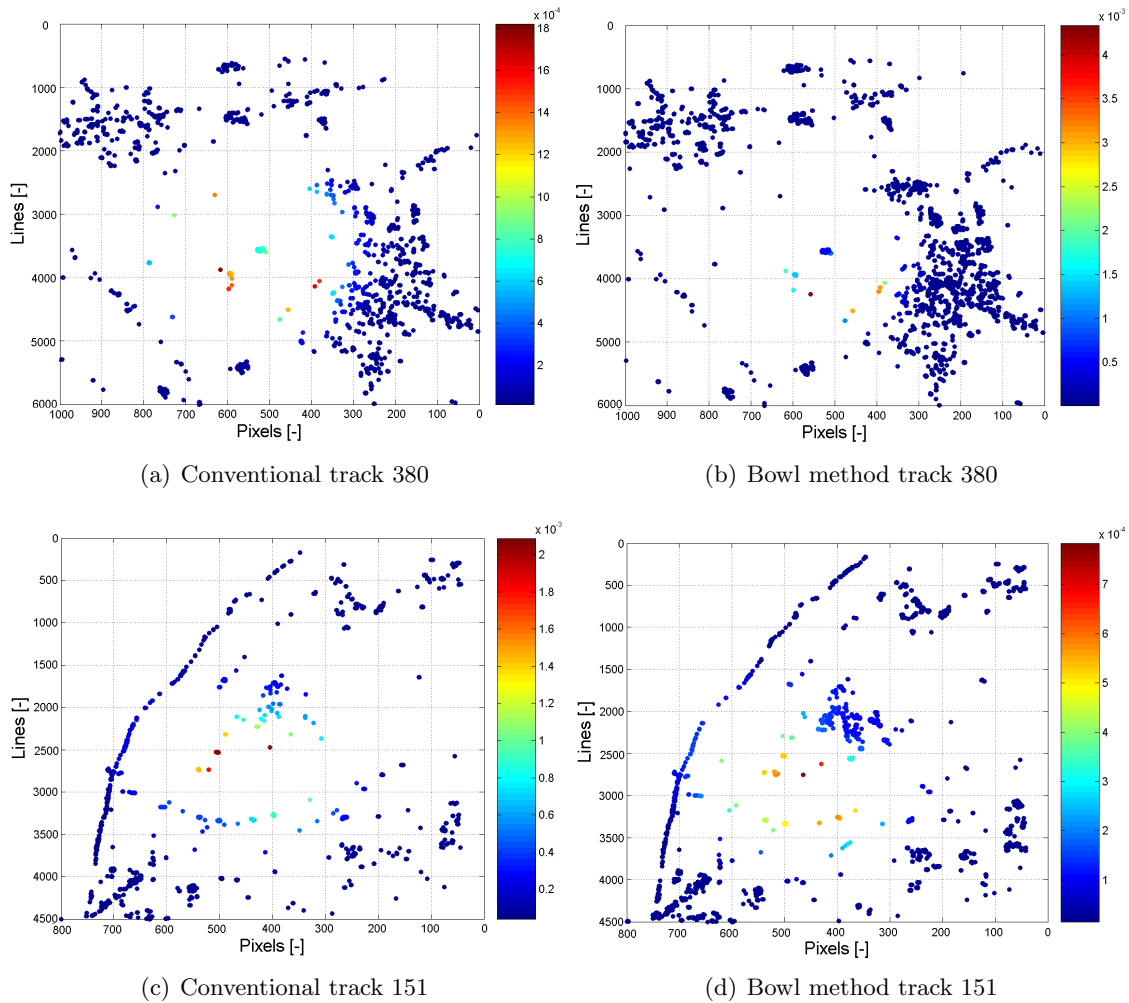


Figure 5.23: (a) Internal precision of track 380 making use of the conventional method (a) and the bowl method (b). Figure (c) and (d) present the internal precision of the conventional respectively the bowl method of track 151. The entries on the diagonal matrix of the $Q_{\hat{y}}$ matrices are plotted in the figures.

can be used. In the final processing step the PSPs are tested against PSCs constructing the initial network. A PSP is connected to the three closest PSCs. The arc between PSC1 and the PSP, $PSC1/PSP$, is unwrapped and the estimated ambiguity is applied to test the PSP. When this ambiguity corresponds to the two ambiguities obtained with:

$$\begin{aligned}
 PSC2/PSP_{amb} - PSC2/PSC1_{amb} &= PSC1/PSP_{amb} \\
 &\text{and} \\
 PSC3/PSP_{amb} - PSC3/PSC1_{amb} &= PSC1/PSP_{amb},
 \end{aligned}$$

the PSP is accepted as PS. The difference between the two breakpoint models is that in one of the breakpoint methods all three obtained ambiguities should be similar, else the PSP is rejected. In the other breakpoint method two or more obtained ambiguities should be similar, else the PSP is rejected. The testing assumptions are more strict when three out of the three estimated arcs have to fit, therefore it is expected that in this case less PSs are identified compared to the case where two out of three arcs fit. Since the conventional method accepts PSPs when the ambiguities of at least two arcs fit, the results between conventional and breakpoint model are

Track	$Q_{\hat{x}}/Q_{\hat{x},conv}$	$Q_{\hat{y}}/Q_{\hat{y},conv}$
108	0.66	precision increase
380	0.53	precision increase
487	0.76	precision increase
151	0.41	precision increase
258	1.46	precision decrease

Table 5.10: Internal and external precision investigated for the bowl cases of all tracks.

only comparable when the same method is used in the breakpoint model. When a large amount of outliers is present in the final PS dataset, the method accepting PSPs when the ambiguities between three arcs are similar can be used to remove outliers. This is discussed in appendix C. This method identified significantly less PSs. Outliers are removed, but the density and distribution of PS decreases compared to the conventional method.

Figure 5.24 presents the conventional deformation velocity of track 108 and the results of the breakpoint model. The density of the PSs does not differ between the conventional method and the breakpoint model, when applying the elimination of arcs with less than two fitting ambiguities. The method assuming three arcs to fit, results in a significant reduction of PSs, which is expected since the criterion became more strict. Also PSs of interest are eliminated with this method. The small difference in identified PSs in the two fitting ambiguity acceptance method and identified PSs in the conventional method is introduced by the deformation behavior of PSs. Because the PSs present experiencing breakpoint behavior in the subsidence area can approximately be estimated by linear subsidence, the implementation of a breakpoint model will not identify many extra PSs.

The maximum subsidence is exactly the same in the breakpoint model as in the conventional model, which is not expected, since the breakpoint model influences the deformation velocity and known is that at the edges of the subsidence bowl breakpoint models are present. Comparing the conventional and breakpoint method results, indicated that certain PSs in urban area influenced correct estimation of the breakpoint epoch. The implemented model accepts one epoch as breakpoint for all the PSs obeying the breakpoint model, set by the most often occurring epoch. This resulted in a chosen breakpoint epoch which was not influenced by mining activities, hence manually fixing the breakpoint is applied to achieved the desired results. The breakpoint epoch is set to the 13th epoch, which occurs directly after the period in which no images are available at -2.11 years from the master image. The deformation velocity estimated with a manually set breakpoint are shown in figure 5.29. An decrease in the PS density has occurred, which is not expected since the PSs are also tested against the linear model. The time series plot the deformation of a PS through time. If they are estimated with the manually set breakpoint, the time series for track 108 result generally in the same unwrapped deformation. Whether a signal is unwrapped correctly or not can visually be estimated. Following the shape of the deformation graph can indicate if unwrapping errors are present or not. Unwrapping errors are discussed in section 5.7. Two time series which are influenced by the breakpoint model are presented in figure 5.25. The graphs show an improvement of the time series 5.25(a) and a deterioration of the time series 5.25(b). The improved PS is located at the boundaries of the bowl and the deteriorated PS is located in the center of the bowl. Hence usage of the breakpoint model does not necessary implies better results. The percentage of PSs experiencing a change in deformation per epoch with one or more PSs is less than 1%.

Histograms of the distance between a central position and PSs located in the subsidence bowl are presented in figure 5.26(a). The difference between the conventional method and the break-

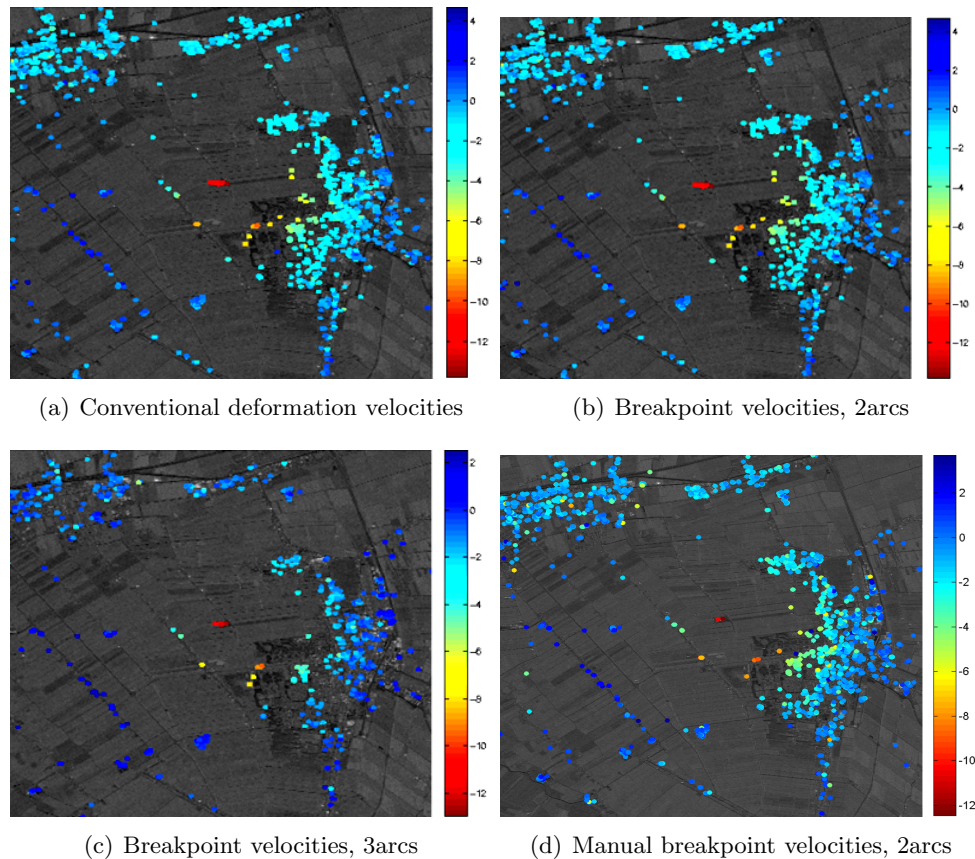


Figure 5.24: The influence of the breakpoint model track 108. Figure (a) presents the conventional velocities. Figures (b), (c) and (d) present the velocities making use of the breakpoint model. In (b) accepted PSs are shown based on the criterion unwrapped parameters of at least 2 arcs fit the network, and in (c) the criterion that 3 arcs fit is implemented. Figure (d) presents the velocities when the breakpoint is manually set to the 13th epoch and at least 2 arcs fit the network.

point method is visualized in figure 5.26(b). The difference indicates that the distribution and density of the PSs decreased. Which is not expected since both the linear model and the breakpoint model are applied to estimate the parameters for a PS. Hence when the linear model is accepted in the conventional analysis, it should be accepted in the breakpoint analysis also. An explanation for this is not yet found.

The breakpoint model has been applied to track 151 covering the Barradeel test site. In figure 5.27 the annual velocities of the conventional and breakpoint method are presented. The breakpoint in this case is manually set to epoch 28, which occurs in May 1996. Investigation of the time series of PSs indicated a correct applied breakpoint (figure 5.28). And in contradiction to track 108 the density and distribution of PSs stays close to the conventional case. This has been investigated with the distances from a central chosen PS in the area of subsidence to the PSs present in the area.

Discussion on all tracks Plots of the annual deformation velocities for all the tracks are found in appendix C. The density and distribution of the PSs increased for none of the tracks, but stayed equal or decreased. Since track 108 and track 151 are the only tracks where manually a

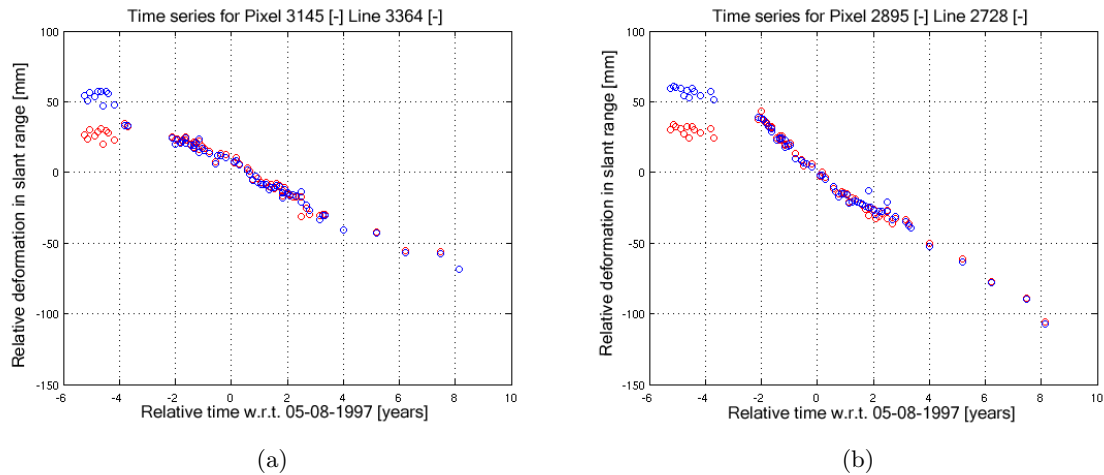


Figure 5.25: (a) Time series of a PS located on the edge of the subsidence bowl. The blue circles represent the conventional time series and the red circles represent the breakpoint model time series with manually set breakpoint. (b) Time series of a PS located on the right side in the center of the subsidence bowl.

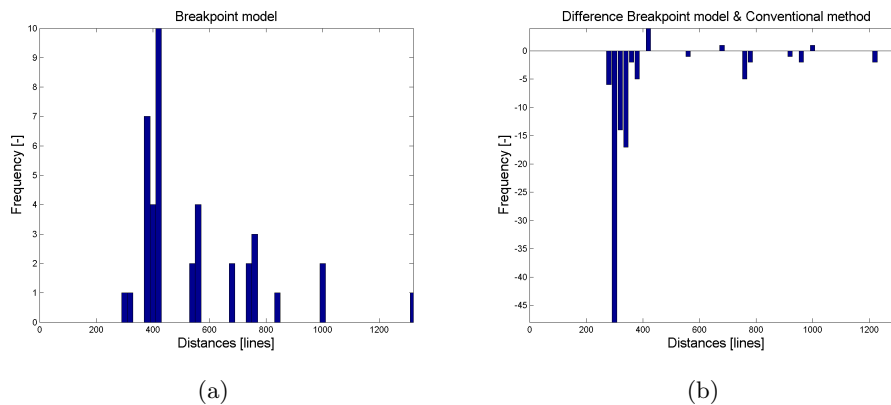


Figure 5.26: (a) Histogram of the distances between the central point in the subsidence bowl to neighboring PSs obtained with the breakpoint model track 108. The breakpoint is manually set to epoch 13. Figure (b) represents the difference between the conventional distances and histogram (a). Both distributions are comparable.

breakpoint is set, the results of the other tracks approach the results of the conventional method. The same holds for the deformation patterns. In the results of track 151 a clear difference is present, since the unwrapping errors before mining and at the last epochs are corrected the deformation differs from the conventional deformation.

The annual velocities of the different tracks are presented in table 5.11. In the Veendam cases these are the velocities of the center of the bowl and, like in the previous cases, in the Barradeel case track 151 this is the closest area containing PSs to the west of the subsidence bowl center. The breakpoint models applied to the ascending tracks are the models accepting a PSP when three out of three estimated ambiguities of a similar arc are equal. This is performed since in ascending tracks the chance a linear deformation model fits the differential phase is larger, since less images are present over an equal timespan as in a descending track. Difference in annual velocities are present in track 487, 151 and 258.

The PSs in the subsidence bowl in Veendam test site experiences a deformation velocity

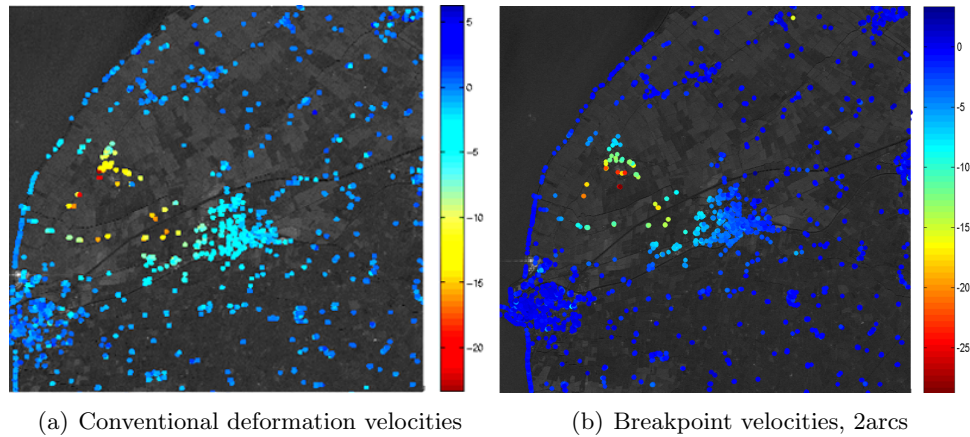


Figure 5.27: The annual velocities track 151 obtained with the breakpoint model. Figure (a) presents the conventional velocities. Figures (b) present the velocities making use of the breakpoint model. In (b) accepted PSs are shown based on the criterion unwrapped parameters of at least 2 arcs fit the network and a manually set breakpoint to epoch 28.

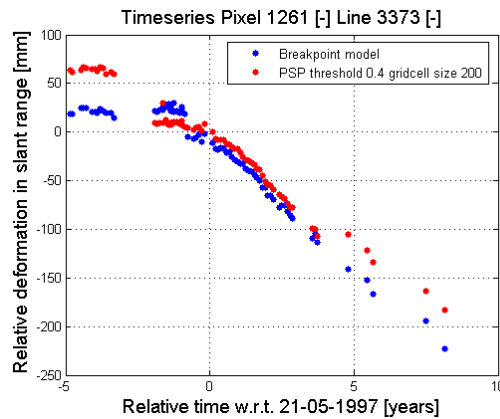


Figure 5.28: Time series of a PS located close to the center of the subsidence bowl. The red graph presents the time series of the conventional PS and the blue time series presents the graph of the PS obtained with the breakpoint model. Unwrapping errors are generally eliminated with the breakpoint model.

of -11.6 mm/year. In the area investigated to get the annual velocity of the center of the subsidence bowl, two PSs are present. One of the PSs is presented in figure 5.25 and as can be seen the deformation velocity decreased due to the correction of the images acquired between 1992 and 1994. This influences the deformation velocity, hence a lower velocity is measured than in the conventional method. The number of identified PSs in the breakpoint method for track 487 is small. Three PSs are identified. Their annual velocities are almost equal to the annual velocities found in the conventional method for the same PSs. The other identified PSs in the conventional method experience smaller velocities, hence the average results into a smaller velocity. The maximum deformation velocities of the subsidence bowl in Barradeel increased to -20.1 mm/year. This due to corrected unwrapping errors as seen in figure 5.28. At the period experiencing no deformation the unwrapping error is eliminated. At the final epochs the estimated deformation is larger than the conventional case. Combing these two unwrapping differences results into a larger deformation velocity. The difference in velocity for track 258 is introduced by a different reference coordinate.

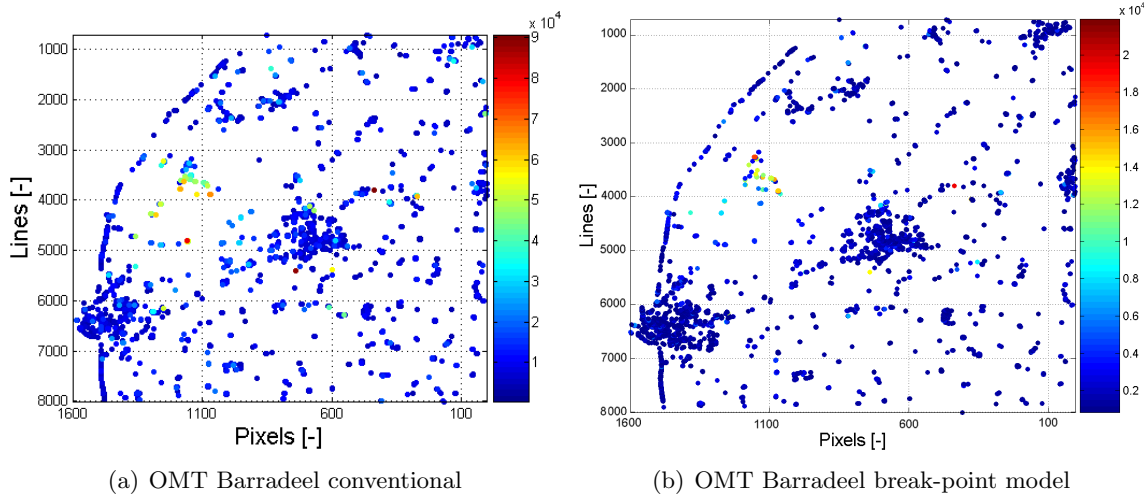


Figure 5.29: (a) The Overall Model Test between the linear model and the estimated deformation for every epoch for track 151 in the conventional case. (b) The Overall Model Test between the linear model and the estimated deformation for every epoch for track 151 in the break-point case. The OMT results into smaller values in the break-point case than in the conventional case since a breakpoint model represents reality more accurate.

Track	Velocity breakpoint method [mm/year]	Velocity conventional [mm/year]
108	-11.6	-12.2
380	-13.0	-13.2
487	-14.1	-13.1
151	-20.1	-18.8
258	-18.9	-19.7

Table 5.11: Annual velocities investigated for all tracks in the breakpoint method.

Quality description The slopes of the breakpoint linear functions is not specified in the output, but the residuals are stored which describe the breakpoint model in combination with the linear model stored. Making use of this information, the OMT results into smaller values than the conventional case, see figure 5.29.

The external and internal precision are acquired for both test sites in the bowl method making use of a Gaussian function, describing the subsidence bowl. Table 5.12 presents the ratio between the bowl cases and the conventional case. Three of the five tracks experience a decrease in the external precision. This is introduced by the number of PSs present. Since less PSs are present in these cases the parameters can be estimated less precise and hence the external precision decreases.

Whether the internal precision, $Q_{\hat{y}}$, increased or decreased compared to the conventional method with same gridcell size and PSP threshold, can be found in the same table 5.12. This is based on the diagonal values in the matrix. The same tracks experiences a decrease in internal precision as the tracks experiencing a decrease in external precision. This is also due to the number of PSs present in the area of interest. Figure 5.30 presents the plots displaying the diagonal entries of the $Q_{\hat{y}}$ matrix for track 108 and 151. A clear decrease in the internal precision between the cases of track 108 is present. The figures displaying the conventional and breakpoint internal precisions of track 151 show less difference. The calculated internal precisions in the breakpoint method increase compared to the conventional method. Since these precisions are

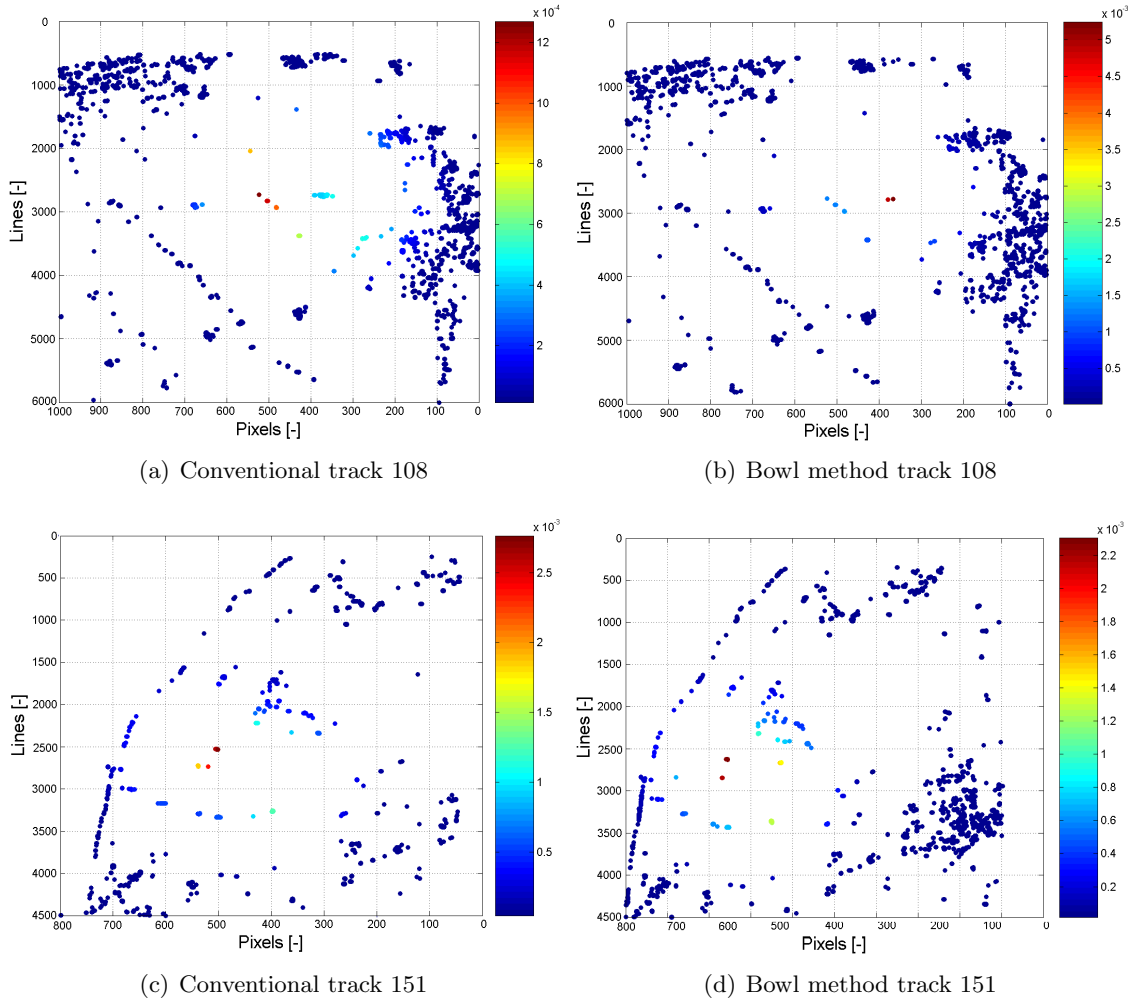


Figure 5.30: (a) Internal precision of track 108 making use of the conventional method (a) and the breakpoint model method (b). Figure (c) and (d) present the internal precision of the conventional respectively the breakpoint model method of track 151. Plotted are the entries on the diagonal matrix of the $Q_{\hat{y}}$ matrices.

calculated for one epoch, not including the period before mining or the last 2 epochs, it can be stated that the difference in distribution and density in the breakpoint model results introduces an increase in the precisions.

Track	$Q_{\hat{x}}/Q_{\hat{x},conv}$	$Q_{\hat{y}}/Q_{\hat{y},conv}$
108	3.52	precision decrease
380	0.84	precision increase
487	2.57	precision decrease
151	0.76	precision increase
258	2.64	precision decrease

Table 5.12: Internal and external precision investigated for the breakpoint method of all tracks.

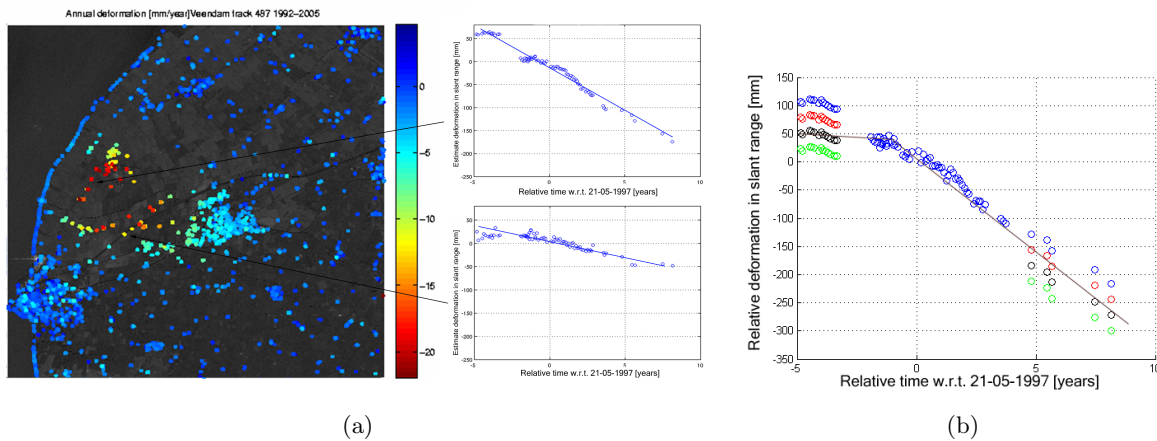


Figure 5.31: Unwrapping errors in the Barradeel test site. Figure (a) presents two time series obtained from the conventional PS analysis of track 151. The linear line, presents the estimated linear deformation. Figure (b) gives unwrapping possibilities for the time series. The blue dots present the estimated deformation.

5.7 Unwrapping errors

Ambiguities are the number of phase cycles the signal traversed before arriving back at the satellite, which can not be measured by the SAR instrument. The phase is unwrapped to obtain the unknown number of ambiguities. Hence unwrapping errors are introduced by an incorrect estimated ambiguity. Correction is performed by addition or subtraction of n -times half the wavelength, 28 mm for ERS, since the ambiguity is an integer. The contribution of deformation on the phase differences is estimated according to the functional model describing linear deformation. This can introduce unwrapping errors as presented in figure 5.31. Frisia Salt started mining activities in 1996, assuming external deformation is neglect able, no deformation should be measured from 1992 to 1996. The figure shows estimated deformation present at the timespan 1992-1995, introduced by the linear model implemented. The estimated deformation from 2000 is therefore also questionable, since they are unwrapped according to the linear model, but when the unwrapped deformation over the period 1996-2000 is followed according to a linear line, a different deformation should be present. Different unwrapping possibilities are shown in figure 5.31. Over the period 1996-2000 enough images are present to constraint the unwrapping, hence no unwrapping errors are present.

The Veendam concession does not experience obvious unwrapping errors. The time series of PSs in the subsiding area are best described by a breakpoint model, but since the deformation velocity is small compared to the Barradeel case and the period experiencing a smaller deformation velocity is shorter, unwrapping errors are less present compared to the Barradeel test case. Because the linear model and specified boundaries give the estimated deformation enough variability the actual deformation can be captured. Figure 5.32 presents time series of PSs located in the subsidence area of Veendam.

This section analyzes the changes in time series due to the three different methods implemented to overcome rejection of PSs with the subtraction of estimated deformation surfaces. Also two methods to correct unwrapping errors are discussed. The manual PS identification algorithm does not affect the time series, but the indicated PSs, hence no time series analysis is performed.

Since the estimation of the subsidence bowls is based on the PS estimated deformation, it

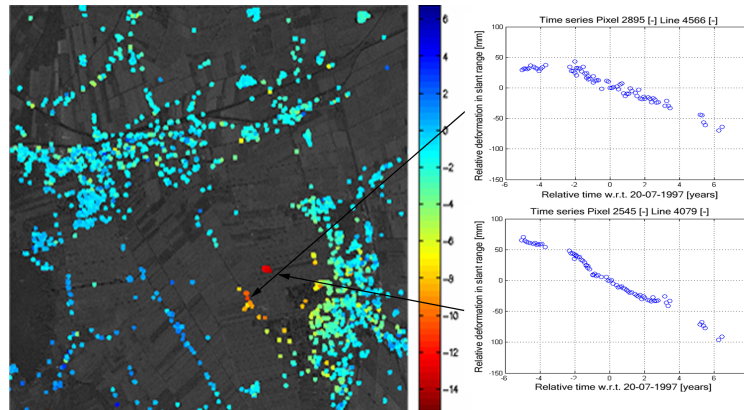


Figure 5.32: Time series from the Veendam test site. Two time series obtained from the conventional PS analysis of track 380.

is expected that unwrapping errors are not removed. Time series of the bilinear interpolation method and the Gaussian bowl method are presented in figure 5.33. As the plots indicate, the time series do not significantly differ. The Gaussian bowl annual velocities for the last two epochs in the first plot differ one fringe (28 mm) with the conventional case. This is most likely introduced by the estimated bowl parameters. The difference in time between the last epoch and the previous is large, which resulted into sensitive temporal deformation behavior for unwrapping errors since a linear temporal deformation model is used. The subtracted deformation approaches the actual deformation and therefore small velocities are estimated for the epochs based on the residual phases. The deformation for the last epoch is therefore also estimated small. Thus when the subtracted deformation differs 1 fringe with reality, the estimated plus the subtracted deformation also differs 1 fringe.

Time series of the breakpoint model in track 108 are displayed in figure 5.25. Most PS time series are minorly changed due to the breakpoint model, the variance decreased, but unwrapping changes did not significantly occur. The two time series are examples of PSs where the time series of a PS is expected to be corrected for unwrapping errors and the time series of a PS is deteriorated. When comparing the conventional an breakpoint model time series of a PS experiencing a breakpoint model in track 151, it can be seen that an unwrapping errors are corrected. This is shown in figure 5.28. It can be concluded that the breakpoint method gives

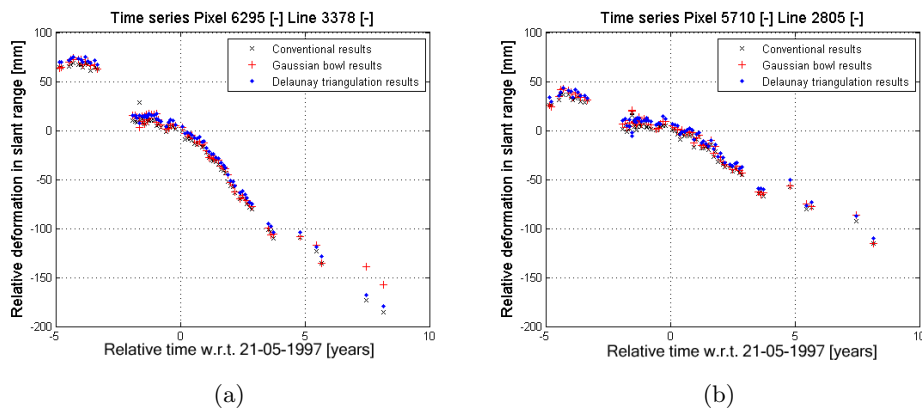


Figure 5.33: Time series of two PSs situated in the Barradeel subsidence bowl experiencing unwrapping errors.

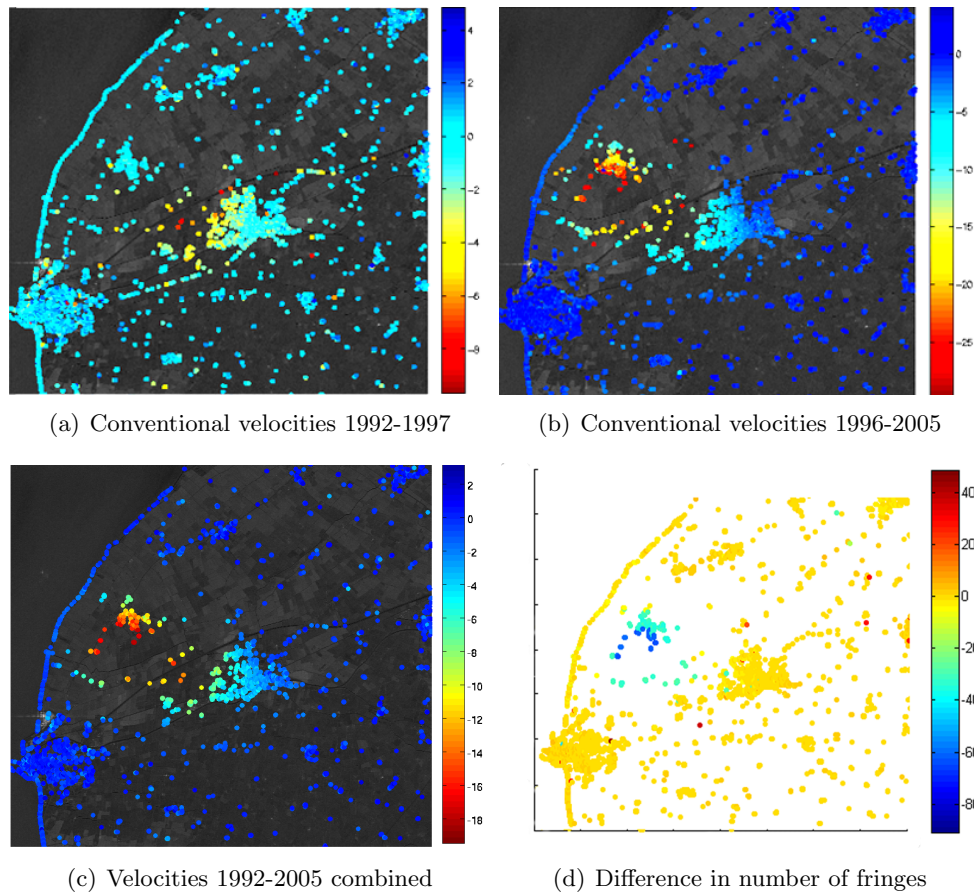


Figure 5.34: To overcome unwrapping errors the corresponding pixels in the PS results of the stack with images over the period 1992-1997 (a) and 1996-2005 (b) are combined (c). The results are compared with the conventional dataset and the difference in number of fringes for the period 1992-1995 is plotted in figure (d).

the wanted result in the Barradeel test site, but not in the Veendam test site. Hence two other correction methods are discussed.

One method to overcome unwrapping errors in the Barradeel test case, is to perform two PS analysis, where one analysis processes the images acquired in the period 1992 to 1997, when mining just started in the area, and a analysis processing the stack containing images acquired in 1996 until 2005. The estimation of atmosphere is based on the full interferogram stack. After acquisition of the parameters for both cases, the time series of corresponding PSs are connected. This process can be compared to the breakpoint model, since two PS analysis are run, hence two deformation velocities are estimated. Time series of this method are displayed in figure 5.34. The conventional deformation results are compared to the new results. The difference in fringes for the period 1992-1995 is spatially plotted. A clear pattern becomes visible, enabling the correction of all PSs in the surroundings of the subsidence bowl. The nearest PS with known correction is determined for a specific PS. The correction applied to the PS with obtained correction is also applied to the specific PS. Correction of the deformation in the last epochs is manually performed, and based on the assumption that the deformation has a linear behavior from 1998. Two time series presenting the corrected deformation are found in figure 5.35.

This method is labor intensive, hence a different method is applied for the correction of the

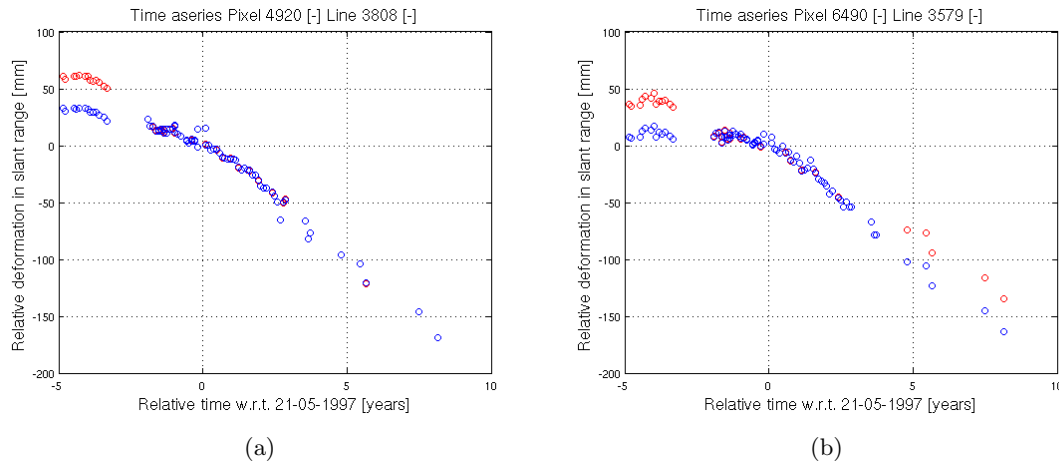


Figure 5.35: Time series of PS in the Barradeel concession corrected by combining PS deformation results acquired from the interferogram stack contain images from 1992-1997 and the stack over the period 1996-2005. The red scatter plots contain estimated deformation for the conventional case and the blue scatter plots contain corrected deformation estimates.

unwrapping errors. In the Barradeel concession, deformation started in 1996. A linear function can be estimated through the estimated deformation from the period 1995-1996, where the first image after the temporal gap of images is used to start with. The images over the period 1992 to 1994 are aligned to this function, taken into account the possible solutions, which are the addition or subtraction of n -times 28 mm since unwrapping is based on the ambiguities. Also for the period 2000 until 2005 a linear function is applied. The period 1998-1999 is used to estimate a linear function, which the images of the sequential period have to obey. But it does not necessarily have to be reality that the linear function describes the linear time behavior. Hence the unwrapping possibilities between a difference of several fringes should be displayed in the plots. The corrected deformation velocity and the distribution of the difference in amount of fringe between the corrected and conventional deformations for the Barradeel concession is displayed in figure 5.36. For every epoch a correction is calculated and assumed is a linear behavior of the deformation after 1999, hence no extra possibilities are shown in the figure. With the use of this method several extra outliers present in the subsidence bowl are detected, since their deformation behavior was linear, and hence no correction is performed on these point. The annual velocities of the areas close to the center of the subsidence bowl are obtained for both cases.

5.8 Validation PS results

This section treats the validation of the PS results using leveling measurements. To be able to compare the deformations of two datasets, the PSs and measurement points have to be situated in the same coordinate system. The PS results will be transformed to the RD-coordinate systems in which leveling measurements are given. The correlation between the two datasets is presented with the correlation coefficient.

Before validating the PS results, first the different datasets composed out of the images of one track are combined to obtain a dense distribution of PSs. The deformation of combined datasets in the Veendam and Barradeel concession are compared to check whether the found deformations are similar.

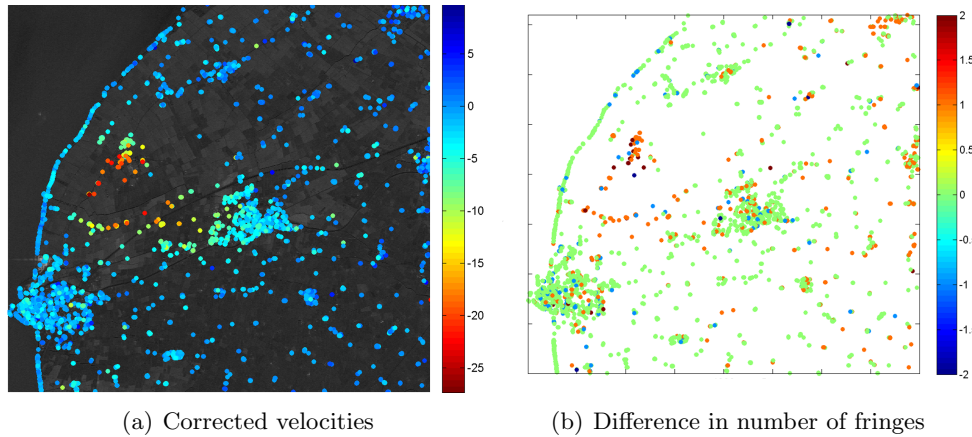


Figure 5.36: (a) The corrected deformation pattern for track 151 with a PSP threshold of 0.45 and gridcell size of 200. The deformation is corrected with a linear model. (b) The difference of number of fringes between the conventional and corrected deformations for epoch 1.

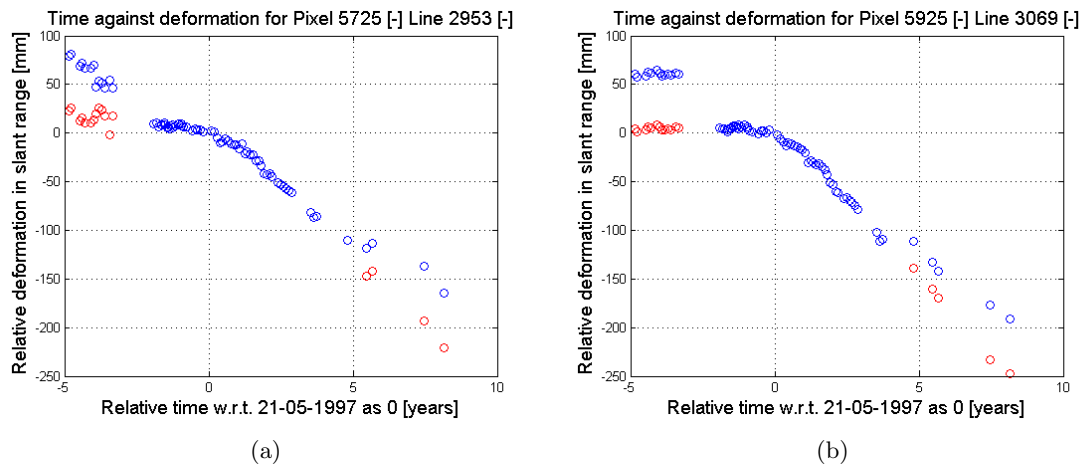


Figure 5.37: Time series of PS in the Barradeel concession corrected by linear functions. The blue scatter plots contain estimated deformation for the conventional case and the red scatter plots contain corrected deformation estimates.

Combination datasets of a track To obtain a dense distribution of PSs, the different datasets of a track acquired with different processing methods are combined. In the Veendam test cases the unwrapping errors are less present and therefore the datasets can be combined not taking into account unwrapping errors. In the Barradeel test case the datasets are combined and afterward corrected for unwrapping errors with the calculation tool as explained in section 5.7.

To combine the datasets the reference coordinates need to be similar. One dataset is chosen as master dataset. All PSs in this dataset are selected. Corresponding PSs between the master and an other dataset are compared. If the deformation patterns and reference coordinates are comparable, the datasets can be combined. The addition of a deformation offset for every epoch can solve a difference between reference coordinates. In most of the cases where reference coordinates were unequal, the reference coordinate was present in the master dataset. This enables an easy determination of the offset, since this is equal to the deformation of the PSs with equal coordinates in the master dataset. When the deformation for every epoch corresponds to the master dataset, the PSs in the observed dataset not present in the master dataset are

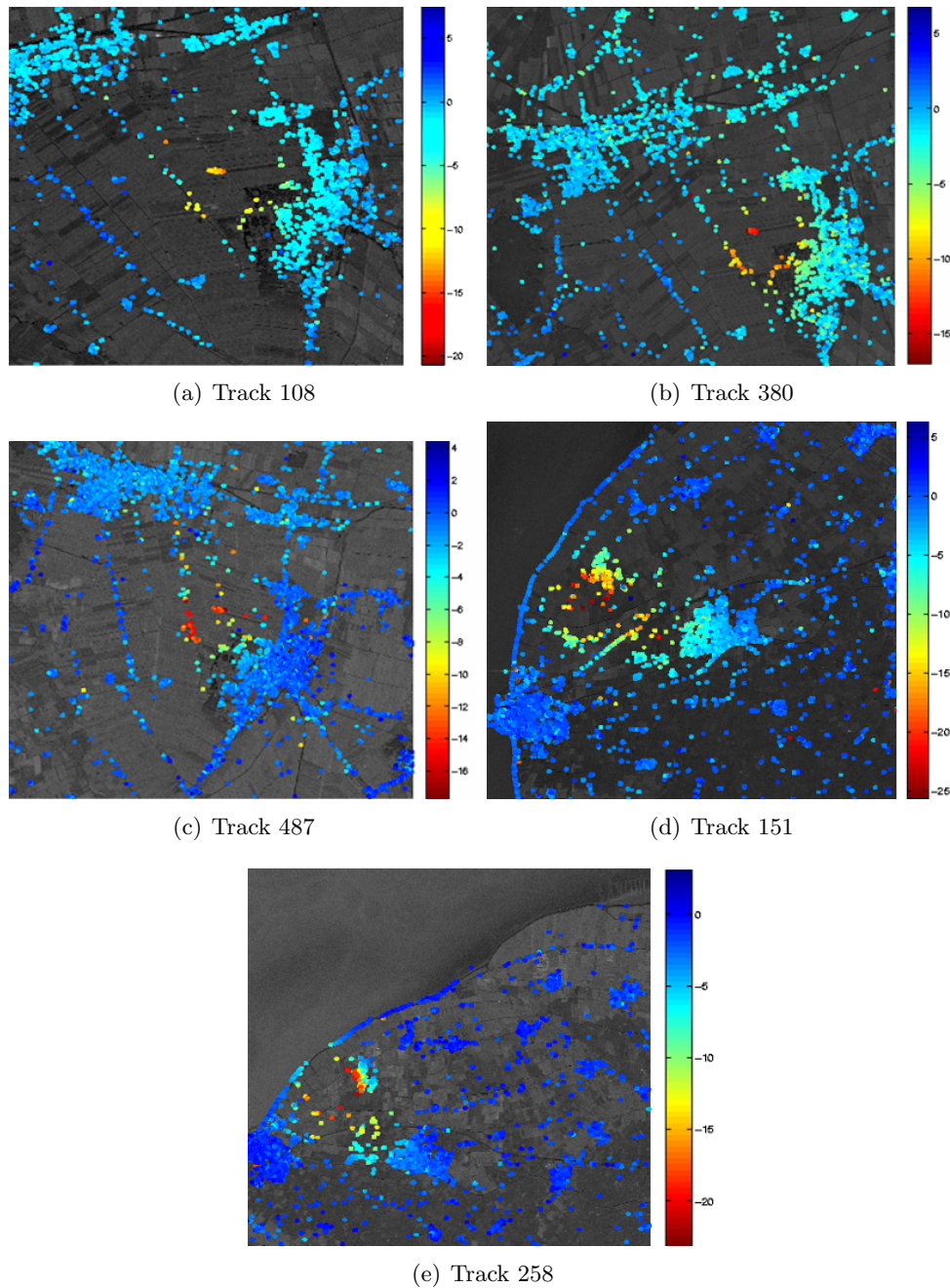


Figure 5.38: The combined datasets of the five different tracks covering the Veendam or Bar-radeel concession. All combined datasets are transformed to the reference coordinate of one master dataset chosen for a track.

added to the master dataset, resulting in a denser distribution of PSs. The combined datasets are presented in figure 5.38. Note that the manual PS identification results in track 258 are not combined. Many outliers are present in the manual PS identification case, hence this case is not taken into account. For the Veendam test case track 380 represents the most dense distribution. Track 487 contains the largest variance in the deformation of PSs in the subsidence area, hence possibly errors are still present in the dataset.

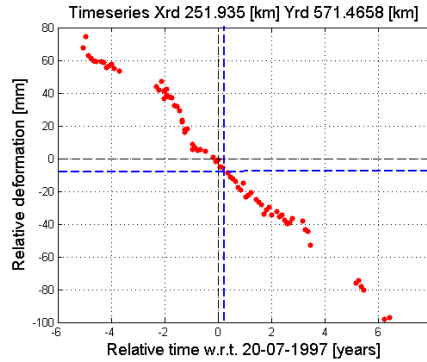


Figure 5.39: Timeseries of a PS situated in the subsidence bowl of track 380. The reference date is to be shifted to the reference date of track 108. The black dashed line represents the reference axis for track 380. The line crosses 0 deformation at 0 years. The blue line represents the shift in years and deformation which has to be performed to rest with the reference date of track 108.

Comparing tracks The SAR acquisition dates and the timespan of a track differ between tracks. Hence when the deformation of the tracks are compared, this has to be taken into account. To overcome this problem the master image date of one track is transformed to the master image date of the other track used for comparison. Applying a shift through time also acquires a shift of the deformation, since zero deformation is set to a different date, see figure 5.39. And when the reference coordinates are not similar, every epoch needs a shift in deformation due to the difference in reference coordinate.

Previous results were still presented in the radar coordinate system, but need to be transformed into the RD-coordinate system to be able to compare the results with the leveling measurements and to be able to compare the different tracks with each other. With the knowledge of the height of the reference coordinate above WGS84 ellipsoid and the orbit parameters of the satellite, the transformation between radar coordinates and RD-coordinates can be performed. The height of the reference coordinate above Earth's surface is first determined with the histogram of the estimated heights by the PS analysis. It is expected that most identified PSs are positioned on the Earth's surface, hence when the peak of the histogram differs from zero the reference coordinate is not positioned on the Earth's surface and also height of the reference coordinate above/below the Earth's surface is known. With the knowledge of this height and the approximate position of the reference coordinate in RD-coordinates, the height above the WGS84 ellipsoid is calculated. With this method still timing errors can be present, resulting in a shift of the RD-coordinates of the dataset. Aligning the PSs with clear features like buildings, dikes etc. removes the timing error.

The PS deformation is given in slant range by the PS analysis, a conversion factor is applied to calculate the displacements in vertical direction as measured by the leveling technique. The relation between the incidence angle, θ_{inc} , and the deformation in slant, d_{slant} , and ground, d_{vert} , range is given as

$$d_{vert} = d_{slant} / \cos(\theta_{inc}). \quad (5.3)$$

The incidence angle is derived from the orbit parameters stored in the SAR files.

The transformation to the chosen reference date is applied as follows. Since the acquisition dates of the images of the tracks are at different moments, the deformation at the epochs can not directly be compared. The temporal baseline is corrected to one of the two baselines of the two tracks. Table 5.13 presents the shift in years to transform the tracks 380 and 487 to the same master image date of track 108, and the shift to transform track 258 tot the same master date

as track 151. Multiplication of the temporal offset with the annual velocities of the PSs, results in the deformation at the moment of the master image of the other track. Hence subtraction of this deformation sets the deformation to zero at the new master date. When observing the timeseries it could be that the deformation at the reference moment is not set to zero. This is introduced by the addition of the residuals of a PS.

Track	Master image date	Shift in years
108	05-AUG-1997	0
380	20-JUL-1997	0.044
487	27-JUN-1999	-1.893
151	21-MAY-1997	0
258	06-JUN-1997	-0.044

Table 5.13: The temporal baseline shift in years to obtain equal reference dates in the Veendam and Barradeel cases.

The deformation of both datasets is now observed from the same acquisition date. When different reference coordinates are used, a deformation offset for every epoch is necessary. The deformation offset for every epoch is estimated as follows. First the PSs within 100 meters distance between tracks are selected. The estimated heights are used as extra check. When the height of a PS differs more than 2 meters from the height of the corresponding PS in the different track, the PS will not be taken into account. Note that the difference between the heights of the reference coordinates in both tracks has to be taken into account. To be positive a correct deformation offset is estimated, the PSs need to be distributed over the total crop and not cluttered together, hence the selected PSs are plotted to check the distribution of PSs. With correct distributed PSs the offsets for the epochs can be calculated. The annual velocities are applied to find these offsets. At equal epoch moments between the two datasets the deformation is calculated with the multiplication of the temporal baseline with the annual velocities. This results in deformation estimates of the two tracks at similar epochs. A histogram of the difference between the deformations of the tracks at one epoch is created. Most histograms are normal distributed and hence experience a clear peak. This peak is taken as the offset at similar epochs between the two tracks. When assuming that the deformation of most PSs can be represented by a linear deformation model, usage of the annual velocities will not oppose any problems. When most PSs experience unwrapping errors, usage of the annual velocities will become a problem, since a linear model does not capture the correct deformation pattern. Both in the Veendam and Barradeel crops most PSs are non-deforming or small deforming PSs since more than half of the crop is stable area, hence this method can be applied to these test cases.

Transforming the deformation results into timeseries as presented in figure 5.40. The figures present several graphs. The circled graphs are the original timeseries of PSs situated close together, preferably situated in the subsidence bowl, both observed from the same reference date. The dotted lines are the deformations based on the annual velocities of both tracks at similar epochs. The blue line is the original linear deformation of the master track. The red line is the shifted linear deformation of the slave track for the reference date. And the black line is the reference shifted and reference coordinate shifted linear deformation of the slave track. Addition of the difference between the red and black dotted line to the red circled line, gives approximate the corrected deformation for the difference in reference coordinate. Note that this can not be applied straightforward since the acquisition dates of the black dotted and red circled line are different. Observing the graphs in figure 5.40 taking into account the difference in deformation due to different reference coordinates results into the conclusion that the estimated deformation between tracks 108, 380 and 487 are comparable. But as showed in figure 5.40(c) this does not

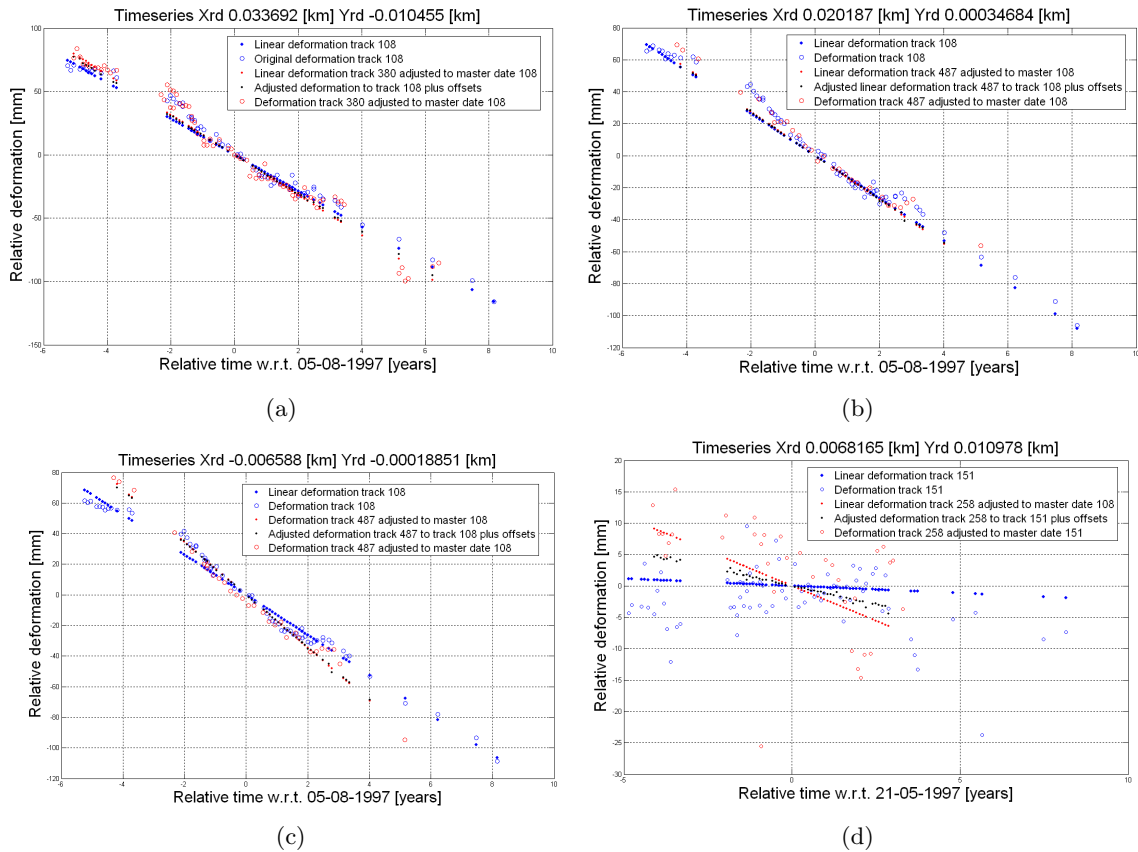


Figure 5.40: Comparing PSs of different tracks. To be able to compare between different tracks a similar reference date and reference coordinate needs to be chosen. A shift of the temporal baseline and relative deformation transforms the reference date and reference coordinate.

necessarily have to be true for all PSs. Compared to track 108, unwrapping errors can easily occur since less images are present in track 487 in the timespan until 1996. This results into a different annual velocity, hence the deformations are not comparable outside the timespan 1996 until 2000.

Comparison of the estimated deformation of track 151 and 258 is less straightforward since in the datasets of track 258 no PSs are present in the subsidence bowl. Deformation is small compared to the accuracy of the technique, hence drawing conclusions on the similarity of deformation is difficult. As can be seen in figure 5.40(d), taking into account the difference in deformation due to difference in the reference coordinates, the deformation patterns approach each other, but still differ about 5 mm per epoch. Since the assumed standard deviation throughout this thesis is 6 mm, track 151 and 258 can be assumed comparable.

The deformation differences due to different reference coordinates are estimated at corresponding epochs. As the actual estimated deformation can differ significant, due to non-linear deformation, from the linear estimated deformation the linear shifted deformation of the slave tracks can not be combined with the master track. Hence the deformation shift at slave epochs should be known or the linear deformation plus residuals at master epochs should be known to be able to combined the tracks. Since this requires another interpolation step, which can easily result into errors, the tracks are not combined.

Correlation leveling measurements and PS estimations The PS deformations transformed to RD-coordinates can be compared to the leveling results, when the reference date and

reference coordinates are similar. The shift in date and deformation is performed in the same manner as discussed during this section. The difference in reference coordinate introduces an offset, which is estimated with the use of a histogram describing the difference between the estimated PS deformation and the measured leveling deformation.

In the Veendam concession the used leveling measurements are obtained at 1995, 1999, 2000 and 2004 [6]. In the Barradeel concession the used leveling measurements are obtained in 1995, 2002 and 2004 [5]. If the distance between a PS and closest leveling measurement point is less than 200 meters, a PS is used to calculate the correlation between the datasets. The PSs and leveling measurement locations of track 380 and 151 are found in figure 5.41 and figure 5.42. In these figures the error between the estimated PS deformation and leveling deformation is also presented. In figure 5.41 the errors approach -10/-15 mm in the subsidence bowl for all three cases. Hence an under-estimation of the deformation is present in the estimated PS results compared to the leveling measurements. The under-estimation can be introduced by unwrapping errors. Note that besides the center of the subsidence bowl the western area of the bowl experiences errors in the same magnitude as the center of the bowl.

In figure 5.42 the PS deformations compared to the leveling measurements are underestimated in the west of the subsidence bowl. The PSs closest to the BAS-1 location approximates the leveling results within the assumed standard deviation. Other PSs are probably underestimated due to unwrapping errors. Most likely this under-estimation appeared in the final epochs of the image stack, introduced by a large time period is present between the images.

Correlation between the datasets is calculated with the correlation coefficient

$$\rho(d_1, d_2) = \frac{C(d_1, d_2)}{\sigma_{d_1} \sigma_{d_2}}, \quad (5.4)$$

where d_1 and d_2 are the PS and leveling deformations, $C(d_1, d_2)$ is the covariance matrix between the datasets, and σ_{d_1} and σ_{d_2} are the standard deviations of the deformation in the datasets. Table 5.14 presents the correlation coefficients of the different tracks. Because no PSs in the deforming area are present in the track 258 results, the correlation coefficients of that track are not presented in the table. The correlation between the PS results and leveling results is high when taking into account the correlation coefficients.

Timespan	$\rho_{1995-1999}$	$\rho_{1995-2000}$	$\rho_{1995-2004}$	$\rho_{1999-2004}$
Track				
108	0.942	0.918	0.950	0.931
380	0.901	0.907	0.923	0.887
Timespan	$\rho_{1995-2000}$	$\rho_{1995-1999}$	$\rho_{1999-2000}$	
487	0.881	0.891	0.827	
Timespan	$\rho_{1995-2002}$	$\rho_{1995-2004}$	$\rho_{2002-2004}$	
151	0.939	0.948	0.915	

Table 5.14: Correlation coefficients between datasets containing leveling measurements and datasets containing estimated PS deformations.

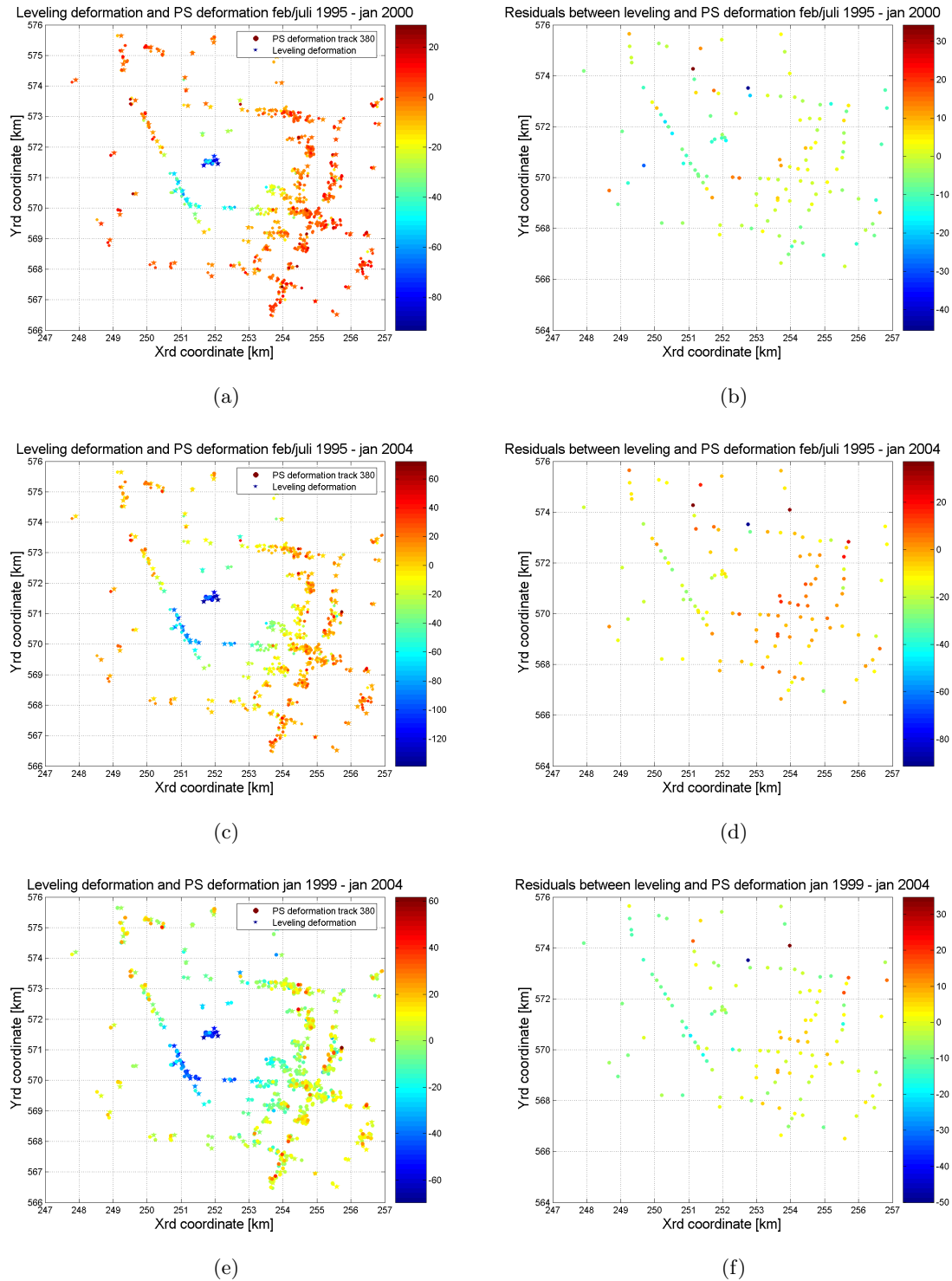


Figure 5.41: The figures on the left present measured leveling deformation and estimated PS deformation in the Veendam concession in mm. The figures on the right present the difference between measured leveling deformation and estimated PS deformation in mm.

5.9 Conclusions

This chapter presented the results of different PS optimization methods performed on the SAR images covering the Veendam or Barradeel concession. In section 5.2 the relevance of the initial

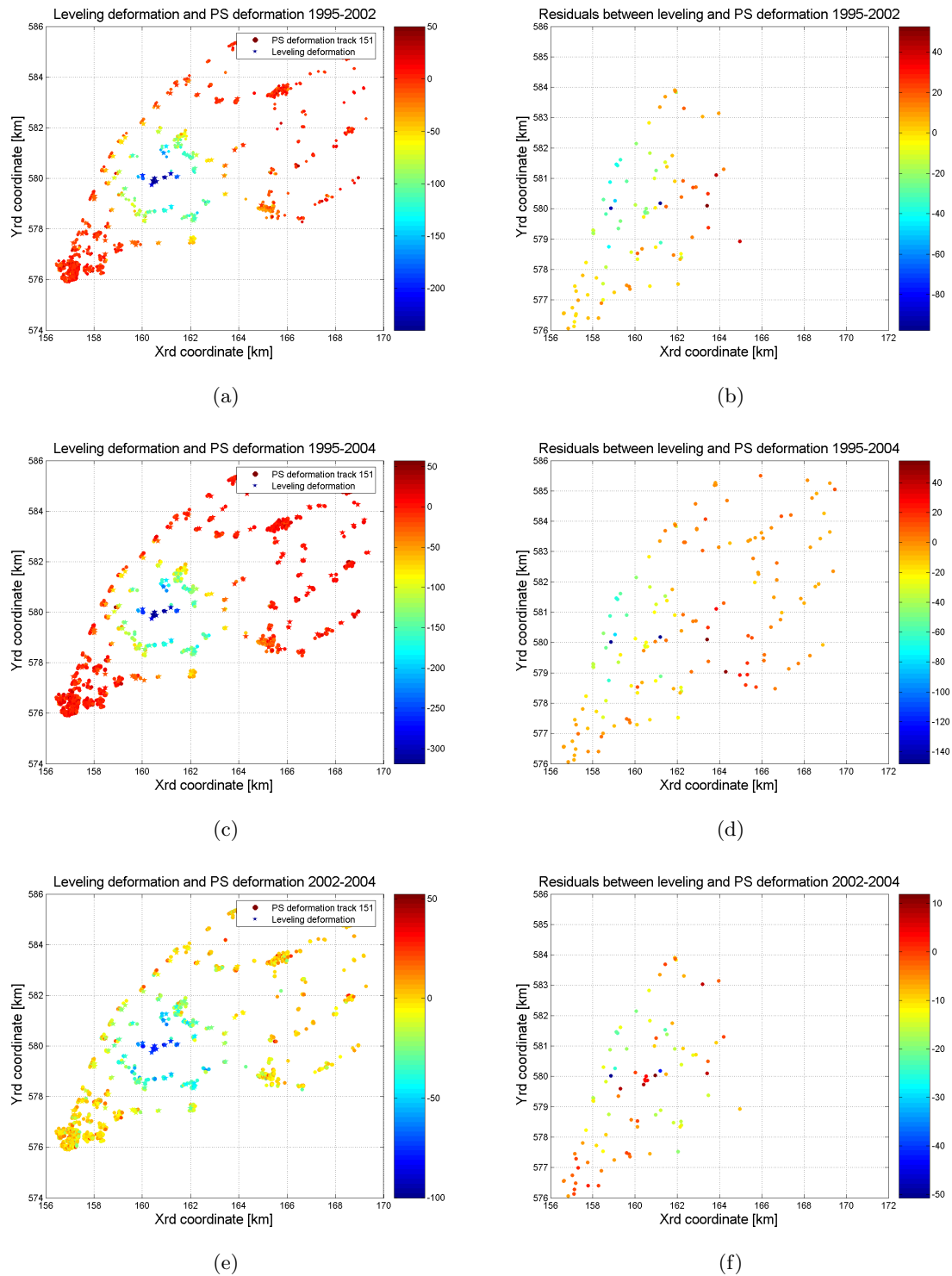


Figure 5.42: The figures on the left present measured leveling deformation and estimated PS deformation in the Barradeel concession in mm. The figures on the right present the difference between measured leveling deformation and estimated PS deformation in mm.

network and PSP threshold are discussed. It can be concluded that the initial network influences the final identified PS, hence investigation of the initial network before proceeding with the densification of PSs is required. The presence of PSs in the main subsiding area are of importance

for this research. A low PSP threshold increases the computation time, but also the number of identified PSs. The threshold of 0.45 resulted throughout the research in more dense PS distributions.

Investigation of the optimization methods results showed an increase in density and an increase in the quality of the estimated deformation for the manual PS identification method, bilinear interpolation method and bowl method. This increase holds for the bowl and bilinear interpolation method only when the deformation, on which the deformation surface estimation is based, captures the deformation of interest. Subtraction of an incorrect deformation pattern can increase the variability of the deformation pattern, hence resulting in less identified PSs. Examples indicating this relevance are the cases in which the initial network did not describe the subsidence in the center of the bowl, since the PSs at the cavern locations was not identified. The deformation signal was not correctly estimated, hence the identified PSs approached the number of identified PSs in the conventional case.

Usage of the break-point model avoids unwrapping errors, provided that the break-point is chosen at the epoch of interest. Nevertheless the increase of PS density is not noteworthy. The reason for the lack of increase of PS density is not identified.

The other optimization methods experience unwrapping errors. In the Veendam concession these errors are less present than in the Barradeel concession. The unwrapping errors are removed by an algorithm which estimates the unwrapping error making use of linear graphs matched to the timeseries. A correction is based on the estimated graphs.

The estimated deformation between the datasets based on the different tracks is comparable. Correlation coefficients of the estimated deformation and compared to leveling measurements resulted in large values ranging from 0.827 to 0.950 for the Veendam concession. Track 108 experienced the largest correlation coefficients (0.918 to 0.950) and track 487 the smallest (0.827 to 0.891). Between PS results of track 108 and leveling measurements in the Veendam concession a difference of -10 to -15 mm is present for all three time periods, where the PS results are underestimated compared to the leveling results. This can have been introduced by unwrapping errors at the cavern locations. In the Barradeel concession the correlation coefficients between the leveling measurements and PS results range from 0.915 to 0.939. The leveling datasets correspond to the PS closest to BAS-1. The west of the subsidence bowl is underestimated. Investigation of the timeseries indicates a break-point around 1997 in this area. Hence this likely has introduced an underestimation of the deformation after 1997.

The subsidence in the Veendam concession is estimated to be -13 mm/year in slant range and -14 mm/year in vertical direction within a timespan starting from July 1992 until December 2003. The total estimated vertical deformation is -155 mm over the mentioned timespan. In the Barradeel concession the maximum vertical deformation estimated in the subsidence bowl is -334 mm over a timespan of 12 years starting in May 1992. Note that mining activities in the Barradeel concession started in 1996. Therefore the deformation estimated over the timespan approaches the deformation from 1996 until 2005. Franeker is tilting due to gas extraction near Franeker and the salt extraction in the Barradeel concession. In 2005 Franeker experienced a tilt of -15.8 mm/km, May 1992 taken as reference date. Maximum subsidence of Franeker is -90 mm measured over the same timespan.

Chapter 6

Physical subsidence modeling

Deformation of the Earth's surface due to mining activities is caused by physical process taking place in the subsurface. Hence measured surface deformation holds information on the physical process introducing this land subsidence. This chapter deals with inverse modeling subsurface processes. The Mogi model [38] is used as inverse model throughout this chapter. This model describes volume changes of a point source derived by the measured deformation. Understanding of the physical process can be used to predict subsidence introduced by arbitrary volume change.

In the Barradeel concession area two subsidence bowls interfere. The subsidence caused by the sources separately is unknown. With addition of n Mogi models (point sources) the unknown parameters for n sources can be estimated, resulting into a separation of introduced deformation due to different subsurface activities.

In the first section of this chapter the Mogi model and acquisition of unknown parameter estimates is treated. The second section present the results of the parameter estimation for the Veendam and Barradeel concession area. Conclusions are given in the third section.

6.1 Mogi model

The Mogi model describes deformation of the land surface height due to volume changes of a point source located in the subsurface. Originally it has been developed to relate changes in magma chambers with measured surface displacements of the volcano. Currently this model still is used on volcano deformation [10]. Expected is a comparable relationship between surface deformation and volume changes of mining caverns, only in this case a volume decrease is present instead of volume increase introduced by expansion of a magma chamber. A salt cavern can be considered having a start volume which decreases due to extraction of the salt, causing the volume to shrink. The development of the cavern causes the overburden to sink into the cavern, resulting into bowl-shaped deformation on the surface. This deformation is related to the amount of salt subtracted from the subsurface.

Throughout this research the Mogi model and one alternative to this model are used. The conventional Mogi model is used to estimate the unknown parameters at the Veendam concession area. It is not expected that the gas subtraction in the northeast of the Netherlands influences the estimated deformation of the PS datasets in Veendam, since the reference coordinate of the PS data is located in the surroundings of the subsidence bowl. The alternative model is used for the Barradeel concession area where two subsidence bowls interfere. Both salt mining and gas subtraction near Franeker cause subsidence in this area. The bowls are described by the addition of two Mogi sources with different depths, locations and volume changes.

Land subsidence z in millimeters on a given location (x, y) is described by the Mogi model

$$z = \frac{(1 - \nu)\Delta V}{\pi d^2} \frac{1}{(1 + (R/d)^2)^{3/2}}, \quad (6.1)$$

with ν Poisson's ration, ΔV the volume change of the source, d the depth of the source and (x_s, y_s) the location of the source. R is the horizontal distance between the observation location and point source $R = \sqrt{(x - x_s)^2 + (y - y_s)^2}$. Poisson's ratio is taken to be 0.25 [13].

The Least Squares Method is used to estimate the unknown parameters p [45]. This method is restricted to linear equation systems. Neglecting the second order remainder results into the equation

$$A(p) \approx A(p_0) + \partial_{p^T} A(p_0)(p - p_0), \quad (6.2)$$

describing a linearization of non-linear systems $A(p)$, with p_0 an approximation of p . The gradient vector of the Mogi model is given as

$$\partial_{p^T} A(p_0) = \begin{bmatrix} \frac{\partial}{\partial p_1} z^1(p_0) & \cdots & \frac{\partial}{\partial p_n} z^1(p_0) \\ \vdots & & \vdots \\ \frac{\partial}{\partial p_1} z^m(p_0) & \cdots & \frac{\partial}{\partial p_n} z^m(p_0) \end{bmatrix}, \quad (6.3)$$

where the partial derivatives in the matrix are

$$\begin{aligned} \frac{\partial}{\partial x_s} z &= 3 \frac{(1 - \nu)\Delta V}{\pi d^4} \frac{x_s - x}{(1 + (R/d)^2)^{5/2}}, \\ \frac{\partial}{\partial y_s} z &= 3 \frac{(1 - \nu)\Delta V}{\pi d^4} \frac{y_s - y}{(1 + (R/d)^2)^{5/2}}, \\ \frac{\partial}{\partial x_s} z &= -2 \frac{(1 - \nu)\Delta V}{\pi d^3} \frac{1}{(1 + (R/d)^2)^{3/2}} + \\ &\quad 3 \frac{(1 - \nu)\Delta V}{\pi d^5} \frac{R^2}{(1 + (R/d)^2)^{5/2}}, \\ \frac{\partial}{\partial \Delta V} z &= \frac{(1 - \nu)\Delta V}{\pi d^2} \frac{x_s - x}{(1 + (R/d)^2)^{3/2}}. \end{aligned} \quad (6.4)$$

The gradient vector is composed out of the number of deformation measurements per epoch m times the number of parameters n . Because the linearized system is an approximation of reality, iteration is used to approach the actual parameter values. To initialize the iteration p_0 is needed. The iteration stop criterium for the different models is chosen to be 0.1 meter difference between consecutive estimated source locations

$$\sqrt{(x_{i+1} - x_i)^2 + (y_{i+1} - y_i)^2 + (d_{i+1} - d_i)^2} \leq 0.1[\text{m}],$$

a difference of 1% is the volume change

$$\frac{\|\Delta V_{i+1} - \Delta V_i\|}{\Delta V_i} \leq 0.01.$$

If for an epoch after 100 iterations the stop criterium is not met, the epoch is not taken into account.

Making use of two Mogi sources the physical situation in the Barradeel concession area can be described. This results into the model

$$z = \frac{(1-\nu)\Delta V_1}{\pi d_1^2} \frac{1}{(1+(R_1/d_1)^2)^{3/2}} + \frac{(1-\nu)\Delta V_2}{\pi d_2^2} \frac{1}{(1+(R_2/d_2)^2)^{3/2}}, \quad (6.5)$$

where the subsidence at an observed location (x, y) is the addition of the subsidence caused by the two point sources. Partial differentiation results in a linearized matrix consisting out of eight columns composed by twice matrix 6.1 with parameters ΔV_k , d_k and (x_{sk}, y_{sk}) where k represents the k^{th} source.

The Overall Model Test (OMT) is used to describe the reliability of the estimated parameters [45]. Correlation between estimated PS deformations are neglected resulting into a diagonal covariance matrix containing identical entries on the diagonal. The test statistic T is $T = \hat{\underline{e}}^T \hat{\underline{e}}$ with $\hat{\underline{e}} = z - \hat{z}$.

Parameters per epoch are estimated with the least-squares method. To be able to compare estimated source position with the actual cavern position the temporal behavior of the estimated parameters is analyzed. It is assumed that the mining location and depth of the cavern does not change with time and therefore the temporal behavior of the estimated position parameters is taken constant. After elimination of outliers indicated with the w-test and confidence area of 95%, the mean of the estimates is assumed to be the temporal behaviour of the estimated parameters.

The volume change and uniform deformation depend on the retrieved volumes by gas or salt extraction and therefore are not necessary constant or linear over time. When assuming a linear relation between time and the volume change, the temporal behavior, ΔV^{tb} , is described as

$$\Delta V^{tb} = \Delta V_c + \Delta V_t, \quad (6.6)$$

where ΔV_c is a constant volume change and ΔV_t is the volume change per year. The temporal behavior of the volume change is estimated with [45]

$$\begin{bmatrix} \Delta V_c \\ \Delta V_t \end{bmatrix} = (A^T A)^{-1} A^T \Delta V_e,$$

where ΔV_e is the estimated volume change by the Mogi model and the A matrix is composed as

$$A = \begin{bmatrix} 1 & t_1 \\ 1 & t_2 \\ \vdots & \vdots \\ 1 & t_m \end{bmatrix}.$$

Interpolation is necessary to be able to compare the provided production volumes and the estimated volume changes. The production volumes are linear interpolated to acquire volumes at corresponding acquisition dates of the used SAR data. A factor between the production volumes, P , and estimated volume changes, ΔV_e , is calculated to give a relationship between the different datasets. This factor, f , is calculated with

$$f = (P^T P)^{-1} P^T \Delta V_e. \quad (6.7)$$

Making use of this factor enables the calculation of a correlation coefficient between the production volumes and the volume change estimated by the Mogi model. The correlation coefficient is calculated as described in section 5.8.

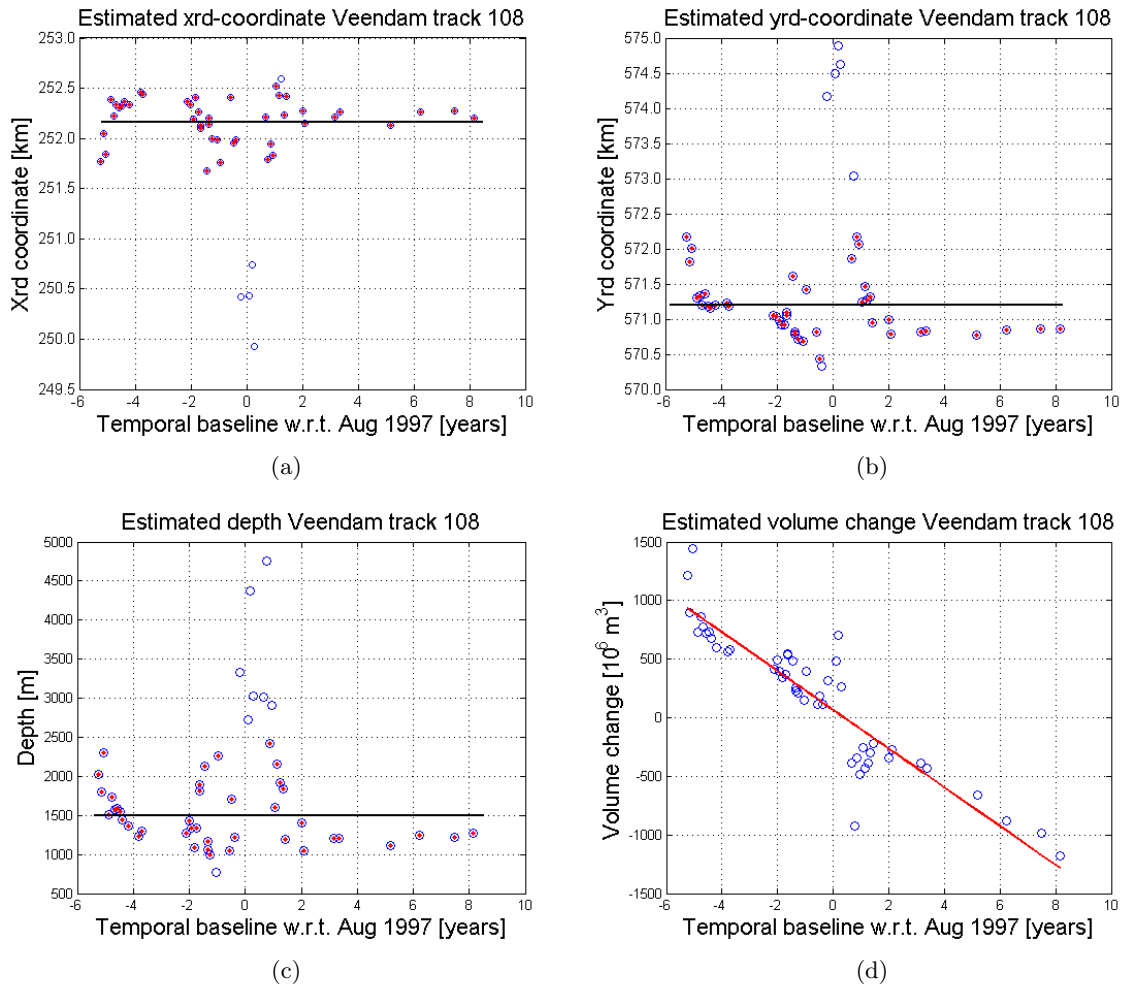


Figure 6.1: Estimated source parameters for the Veendam concession. The blue lines represent the estimated parameters. In subfigures (a), (b) and (c) the red points display the epochs accepted by the w-test. In subfigure (d) the red line displays the linear temporal behavior.

6.2 Results Mogi model

The densified Persistent Scatterer (PS) deformations of different tracks, found in chapter 5, are used as observed values for the Mogi model. Characteristics on these sets can be found in table 5.1 and table 5.2. Clear outliers are removed from these datasets, see section 4.2.1, and track 151 containing the Barradeel concession area is corrected for unwrapping errors. A deformation pattern on macro scale is used for the Mogi estimation and therefore micro scaled deformation not behaving according to the macro scaled deformation are removed.

6.2.1 Results Mogi Model Veendam concession area

One Mogi source is used for estimation of the unknown parameters (x_s, y_s) , ΔV and d in the Veendam concession area. The initial values of the Least Squares Model can be found in table 6.2.1. Figure 6.1 presents the plotted estimates for the unknown parameters (x_s, y_s) , ΔV and d of dataset track 108. The temporal behavior of the estimated position parameters and the estimates on which this behavior is based are also displayed in these plots and are shown in table 6.2.1. As can be seen in figure 6.2 the estimated (x_s, y_s) is comparable to the location of

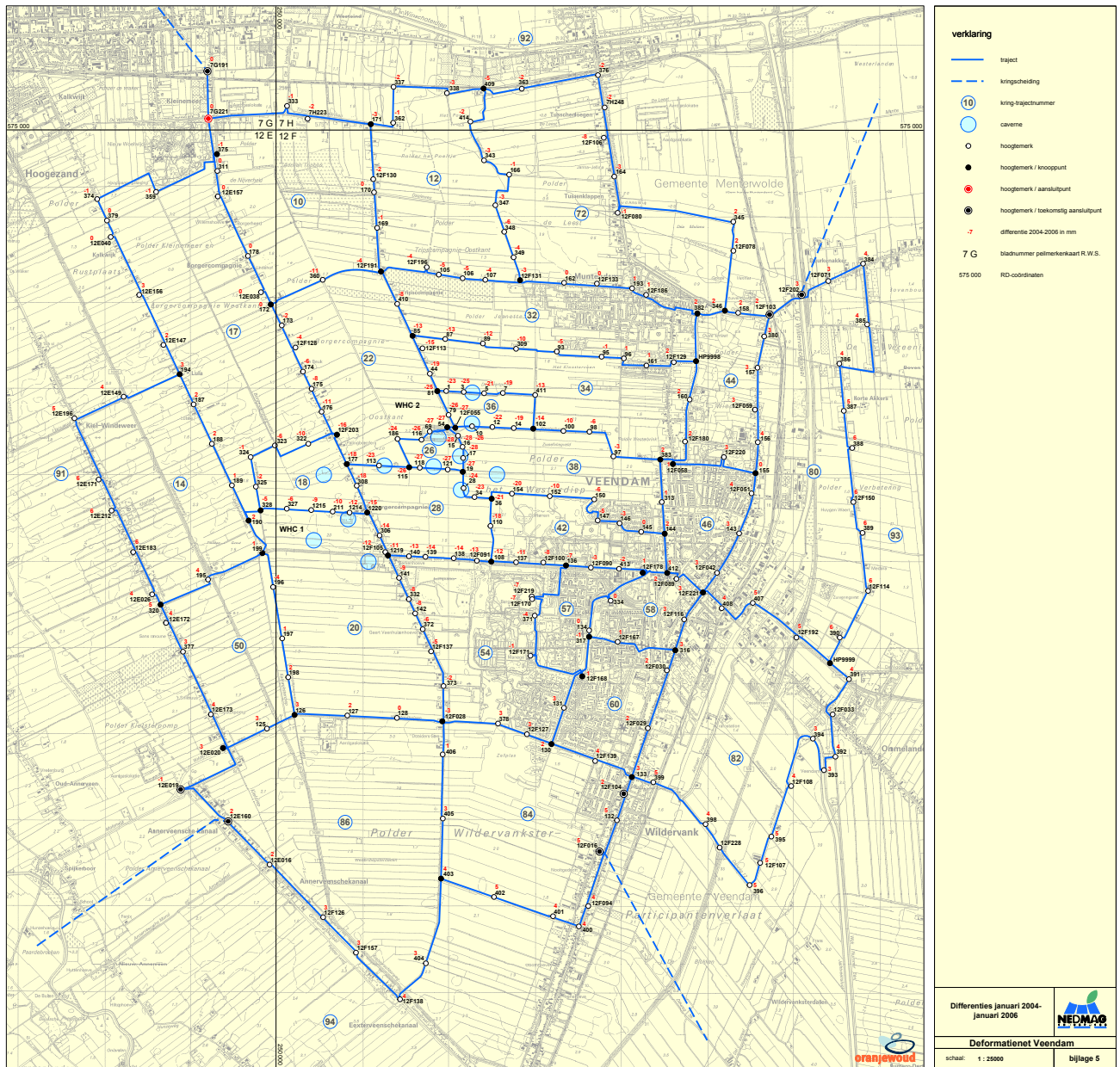


Figure 6.2: Leveling network Veendam concession [6]. The filled blue circles encapsulate the cavern locations.

the major part of caverns in the Veendam concession. According to [36] Nedmag extracts salt from depths over 1500 m, hence the estimated depth approximates the gaining depth mentioned by Nedmag. Appendix D contains the plots of estimated parameters for all datasets.

The estimated parameters of the different tracks results into similar values. The difference between the source coordinates is 248 meters for the xrd coordinate and 35 meters for the yrd coordinate when observing track 108 and 380, see table D.3. For the tracks 108 and 487 the difference in the xrd coordinate is 799 meters and the yrd coordinate is 105 meters, see table D.1. The difference in depth is 210 meters between 108 and 487 and 261 meters for tracks 108 and 380. Despite the relatively large differences between the estimated depths of the tracks,

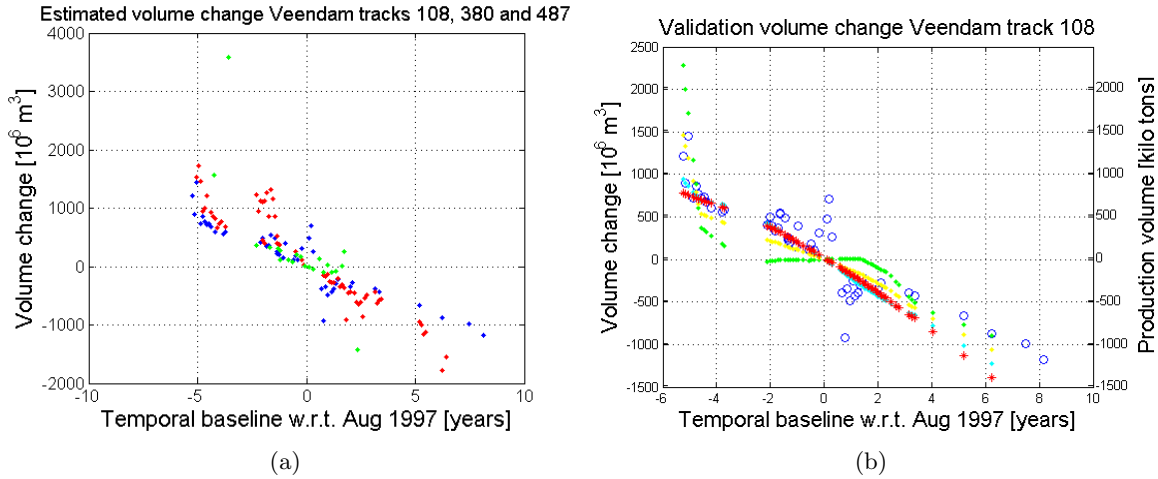


Figure 6.3: (a) Estimated volume change Veendam. The blue dots represent track 108, the red dots track 380 and the green dots tracks 487. (b) The blue line shows the interpolated estimated volume change for track 108. The red line shows the Veendam production data. Underground volumes, squeeze volumes and the summed underground and squeeze volumes are represented by the green, cyan and yellow line respectively. The squeeze volumes, summed volumes and production volumes experience approximately the same behavior. Except for the final 4 epochs the volumes approach the estimated volume change.

Parameter	Initial value	Estimated values
x_s	252000 m	252178 m
y_s	571500 m	571175 m
d	1500 [m]	1512 m
ΔV	-300 m^3	-
ΔV_c	-	$63.23 \cdot 10^3 m^3$
ΔV_t	-	$-165.50 \cdot 10^3 m^3/year$

Table 6.1: Initial values for LSQ estimation and estimated values making use of the Mogi model for the Veendam concession covered by track 108.

the volume changes are comparable, see figure 6.3. The correlation coefficient between tracks 108 and 380 is 0.9. The coefficient between tracks 108 and 487 is 0.68, but considering the line of the volume changes, the estimates of track 487 fit in the linear line the data of track 108 follows.

The estimated volume changes are validated with annual production volumes, underground volumes and squeeze volumes provided by Nedmag Industries. Underground volume is the total volume of salt-water mixture in the subsurface and squeeze volume is the volume of salt crept into the cavern. Creep is introduced due to the low pressure in the cavern, resulting into a pressure difference making the salt flow to the cavern. The volumes are annually available over an time period starting in 1991 until 2005.

To be able to calculate the correlation coefficient between the provided volumes and the estimated volume changes by Mogi, the provided volumes need to be interpolated to equal epochs as the volume changes. The interpolated volumes and the estimated volume change by Mogi are presented in figure 6.3(b). A factor, describing the relation between provided and estimated volumes, is calculated for the different provided volumes. The factor is obtained according to eq. (6.7). The underground and squeeze volumes are plotted taking into account the

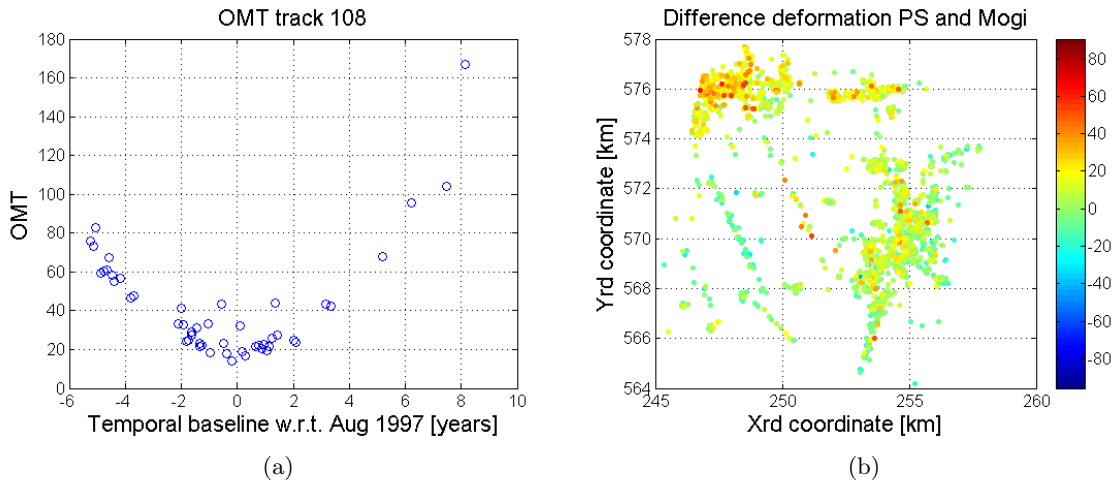


Figure 6.4:

Dataset	Correlation coefficient1	Correlation coefficient2
Production volumes	0.876	0.931
Underground volumes	0.715	0.771
Squeeze volumes	0.898	0.955
Summed underground & squeeze volumes	0.871	0.930

Table 6.2: Correlation coefficients between the estimated volume changes with Mogi and the provided underground, squeeze and production volumes. Correlation coefficient1 is based on all epochs. Correlation coefficient2 is based on the epochs selected by the w-test performed on the estimated xrd, yrd coordinates and depth.

factor. Subsequently the correlation coefficients are calculated, see table 6.2.1. The correlation coefficients are not particularly high, this due to the estimations of volume changes approaching the reference epoch. After the w-test on estimated xrd and yrd coordinates several epochs near the reference epoch are eliminated, see figure 6.1. Not taking into account these epochs results into higher coefficients as presented by correlation coefficient 2 in table 6.2.1. The correlation factor is lowest for the underground volume, as expected since the behavior differs from the estimated volume changes. The largest coefficient is achieved with the summation of the underground and squeeze volumes.

Appendix D presents the results of the tracks 380 and 487. The correlation coefficients between estimated volume changes in track 380 and provided volumes, resulted into comparable values to track 108 as shown in table D.4. Track 487 estimated volume changes experiences significant smaller coefficients around 0.65, see table D.2. This is introduced by uncorrect estimated epochs. Close to the reference epoch, small deformation is present. When the deformation approaches the variance of the dataset, it is impossible to estimate a subsidence bowl. Elimination of the epochs resulted in much higher correlation factors.

To investigate the reliability the OMT is calculated between the PS deformation and the Mogi deformation obtained with the estimated parameters. Figure 6.4 displays the OMT and the errors in millimeters between the two datasets at the final epoch. The OMT increases when the time difference from the reference epoch increases. This is introduced by an increase or decrease of the relative deformation compared to the reference epoch. The residuals between the models presented in subfigure 6.4(b) approach 0 *mm* in the city Veendam and the center of

the subsidence bowl. The west of the crop experiences larger errors, between -20 and 20 mm difference.

The provided volumes are comparable to the estimated volume changes by Mogi. The summation of underground volumes and the squeeze volumes approach the estimated volume changes best. Correlation coefficients around 0.96 are reached for the summed dataset and the estimated dataset. Despite the high correlation, the final epochs differ from the provided volumes. This can be introduced by increasing deformations compared to the reference epoch, and therefore also increasing errors between the estimated Mogi deformation and the deformation obtained by the PS analysis. Based on previous discussed results it can be concluded that for this case Mogi shows to be suitable to estimate the deformation parameters based on PS deformation.

6.2.2 Results Mogi model Barradeel concession area

Two subsidence bowls interfere in the Barradeel concession area. These bowls are introduced by salt mining by Frisia Salt and gas subtraction by Vermilion Energy. One point source does not represent the actual physical situation and, as expected, results into estimated parameters reaching infinity, hence the parameters do not want to be estimated within specified bounds. The use of two point sources approaches reality and therefore is modeled as described in eq. (6.5).

The eight unknown parameters iterate to infinity when the parameters are estimated based on PS deformation obtained from track 151 or track 258. Division of the datasets into sets containing only the subsidence bowl of the Barradeel concession area or the Franeker concession, where Vermilion extracts gas, does not result into proper estimates. To be able to solve this iteration problem, certain variables are taken fixed. The position of the center of the subsidence bowl is deduced from the locations of BAS-1 and BAS-2 operating in the period of interest. The depth of the cavern is approximately know. These three parameters are fixed throughout the least squares estimation. Table 6.2.2 shows the known parameters (x_{s1}, y_{s1}) and d_1 .

Fixed parameter	Fixed value	Estimated parameter	Initial value
x_{s1}	160500 <i>m</i>	ΔV_1	$-300 \cdot 10^3 \text{ m}^3$
y_{s1}	580000 <i>m</i>	x_{s2}	163500 <i>m</i>
d_1	2800 <i>m</i>	y_{s2}	578600 <i>m</i>
		d_2	1500 <i>m</i>
		ΔV_2	$-300 \cdot 10^3 \text{ m}^3$

Table 6.3: Initial values for the LSQ estimation Barradeel concession.

Making use of these fixed parameters and initial values as presented in table 6.2.2, results into estimated parameters as found in table 6.7 and figure 6.5. In the table $\Delta V_{c1,t1}$ is the volume change of the combination BAS-1 and BAS-2, (x_{s2}, y_{s2}) and d_2 is the position of the points source representing the gas reservoir of Vermilion energy and $\Delta V_{c2,t2}$ the volume change of the Vermilion point source. The exact location of the Vermilion bore holes is unknown. Comparing the estimated xrd and yrd coordinates to the estimated deformation in the PS dataset and a rough estimation based on the topographic map as displayed in figure 2.5(a), results into approximately similar coordinates. Hence it is assumed that the estimated xrd and yrd coordinates with the use of Mogi are comparable with reality. Unlike for the Barradeel parameters, information on the depth and the volume change of the gas reservoir is unknown and thus can not be validated.

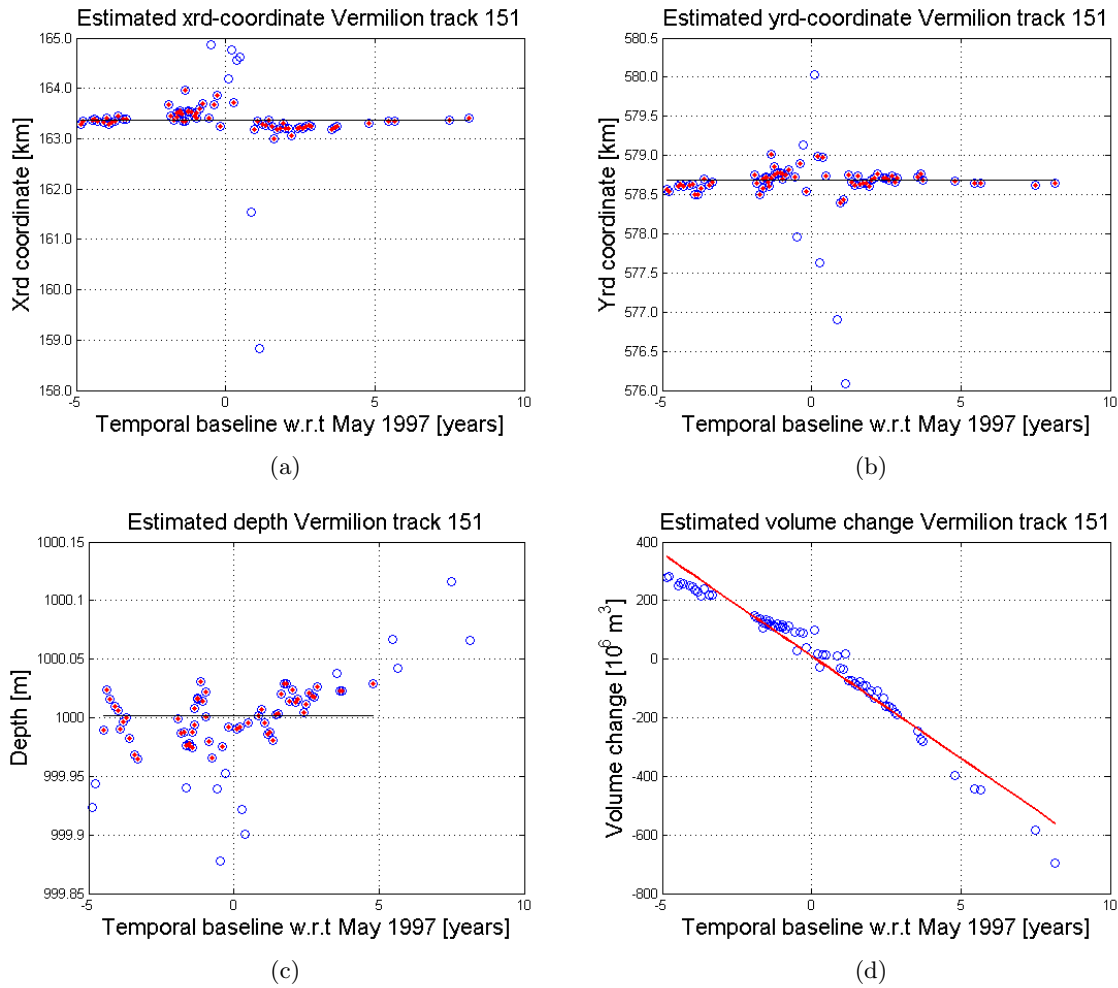


Figure 6.5: Estimated source parameters of the gas subtraction near Franeker. The blue lines represent the estimated parameters. In subfigures (a), (b) and (c) the red points display the epochs accepted by the w-test. In subfigure (d) the red line displays the linear temporal behavior.

A correlation factor can be estimated between the estimated volume changes for salt subtraction and the provided production volumes by Frisia Salt. The provided production data spans a time period starting from 1995 until 2006. Since the last epoch of the SAR data is acquired in May 2005, production data past this date is not taken into account.

To be able to calculate the correlation coefficient, the production volumes are shifted to the reference date of track 151. This shift is performed by the subtraction of the production volume obtained at the reference date from all the production volumes, hence resulting into a volume of 0 at the reference date. Subsequently the production volumes are linearly interpolated to the epochs of the SAR data, and the factor describing the relationship between the two datasets is calculated. This factor resulted into 0.68358. Shifting the production volumes to the reference date of the PS dataset and multiplying the volumes with the calculated factor, results into figure 6.2.2. The correlation coefficient between the datasets is 0.989.

Figure 6.2.2 shows a minor difference between the production volumes and the estimated volume changes. The red line presents the production volumes and the blue line presents the estimated volume change. Note that the production volumes are set negative since the production of the magnesium required salt extracted from the salt layers, increasing the cavern present in the salt layers. According to the production volume an underestimation of volume change

Parameter	Estimated values	Parameter	Estimated values
$\Delta V_{c1(\text{part } 1)}$	$227.56 \cdot 10^3 \text{ m}^3$	x_{s2}	163380 m
$\Delta V_{t1(\text{part } 1)}$	$-26.79 \cdot 10^3 \text{ m}^3/\text{year}$	y_{s2}	578680 m
$\Delta V_{c1(\text{part } 2)}$	$328.80 \cdot 10^3 \text{ m}^3$	d_2	1000 m
$\Delta V_{t1(\text{part } 2)}$	$-774.51 \cdot 10^3 \text{ m}^3/\text{year}$	ΔV_{c2}	$9.42 \cdot 10^3 \text{ m}^3$
		ΔV_{t2}	$-69.91 \cdot 10^3 \text{ m}^3/\text{year}$

Table 6.4: Parameter estimates for the Barradeel concession obtained with 2 modeled sources.

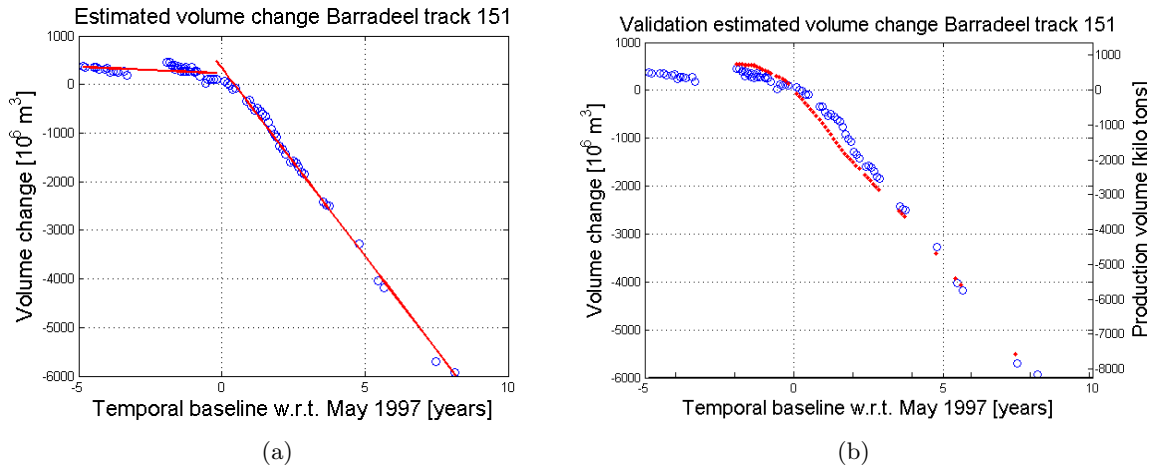


Figure 6.6: Estimated volume change of the cavern in the Barradeel concession. The blue lines represent the estimated volume changes. In subfigure (a) the red line displays the linear temporal behavior. Since two obvious linear graphs are present, the temporal behavior is calculated for the two periods. The red line in subfigure (b) represents the production volume of Frisia Salt.

is present. Considering the last five epochs, a difference in the slope of the volume change and production data is present. Interesting to see is a difference in the breakpoint (see section 4.2.2). This difference seems to approach one or two months, but the production data from 1995 until May 2001 is given on annual base. Production volumes in between are results from a linear estimation, hence this data is less reliable compared to epochs from May 2001.

To be able to investigate the reliability of the Mogi parameter estimation, the OMT between the PS dataset and the deformation calculated with the estimated Mogi parameters is plotted in figure 6.7(a). The deformation at the final epoch (May 2005) is plotted as additive visualization. The deformation is based on the estimated parameters as given in table 6.7 and is displayed in millimeters. Figure 6.7 shows the estimated deformation for both sources and for the separate sources. The difference between the PS dataset and the Mogi deformation is displayed in the same figure. The Overall Model Test shows a large error in the last five epochs. The residuals in previous epochs resulted are smaller. This is displayed in figure 6.7(f). The main area introducing this increase in OMT is the dike area as can be seen in figure 6.7(e). This was also the case in the comparison of PS deformation and leveling measurements. When assuming correct leveling measurements, the error in the measured PS deformation introduces the increasing OMT.

When the PS deformation represents reality, the errors between PS deformation and Mogi deformation can also be introduced by the assumption of a point source. The Mogi model assumes a point source increasing in size. But the salt extraction in Barradeel depends on solution of salt surrounding the cavern taking advantage of creep, which introduces a difference in the deformation pattern compared with a point source. The deformation in the creep case is

smaller than in the case with a cavern experiencing equal extracted salt volumes and a larger area experiences subsidence. This can have introduced the large difference in deformation between in the datasets in the center of the subsidence bowl and the difference in the estimated radius of the bowl. In the PS dataset the radius is smaller (with equal deformation) and the deformation in the center of the bowl is larger than in the Mogi dataset. Since the exact volume changes in the cavern and squeeze volumes are not known it is not possible to accept or reject this hypothesis.

An extra possibility for the errors between PS and Mogi estimated deformation, is the direction of the track. Comparing the PS estimated of track 151 and track 258 (see appendix C), shows an difference in the deformation in the dike area. PS in track 258 at the dike experiencing deformation according to leveling measurements are rejected. Several PS adjacent to the area are estimated and show deformation. Hence the angle of monitoring the area can be the cause of a difference in the measured deformation. An example to visualize this. Dikes in the north of the Netherlands are covered with stones on the sea side and meadow on the land side. Track 151 is descending and therefore most likely monitors the sea side of the dike. When the stability of the dike on the sea side is larger than on the land side it can be possible that less deformation is monitored.

The contribution of subsidence in Franeker introduced by the mining activities of Frisia based on the Mogi model are presented in figure 6.8. Subfigure 6.8(a) presents the total deformation at the final epoch (May 2005) in millimeters measured from May 1997. The percentage of subsidence introduced by salt mining is presented in in subfigure 6.8(b). Note that this contribution is based on the Mogi model, which experiences large residues with the estimated PS deformation. According to the estimated Mogi deformation, the contribution of salt mining to the subsidence in Franeker is noteworthy.

The estimated Mogi parameters for track 258 approach the parameters for track 151. Similar to track 151, the parameters for two bowls, salt and gas subtraction, are estimated. Results of the estimation is presented in appendix D. The difference in the mean of the estimated xrd coordinate of the Vermilion source is 610 meters and in the yrd coordinate 190 meters. The estimated depths of the Vermilion source are in both tracks equal to 1000 meter. The volume changes are approximate similar. In the Barradeel volume change uncorrected unwrapping errors present in the first epochs introduce a difference. The OMT in track 258 is smaller compared to the OMT of track 151, but note that the relative deformation is smaller in the epochs since images over a smaller time period are available. As can be seen in figure D.6, the deformation modeled by the Mogi source at the salt extraction location is smaller than the deformation in the PS dataset. Subsidence at the dike is is larger than in track 151. The results of track 258 correspond to the track 151 result, and do not clarify whether the estimated PS deformation is not correct, or whether the deformation can not exactly be modeled by the Mogi source possibly due to the creep phenomenon. But despite the fact that the last epochs experience larger differences with the modeled Mogi deformation, the production data has a high correlation factor with the estimated volume changes. Hence in this case it is possible to relate estimated volume changes based on deformation to production data.

6.3 Conclusions

Comparison of the estimated parameters based on the PS deformation in the Veendam case with the provided production volumes and cavern locations resulted into comparable values. The largest correlation coefficient between the estimated volume changes and the provided volumes is 0.955 for track 108, 0.843 for track 487 and 0.950 for track 380. Best fitting volumes

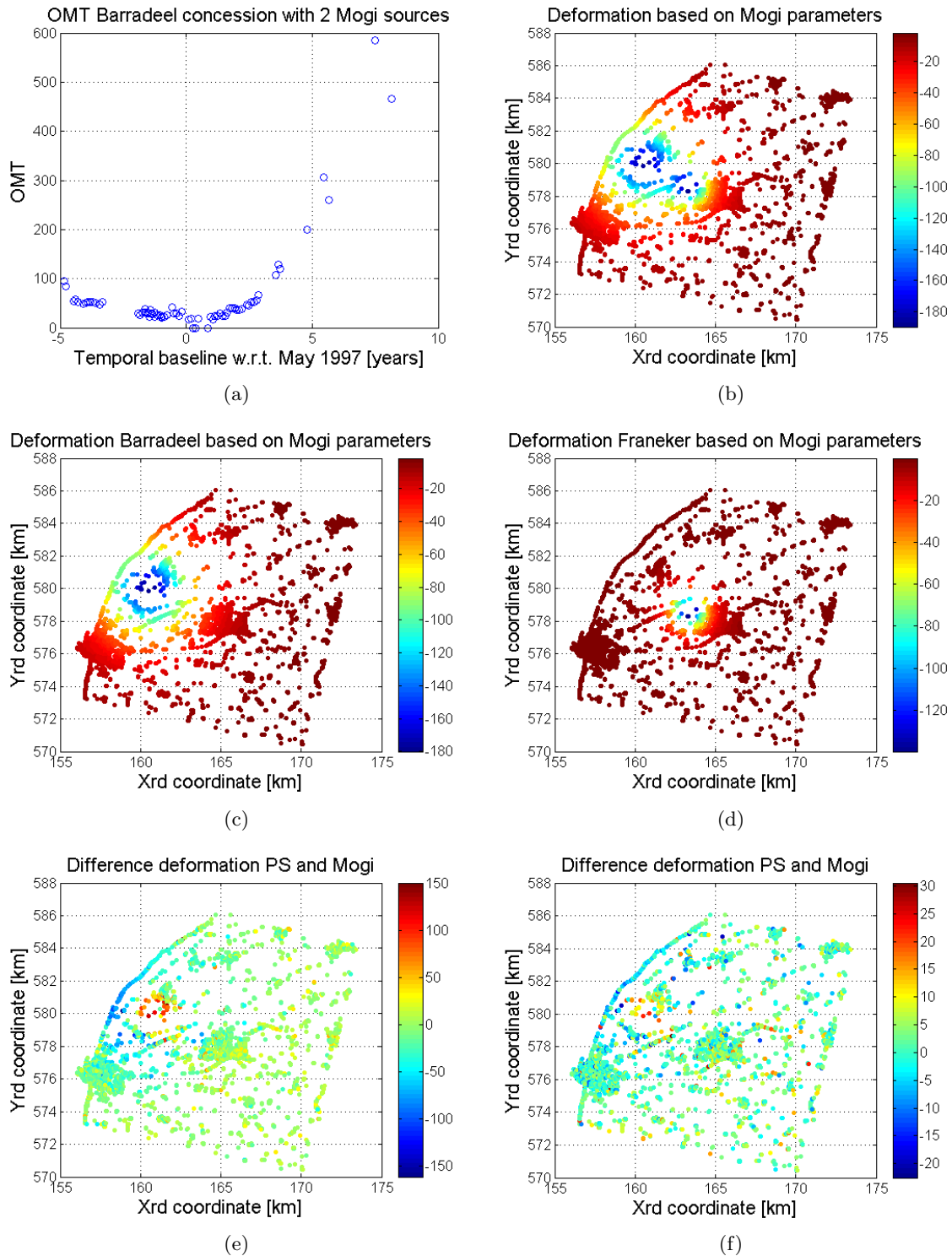


Figure 6.7: The reliability of the Mogi parameter estimation. Subfigure (a) displays the OMT between the PS data and the estimated data with Mogi. The figures (b), (c) and (d) represent the deformation in mm estimated by the Mogi parameters. The difference between the estimated deformation with Mogi and the estimated deformation by the PS analysis is displayed in subfigure (e). The deformation plots visualize the deformation at May 2005 respectively to May 1997. Subfigure (f) shows a plot of the error between Mogi and PS at August 1998.

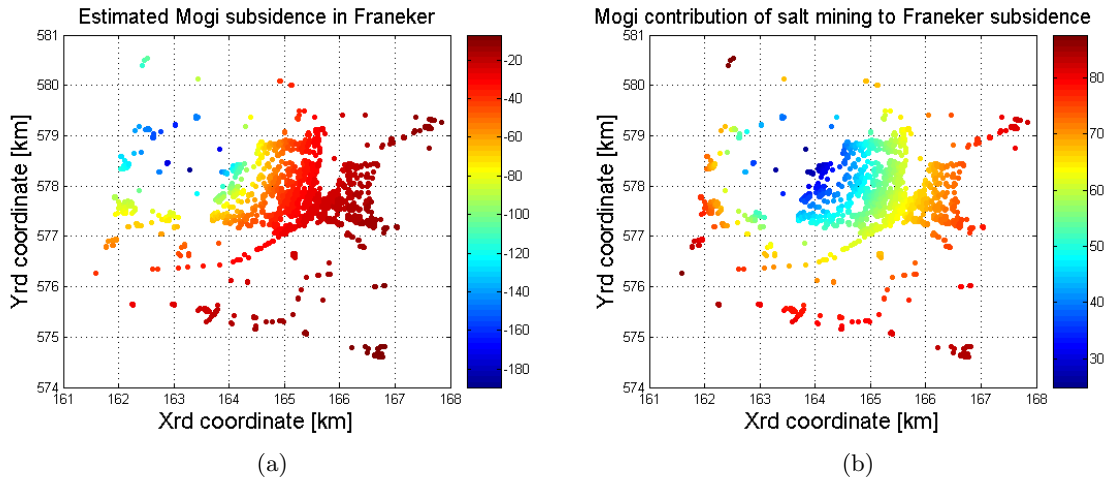


Figure 6.8: (a) Deformation in Franekeer in millimeters measured from May 1997. (b) The contribution to the subsidence by salt mining, displayed in percentage of the total subsidence. Both figures are based on the deformation at May 2005.

are the squeeze volumes and the production volumes. The residues between the estimated PS deformation and the Mogi deformation variate from -20 to 20 mm at the final epoch, which is about 15% of the total deformation. These residues are present in the North and the West of the subsidence bowl. Based on the high correlation factor and the residues between the datasets, it can be concluded that in the Veendam case Mogi shows to be suitable to estimate the deformation parameters based on PS deformation.

The correlation factor between the estimated volume changes by Mogi and the provided production volumes in the Barradeel case is 0.989. Despite the high correlation coefficient between the PS deformation of the Barradeel test case and the estimated Mogi deformation, the residuals between the datasets are large in the salt mining subsidence bowl. Underestimation of the deformation in the center of the bowl by the Mogi model and overestimation of the deformation at the dikes situated in the West of the bowl results into errors of 150 mm over 8 years. Several reasons can have introduced the large residuals.

- The PS deformation can differ from reality. This is emphasized by the leveling measurements which indicated larger deformation at the dike than the PS deformation.
- The looking direction of the satellite can have caused a difference in the measured deformation. Subsidence can be larger on the sea side of a dike than on the land side.
- Mogi assumes a point source, but Frisia Salt makes extensive use of the creep properties of salt, resulting into a different subsidence pattern.

It is not clarified in the research whether the estimated PS deformation is not correct, or whether the deformation can not exactly be modeled by the Mogi source possibly due to the creep phenomenon.

Based on the calculated correlation coefficients between provided production volumes and estimated volume changes, the Mogi model proves to be a feasible model to estimate reservoir parameters from PS deformation. Despite high correlation coefficients the deformation pattern calculated with Mogi parameters does not necessary represent the PS deformation.

Chapter 7

Conclusions and recommendations

The research goal of this thesis as stated in chapter 1 is:

”present methods optimizing the success rate of identifying Persistent Scatterers, and determine the feasibility of modeling physical subsurface processes from the temporal deformation results obtained from the Persistent Scatter analysis.”

The first section of this chapter gives the conclusions on the research and will describe whether the research goal is achieved. Section 7.2 discusses recommendations for further research on this topic.

7.1 Conclusions

The research goal contains two topics. The first topic focuses on the optimization of the success rate making use of different optimization methods. The second topic deals with modeling of physical processes introducing. The estimation of model parameters is based on the deformation obtained from optimized datasets. This section will treat the conclusions on both topics.

The first topic mentions optimization methods. In this research three methods are investigated, which are the manual PS identification, deformation subtraction and breakpoint model. The optimization models are tested on two test cases. These cases are the Veendam concession covered by tracks 108, 380 and 487 and the Barradeel concession covered by track 151 and 258. Conventional PS analysis is used to obtain a dataset used as reference dataset. Subsequently the optimization methods calculate new datasets which are compared to the conventional datasets. The distribution and density of PS is used to describe the optimization degree of the datasets. Conclusions based on the research on success rate identification are listed.

- The initial network influences the final identified PS, hence investigation of the initial network before proceeding with the densification of PSs is required. The presence of PSs in the main subsiding area are of importance for this research. A low PSP threshold increases the computation time, but also the number of identified PSs. The threshold of 0.45 resulted throughout the research in more dense PS distributions.
- The manual PS identification method and deformation subtraction methods increase the density of the identified PSs and obtain a more homogeneous distribution of PSs compared to the conventional method. This improvement of density and distribution results in an increase of internal and external precision, acquired with a Gaussian bowl model. This increase holds for the deformation subtraction methods only when the deformation,

on which the deformation surface estimation is based, captures the deformation of interest. Subtraction of an incorrect deformation pattern can increase the variability of the deformation pattern, hence resulting in less identified PSs.

- Unwrapping errors are present in both test cases. Making use of the manual PS identification method or deformation subtraction method does not eliminate unwrapping errors. When the estimation of deformation to be subtracted by the deformation subtraction methods are based on PS/PSC results, unwrapping errors, if present in the conventional method, are also present in the results of these optimization methods, since the subtracted deformation is added to the estimated deformation at the final step. Unwrapping errors are eliminated with the assumption that the deformation behavior is linear, or exists out of several linear models. The deformation according to the linear model is calculated and the difference in ambiguity is subtracted from the actual deformation.
- The breakpoint model, as implemented, does not improve the density and distribution of the PSs. But unwrapping errors are eliminated by the model. Investigation of the accepted breakpoint is crucial, since the algorithm as implemented does not necessary accept the wanted breakpoint, but the most occurring breakpoint. The reason for the lack of increase of PS density is not identified.

The success rate of identified PSs increases with the use of the methods manual PS selection and deformation subtraction. Hence these methods optimize the PS datasets. The breakpoint model does not increase the success rate of the identified PSs, but does eliminate unwrapping errors and therefore can be called an optimization method.

The deformation of the different PS datasets is analyzed.

- The estimated deformation between the datasets based on the different tracks is comparable.
- The subsidence in slant range in the Veendam concession is estimated to be -13 mm/year and in vertical direction -14 mm/year within a timespan starting from July 1992 until December 2003. The total estimated vertical deformation is -155 mm over the mentioned timespan.
- In the Barradeel concession the maximum vertical deformation estimated in the subsidence bowl is -334 mm over a timespan of 13 years starting from 1992. The maximum deformation velocity in the Barradeel concession area in vertical direction is -25 mm/year.
- Franeker is subsiding. The combination of deformation introduced by gas extraction near Franeker and salt extraction in the Barradeel concession, introduce a tilt in Franeker. The tilt in 2005 is -15.8 mm/km with May 1992 taken as reference date. Maximum subsidence of Franeker is -90 mm measured over the same timespan.
- Correlation coefficients of the estimated deformation and compared to leveling measurements resulted in large values ranging from 0.827 to 0.950 for the Veendam concession. Track 108 experienced the largest correlation coefficients (0.918 to 0.950) and track 487 the smallest (0.827 to 0.891). Between PS results of track 108 and leveling measurements in the Veendam concession a difference of -10 to -15 mm is present for all the investigated time periods, where the PS results are underestimated compared to the leveling results. This can have been introduced by unwrapping errors at the cavern locations. The largest used leveling time period ranges from 1995 until 2004.

- In the Barradeel concession the correlation coefficients between the leveling measurements and PS results range from 0.915 to 0.939. The leveling datasets correspond to the PS closest to BAS-1. The West of the subsidence bowl is underestimated. Investigation of the timeseries indicates a break-point around 1997 in this area. Hence this has introduced an underestimation of the deformation after 1997.

The Mogi model has been used to investigate the second topic of the research goal. This model is applied as inverse model and describes deformation assuming a point source, depending on the parameters describing the x and y coordinates of the source, the depth and the volume change. In both test cases the x rd and y rd coordinates and the depth of the caverns are known. Production data is used to validate the estimated volume changes.

- The estimated parameters for the Veendam concession are approximate similar. The parameters are presented in tables 6.2.1, D.2 and D.4. The x rd coordinate estimated for track 487 is not comparable to the other tracks, but deviates 799 meters from track 108. This is introduced by the distribution and density of PSs in the subsidence bowl.
- The estimated parameters for the Veendam concession approach reality. This conclusion is based on the cavern locations, provided depth of the salt layer and the provided volumes, which are the production volumes, underground volumes and squeeze volumes. The highest correlation coefficient between the estimated volume changes and the provided volumes is 0.955 for track 108, 0.843 for track 487 and 0.950 for track 380. Best fitting volumes are the squeeze volumes and the production volumes.
- The deformation in the Barradeel concession is estimated by two sources. One source describes the Barradeel deformation which is the deformation caused by salt mining, and the other source describes the Franeker deformation which is deformation caused by gas subtraction. The estimated parameters for both sources correspond in both tracks, except for the x rd coordinate. This coordinate deviates in track 258 610 meters from track 151. This is introduced by the distribution and density of PSs in the subsidence bowl. PSs are not present in the centre of the subsidence bowl, introducing an error in the estimated volume change of the Barradeel source.
- The estimated parameters for the Barradeel concession approach reality. The estimated parameters are the volume change of the salt reservoir, the location, depth and volume change of the gas reservoir and are presented in tables 6.7 and D.5. The location and depth of the salt reservoir are taken fixed, based on the location of BAS-1 and BAS-2 and the depth of the salt layer. The volume change of the salt reservoir is validated with provided production data and has a correlation coefficient of 0.989 for track 108.
- Despite the high correlation coefficient between the PS deformation of track 151 and the estimated Mogi deformation, the residuals between the datasets are large in the salt mining subsidence bowl. Underestimation of the deformation in the center of the bowl by the Mogi model and overestimation of the deformation at the dikes situated in the West of the bowl results into errors of 150 mm over 8 years. The final five epochs starting in 2001 experience the largest errors. Several reasons can have introduced the large residuals. The PS deformation can differ from reality. This is emphasized by the leveling measurements which indicated larger deformation at the dike than the PS deformation. The looking direction of the satellite can have caused a difference in the measured deformation. Subsidence can be larger on the sea side of a dike than on the land side. Another reason can be the model. Mogi assumes a point source, but Frisia Salt makes extensive use of the creep properties of salt, resulting into a different subsidence pattern. The results of

track 258 correspond to the track 151 result, and do not clarify whether the estimated PS deformation is not correct, or whether the deformation can not exactly be modeled by the Mogi source possibly due to the creep phenomenon.

- According to the estimated Mogi deformation, the contribution of salt mining to the subsidence in Franeker is noteworthy.

The Mogi model proves to be a feasible model to estimate reservoir parameters from PS deformation. This conclusion is based on the calculated correlation coefficients between provided production volumes and estimated volume changes. Despite high correlation coefficients the deformation pattern calculated with Mogi parameters does not necessary represent the PS deformation. Further research on this difference is needed.

7.2 Recommendations

Several recommendation for further research on this topic are discussed in this section.

- The implemented methods are investigated and not combined throughout this research. Further research on the combination of the optimization methods and the increase of the success rate of identified PSs is recommended. An increase is expected in the success rate compared to the optimization methods separate.
- The breakpoint model does not increase the success rate of identified PSs, while this is expected. The reason for this is not identified during this research. It is recommended to investigate why the breakpoint model does not result into an increase of PS density and distribution.
- The breakpoint algorithm does not store the selected breakpoint and whether a linear model or breakpoint model is applied. Giving the breakpoint epoch and applied model as output will save time during research.
- The deformation subtraction method estimates a deformation surface for every epoch. This surface is transformed in radians and subtracted from the phase. The residual phase is used as input for the PS analysis. Estimation of the deformation surfaces in this research is based on a Delaunay triangulation or a Gaussian bowl. Deformation patterns defined in different tracks covering the area of interest could also be used to estimate deformation surfaces. The PS deformation in a track has to be transformed to the radar coordinates of the track of interest. Most likely the acquisition dates are not at the same date, hence interpolation is required. The same holds for deformation surfaces acquired by other monitoring techniques like leveling.
- Geostatistical interpolation methods like kriging can be used to define deformation surfaces. Large scaled deformation is identified by this technique, which is required for the deformation subtraction. With the implemented algorithms local deformation can have large influence on the estimated surfaces. Making use of a nugget model smooths the effect of local deformations.
- Further research on the difference between the modeled deformation by Mogi and the estimated PS deformation for track 151 is necessary. The reason introducing this difference can not be found. Several assumptions are given, but they can not be grounded. If the difference is introduced by creep properties, more insight in the properties can be obtained by further research.

- The estimated volume changes with Mogi are throughout this research based on the optimized dataset. The difference between the estimated volume changes based on the conventional dataset and the optimized dataset is of interest. This will verify whether the increase in the success rate of identification of the PS results is necessary to estimate correct source parameters.
- During this research many hours are spend on filtering local deformations and uncorrect estimated PSs. These deformation had a large influence on deformation surface estimation or OMT calculation. A filter applicable in all cases would have reduced the time.

Bibliography

- [1] F Amelung, S Jónsson, H Zebker, and P Segall. Widespread uplift and trap door faulting on Galápagos volcanoes observed with radar interferometry. *Nature*, 407(6807):993–996, October-26 2000.
- [2] J N Breunese and R M H E van Eijs. Solution mining in the barradeel concession. *TNO-NITG InFormation*, 12(2):5–9, 2003.
- [3] R Buder. *The invention that changed the world*. Simon & Schuster, New York, 1996.
- [4] Oranjewoud B.V. Bodemdaling steenzoutconcessie barradeel 1 en 2. Technical report, 2004.
- [5] Oranjewoud B.V. Meetregister bij het meetplan barradeel en barradeel ii. Technical report, 2005.
- [6] Oranjewoud B.V. Meetregister bij het meetplan veendam. Technical report, 2006.
- [7] Adviescomité congregatie Franekerdeel. Notulen vergadering adviescomité franekerdeel, 16 February, 2006.
- [8] C C Counselman and S A Gourevitch. Miniature interferometer terminals for earth surveying: ambiguity and multipath with the Global Positioning System. *IEEE Transactions on Geoscience and Remote Sensing*, 19(4):244–252, 1981.
- [9] F Schokking J P A Roest D G Price, F R van Veen and H Houwink. Bodemdaling in nederland. In *Symposium report*.
- [10] J J Dvorak and D Dzurisin. Volcano geodesy: the search for magma reservoirs and the formation of eruptive vents. *Reviews of Geophysics*, 35:343–384, 1997.
- [11] Wikipedia Online encyclopedia. (Accessed 27 Oktober, 2007) <<http://www.wikipedia.nl>>.
- [12] ESCO. (Accessed 9 September, 2007) <<http://www.esco-salt.com/>>.
- [13] W E Farrell. Deformation of the earth by surface loads. *Rev. Geophys. Space. Phys.*, 10:761–797, 1972.
- [14] A Ferretti, C Prati, and F Rocca. Nonlinear subsidence rate estimation using permanent scatterers in differential SAR interferometry. *IEEE Transactions on Geoscience and Remote Sensing*, 38(5):2202–2212, September 2000.
- [15] A Ferretti, C Prati, and F Rocca. Permanent scatterers in SAR interferometry. *IEEE Transactions on Geoscience and Remote Sensing*, 39(1):8–20, January 2001.
- [16] R A Finkel and J L Bentley. Quad trees a data structure for retrieval on composite keys. *Acta Informatica*, 4(1):1–9, 1974.

- [17] A K Gabriel and R M Goldstein. Crossed orbit interferometry: theory and experimental results from SIR-B. *Int.J. Remote Sensing*, 9(5):857–872, 1988.
- [18] R M Goldstein. Venus characteristics by earth-based radar. *Astronomical Journal*, 69(1):12–18, 1964.
- [19] J Groot. Cross section computation of trihedral corner reflectors with the geometrical optics approximation. *ETT*, 3(6):637–642, November 1992.
- [20] R F Hanssen. Assessment of the role of atmospheric heterogeneities in ERS tandem SAR interferometry. Technical report, Delft Institute for Earth-Oriented Space Research, Delft, the Netherlands, 1998. Report for the European Space Agency.
- [21] R F Hanssen. *Radar Interferometry: Data Interpretation and Error Analysis*. Kluwer Academic Publishers, Dordrecht, 2001.
- [22] R F Hanssen, B Vermeersen, R Scharroo, B Kampes, S Usai, R Gens, and R Klees. Deformatiepatroon van de aardbeving van 17 augustus 1999 in Turkije gemeten met satelliet radar interferometrie. *Remote Sensing Nieuwsbrief*, 90:42–44, February 2000. In Dutch.
- [23] C Hulsmeyer. Herzian-wave projecting and receiving apparatus adopted to indicate or give warning of the presence of a metallic body such as a ship or a train. *British Patent No. 13,170*, 1904.
- [24] M L Jemic, editor. *Rock mechanics in salt mining*. Taylor and Francis, Londen, 1994.
- [25] B M Kampes. *Displacement Parameter Estimation using Permanent Scatterer Interferometry*. PhD thesis, Delft University of Technology, Delft, the Netherlands, September 2005.
- [26] B M Kampes and N Adam. Velocity field retrieval from long term coherent points in radar interferometric stacks. In *International Geoscience and Remote Sensing Symposium, Toulouse, France, 21–25 July 2003*, pages cdrom, 4 pages, 2003.
- [27] V B H Ketelaar and R F Hanssen. Separation of different deformation regimes using INSAR data. In *Third International Workshop on ERS SAR Interferometry, 'FRINGE03', Frascati, Italy, 1-5 Dec 2003*, page 6 pp., 2003.
- [28] V B H Ketelaar, P Marinkovic, and R F Hanssen. Validation of point scatterer phase statistics in multi-pass InSAR. In *ENVISAT & ERS Symposium, Salzburg, Austria, 6–10 September, 2004*, page 10 pp, 2004.
- [29] V B H Ketelaar, F van Leijen, P Marinkovic, and R F Hanssen. On the use of point target characteristics in the estimation of low subsidence rates due to gas extraction in Groningen, the Netherlands. In *Fourth International Workshop on ERS/Envisat SAR Interferometry, 'FRINGE05', Frascati, Italy, 28 Nov-2 Dec 2005*, page 6 pp., 2006.
- [30] R M Koevoets. Verbetering van het netontwerp voor analyse van bodemdaling door oplosmijnbouw. Master's thesis, Faculty of Geodetic Engineering, Delft University of Technology, 2001.
- [31] H Leenaers. Zoutgletsjer op drift. *NRC*, May 2004.
- [32] F Li and R Goldstein. Studies of multi-baseline spaceborne interferometric synthetic aperture radar. In *International Geoscience and Remote Sensing Symposium, Ann Arbor, 18–21 May 1987*, pages 1545–1550, 1987.

- [33] D Massonnet, P Briole, and A Arnaud. Deflation of Mount Etna monitored by spaceborne radar interferometry. *Nature*, 375:567–570, June-15 1995.
- [34] D Massonnet, M Rossi, C Carmona, F Adagna, G Peltzer, K Feigl, and T Rabaute. The displacement field of the Landers earthquake mapped by radar interferometry. *Nature*, 364(8):138–142, July-8 1993.
- [35] Nedmag Industries Mining and Manufacturing B.V. (2006). Personal contact.
- [36] Nedmag Industries Mining and Manufacturing B.V. (Accessed 19 May, 2007) <<http://www.nedmag.nl>>.
- [37] Nedmag Industries Mining and Manufacturing B.V. Milieu editie. *Nedmag nieuws*, 5, 2004.
- [38] K Mogi. Relations between eruptions of various volcanoes and the deformation of the ground surface around them. *Bulletin of the Earthquake Research Institute, University of Tokyo*, 36:99–134, 1958.
- [39] D Odijk and F Kenselaar. Subsidence modeling, user’s manual of the sumo software (version 4). Technical report, NAM, geodetic department, 2003.
- [40] K K Pankratov. (Accessed 24 May, 2007) <<http://puddle.mit.edu/glenn/kirill/SAGAHTML>>.
- [41] J P A Roest. Engineering geology - subsidence, 1990. Lecture notes, Delft University of Technology, Faculty of Applied Earth Sciences.
- [42] P J G Teunissen. Least-squares estimation of the integer GPS ambiguities. In *Invited Lecture, Section IV Theory and Methodology, IAG General Meeting, Beijing, China, august 1993*, 1993. Also in: Delft Geodetic Computing Centre, LGR Series, No. 6, 1994.
- [43] P J G Teunissen. Least-squares estimation of the integer GPS ambiguities. In *Publications and annual report 1993*, number 6 in LGR-Series, pages 59–74. Delft geodetic computing centre, September 1994.
- [44] P J G Teunissen. Success probability of integer GPS ambiguity rounding and bootstrapping. *Journal of Geodesy*, 72:606–612, 1998.
- [45] P J G Teunissen, D G Simons, and C C J M Tiberius. *Probability and observation theory*. Delft Institute of Earth Observation and Space Systems (DEOS), Delft University of Technology, The Netherlands, 2005.
- [46] TNO. (Accessed 9 September, 2007) <<http://www.dinoloket.nl/>>.
- [47] S Usai and R Klees. SAR interferometry on very long time scale: A study of the interferometric characteristics of man-made features. *IEEE Transactions on Geoscience and Remote Sensing*, 37(4):2118–2123, July 1999.
- [48] H A Zebker and J Villasenor. Decorrelation in interferometric radar echoes. *IEEE Transactions on Geoscience and Remote Sensing*, 30(5):950–959, September 1992.

Appendix A

ERS data baseline plots

Baseline plot track 108

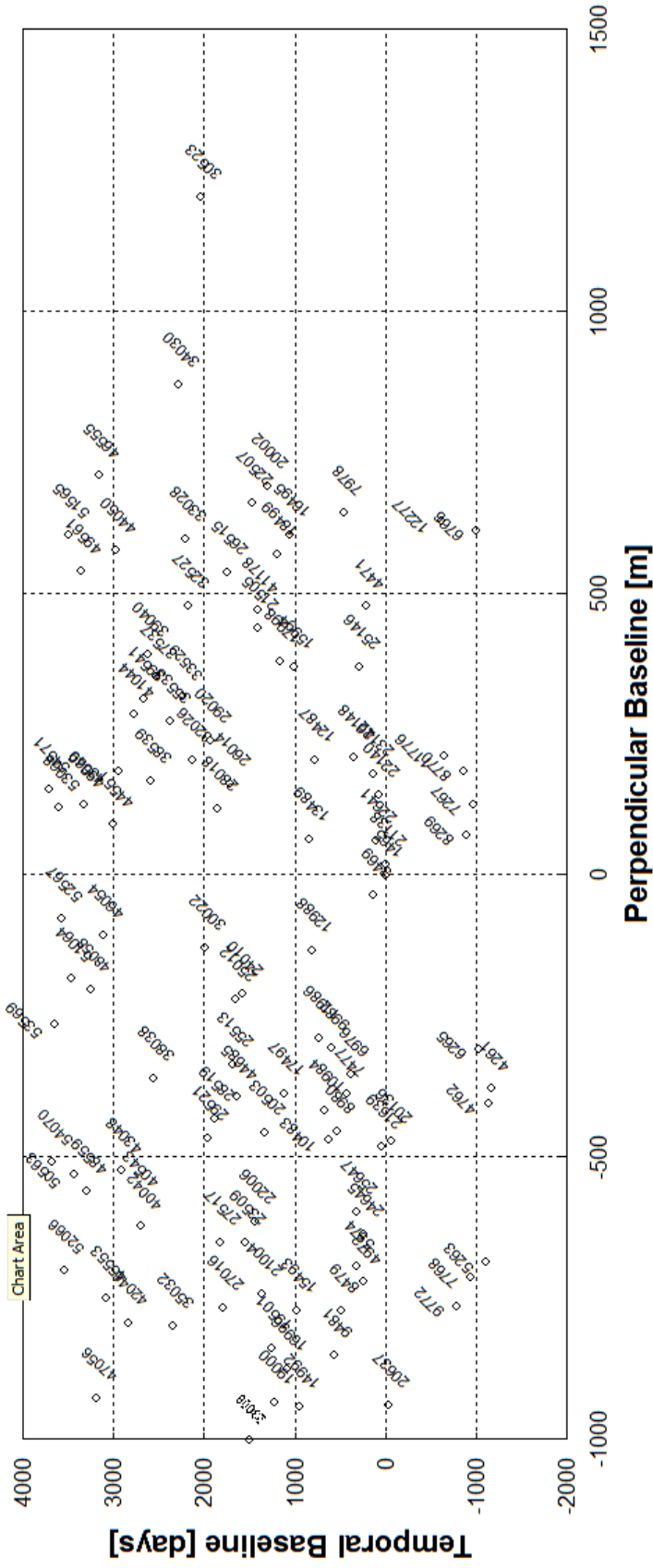


Figure A.1: Baseline plot describing the distribution of SAR images, of track 108, over time and space. The x-axis presents the spatial separation perpendicular to the look-direction. The y-axis presents the time interval counted from a set reference moment. The orbitnumbers are displayed next to the datapoints.

Baseline plot track 380

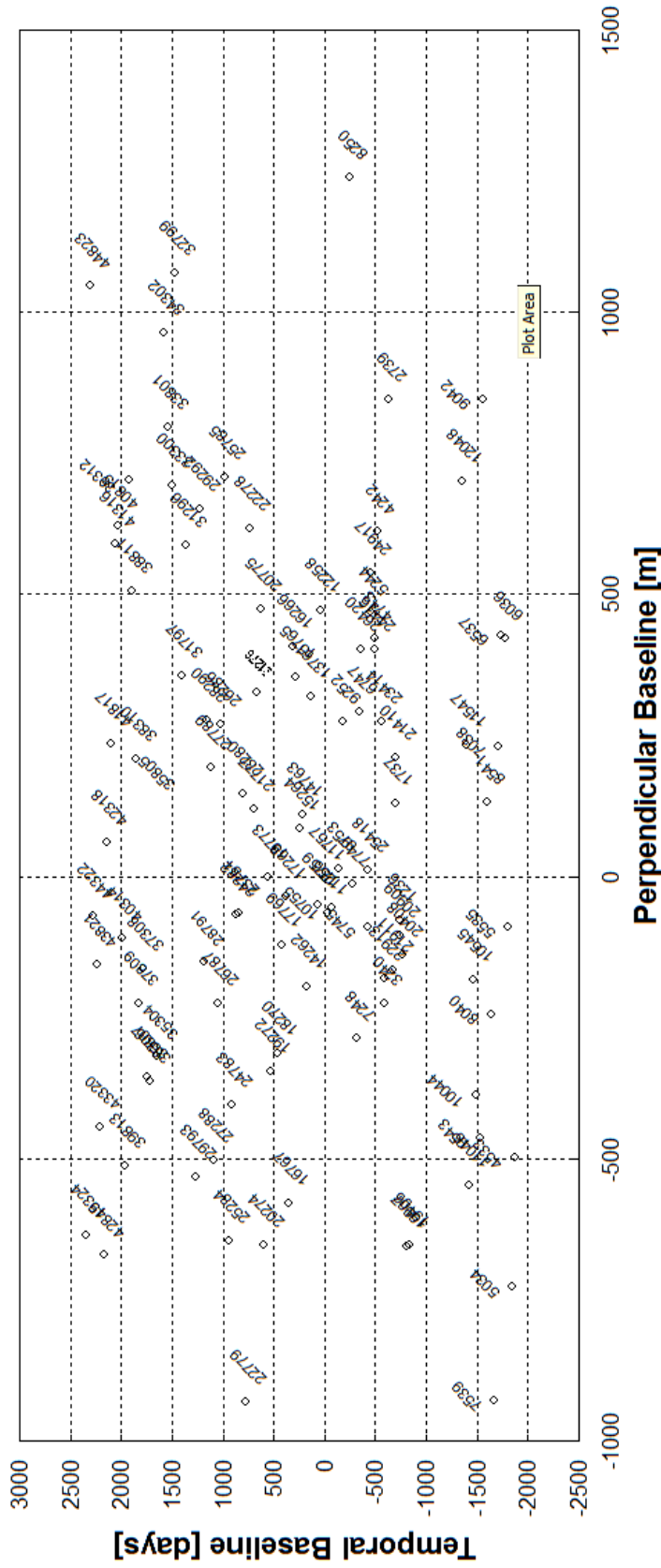
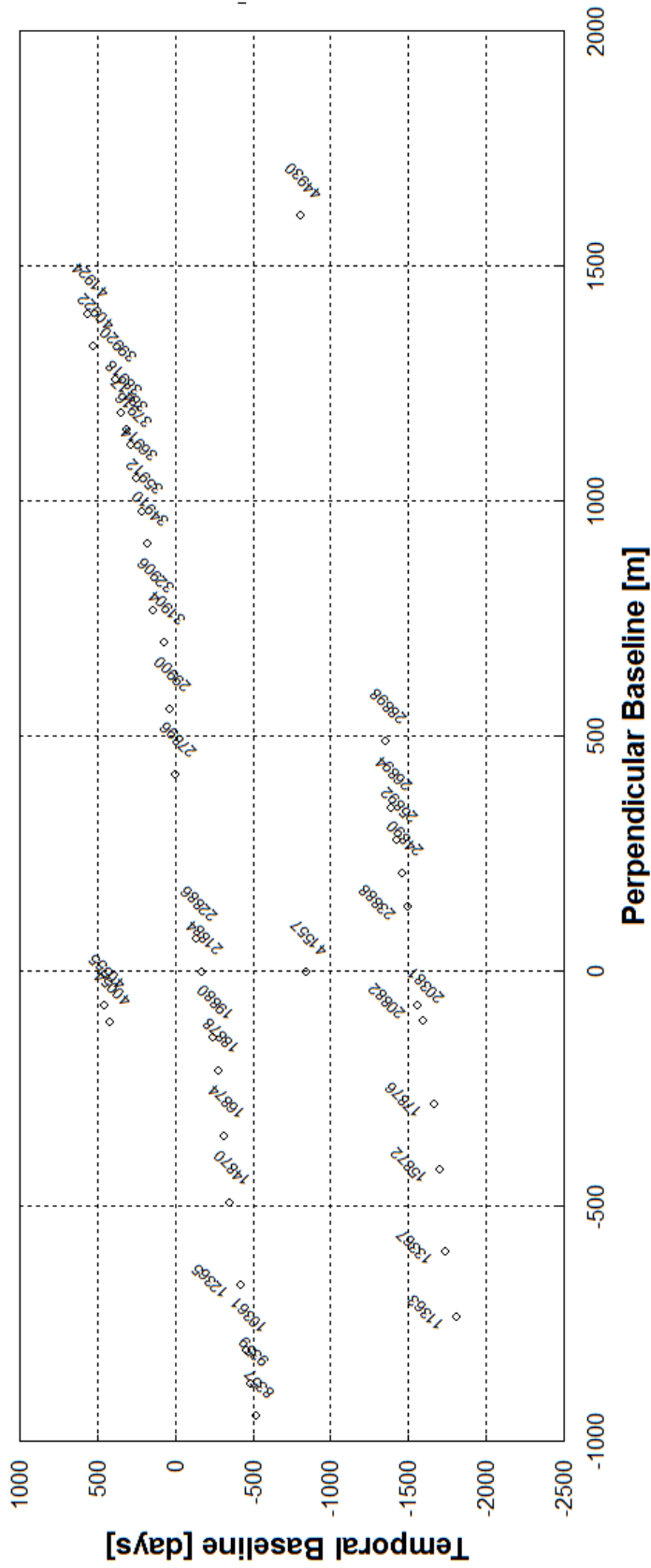


Figure A.2: Baseline plot describing the distribution of SAR images, of track 380, over time and space. The x-axis presents the spatial separation perpendicular to the look-direction. The y-axis presents the time interval counted from a set reference moment. The orbitnumbers are displayed next to the datapoints.

Baseline plot track 487



Baseline plot track 151

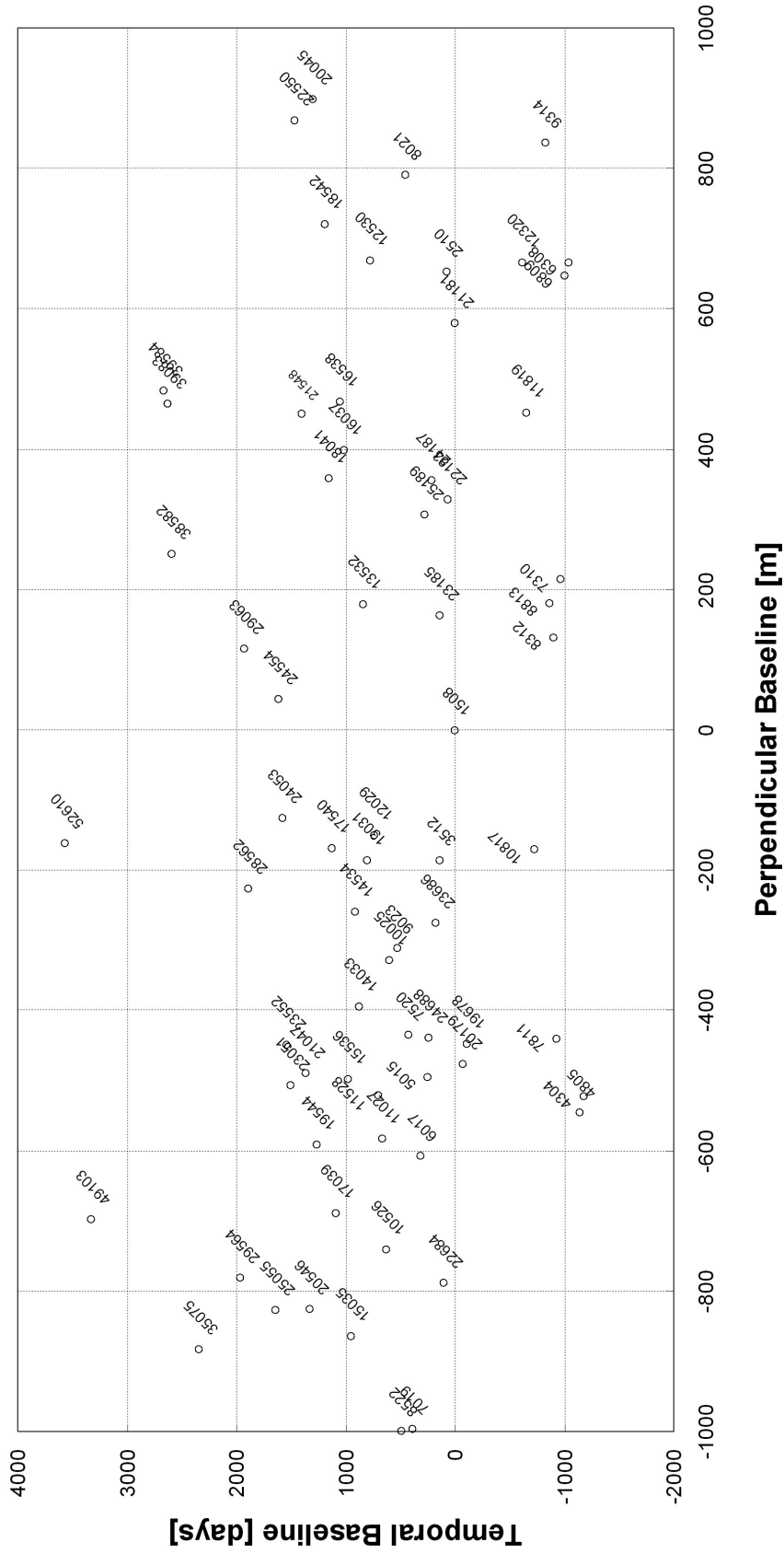


Figure A.4: Baseline plot describing the distribution of SAR images, of track 151, over time and space. The x-axis presents the spatial separation perpendicular to the look-direction. The y-axis presents the time interval counted from a set reference moment. The orbit numbers are displayed next to the datapoints.

Baseline plot track 258

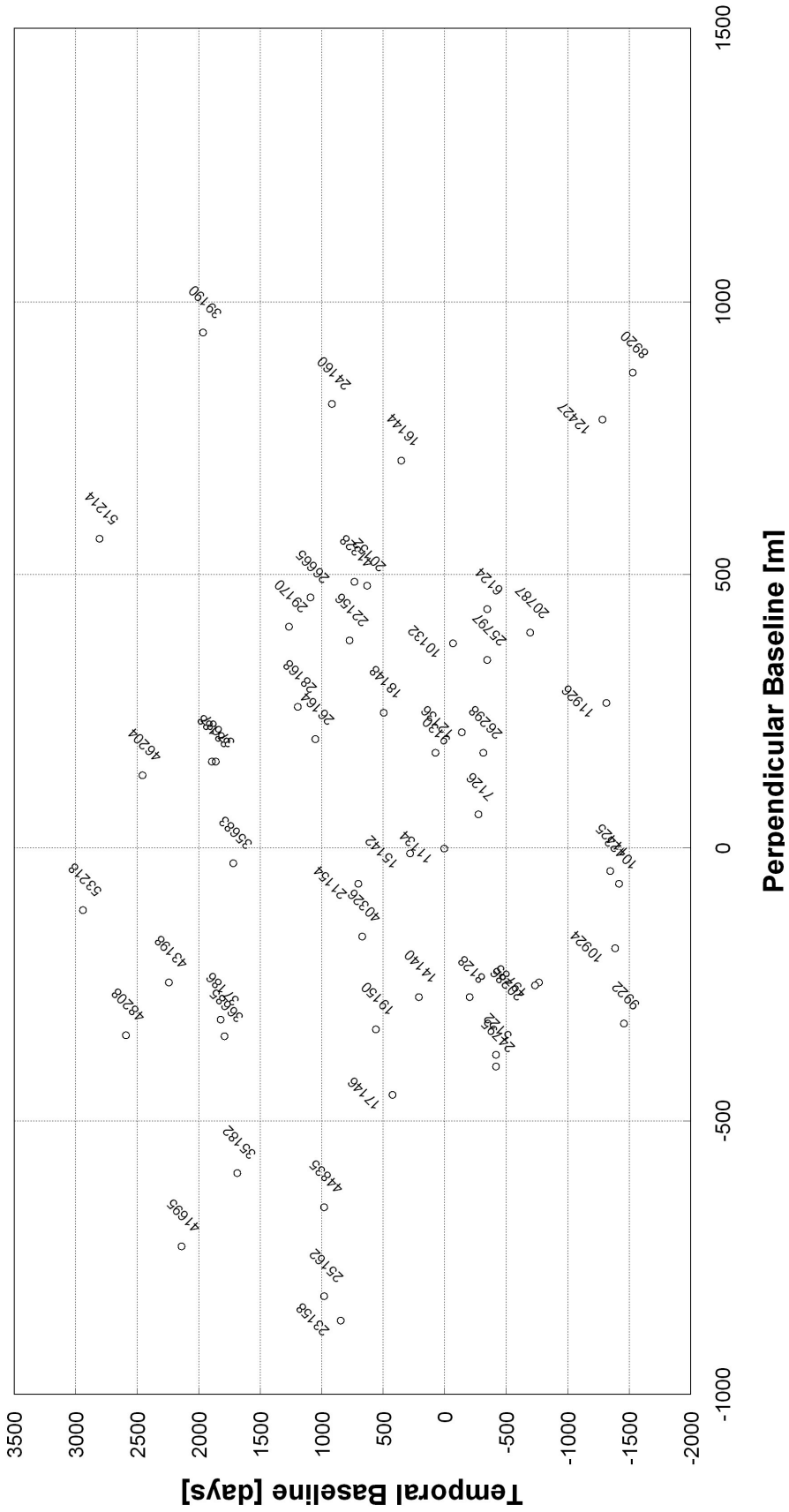


Figure A.5: Baseline plot describing the distribution of SAR images, of track 258, over time and space. The x-axis presents the spatial separation perpendicular to the look-direction. The y-axis presents the time interval counted from a set reference moment. The orbitnumbers are displayed next to the datapoints.

Appendix B

Linearized Least Squares system bowl estimation

The subsidence bowls present in Veendam and Barradeel concession are described by a Gaussian function

$$z(x, y) = d \cdot e^{-\frac{1}{2} \frac{(x - x_c)^2 + (y_c - y)^2}{r^2}} + z_c, \quad (\text{B.1})$$

where d stands for the maximum depth of the bowl, r is the radius of the bowl, and (x_c, y_c, z_c) the origin location. The estimation of the unknown parameters, is performed with least-squares and since least-squares deals with linear systems of equations, the bowl function has to be linearized. The linearization of the least squares model for a non-linear problem becomes

$$A(x) = \begin{bmatrix} a_1(x^0) \\ \vdots \\ a_m(x^0) \end{bmatrix} + \begin{bmatrix} \partial_x^T a_1(x^0) \\ \vdots \\ \partial_x^T a_m(x^0) \end{bmatrix} \cdot \Delta x. \quad (\text{B.2})$$

Subsequently the linearized model of observation equations will be

$$E \{ \Delta y \} = \partial_x^T A(x^0) \Delta x; \quad D \{ \Delta y \} = Q_y \quad (\text{B.3})$$

where $\partial_x^T A(x^0)$ is the gradient vector, $\Delta y = y - A(x^0)$, $\Delta x = x - x^0$ and Q_y the variance-covariance matrix of the observations. The derivatives of the bowl model are given as

$$\begin{aligned} \frac{\partial}{\partial r} z_i(x^0) &= d^0 \cdot \frac{(x_i - x_c)^2 + (y_c - y_i)^2}{(r^0)^3} \cdot e^{-\frac{1}{2} \frac{(x_i - x_c)^2 + (y_c - y_i)^2}{(r^0)^2}} \\ \frac{\partial}{\partial d} z_i(x^0) &= e^{-\frac{1}{2} \frac{(x_i - x_c)^2 + (y_c - y_i)^2}{(r^0)^2}} \\ \frac{\partial}{\partial x_c} z_i(x^0) &= d^0 \cdot \frac{x_i - x_c^0}{(r^0)^2} \cdot e^{-\frac{1}{2} \frac{(x_i - x_c)^2 + (y_c - y_i)^2}{(r^0)^2}} \\ \frac{\partial}{\partial y_c} z_i(x^0) &= -d^0 \cdot \frac{y_c^0 - y_i}{(r^0)^2} \cdot e^{-\frac{1}{2} \frac{(x_i - x_c)^2 + (y_c - y_i)^2}{(r^0)^2}} \\ \frac{\partial}{\partial z_c} z_i(x^0) &= 1. \end{aligned} \quad (\text{B.4})$$

The initial values are indicated with the superscript 0 and i stands for the i^{th} PSs observed.

When all the observations for every epoch are applied, the iteration can approach infinity due to the differences in estimated relative deformation of PSs, experienced as noise for the least-squares method. To constrain the estimation less, three different cases are programmed

- the parameter vector is solved for all epochs in one estimation, assuming fixed origin,
- the parameter vector is solved for all epochs in one estimation, assuming changing origin, and
- the parameter vector is solved for one epoch in one estimation.

The linearized system of equations, with k the number of epochs and n the number of PSs, for the first case is composed as

$$\begin{bmatrix} z_1^1 \\ \vdots \\ z_1^k \\ z_2^1 \\ \vdots \\ z_2^k \\ \vdots \\ z_n^1 \\ \vdots \\ z_n^k \end{bmatrix} = \begin{bmatrix} d^{01} \cdot e \frac{1}{2} \frac{(x_1 - x_c^0)^2 + (y_c^0 - y_1)^2}{(r^{01})^2} + z_c^0 \\ \vdots \\ d^{0k} \cdot e \frac{1}{2} \frac{(x_1 - x_c^0)^2 + (y_c^0 - y_1)^2}{(r^{0k})^2} + z_c^0 \\ d^{01} \cdot e \frac{1}{2} \frac{(x_2 - x_c^0)^2 + (y_c^0 - y_2)^2}{(r^{01})^2} + z_c^0 \\ \vdots \\ d^{0k} \cdot e \frac{1}{2} \frac{(x_2 - x_c^0)^2 + (y_c^0 - y_2)^2}{(r^{0k})^2} + z_c^0 \\ \vdots \\ d^{01} \cdot e \frac{1}{2} \frac{(x_n - x_c^0)^2 + (y_c^0 - y_n)^2}{(r^{01})^2} + z_c^0 \\ \vdots \\ d^{0k} \cdot e \frac{1}{2} \frac{(x_n - x_c^0)^2 + (y_c^0 - y_n)^2}{(r^{0k})^2} + z_c^0 \end{bmatrix} + \partial_x^T A(x^0) \cdot \begin{bmatrix} \Delta x_c \\ \Delta y_c \\ \Delta z_c \\ \Delta r^1 \\ \vdots \\ \Delta r^k \\ \Delta d^1 \\ \vdots \\ \Delta d^k \end{bmatrix}. \quad (\text{B.5})$$

The gradient vector belonging to the subsidence bowl is

$$\partial_x^T A(x^0) = \begin{bmatrix} \frac{\partial}{\partial x_c} a_1^1 & \frac{\partial}{\partial y_c} a_1^1 & \frac{\partial}{\partial z_c} a_1^1 & \frac{\partial}{\partial r^1} a_1^1 & \dots & \frac{\partial}{\partial d^1} a_1^1 & \dots \\ \vdots & \vdots & \vdots & \vdots & \ddots & \vdots & \ddots \\ \frac{\partial}{\partial x_c} a_1^k & \frac{\partial}{\partial y_c} a_1^k & \frac{\partial}{\partial z_c} a_1^k & \dots & \frac{\partial}{\partial r^k} a_1^k & \dots & \frac{\partial}{\partial d^k} a_1^k \\ \frac{\partial}{\partial x_c} a_2^1 & \frac{\partial}{\partial y_c} a_2^1 & \frac{\partial}{\partial z_c} a_2^1 & \frac{\partial}{\partial r^1} a_2^1 & \dots & \frac{\partial}{\partial d^1} a_2^1 & \dots \\ \vdots & \vdots & \vdots & \vdots & \ddots & \vdots & \ddots \\ \frac{\partial}{\partial x_c} a_2^k & \frac{\partial}{\partial y_c} a_2^k & \frac{\partial}{\partial z_c} a_2^k & \dots & \frac{\partial}{\partial r^k} a_2^k & \dots & \frac{\partial}{\partial d^k} a_2^k \\ \vdots & \vdots & \vdots & \vdots & \ddots & \vdots & \ddots \\ \frac{\partial}{\partial x_c} a_n^1 & \frac{\partial}{\partial y_c} a_n^1 & \frac{\partial}{\partial z_c} a_n^1 & \frac{\partial}{\partial r^1} a_n^1 & \dots & \frac{\partial}{\partial d^1} a_n^1 & \dots \\ \vdots & \vdots & \vdots & \vdots & \ddots & \vdots & \ddots \\ \frac{\partial}{\partial x_c} a_n^k & \frac{\partial}{\partial y_c} a_n^k & \frac{\partial}{\partial z_c} a_n^k & \dots & \frac{\partial}{\partial r^k} a_n^k & \dots & \frac{\partial}{\partial d^k} a_n^k \end{bmatrix}. \quad (\text{B.6})$$

When the origin is assumed to change over time, which is the second case, the parameter vector is composed as the parameter vector in the first case, only now extra location parameters are introduced for every epoch, resulting into $5 \times k$ parameters to be solved. As a consequence the gradient vector is also quite similar to the gradient vector of the first case, only the columns for the estimated locations are constructed as for estimation of the radius and depth of the bowl of the first case.

In the third case when the parameters are estimated for one epoch at the time, the system of equations and design matrix are composed as

$$\begin{bmatrix} z_1 \\ z_2 \\ \vdots \\ z_n \end{bmatrix} = \begin{bmatrix} d^0 \cdot e^{-\frac{1}{2} \frac{(x_1 - x_c^0)^2 + (y_1^0 - y_1^0)^2}{(r^0)^2}} + z_c^0 \\ d^0 \cdot e^{-\frac{1}{2} \frac{(x_2 - x_c^0)^2 + (y_2^0 - y_2^0)^2}{(r^0)^2}} + z_c^0 \\ \vdots \\ d^0 \cdot e^{-\frac{1}{2} \frac{(x_n - x_c^0)^2 + (y_n^0 - y_n^0)^2}{(r^0)^2}} + z_c^0 \end{bmatrix} + \partial_x^T A(x^0) \cdot \begin{bmatrix} \Delta x_c \\ \Delta y_c \\ \Delta z_c \\ \Delta r \\ \Delta d \end{bmatrix}. \quad (\text{B.7})$$

Where the gradient vector is composed as

$$\partial_x^T A(x^0) = \begin{bmatrix} \frac{\partial}{\partial x_c} a_1 & \frac{\partial}{\partial y_c} a_1 & \frac{\partial}{\partial z_c} a_1 & \frac{\partial}{\partial r} a_1 & \frac{\partial}{\partial d} a_1 \\ \frac{\partial}{\partial x_c} a_2 & \frac{\partial}{\partial y_c} a_2 & \frac{\partial}{\partial z_c} a_2 & \frac{\partial}{\partial r} a_2 & \frac{\partial}{\partial d} a_2 \\ \vdots & \vdots & \vdots & \vdots & \vdots \\ \frac{\partial}{\partial x_c} a_n & \frac{\partial}{\partial y_c} a_n & \frac{\partial}{\partial z_c} a_n & \frac{\partial}{\partial r} a_n & \frac{\partial}{\partial d} a_n \end{bmatrix}. \quad (\text{B.8})$$

This estimation is performed for every epoch.

According to the least squares method the estimators and covariances are calculated with the formulas

$$\begin{aligned} \hat{x} &= x^0 + (\partial_x^T A(x^0) Q_y^{-1} \partial_x A(x^0))^{-1} \partial_x^T A(x^0) Q_y^{-1} (y - A(x^0)) \\ \hat{y} &= A(\hat{x}) \\ \hat{e} &= \underline{y} - \hat{y} \end{aligned} \quad (\text{B.9})$$

$$\begin{aligned} Q_{\hat{x}} &= (\partial_x^T A(x^0) Q_y^{-1} \partial_x A(x^0))^{-1} \\ Q_{\hat{y}} &= \partial_x^T A(x^0) Q_{\hat{x}} \partial_x^T A(x^0) \\ Q_{\hat{e}} &= Q_y - Q_{\hat{y}} \end{aligned}$$

Appendix C

Densification results

Different methods are implemented to increase the density of the number of Persistent Scatterers obtained with the Persistent Scatterer analysis. These methods are:

- manual PS identification,
- non-linear deformation subtraction estimated with bilinear interpolation,
- non-linear deformation subtraction estimated with a Gaussian bowl,
- breakpoint model.

A discussion on these model case be found in chapter 4. With these models an increase in the density of PSs is strived for. This to achieve an increase in the precision and reliability of the estimated deformation pattern, based on the relative deformation of the PSs. The precision and reliability is investigated with the estimated variance-covariance matrices $Q_{\hat{x}}$, $Q_{\hat{y}}$ and Overall Model Test. This appendix contains the results of the PS analysis making use of the conventional method with changing input parameters, and the results of the four different optimization methods. The methods are applied to the tracks 108, 380 and 487 covering the Veendam concession and tracks 151 and 258 covering the Barradeel concession.

Notice that the precision and reliability tests are performed on one epoch experiencing a clear deformation pattern in comparison to the master epoch. And also notice that the datasets are filtered to eliminate local deformation or unrealistic deforming PSs. The filters can be performed in several ways explained in chapter 5. Filtering can result into a dataset composed out of less PSs compared to a different dataset, but the density and distribution in the area of subsidence can be larger and more homogeneous. Therefore the number of PSs for the complete dataset will not be taken into account during the analysis of increase in precision and reliability.

When the expression density is used, the density of a part of the total crop is meant. Measurement of the density and distribution is performed with the calculation of distances from a central point in the area of interest to surrounding PSs. Hence the area depends on the distance taken from the central point. In figure 5.7(b) a histogram is presented with frequencies of PSs against the distance. The density statements given through this chapter are based on the frequency of PSs in a bin, thus local densities. The distribution is used in the global sense. Therefore density and distribution can be used simultaneously.

C.1 Track 108

The figures C.1 and C.2 display the relative deformation results in mm/year for track 108 covering the Veendam test case. The velocities are based on data from the timespan starting in

May 1992 and ending in September 2005. Figure C.1 contains the annual velocities of the PSs calculated with different PS thresholds or gridcell sizes. The last subfigure contains annual velocities obtained with the manual PS identification method, in which pixels likely to be PSs are manually selected. Figure C.2 contains the annual velocities obtained with the use of the breakpoint model and the deformation subtraction methods. The final subfigure displays the combination of different cases discussed in this section.

The figures C.1(a), C.1(b) and C.1(c) are processed with same input parameters except for the gridcell size. The input parameters taken fixed for all the cases discussed during this chapter can be found in table 5.4. As can be seen in the figures the gridcell size influences the final identified PSs. A discussion on the relation between the gridcell size and the final PSs can be found in section 5.2. With a gridcell size of 300 meters a few more PSs, compared to the PSs identified with a gridcell size of 200 meters, are identified in the main subsiding area. To investigate the distribution and density of PSs the distances from the center of the subsidence bowl to all PSs is calculated. These distances are compared to the distances for a reference dataset. Compared to a gridcell size of 200 meters, this resulted into an increase of PSs in the subsidence bowl when a gridcell size of 300 is used. The extra PSs can be valuable for the deformation pattern modeling. As can be seen in figure C.1(c), where the gridcell size is 50 meters, a group of PSs is identified in the south west of the crop, experiencing a subsidence rate approaching the maximum subsidence rate in the bowl. One PS in the network influenced the identified PSs in the surroundings and hence resulted into a different deformation pattern compared to the PSs found with gridcell size 200 or 300 meters. Since a larger number of PSs is present in the latter two cases, and no large deformations are reported in this area, the subsidence of these pixels in the case where the gridcell size is 50 meters is assumed to be incorrect. The gridcell size of 50 meters resulted into a decrease in density and distribution compared with the other two discussed conventional cases.

The figures C.1(d) and C.1(e) display the annual velocities of the PSs in the cases where the PSP threshold is set to 0.45. Hence the chance is larger that a pixel is accepted as PS, see section 3.3.1. As can be seen, and is investigated with the distance measurements to a central point, the distribution of the PSs became more homogeneous and the density increased compared to the cases where the PSP threshold is set to 0.4 instead of 0.45.

The last subfigure C.1(f) presents the annual velocities of the PSs identified with the use of the manual PS identification method. As can be seen, and as has been investigated with the distance measurements to a central point, the distribution of the PSs became significantly better in the north and west of the subsiding area.

The annual velocities of the PSs obtained with the deformation subtraction methods or breakpoint model are presented by figure C.2. The first two subfigures show the breakpoint model results. Two different approaches of this model can be used. In the final processing step the PSPs are tested against PSCs constructing the initial network. A PSP is connected to the three closest PSCs. The arc between PSC1 and the PSP, $PSC1/PSP$, is unwrapped and the estimated ambiguity is applied to test the PSP. When this ambiguity corresponds to the two ambiguities obtained with:

$$PSC2/PSP_{amb} - PSC2/PSC1_{amb} = PSC1/PSP_{amb}$$

and

$$PSC3/PSP_{amb} - PSC3/PSC1_{amb} = PSC1/PSP_{amb},$$

the PSP is accepted as PS. The difference between the two breakpoint models is that in the first breakpoint method, breakpoint 3 amb., all three obtained ambiguities should be similar, else

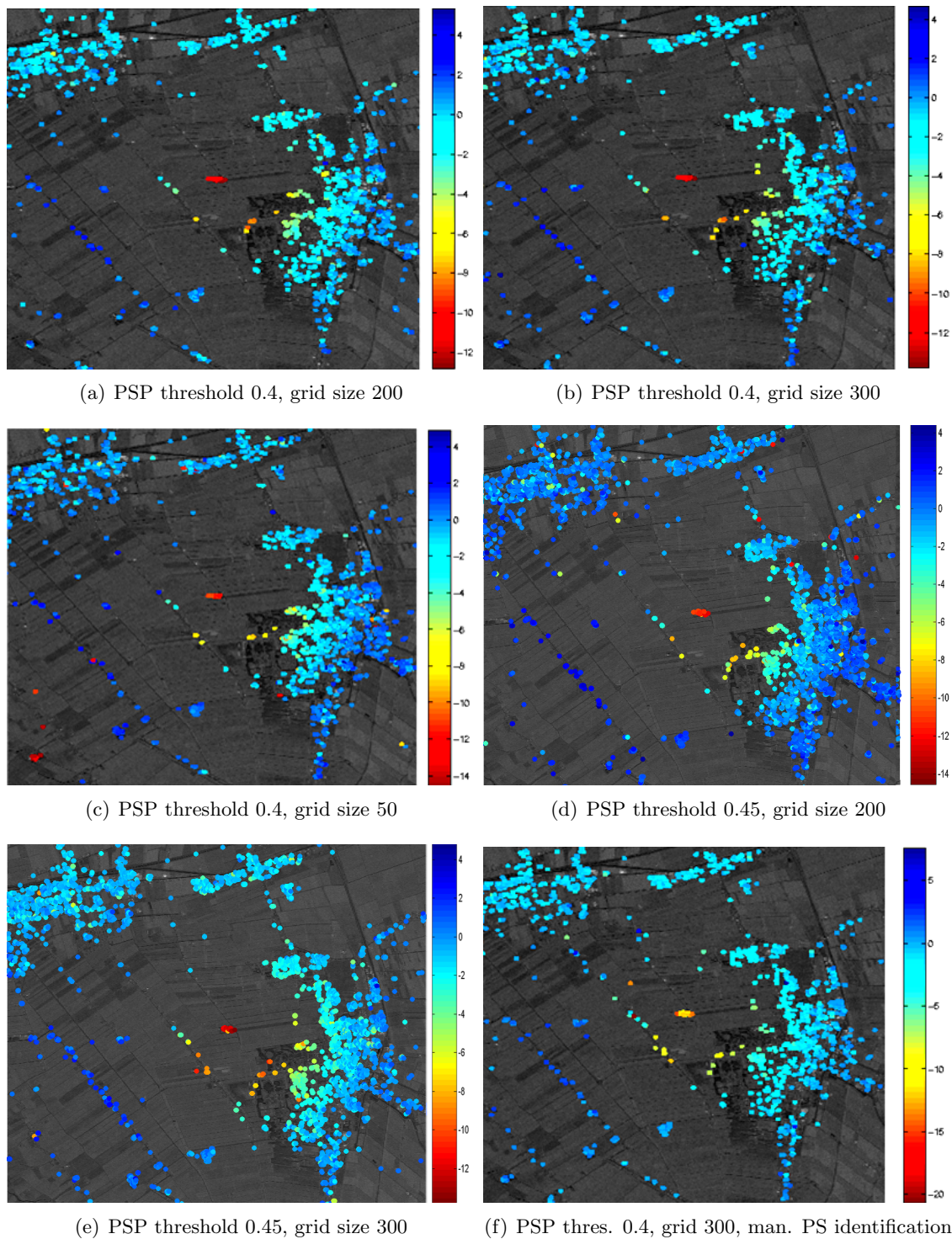


Figure C.1: Annual PS velocities [mm/year] track 108 covering the Veendam concession. The figures C.1(a) up and including figure C.1(e) display the annual velocities of the PSs identified with the conventional PS analysis, but changing PSP threshold and/or gridcell size. The last subfigure is obtained making use of the manual PS identification method. The annual velocities are retrieved from a timespan starting in May 1992 until September 2005.

the PSP is rejected. In the second breakpoint method, breakpoint 2 amb., two obtained

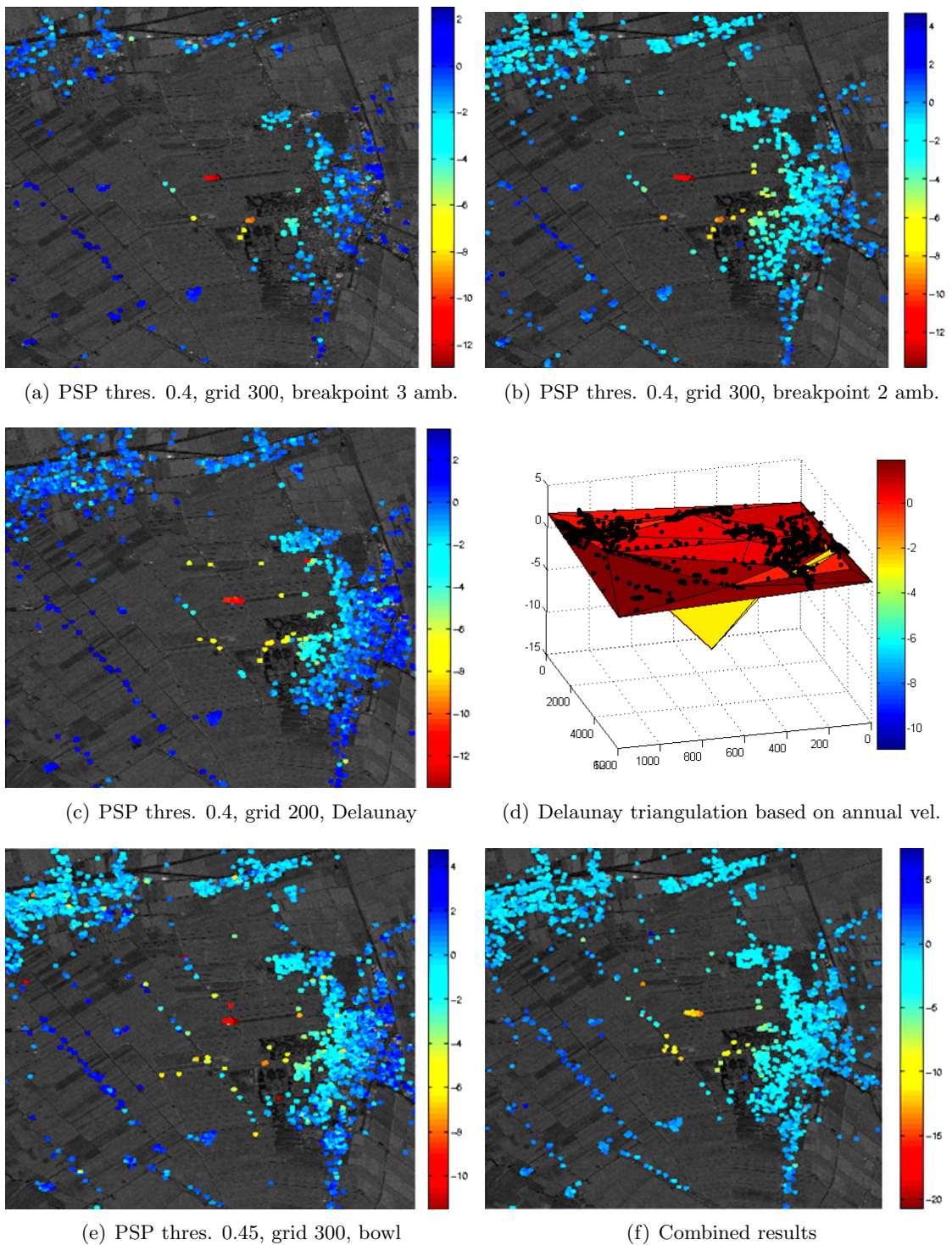


Figure C.2: Annual PS velocities [mm/year] track 108 covering the Veendam concession. The figures C.2(a) and C.2(b) are results of the breakpoint model. The next three figures present Delaunay or Gaussian bowl deformation subtraction results. Notice that the velocities shown in the figures C.2(c) and C.2(e) are the calculated velocities added to the removed estimated velocities, obtained by the deformation estimation methods. The maximum subsidence in the triangulation plot is -11 mm/year. The last figure shows the combined results of the cases.

ambiguities should be similar, else the PSP is rejected. The testing assumptions are more strict when three out of the three estimated arcs have to fit, therefore it is expected that in this case less PSs are identified compared to the case where two out of three arcs fit. As expected less PSs are identified when three out of three arcs have to fit. Minor differences are present between the figure C.2(b), where a breakpoint model is used with acceptance of PSPs when the ambiguities of two arcs are similar, and figure C.1(b), the conventional case. This is because the subsidence area experiences an approximate linear subsidence. Therefore the implementation of a breakpoint model will not identify many extra PSs. After investigation it became clear that the program had picked a different epoch as breakpoint then the epoch wanted. Manually setting this breakpoint resulted in less identified PSs. A discussion on this is found in section 5.6. Through this section the results as shown in figure C.2(b) are discussed.

The figures C.2(c) and C.2(e) show the results of the deformation subtraction methods. Deformation surfaces are estimated by the bilinear interpolation or Gaussian bowl estimation and subtracted from the differential phase. The resulting, residual phase is used as input for the PS analysis. Notice that the output, the annual velocities, displayed in the figures, are the velocities resulting from the PS analysis plus the subtracted velocities. Therefore a subsidence bowl is visualized again. The two figures can not be compared since the bilinear interpolation results are based on a PSP threshold of 0.4 and the Gaussian bowl results are based on a PSP threshold of 0.45. But after comparing them to the conventional results with corresponding gridcell size and PSP threshold, for both methods an increase in PSs and an increase in the density resulted. Although comparing roughly both results, two different deformation patterns are indicated. Because the bowl method contains a more homogeneous and more dense distribution of PSs in the north of the bowl, rejection of the bilinear interpolation method deformation pattern would be plausible. The difference in the identified PSs in the north of the bowl depends on the deformation pattern subtracted.

The final subfigure C.2(f) presents combined datasets. The sets combined are based on the same reference point. In this figure the combined PSs of all cases except for cases 1, 3 and 5 are present.

Table C.1 presents the velocities of the center of the bowl for the different investigated cases. The annual velocity of the center of the bowl is similar between all results except for the bowl estimation method. The average velocity is -12 mm/year over a timespan of 13 years. The difference in velocity for the bowl estimation method is introduced by uncorrect unwrapped time series, as presented in figure C.3. For this track the deformation estimation was uncorrect at two epochs, resulting in unwrapping errors. The calculated velocity became larger than in reality. This resulted in a smaller annual velocity for the bowl estimation method. Next to the unwrapping errors 3 PSs experiencing no deformation over time are identified. This also reduces the annual deformation.

The density and distribution, compared to a reference case, decreased in the cases 3 and 7. The density and distribution in case 8 stayed approximate constant, since most PSs deform linear, the breakpoint model does not identify extra PSs. Explanations for the decrease are given in the aforementioned text.

To investigate the precision the assumption is made that for both test cases the deformation is bowl shaped. With the Gaussian bowl estimator, explained in chapter 4, bowl parameters are estimated for every case based on one epoch. With the use of the equations discussed in section 3.3.2, the external and internal precisions were obtained. The subsequent discussion is mainly based on the diagonals of the $Q_{\hat{x}}$ and $Q_{\hat{y}}$ matrices. Because the deformation pattern is not a

Case N ⁰	Case	Velocity [mm/year]	OMT
1	PSP thres. 0.4, gridcell size 200	-11.55	1054
2	PSP thres. 0.4, gridcell size 300	-12.21	1388
3	PSP thres. 0.4, gridcell size 50	-11.60	2288
4	PSP thres. 0.45, gridcell size 200	-11.58	1084
5	PSP thres. 0.45, gridcell size 300	-12.23	1448
6	PSP thres. 0.4, gridcell size 300 area	-12.07	1337
7	PSP thres. 0.4, gridcell size 300 breakpoint 3 amb.	-12.24	1131
8	PSP thres. 0.4, gridcell size 300 breakpoint 2 amb.	-12.21	1379
9	PSP thres. 0.4, gridcell size 200 Delaunay	-11.52	1125
10	PSP thres. 0.45, gridcell size 300 bowl	-10.51	1185

Table C.1: Internal and external precision investigated cases of track 108.

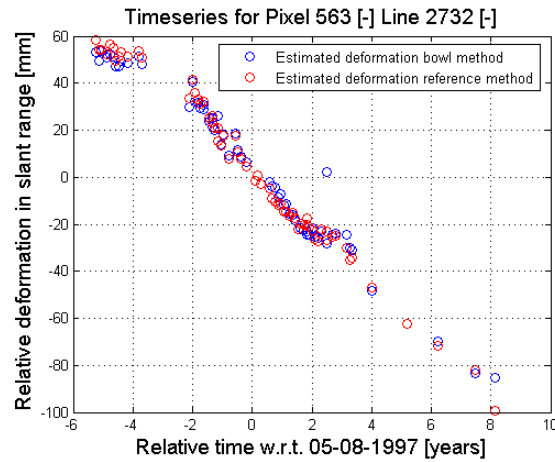


Figure C.3: The bowl method and conventional time series of one PS in the center of the subsidence bowl. Uncorrected unwrapping in the bowl method case resulted into a different annual velocity in the center of the subsidence bowl compared to the conventional method.

perfect spherical bowl in certain cases the estimation of a bowl is difficult or impossible with the implemented algorithm. Therefore the parameters of the bowl are set fixed and the precision is investigated for all cases based on these parameters. The parameters are derived from leveling results for epoch 60 and can be found in table C.2. A plot of the bowl is presented in figure C.4.

The external precision, $Q_{\hat{x}}$, compared to a reference case increased in most cases. Table C.3 presents the ratio between the investigated case and a reference case. Every covariance coefficient on the diagonal of the $Q_{\hat{x}}$ matrix is divided by the corresponding coefficient of the conventional $Q_{\hat{x}}$ matrix. The mean of these ratios is presented in the table. The cases in which the external precision did not increase are case 3, 7, 8 and 10. The precision decreased in the cases 3 and 7 due to decrease in number of PSs and no change in the distribution of PSs. The precision stayed equal in case 8 since the PSs deform approximate linear and therefore no extra PSs are expected to be identified. The precision decrease for case 10 can be explained by the obtained deformation velocities in the center of the bowl. The precisions found in this area deviate most from the conventional case. The mean of the velocities in the bowl method case is 3 mm smaller than the obtained mean velocities in the conventional case. Hence the center approximates the estimated bowl less than the conventional case, resulting into smaller precisions.

Whether the internal precision, $Q_{\hat{y}}$, increased or decreased can be found in table C.3. This

Parameter	Value
x_c	600 [pixels]
y_c	2950 [lines]
z_c	0.31 [mm]
$radius$	1012 [lines]
$depth$	-45 [mm]

Table C.2: Bowl parameters used for precision estimate of track 108.

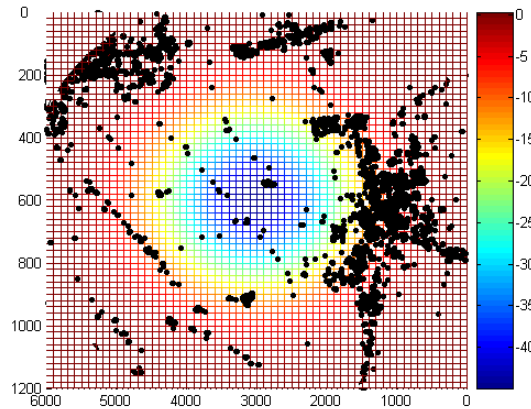


Figure C.4: Plot of the subsidence bowl composed with the parameters as found in table C.2 for track 108. The PSs identified by the bowl method are displayed in black.

is based on the diagonal values in the matrix. Explanation on research to the internal precision increase or decrease is given in chapter 5. Most cases experienced an increase. The cases that do not experience an increase are the same cases as for the external precision. The same reasons as for the external precision introduce this decrease.

The reliability of the model is described by the Overall Model Test. In table C.1 the OMT for the different cases scaled according to the number of PSs can be found. The difference between the reference case OMT and the OMT of the case of interest is presented in table C.3. A negative number indicates a more reliable fit of the model to the dataset. The differences in OMT for cases 2, 3, 4 are introduced due to the extra PSs in the south and the southwest of the subsidence bowl, as can be found in figure C.1. The bowl is not a perfect sphere and therefore extra PSs emphasizing this influence the OMT. Notice that although many incorrect PSs seem to be identified in the bowl method case and the velocity in the center of the bowl deviates from the bowl used for precision estimation, the OMT still increased. It can be concluded that the increase in density had a larger influence than the latter mentioned events.

C.2 Track 380

The figures C.5 and C.6 display the relative deformation results in mm/year for descending track 380 covering the Veendam test case. The velocities are based on data from the timespan starting in July 1992 and ending in December 2003. Figure C.5 contains the annual velocities of the PSs calculated with different PS thresholds or gridcell sizes. Also the annual velocities obtained with the manual PS identification method, in which pixels likely to be PSs are manually selected, and the velocities obtained with the implemented breakpoint model are included in this figure.

Case	Ref. Case	$Q_{\hat{x}}/Q_{\hat{x},ref}$	$Q_{\hat{y}}/Q_{\hat{y},ref}$	ΔOMT
2	1	0.87	precision increase	333
3	1	1.12	precision decrease	1234
4	1	0.63	precision increase	30
5	2	0.66	precision increase	60
6	2	0.80	precision increase	-51
7	2	2.67	precision decrease	-257
8	2	1.01	precision equal	-9
9	1	0.66	precision increase	-70
10	5	1.23	precision decrease	-302

Table C.3: Internal and external precision investigated cases of track 108.

Figure C.6 contains the annual velocities obtained with the deformation subtraction methods and the final subfigure in C.6 displays the combination of different cases discussed in this section.

The reaction of the conventional PS results to changing PSP thresholds or gridcell size is comparable between track 380 and 108. As can be seen in the figures C.5(a), C.5(b) and C.5(c) the gridcell size influences the identified PSs and a lower PSP threshold introduces a more densely distributed PS pattern. The density and distribution of PSs has been investigated by calculation of the distances between a PS and the center of the subsidence bowl. Comparison of these distances with a reference case, results into a decrease in the distribution, but an increase in density between case PSP threshold 0.4 gridcell size 300 versus PSP threshold 0.4 gridcell size 200. And for the case PSP threshold 0.45 gridcell size 300 versus PSP threshold 0.4 gridcell size 300 an increase in density and a more homogeneous distribution is the result.

Still the northern region of the subsiding area is poorly represented by PSs. When observing figure C.5(d) it can be seen that the northern regions in the manual PS identification case are also denser. The deformation pattern is comparable to the pattern of the conventional method, hence a correct densification is expected. Investigation of the distances to a central point indeed indicated an increase in density and distribution.

The last two subfigures show the annual velocities obtained with the breakpoint model. As expected the number of PSs identified in the subsidence area is smaller in figure C.5(e) compared to figure C.5(f). The difference between them is the amount of corresponding estimated ambiguities for an arc based on the three closest PSCs, see section C.1. The first case is the breakpoint model accepting PSPs when ambiguities of three out of three arcs between PSP and PSCs from the initial network fit the ambiguities instead of the ambiguities of two out of three arcs as in the second case. This latter subfigure resembles the conventional method with same gridcell size and PSP threshold. This is due to the time series of the points. The time series approach linear behavior and therefore no extra PSs are expected to be identified since they are already identified with the linear model. Investigation of the distances to a central point in the subsidence bowl indicated that several extra PSs were identified with the breakpoint model. But comparing the dataset to the original dataset of the conventional method, showed that the extra found PSs were removed in the conventional dataset due to the filter used.

Figure C.6 presents the annual velocities acquired with the deformation subtraction methods. These are the bilinear interpolation based on the PSCs and the Gaussian bowl estimation based on the final PSs or PSCs. Subfigure C.6(c) and C.6(d) represent the annual velocities acquired with the Gaussian bowl estimation based on the PSs respectively the PSCs. Notice that the annual velocities displayed in the figures are the velocities resulting from the PS analysis plus

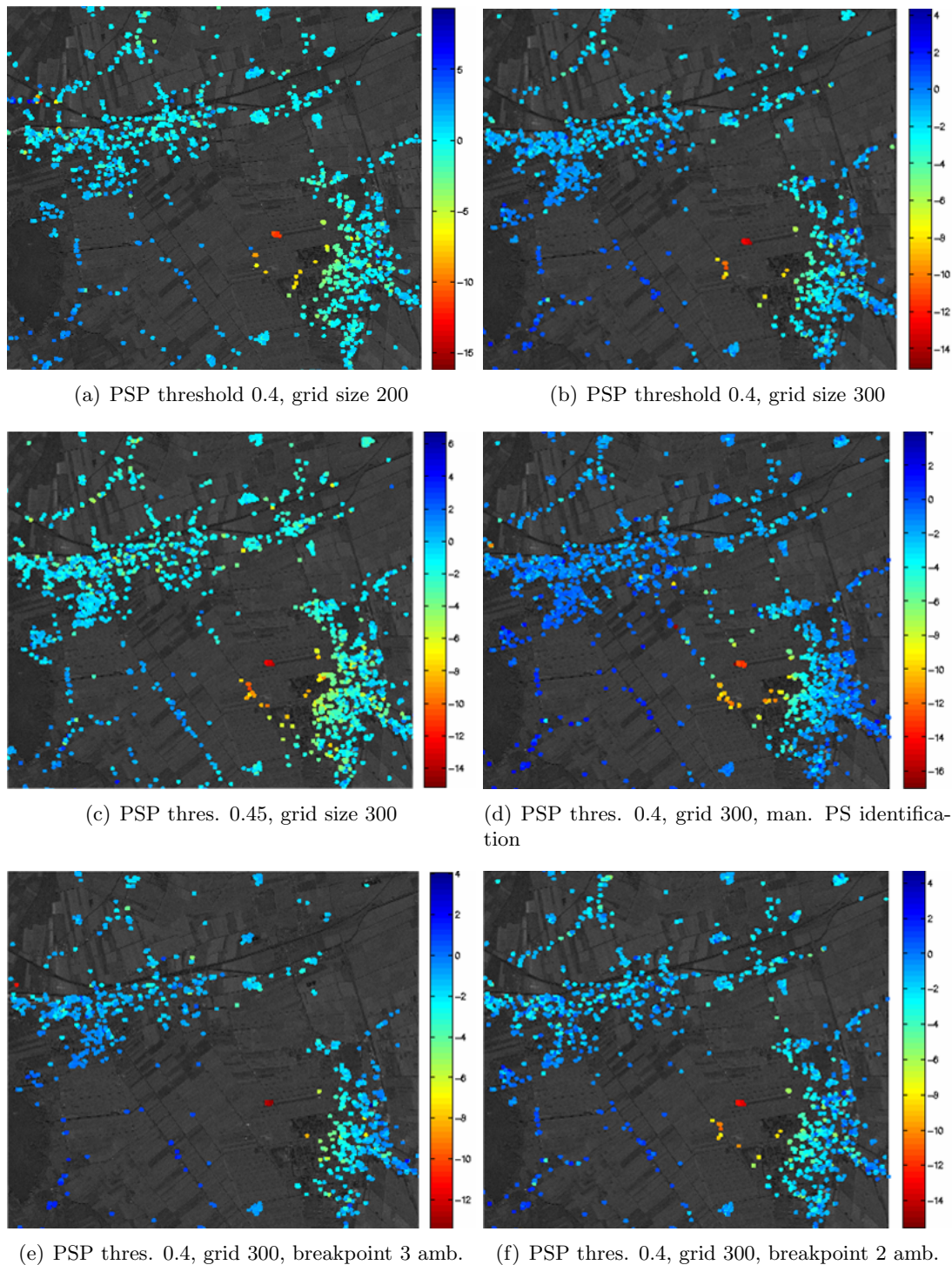


Figure C.5: Annual PS velocities [mm/year] track 380 covering the Veendam concession. The figures C.5(a) up and including figure C.5(c) display the annual velocities of the PSs identified with the conventional PS analysis, but changing PSP threshold and/or gridcell size. Subfigure C.5(d) is obtained making use of the manual PS identification method. The last two subfigures are results of the breakpoint model. Annual velocities are retrieved from a timespan starting in July 1992 until December 2003.

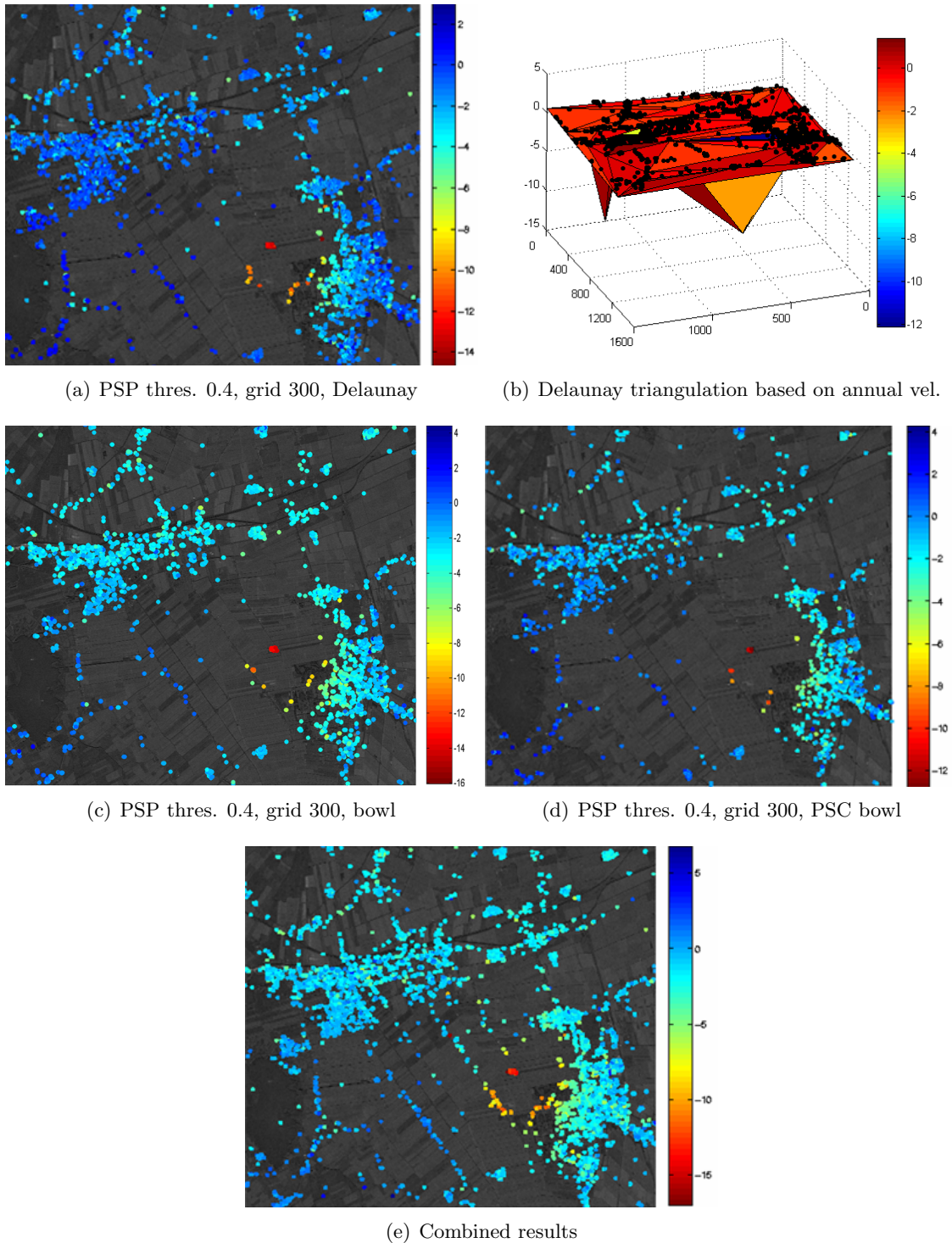


Figure C.6: Annual PS velocities [mm/year] track 380 covering the Veendam concession. The figures C.6(a) up and including C.6(d) present Delaunay or Gaussian bowl deformation subtraction results. Notice that the PS velocities presented in the figures are the calculated velocities added to the removed estimated velocities, obtained by a deformation estimation methods. Figure C.6(b) experiences a maximum subsidence of -12 mm/year. The bowl estimation in figure C.6(d) is based on the initial network instead of PSs. The last figure shows the combined results.

the subtracted velocities based on the deformation estimation method. In the Delaunay results the distribution of PSs is a bit denser in the southern area of the bowl, but also the variation of velocities is rather large, hence it is doubtful if the results present the reality. The overall deformation pattern is comparable to the conventional method though.

The PS distribution acquired with the bowl deformation based on the PSCs is less dense than in the conventional method with comparable gridcell size and PSP threshold. The difference between the Gaussian bowl estimation based on PSs or PSCs is significant, hence for this case the process can not be excellerated by basing the estimation on the PSCs instead of the PSs. When the PSs are used, the whole PS analysis has to be ran, when the PSCs are used the PS estimation step is left out, saving about 75% of the computation time. Investigation of the initial network showed that the PSC at the mining location is not present. Compiling a triangulation based on the rest of the PSCs does not represent the subsidence bowl, but triangulates an almost flat terrain. Due to this the variability of the phase most likely has increased or stayed equal instead of decreased. Therefore less PSs are identified in the subsiding area. Compared to the conventional case the Delaunay and bowl estimation method based on PSs introduced extra identified PS. The density and distribution has increased.

Over a timespan of 11 years the annual velocities of the subsidence bowl center, increase in density and distribution, and precision and reliability are investigated. In table C.4 the annual velocities of the center of the subsidence bowl are presented. The annual velocities of the different cases are rather comparable. The velocity can be assumed to be -13 mm/year, which is comparable to the velocity of the center found in the dataset of track 108 (see chapter 5). The velocities of three cases differ from the just mentioned velocity. These are the conventional case in which the PSP threshold is set to 0.4 and the gridcell size to 200, and the bowl estimation cases based on PSs or PSCs. The velocity of the first case deviates from the rest since a different reference coordinate is used. The behavior of this point is not comparable to the reference point selected for most of the cases and therefore the velocity can not be compared. The dataset of case 2 contained the PSs which is assigned as reference point in case 1. Hence the difference in velocity between the two different reference points in both cases is the deformation behavior found in the dataset of case 2. Adding this velocity results in a time series as shown in figure C.7(a), which is comparable to the time series of case 2. Notice that the chosen PS is a PS in the center of the subsidence bowl.

The bowl method also differs with the conventional case, despite the same reference coordinate. This is introduced by unwrapping differences. For the bowl method based on PSCs investigation showed that the first two epochs in case 2 are estimated different from the bowl case. This difference resulted into a larger subsidence rate for the reference case compared to the bowl method case based on PSCs. The same phenomena introduced a larger subsidence velocity for case 8, the bowl method based on PSs. The estimated deformation for the first epoch in this case is larger than in the reference case, resulting in a larger annual velocity. The time series of the bowl method based on PSs and the reference case are presented in figure C.7(b).

The density and distribution increased in all cases compared to the conventional case, except for the breakpoint model where three arcs are needed to accept a PSP and the bowl estimation case based on the PSCs. Also the distribution for case 2 did not become more homogeneous and the density and distribution in case 6 stayed equal compared to the reference case.

The density of the combined PS analysis results is larger compared to the combined results of track 108. This is mainly caused by the results of the manual PS identification method, which showed a large increase of the density of identified PSs.

Investigation of the external and internal precision resulted into a larger precision in most

Case N ⁰	Case	Velocity [mm/year]	OMT
1	PSP thres. 0.4, gridcell size 200	-11.74	724
2	PSP thres. 0.4, gridcell size 300	-13.21	564
3	PSP thres. 0.45, gridcell size 300	-13.28	1347
4	PSP thres. 0.4, gridcell size 300 area	-13.00	585
5	PSP thres. 0.4, gridcell size 300 breakpoint 3 amb.	-13.21	758
6	PSP thres. 0.4, gridcell size 300 breakpoint 2 amb.	-13.02	658
7	PSP thres. 0.4, gridcell size 300 Delaunay	-13.17	659
8	PSP thres. 0.4, gridcell size 300 bowl based on PSs	-13.84	619
9	PSP thres. 0.4, gridcell size 300 bowl based on PSCs	-12.40	519

Table C.4: Annual velocities [mm/year] obtained from the investigated cases of track 380.

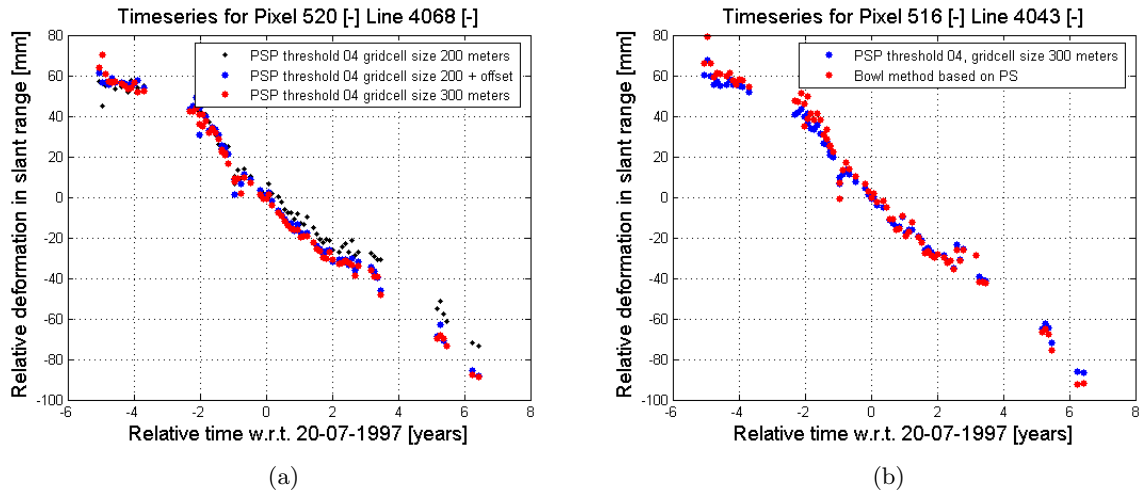


Figure C.7: Figure C.7(a) represents the time series of a PS in the center of the subsidence bowl in the cases 1 and 2. The difference in the reference coordinate introduces a difference in the time series. Addition of the found velocity in the dataset of case 2 for the PS with the same coordinates as the reference coordinate in case 1 to the time series of case 1, results into a comparable deformation. Figure C.7(a) shows the time series of the bowl method case based on PSs and the reference case. The difference in annual velocity is introduced by the difference in estimation of the first epoch and less by the last two.

cases. To investigate the precisions the assumption is made that for both test cases the deformation is bowl shaped. With the Gaussian bowl estimator, explained in chapter 4, bowl parameters are estimated for every case at one chosen epoch. With the use of the equations discussed in section 3.3.2, the internal and external precisions were obtained. The subsequent discussion is mainly based on the diagonals of the $Q_{\hat{x}}$ and $Q_{\hat{y}}$ matrices.

The external precision, $Q_{\hat{x}}$, compared to a reference case increased in most cases. Table C.5 presents the ratio between the investigated case and a reference case. Every covariance coefficient on the diagonal of the $Q_{\hat{x}}$ matrix is divided by the corresponding coefficient of the conventional $Q_{\hat{x}}$ matrix. The mean of these ratios is presented in the table. The cases in which the precision did not increase are case 5, the breakpoint model accepting PSs when the estimated ambiguities of the arc in three cases fit, and case 9, the bowl model based on PSCs. The precision decreased in both cases due to the decrease of PSs in the area of interest. The bowl model experienced a decrease in external precision due to the increase of the covariance coefficient describing the depth of the bowl. Notice that the external precision of case 6 also increased. This is not

Case	Ref. Case	$Q_{\hat{x}}/Q_{\hat{x},ref}$	$Q_{\hat{y}}/Q_{\hat{y},ref}$	ΔOMT
2	1	0.72	precision increase	-160
3	2	0.56	precision increase	783
4	2	0.48	precision increase	21
5	2	1.30	precision decrease	194
6	2	0.84	precision increase	94
7	2	0.45	precision increase	95
8	2	0.53	precision increase	55
9	2	1.04	precision decrease	-45

Table C.5: Internal and external precision investigated cases of track 380.

expected since most PSs experience an approximate linear deformation behavior over time, and therefore the breakpoint model can not identify many new PSs. Inspection of the datasets showed that the original datasets of both cases contain the same PSs and hence the difference in precision is introduced by the filtering performed. In this case it can be seen that filtering has a large influence on the final dataset when comparing this with a reference dataset. Therefore deriving conclusions has to be done with care.

Whether the internal precision, $Q_{\hat{y}}$, increased or decreased can be found in table C.5. This is based on the diagonal values in the matrix. Explanation on research to the internal precision increase or decrease is given in chapter 5. Most cases experienced an increase. The analysis indicated that the manual PS identification had the largest precision, which was approximate 50% less in the subsiding area than the conventional precision results. The precision, spatially approached, scaled in the manual PS identification case compared to the conventional case. But comparison of the deformation subtraction methods, results into different spatial variation as can be seen in figure ???. Observing the bilinear interpolation shows that the precision of the PSs in the south east of the bowl also increases, but the precision of the PSs in the west stays behind. Comparing the PSs identified in the manual PS identification case and the bilinear interpolation case, indicates in the bilinear interpolation case a dense distribution in the south. In the manual PS identification case the distribution of PSs in the west is leading. The estimation of the bowl parameters will be most influenced by these dense areas and therefore the radius of the estimated bowl is smaller for the manual PS identification method than in the bilinear interpolation case. Hence the density of PSs indirectly influences the precision in these cases. But nevertheless this way of calculating the precision is assumed to good enough to approach the problem because there is a clear relation between the number of PSs in the subsiding area and the precision.

The reliability of the model is described by the Overall Model Test. In table C.4 the OMT for the different cases scaled according to the number of PSs can be found. The difference between the reference case OMT and the OMT of the case of interest is presented in table C.5. A negative number indicates a more reliable fit of the PSs to the model. The difference of OMT did only decrease for cases 2 and 9. Since the bowl parameters are estimated for every case and not taken fixed as for track 108, the comparison between the OMT of a case of interest and a reference case is less comparable. In the manual PS identification case the density of PSs is larger, but since the subsidence bowl is not a symmetrical bowl as modeled by the Gaussian model, the residuals between the model and the dataset are larger then in the reference case, where less PSs emphasize the asymmetry of the bowl. Also small differences in PS density and distribution between most cases results in small OMT differences.

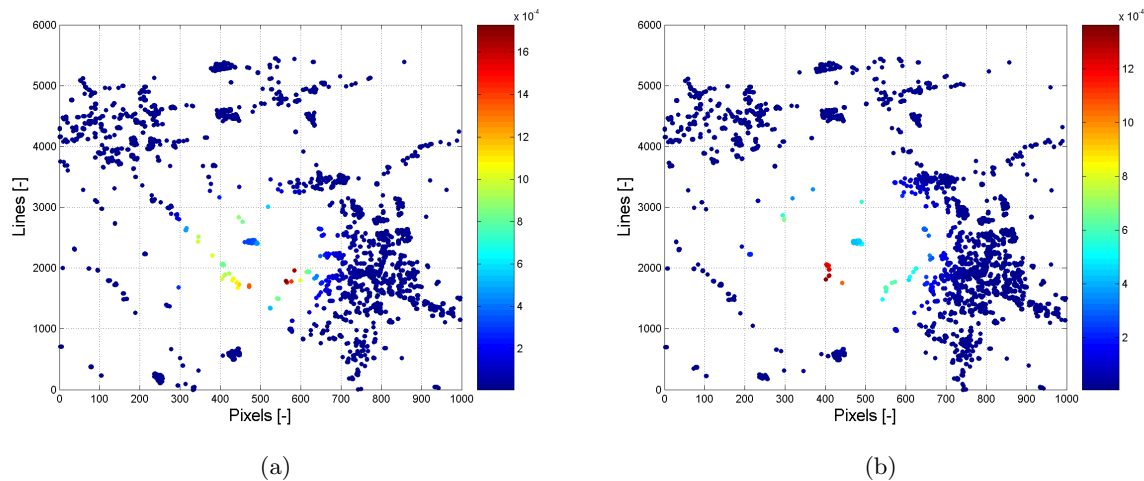


Figure C.8: Diagonal values of the $Q_{\hat{y}}$ matrix plotted in the manual PS identification case C.8(a) and bilinear interpolation case C.8(b). As can be seen the obtained precisions spatially variate between the two images. The radius of the bowl estimated in the manual PS identification case is smaller than estimated in the bilinear interpolation case. This is introduced by the PSs in the west of the subsidence bowl, which do not deform according to a spherical bowl. Since the density of these PSs is larger in the manual PS identification case, the estimated radius is smaller.

C.3 Track 487

The figures C.9 and C.11 display the relative deformation results in mm/year for track 487 covering the Veendam area. In contradiction to the tracks 108 and 380, this track is an ascending track. The velocities are based on data from the timespan starting in April 1993 and ending in September 2002. Figure C.9 contains the annual velocities of the PSs calculated with different PS thresholds or gridcell sizes. Also the annual velocities obtained with the implemented breakpoint model, and the velocities obtained with the Delaunay deformation selection method are included in this figure. Figure C.11 contains the annual velocities obtained with the Gaussian bowl estimation method and the manual PS identification method. The final subfigure displays the combination of different cases discussed in this section.

The number of images of the ascending tracks does not constraint the deformation in time as much as for a descending track, since less images are available taken over a same timespan. Due to this timespan between images, the chance a fitting deformation model is found is larger and thus the chance a PS is identified is larger. Since lowering the PSP threshold to 0.45 already results into more identified PSs, the number of errors will also increase. This is the reason why the only PSP threshold used is 0.4.

Difference between the identified PSs when changing the gridcell size is present as can be seen in the figures C.9(a) and C.9(b). Due to the number of images more errors are present in the identified PSs. As can be seen in both images, some results are doubtful. In the image C.9(a) the southern area of the subsidence bowl contains a large variation in annual velocity, hence it can be possible that errors are present in this area. The density and distribution of PSs has been investigated by calculation of the distances between a PS and the center of the subsidence bowl. Comparison of these distances between the two cases, results into a more homogeneous distribution and a larger density of PSs for the case with gridcell size of 300 meters compared to the case with gridcell size with 200 meters.

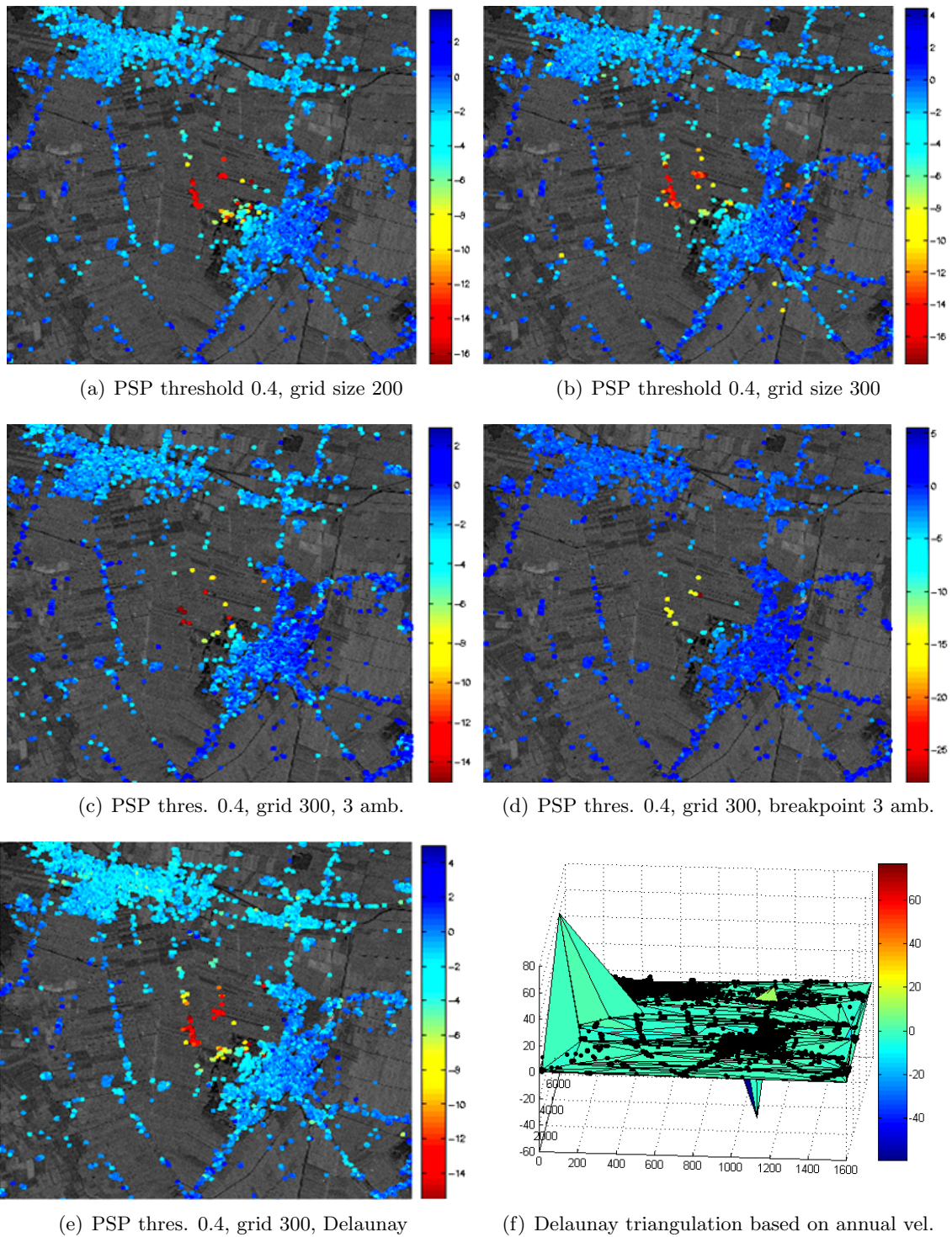


Figure C.9: Annual PS velocities [mm/year] track 487 covering the Veendam concession. The figures C.9(a) and C.9(b) display the annual velocities of the PSs identified with the conventional PS analysis, but changing the gridcell size. For figure C.9(c) the linear model is used, but three arcs have to possess similar ambiguities. The next subfigure is the result of the breakpoint model. And figure C.9(e) presents Delaunay deformation subtraction results. The annual velocities are retrieved from a timespan starting in April 1993 until September 2002.

A different method to eliminate the incorrect PSs, is the identification in the last step, the densification step performed on PSPs. The estimated ambiguity for an arc connecting a PSP and closest PSCs are tested with the ambiguities obtained for the same arcs based on two other closest PSCs composing the initial network. A more detailed explanation is given in section C.1. Using the criterion that three out of three arcs contain a similar ambiguity, results into a stricter demand, thus less PS are accepted. This method is used in plot C.9(c). As can be seen the density and distribution became less compared to the conventional method where two estimated ambiguities have to fit. This method did not bring the wanted results, since the density and distribution is a much poorer than the conventional method. Notice that in this case the linear model describing the deformation behavior is used and not the breakpoint model.

The results of the breakpoint model are less dense than for the conventional results. As expected the breakpoint model accepting PSPs when three arcs fit identifies less PSs than the method where PSPs with two of the three arcs fitting are accepted as in the conventional method. Investigation of the distances from PSs to a central point indicated a decrease in density and distribution of the PSs compared to the conventional method with same gridcell size and PSP threshold.

The subfigure C.9(e) presents the annual velocities obtained with the Delaunay estimation method. Based on the PSCs a triangulation is made estimating the deformation in the area. The deformation is subtracted and residual phase are used as input for the analysis. The objective is to reduce the variability resulting into more identified PSs. The figure presenting the results of the Delaunay and bowl method are the annual velocities acquired with the PS analysis plus the subtracted estimated deformation. Investigation of the distances from the PSs to a central point indicated, as expected, an increase in the density and distribution of PSs for the Delaunay method compared to the conventional method. The velocity of the center of the subsidence bowl corresponds to the conventional acquired velocity. In this case the density increase of PSs is not striking, this could have been introduced by the triangulation made. As can be seen in figure ?? two large deforming PSCs influenced the estimated triangulation. Compared to the other PSCs these PSCs do not represent the global deformation, hence filtering these PSs could result into more identified PSs for the bilinear interpolation case. The maximum subsidence of the PSC is -41 mm, hence unrealistic in this case. Notice also that no PSC in the initial network is present in the center of the subsidence bowl.

Figure C.11(a) shows the annual velocities plus the subtracted deformation signal obtained by the Gaussian bowl estimation. The density and distribution of the PSs did increase, and interesting to see is the difference in the north of the subsidence bowl. These PSs deform less over the time-span than in the Delaunay estimation results is presented, although the same locations seem to be identified. The difference in annual velocities is introduced due to unwrapping errors, especially present at the last epoch where the deformation is estimated 2 fringes smaller than in reality in the bowl method. The unwrapping errors are introduced by the subtracted deformation as can be seen in figure C.10. The difference in time between the last epoch and the previous is large, which resulted into sensitive temporal deformation behavior for unwrapping errors since a linear temporal deformation model is used. The subtracted deformation approaches the actual deformation and therefore small velocities are estimated for the epochs based on the residual phases. The deformation for the last epoch is therefore also estimated small. Thus because the subtracted deformation differed 2 fringes with reality, the estimated plus the subtracted deformation also differs 2 fringes.

The manual PS identification results in figure C.11(b) seem to contain many errors. The variability of the found deformation velocities is large, which is not expected in reality, hence these PSs are assumed to be errors. The distribution and density of PSs did not increase

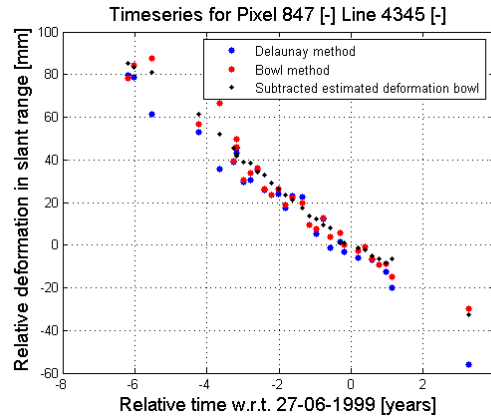


Figure C.10: Unwrapping errors introducing difference in the annual velocities between the bilinear interpolation method and the bowl method. The estimated deformation by the bowl method in combination with the linear functional model for the PS analysis, introduces unwrapping errors especially at the last epoch.

with the manual PS identification, but stayed approximate constant. This could also be due to the fact that most of the PSs identified by the manual PS identification method are also identified in the conventional case. The manual PS identification method tries to identify extra pixels experiencing an amplitude threshold below the set threshold. Hence when all possible PSs experience an amplitude dispersion below the threshold, there will be no difference in the identified PSs when using the manual PS identification method.

The last subfigure presents the combined results of the analysis. This result is rather noisy since many errors were present in the results due to the number of images. The cases with the same reference coordinate are combined. These are all case except for case 1, PSP threshold 0.4 and gridcell size 200, and case 6, the bowl estimation method.

Table C.6 presents the velocities of the center of the subsidence bowl obtained for the different cases based on SAR images available over a timespan of 9 years. As can be seen the velocities differ between cases. Cases 1 and 6 are based on a different reference coordinate compared to the other cases. Therefore the velocities of these points can not be compared to the other cases. As already discussed the velocity of the bowl method differs from the velocity of case 1, due to the unwrapping errors present in the time series of several PSs situated in the subsidence area. The difference in the velocities of the cases 3 and 4 can be explained by the PSs present in the center of the subsidence bowl. Several PSs are available in the center and they experience large velocities compared to the other cases, hence the average is higher than in the cases 2 and 7. In the Delaunay case corrected unwrapping errors introduce a higher velocity. For certain PSs unwrapping errors are eliminated for the last epoch. This results into a larger annual velocity. The annual velocity of the center of the subsidence bowl is assumed to be -14 mm/year. This is comparable with the other tracks 108 and 380 as explained in chapter 5.

The density and distribution increased in the deformation subtraction method cases compared to the conventional case. Explanations for the cases not experiencing an increase in density and distribution are given in the aforementioned text.

The density of the combined PS analysis results is comparable to the density of the combined results from track 380. This is mainly caused by the fact that this track is ascending and hence PSs are less constraint through time, due to less images available, and therefore the chance to identify a PS is larger. Hence implemented optimization methods had less influence.

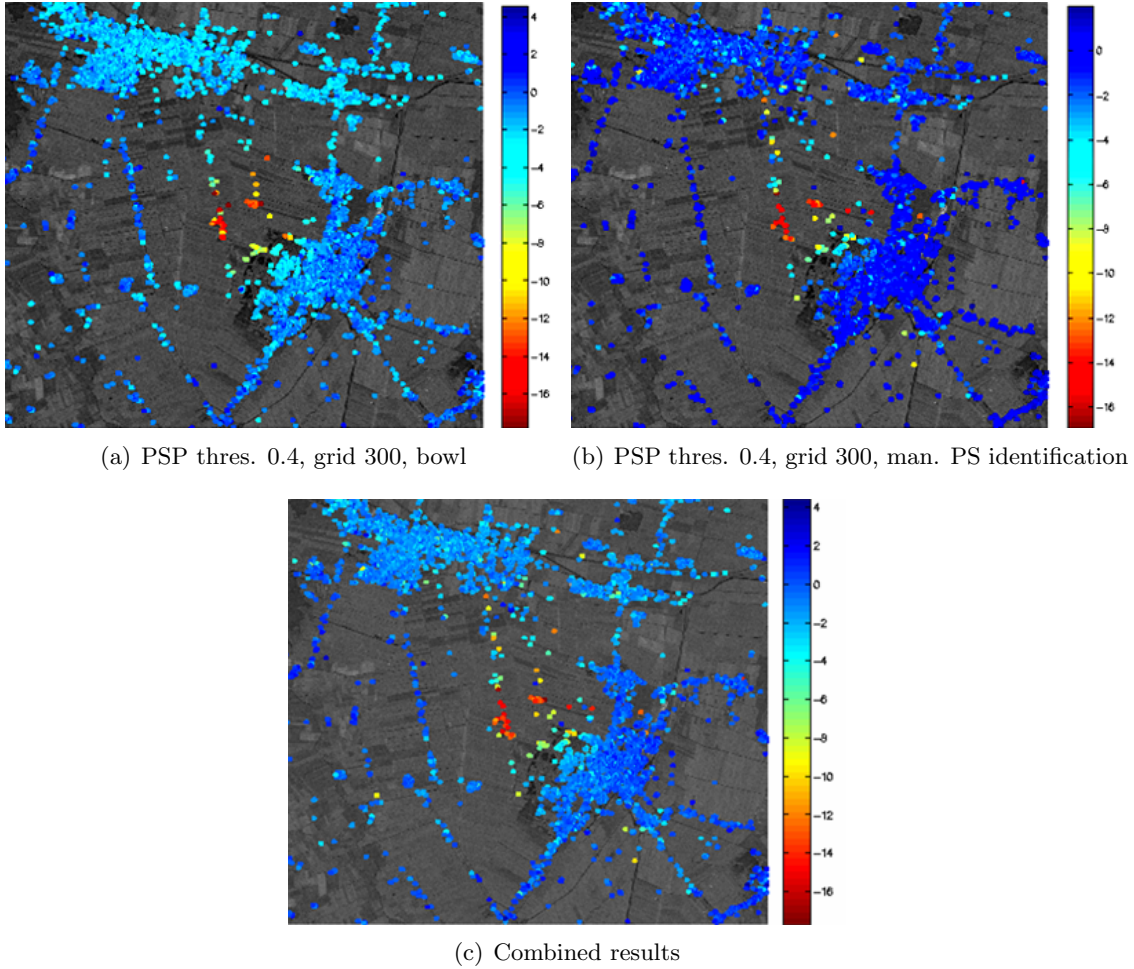


Figure C.11: Annual PS velocities [mm/year] track 487 covering the Veendam concession. Figure C.11(a) presents Gaussian bowl estimation deformation subtraction results. C.11(b) is obtained making use of the manual PS identification method and the final figure presents the annual velocities of combined datasets.

To investigate the precisions the assumption is made that for both test cases the deformation is bowl shaped. With the Gaussian bowl estimator, explained in chapter 4, bowl parameters are estimated for every case. With the use of the equations discussed in section 3.3.2, the external and internal precisions were obtained. The subsequent discussion is mainly based on the diagonals of the $Q_{\hat{x}}$ and $Q_{\hat{y}}$ matrices.

The external precision, $Q_{\hat{x}}$, compared to a reference case increased in half of all cases. Table C.7 presents the ratio between the investigated case and a reference case. Every covariance coefficient on the diagonal of the $Q_{\hat{x}}$ matrix is divided by the corresponding coefficient of the conventional $Q_{\hat{x}}$ matrix. The mean of these ratios is presented in the table. Cases 3 and 4 do not experience an increase compared to the reference case. This is introduced due to the number of PSs identified in these cases. The manual PS identification experiences a decrease since the same number of PSs are identified, but more incorrect PSs are present in the dataset. This influences the precision.

Whether the internal precision, $Q_{\hat{y}}$, increased or decreased can be found in the same table C.7. This is based on the diagonal values in the matrix. Explanation on research to the internal

Case N ⁰	Case	Velocity [mm/year]	OMT
1	PSP thres. 0.4, gridcell size 200	-14.95	695
2	PSP thres. 0.4, gridcell size 300	-13.10	777
3	PSP thres. 0.4, gridcell size 300 3 amb.	-13.82	727
4	PSP thres. 0.4, gridcell size 300 breakpoint 3 amb.	-14.08	711
5	PSP thres. 0.4, gridcell size 300 Delaunay	-14.00	825
6	PSP thres. 0.4, gridcell size 300 bowl	-12.97	742
7	PSP thres. 0.4, gridcell size 300 manual PS	-13.07	842

Table C.6: Annual velocities [mm/year] obtained from the investigated cases of track 487.

precision increase or decrease is given in chapter 5. Increase of the internal precision is present for the same cases as the internal precision. The cases in which the precision increased are case 2, the case with a larger gridcell size, and deformation method cases 5 and 6. The precision decreased in cases 3 and 4 due to the decrease of PSs in the area of interest. Also in the manual PS identification method, case 7, errors are most likely to be present in the PSs, also influencing the bowl estimation and therefore the precision. The bowl parameters estimated for the best fitting bowls are comparable and therefore the precision spatially investigated follows the same pattern in all cases.

Case	Ref. Case	$Q_{\hat{x}}/Q_{\hat{x},ref}$	$Q_{\hat{y}}/Q_{\hat{y},ref}$	Δ OMT
2	1	0.77	precision increased	82
3	2	4.37	precision decreased	-50
4	2	2.57	precision decreased	-66
5	2	0.81	precision increased	47
6	2	0.76	precision increased	-36
7	2	1.12	precision decreased	64

Table C.7: Internal and external precision investigated cases of track 487.

The reliability of the model is described by the Overall Model Test. In table C.6 the OMT scaled to the number of PSs for the different cases can be found. The difference between the reference case OMT and the OMT of the case of interest is presented in table C.7. A negative number indicates a more reliable fit of the PSs to the model. Since the bowl parameters are estimated for every case and not taken fixed as for track 108, the comparison between the OMT of a case of interest and a reference case is less comparable. The differences between the OMT of a case of interest and the reference case are small. Mostly likely the OMT differences between the cases are small instead of presenting a significant decrease due to the asymmetric subsidence bowl present, which influences the bowl parameters estimated, and non-filtered errors.

C.4 Track 151

The figures C.12, C.13 and C.14 display the relative deformation results in mm/year for descending track 151 covering the Barradeel concession. The velocities are based on data from the timespan starting in May 1992 and ending in May 2005. Most results of this track have been discussed in chapter 5. Figure C.12 contains the annual velocities of the PSs calculated with different PS thresholds or gridcell sizes. Also the annual velocities obtained with the manual PS identification method are included in this figure. Figure C.13 contains the annual velocities obtained with the use of the breakpoint model and the bilinear interpolation method. The last figure C.14 displays the annual velocities obtained with the Gaussian bowl estimation method

and the combination of different cases discussed in this section.

Figure C.12 displays the conventional annual velocities for track 151 with changing PSP threshold or gridcell size. The changing PSP threshold causes the same effect as for the other discussed tracks. Due to the lower threshold, more PSs are identified, but also more errors, hence filtering is necessary. The gridcell size causes a different effect. In the Veendam tracks an increase in density and distribution of the PSs is present with a larger gridcell size. The initial network of track 151 with gridcell size of 300 meters contains a PS in the subsiding area and the initial network with gridcell size of 200 does not contain this PS. Therefore we would expect a denser PS distribution for the gridcell size 300 meter case, but this is not the result. Investigation showed that this PS experiences an unwrapping error, which could explain the low density of PSs compared to the gridcell size of 200 meter case. This introduces an opposite effect, as seen for the Veendam track, for increasing gridcell size. Now the density and distribution decreases instead of increases.

As discussed in chapter 5 unwrapping errors are present in these cases, since a linear deformation model is assumed, but the actual deformation is non-linear. Before 1997 no mining activities were present in the Barradeel area. To compile new time series free from unwrapping errors, the image set is split into two sets. One set with images before 1997, before mining started, and one set with data after 1996. The annual velocities of the indicated PSs are presented in the figures C.12(d) and C.12(e). As can be seen in both plots the density and distribution increased. And, as expected, the deformation is close to zero in the image treating data until 1997.

The final subfigure treats the annual velocities identified with the manual PS identification method. This method resulted into many PSs, and therefore also many errors. After filtering the most likely errors, the PS set resulted as seen in figure C.12(f). Investigation of the distance from the PSs to a central point showed an increase in PS density and a more spread out distribution, compared to the conventional method. Although when comparing the annual velocities in the plot, a large variance is present. Since the density is large compared to the other cases it is not clear whether the indicated annual velocities are correct, or if many errors are still present.

The subfigures C.13(a) and C.13(b) present the annual velocities of the PS analysis with implemented breakpoint model. The first case presents the annual velocities of the breakpoint model accepting PSPs in the densification step when the ambiguities of an arc between PSPs and closest PSCs obtained in three different cases, see section C.1, are similar. And the second case handles the breakpoint model when two arcs possess the same ambiguity. As expected the density of PSs decreased in the first case. Investigation in the second case of the distances from the PSs to a point in the center, compared to the distances of a reference case, showed that the density did not change, but the distribution did become more spread out compared to the conventional case.

The annual velocities of the bilinear interpolation method are presented in the figures C.13(c) and C.13(e). Notice that the annual velocities displayed in the figures are the velocities resulting from the PS analysis plus the subtracted velocities based on the deformation estimation method. The first image treats the bilinear interpolation method based on PSP threshold 0.4 and gridcell size 200. Since no PS is present in the initial network in the subsiding area, the phase is not corrected for the subsidence bowl. Subtraction of the triangulated deformation increased the variability of the phase, and PSs in the subsidence area are not recognized as such. When the PSP threshold 0.45 and gridcell size of 300 is chosen, a PS in the subsidence area is present in the initial network. Investigation showed that the density and distribution of PSs increased compared to the conventional case.

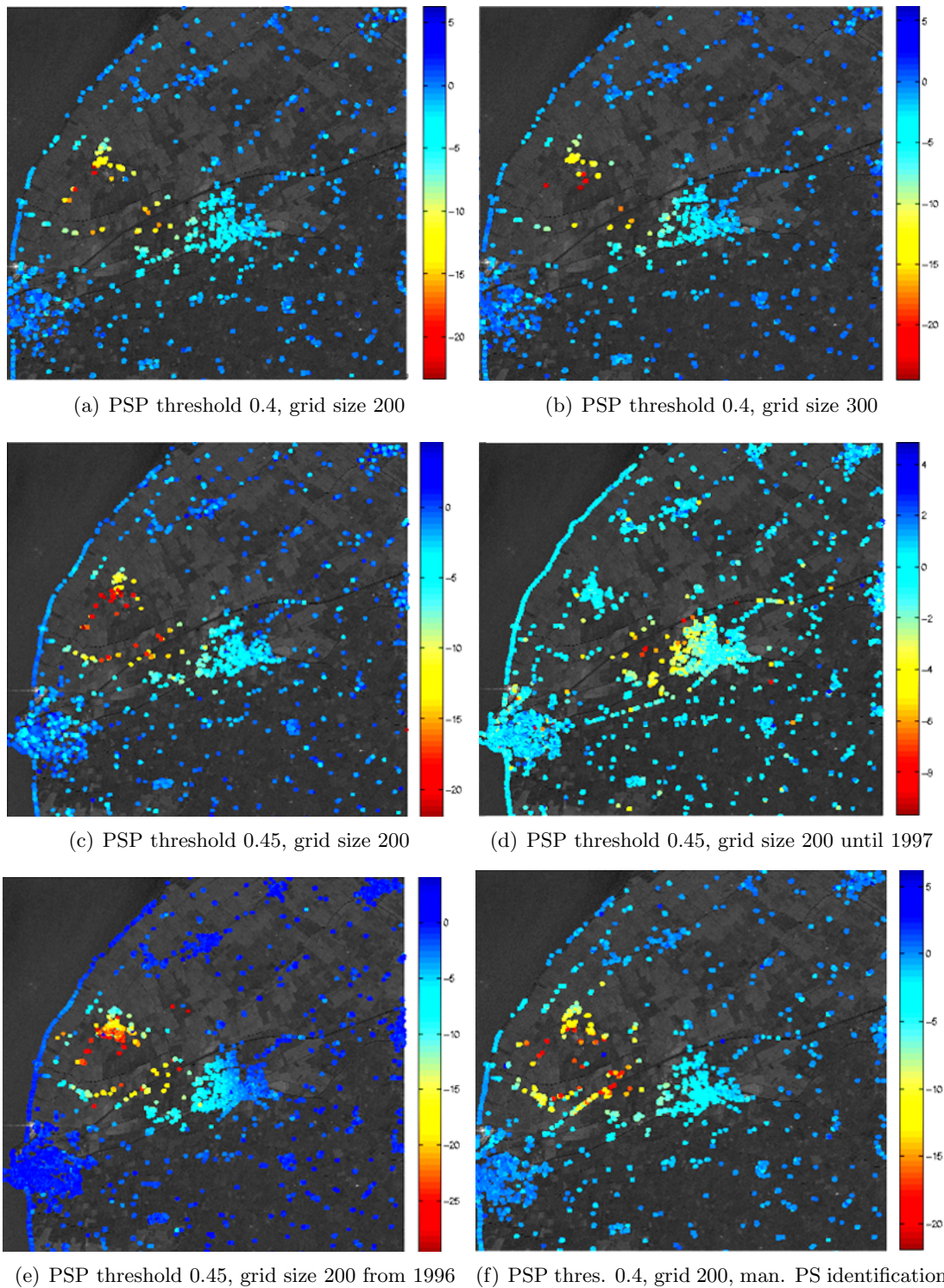


Figure C.12: Annual PS velocities [mm/year] track 151 covering the Barradeel concession. The figures C.12(a) up and including C.12(c) display annual velocities of the PSs identified with the conventional PS analysis, but changing PSP threshold and/or gridcell size. In figure C.12(d) results are presented based on data until 1997 and figure C.12(e) presents the results of the data from 1996 until 2005. The last figure is obtained making use of the manual PS identification method. The annual velocities are retrieved from a timespan from May 1992 until May 2005.

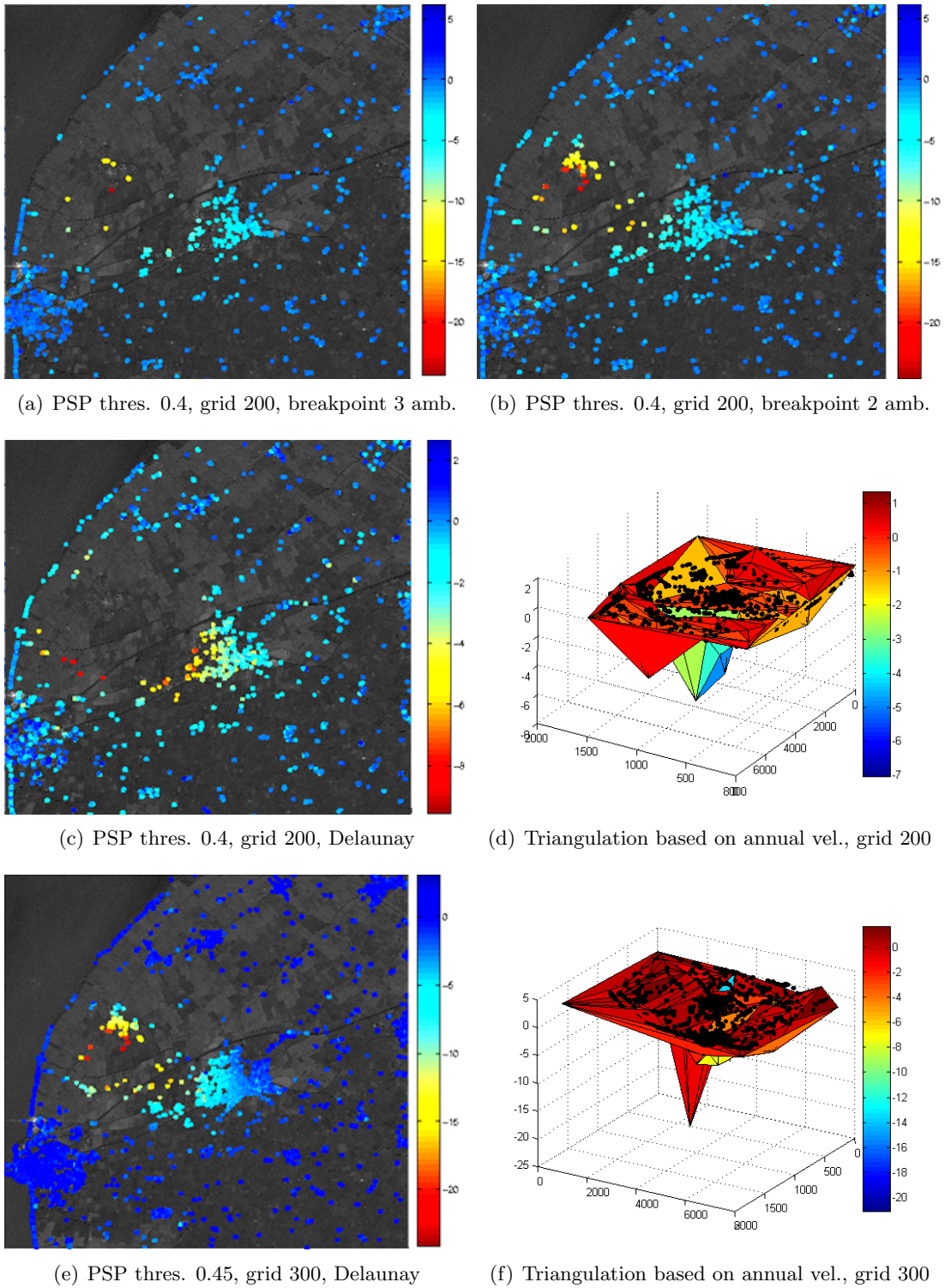


Figure C.13: Annual PS velocities [mm/year] track 151 covering the Barradeel concession. The subfigures C.13(a) and C.13(b) are results of the breakpoint model. The subfigures C.13(c) up to and including C.13(f) present Delaunay deformation subtraction results, but with different PSP threshold and gridcell size. The maximum velocity in triangulation C.13(d) is -7 mm and the maximum velocity in triangulation C.13(f) is -21 mm.

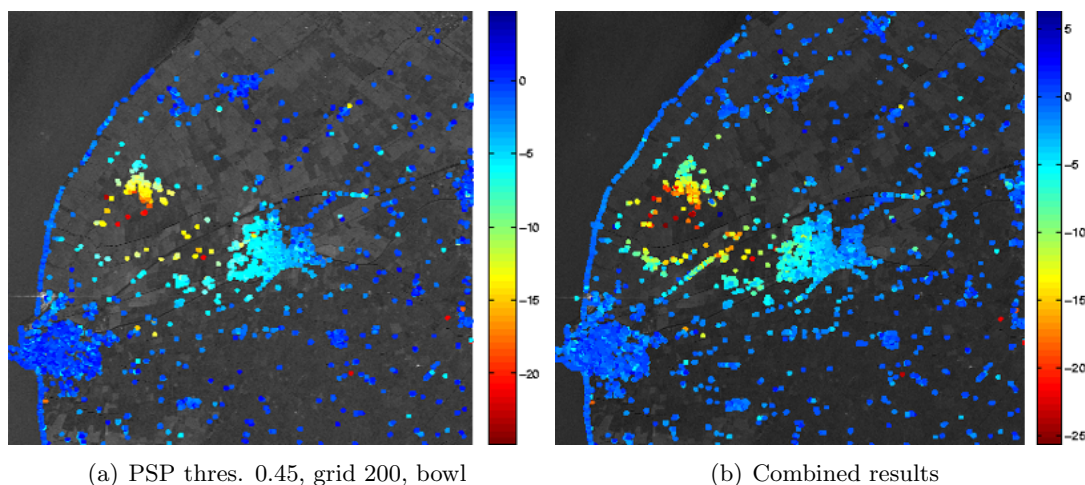


Figure C.14: Annual PS velocities [mm/year] track 151 covering the Barradeel concession. Figure C.14(a) presents Gaussian bowl estimation deformation subtraction results. The figure C.14(b) presents the combined results of the different cases discussed.

The bowl estimation method is presented in figure C.14(a). Since two subsidence bowls, due to gas and salt, are present in this area, the estimated bowl parameters did not represent the Barradeel subsidence bowl and therefore did not result into a better distribution and density of PSs. The usage of a-priori parameters based on leveling data resulted into the annual velocities as presented in the figure. As can be seen, and as has been investigated by the distances between PSs and a point in the center of the bowl, the density and distribution increased. Also now a PS in the center of the subsidence bowl is indicated. This is the only case in which a PS in the center is present.

The subfigure C.14(b) contains the combination of results of the different cases discussed in this section. The cases with corresponding reference coordinates are combined. The only case which has a different reference coordinate is the second delaunay case, but the reference coordinate is situated in a non-deforming area and therefore can be combined with the other cases, since the reference coordinate of these cases is also situated in non-deforming area.

The annual velocities of the subsidence bowl center are difficult to observe since only in the bowl estimation case a PS is present in the center of the subsidence bowl. Therefore a small area west of the center of the subsidence bowl is chosen for which the mean annual velocities are obtained. This resulted in the velocities over a timespan of 13 years as presented in table C.8. The velocity of case 5 can not be measured, since no PSs in the area of interest are available. The annual velocities of two cases differing from the other cases are present. These are case 2, in which the PSP threshold is set to 0.4 and the gridcell size is 300 meters, and case 8, the bowl case. Case 2 experiences higher velocities than the other cases. A PS experiencing an unwrapping error seems to subside faster than actual, since the unwrapping errors show deformation at the period before mining started. Investigation of the PSs present in this area showed an unwrapping error of 4 fringes until 1996, where in the other cases this unwrapping error is 2 fringes. This difference in error causes the difference in velocity as presented by figure C.15(a).

In the bowl case the density of PSs is larger and consists out of two groups. One group deforming as the other cases and one group deforming with -16 mm/year. Hence the mean results into a number in between the group velocities. The difference in subsidence velocity is caused by the unwrapping errors after 2000. For the group subsiding -16 mm/year the data experiences an unwrapping error of at least 2 fringes, and therefore seems to subside slower than

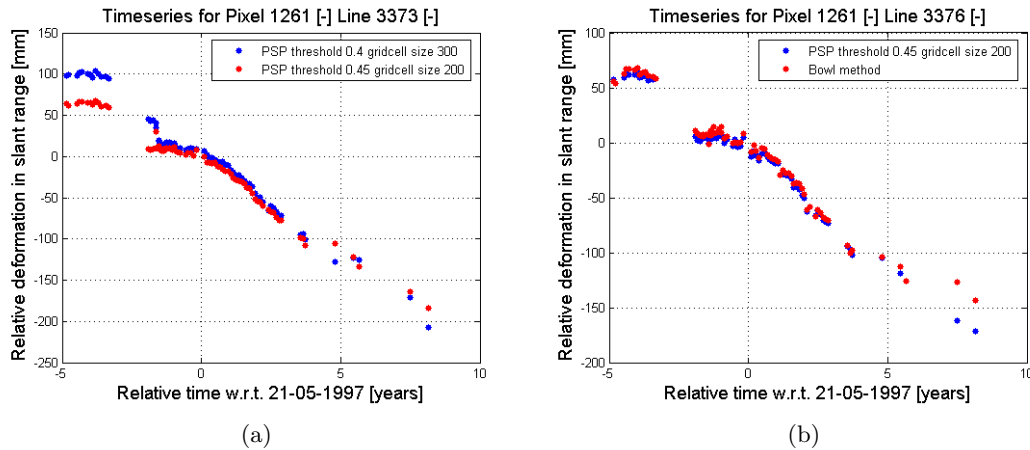


Figure C.15:

in reality, see figure C.15(b). Interesting to see is that in the bowl method the same PSs are identified as for case 3, but only one of the eight PSs experiences an unwrapping error at the last two epochs. The other identified PSs by the bowl method do experience the unwrapping errors at the last epochs. The unwrapping errors are introduced by the estimated parameters. The range of the bowl was estimated to small, resulting into a smaller subsidence away from the center of the bowl.

Case N ⁰	Case	Velocity [mm/year]	OMT
1	PSP thres. 0.4, gridcell size 200	-18.83	3635
2	PSP thres. 0.4, gridcell size 300	-23.71	2960
3	PSP thres. 0.45, gridcell size 200	-18.83	3201
4	PSP thres. 0.4, gridcell size 200 manual PS	-19.92	4287
5	PSP thres. 0.4, gridcell size 200 breakpoint 3 amb.	–	2009
6	PSP thres. 0.4, gridcell size 200 breakpoint 2 amb.	-20.15	2850
7	PSP thres. 0.45, gridcell size 300 Delaunay	-19.94	3560
8	PSP thres. 0.45, gridcell size 200 bowl	-17.81	4210

Table C.8: Annual velocities [mm/year] obtained from the investigated cases of track 151.

The density and distribution increased in all cases compared to the conventional case, except for the breakpoint model where three arcs are needed to accept a PSP and case 2, where the PSP threshold is set to 0.4 and the gridcell size to 300. Explanations for this are given in the aforementioned text. Also the bilinear interpolation method results based on a gridcell size of 200 meters introduced a decrease due to a decrease in the density of the identified PSs in the subsidence area.

To investigate the precisions the assumption is made that for both test cases the deformation is bowl shaped. With the Gaussian bowl estimator, explained in chapter 4, bowl parameters based on the annual velocities are estimated for every case. With the use of the equations discussed in section 3.3.2, the external and internal precisions were obtained. The subsequent discussion is mainly based on the diagonals of the $Q_{\hat{x}}$ and $Q_{\hat{y}}$ matrices. In the Barradeel case two subsidence bowls are present. These are due to gas subtraction and salt mining. This presence of two bowl makes bowl estimation difficult, impossible or unreliable. Therefore bowl parameters based on leveling results are used, and the internal and external precision are calculated based on these

parameters, hence no estimation of the parameters is performed. The parameters used are found in table C.9 and a plot of this bowl is presented in figure C.16.

Parameter	Value
x_c	1216 [pixels]
y_c	3562 [lines]
z_c	0 [mm]
$radius$	550 [lines]
$depth$	-104 [mm]

Table C.9: Bowl parameters used for precision estimate of track 151.

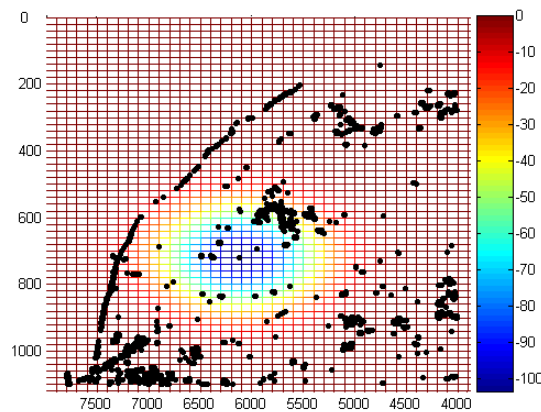


Figure C.16: Plot of the subsidence bowl composed with the parameters as found in table C.9 for track 151. The PSs identified by the bowl method are displayed in black.

Table C.10 presents the ratio between the investigated case and a reference case. Every covariance coefficient on the diagonal of the $Q_{\hat{x}}$ matrix is divided by the corresponding coefficient of the conventional $Q_{\hat{x}}$ matrix. The mean of these ratios is presented in the table. The external precision, $Q_{\hat{x}}$, compared to a reference case increased in most cases. The case in which the precision did not increase is case 2, the PSP threshold set to 0.4 and gridcell size to 300. This decrease of precision is due to the density and distribution of PSs, as discussed in this section. Notice that the breakpoint model with PS acceptance when the ambiguities of three of the three arcs are similar and the bilinear interpolation based on the gridcell size 200 are not present in the table. These are not taken into account since the density became low in the area of interest.

Whether the internal precision, $Q_{\hat{y}}$, increased or decreased can be found in table C.10. This is based on the diagonal values in the matrix. Explanation on research to the internal precision increase or decrease is given in chapter 5. The decrease for case 2 is introduced due to the number of PSs available. The bowl method experienced the best precision which is 67% more precise than the reference case 3.

The reliability of the model is described by the Overall Model Test. In table C.8 the OMT for the different cases scaled according to the number of PSs can be found. The difference between the reference case OMT and the OMT of interest is presented in table C.10. A negative number indicates a more reliable fit of the PSs to the model. The increase in ΔOMT for case 4, 7 is caused by the larger variance in the annual velocities and the fact that the gas subtraction bowl is not modeled. These PSs do not fit the bowl properly and thus the ΔOMT is larger than in

Case	Ref. Case	$Q_{\hat{x}}/Q_{\hat{x},ref}$	$Q_{\hat{y}}/Q_{\hat{y},ref}$	ΔOMT
2	1	1.27	precision decrease	-675
3	1	0.85	precision increase	-433
4	1	0.51	precision increase	652
5	1	0.76	precision increase	-787
6	1	5.92	precision decrease	-951
7	3	0.61	precision increase	363
8	3	0.41	precision increase	1004

Table C.10: Internal and external precision investigated cases of track 151.

the reference case. Thus when more PSs are present in this area, this will also influence the ΔOMT . Case 8 experiences a large OMT due to the larger number of PSs in the center of the bowl. Most PS time series obtain unwrapping errors, resulting into a different velocity than in reality. The model to which the bowl dataset is tested is based on reality, so the total error between the model and deformation found for all PSs in the bowl case is larger compared to the other cases, since more PSs are present with unwrapping errors than in the conventional case.

C.5 Track 258

The figures C.17 and C.18 display the relative deformation results in mm/year for ascending track 258 covering the Barradeel concession. The velocities are based on data from the timespan starting in March 1993 and ending in February 2000. Figure C.17 contains the annual velocities of the PSs calculated with different PS thresholds or gridcell sizes. The annual velocities obtained with the use of the manual PS identification method can be found in figure C.17(f). In figure C.18 the annual velocities of the breakpoint model and the annual velocities obtained with the deformation subtraction methods can be found. The last subfigure contains the annual velocities of the combined datasets.

Figure C.17 displays the annual velocities of different conventional methods. The figures C.17(a) up and including C.17(d) display the annual velocities of the identified PSs when different gridcell sizes and/or PSP thresholds are chosen. The density and distribution of PSs has been investigated by calculation of the distances between a PS and the center of the subsidence bowl. Investigation of the results indicated a similar density and distribution for the cases with PSP threshold 0.4 and varying gridcell size. This could be due to the initial network in both cases. The PSCs composing these networks are quite similar in the area of interest, hence no larger differences are present in the final PS results. A more spread out distribution for the case where the PSP threshold is set to 0.45 and the gridcell size to 300 meters compared to the case where the PSP threshold is set to 0.4 and the gridcell size to 300 meters is found. In the PSP threshold 0.45 and gridcell size 200 case the density increased, but distribution stayed equal to the PSP threshold 0.4 and gridcell size 200 case. Notice that these increases can be introduced by filtering, since the density and distribution of the PSs are almost identical in all cases. None of the cases experience PSs close to the center of the subsidence bowl. In the initial network no PS in the subsidence area are selected. This could introduce the absence of PSs in this area. Based on track 151 it is known that PSs are present in the subsidence bowl. It could be that these PSs are not measurable from ascending tracks. But it could also be the case that SAR images are present in the interferogram stack which pollute the phase stability of a PS over time. Striking to see is the subsidence due to gas subtraction by Vermilion Energy near Franeker. The deformation pattern in this area is more obvious than in the results of track 151.

Frisia started mining in 1996, this introduces a deformation model over time for the PSs in the subsidence bowl according to the implemented breakpoint model. The deformation of the PSs, starting from 1996, can be assumed linear, see section 5.7. Thus when the images after 1996 are investigated the linear method implemented in the conventional method should be able to fit the deformation pattern of the PSs in the subsidence bowl. Figure C.17(e) presents the annual velocities of the conventional PS analysis performed on a dataset containing image of 1996 until 2000. This did not increase the number of PSs identified near the center of the subsidence bowl.

The last subfigure presents the annual velocities acquired with the manual PS identification method. As can be seen a large variability of the annual velocities is present in the subsiding area. Filtering has been performed by thresholding on the annual velocities and the height of the PSs. Spatial filtering can not be applied because the spatial variability of the velocities of PSs is large and therefore no PS will be eliminated.

Figure C.18(a) contains the results of the breakpoint model method. This model accepts a PS when the estimated ambiguity between a PSP and the closest PSCs in three calculation cases is equal. This method uses stricter demands than the conventional method and thus a decrease in the PS density is expected. This expectancy meets the results.

Annual velocities resulting from the PS analysis making use of the bowl estimation method are displayed in figure C.18(b). This bowl is calculated with parameters based on leveling results. The density decreased, but the distribution in the subsidence center became more spread out. Uncorrect estimated bowl parameters could be a reason of these minor changes in identified PSs, but again also the pollution of the image stack by SAR images could be a reason. Notice that the annual velocities displayed in the figures are the velocities resulting from the PS analysis plus the subtracted velocities based on the deformation estimation method. The same holds for the bilinear interpolation method.

The bilinear interpolation method results are presented in figure C.18(c). Investigation showed an more spread out distribution of the PSs in the area of interest. But the variance of the velocities appears unrealistic in the north of Sexbierum and in the south of the subsidence bowl. Therefore it is doubtful whether all the identified PSs are realistic. The density approximated the density of the reference case. Notice that the triangulation made includes unrealistic deformation velocities, hence this could have had a negative influence on the bilinear interpolation method results, and also on the final PS results in general.

The last subfigure C.18(e) shows the results of the combined datasets. The PSs identified by manual PS identification are not included in this figure since the variance in annual velocities is high and therefore it is doubtful whether the results are correct. Three different reference coordinates were used to obtain the estimated in the different cases. Two experienced the same deformation and therefore can be compared. Therefore all datasets based on these two reference coordinates could be combined.

The annual velocities of the subsidence bowl center are difficult to observe since no PSs are present in the center of the subsidence bowl for all cases. Therefore PSs covering a selected area in the north of the center are used as comparison between the tracks. This resulted into the annual velocities presented in table C.11. The velocity of case 4, where the PSP threshold is set to 0.45 and the gridcell size is 300 meters does not resemble the other velocities. This difference is introduced by unwrapping differences between this case and others. These unwrapping differences are introduced by a different reference coordinate.

Plotting the time series of the PSs in track 258 against the time series of the nearest PSs in track 151 resulted into comparable results. The reference coordinates for both tracks are chosen in non-deforming area and hence only the temporal baseline of track 151 had to be shifted to the

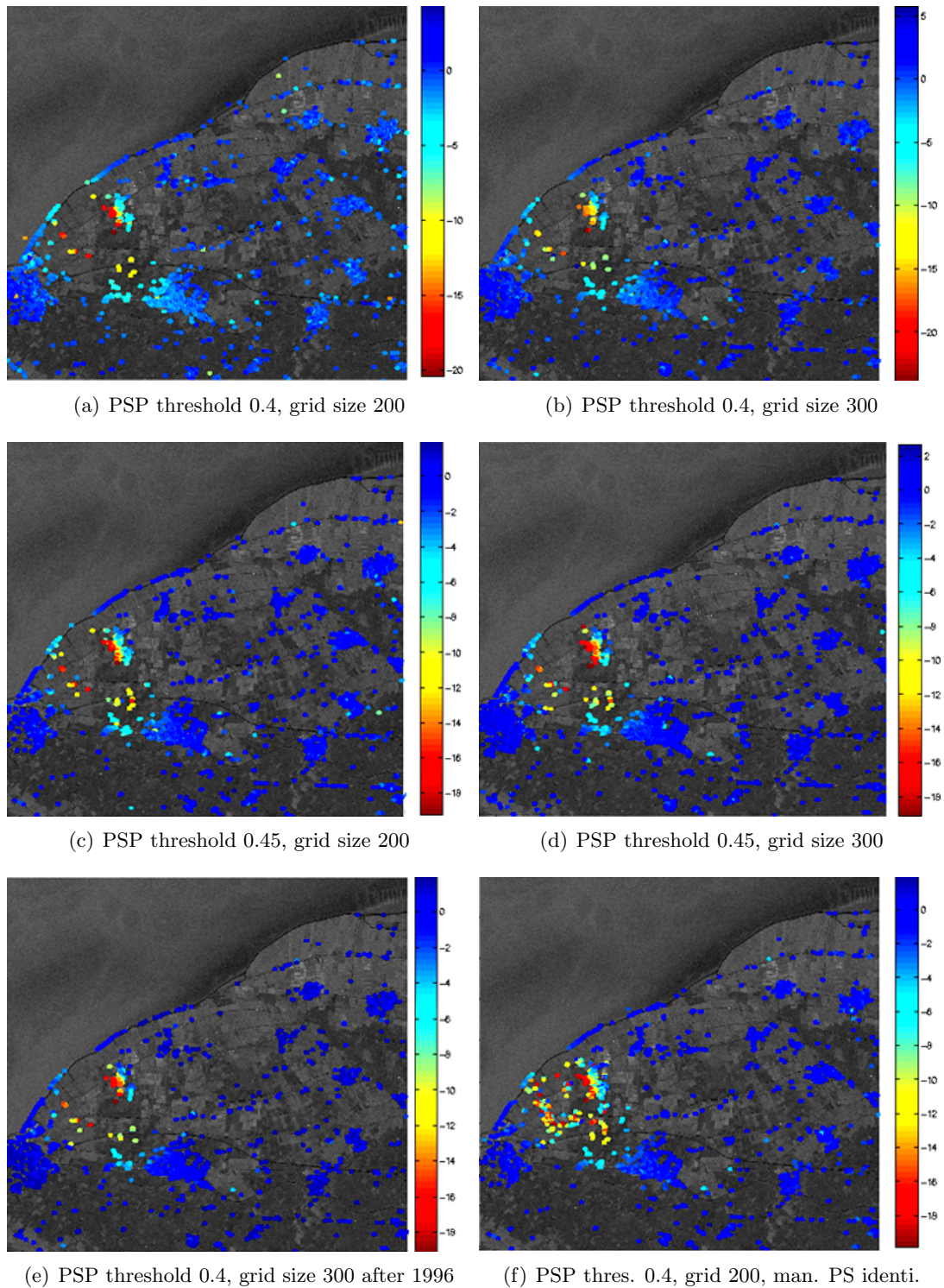


Figure C.17: Annual PS velocities [mm/year] track 258 covering the Barradeel concession. The figures C.17(a) up and including figure C.17(d) display the annual velocities of the PSs identified with the conventional PS analysis, but changing PSP threshold and/or gridcell size. In figure C.17(e) the results obtained by the PS analysis based on the data from 1996 until 2000 are presented. The last subfigure presents manual PS identification results. The annual velocities are retrieved from a timespan starting in March 1993 until February 2000.

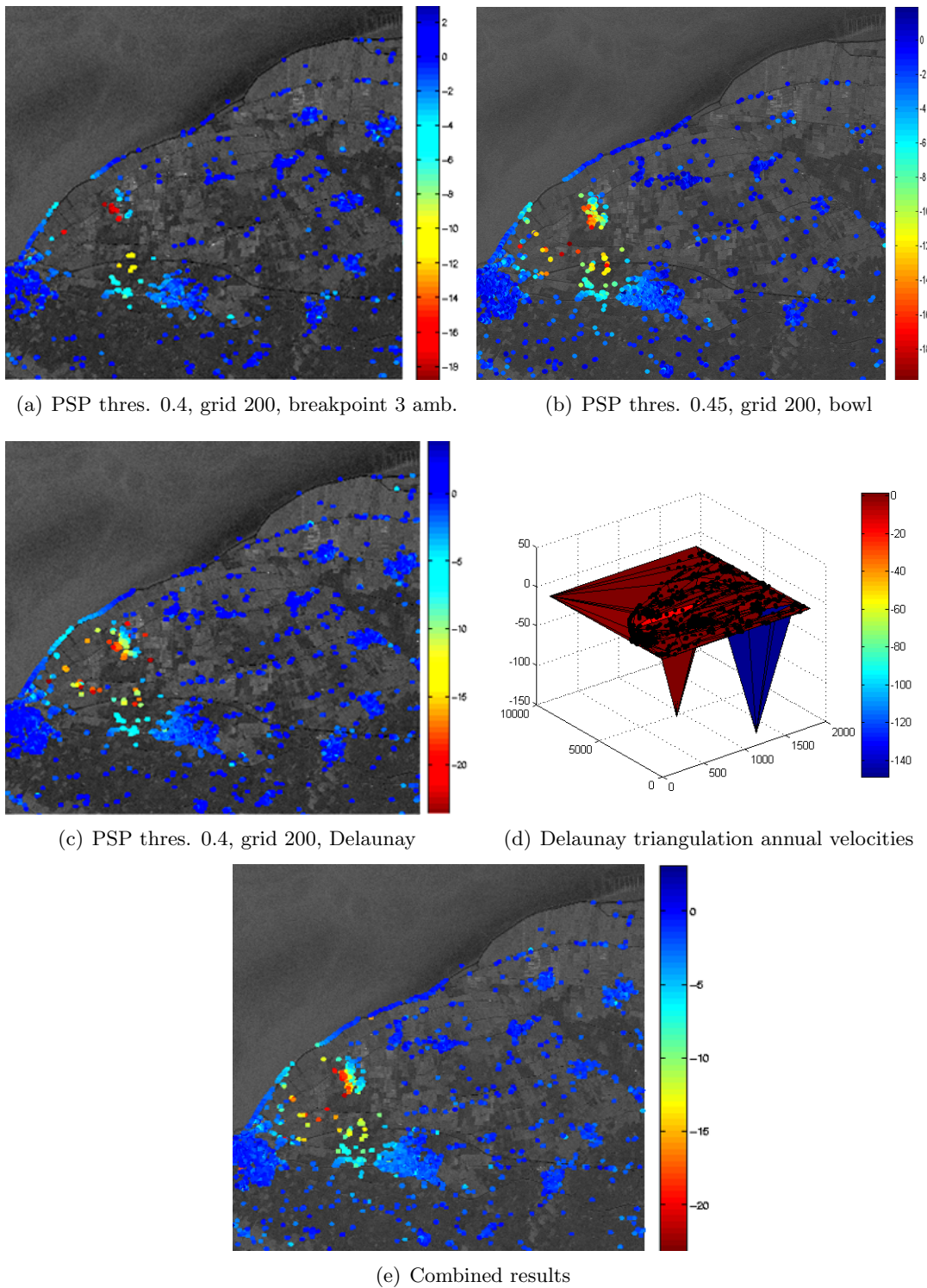


Figure C.18: Annual PS velocities [mm/year] track 258 covering the Barradeel concession. The figure C.2(b) displays the annual velocities of the breakpoint model method. The results of the bowl estimation method are found in figure C.18(b). The Figures C.18(c) and C.18(d) present Delaunay deformation subtraction results. The maximum subsidence in the triangulation is -150 mm/year. Notice that since the variance of the velocities are large the results are doubtful. The last subfigure displays the annual velocities of combined datasets.

temporal baseline of track 258. Shifting the temporal baseline also needs a shift in the relative deformation. This is explained in chapter 5.

Case N0	Case	Velocity [mm/year]	OMT
1	PSP thres. 0.4, gridcell size 200	-19.61	1527
2	PSP thres. 0.4, gridcell size 300	-19.78	938
3	PSP thres. 0.45, gridcell size 200	-18.65	1039
4	PSP thres. 0.45, gridcell size 300	-17.41	1729
5	PSP thres. 0.4, gridcell size 200 manual PS	-19.83	1641
6	PSP thres. 0.4, gridcell size 200 breakpoint 3 amb.	-18.75	1261
7	PSP thres. 0.45 gridcell size 200 bowl	-18.85	1632
8	PSP thres. 0.45, gridcell size 300 Delaunay	-18.70	1195

Table C.11: Annual velocities [mm/year] obtained from the investigated cases of track 258.

The density and distribution increased in some cases compared to the conventional case. Investigation of the results indicated a more spread out distribution for case 4 compared to case 2. In case 3 the density increased, but distribution stayed equal compared to case 1. Density and distribution increased for case 5. And for case 7 and 8 the distribution became more spread out. The densities and distributions are close though. Considering the large variances of the PS velocities and filtering it is possible that the distribution and density become equal.

The density of the PS analysis results is smaller compared to the results of track 151. No PSs in the center of the subsidence bowl and surroundings are identified. This is probably caused by the images compiling the interferogram stack. Most likely a polluting image is present in the set, influencing the stability of the pixel phases over time.

To investigate the precisions the assumption is made that for both test cases the deformation is bowl shaped. With the Gaussian bowl estimator, explained in chapter 4, bowl parameters based on the annual velocities are estimated for every case. With the use of the equations discussed in section 3.3.2, the external and internal precisions were obtained. The subsequent discussion is mainly based on the diagonals of the $Q_{\hat{x}}$ and $Q_{\hat{y}}$ matrices. In the Barradeel case two subsidence bowls are present. These are due to gas subtraction and salt mining. This presence of two bowl makes bowl estimation difficult, impossible or unreliable. Therefore bowl parameters based on leveling results are used, and the internal and external precision are calculated based on these parameters, hence no estimation of the parameters is performed. The parameters used are found in table C.12 and a plot of this bowl is presented in figure C.19.

Parameter	Value
x_c	404 [pixels]
y_c	3600 [lines]
z_c	0 [mm]
$radius$	550 [lines]
$depth$	-79 [mm]

Table C.12: Bowl parameters used for precision estimate of track 258.

Table C.13 presents the ratio between the investigated case and a reference case. Every covariance coefficient on the diagonal of the $Q_{\hat{x}}$ matrix is divided by the corresponding coefficient of the conventional $Q_{\hat{x}}$ matrix. The mean of these ratios is presented in the table. The external precision, $Q_{\hat{x}}$, compared to a reference case increased in most cases. As can be seen in the table case 1 and 2 are very close, hence a precision increase can be due to difference of filtering. The

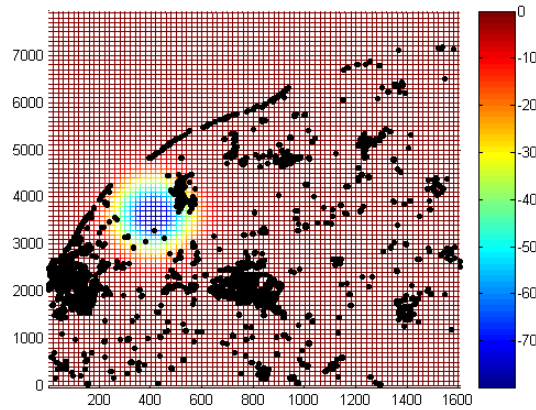


Figure C.19: Plot of the subsidence bowl composed with the parameters as found in table C.12 for track 258. The PSs identified by the bowl method are displayed in black.

precision decreased in case 6, the breakpoint method, due to the decrease of PSs in the area of interest. Also case 7, the bowl case, experienced a decrease in external precision compared to the reference case 3. This is introduced by less PSs in the northern area, Sexbierum, of the subsidence bowl compared to the reference case 3, and a few PSs which are clearly unrealistic, but still present in the dataset.

Whether the internal precision, $Q_{\hat{y}}$, increased or decreased can be found in table C.13. This is based on the diagonal values in the $Q_{\hat{y}}$ matrix. For both the cases 2 and 4 the increase of internal precision is close to the reference case. Most likely the difference is due to several extra PSs present in the case and not in the reference case. Also the manual PS identification introduces an increase in the internal precision. The increase in density of PSs cancels the number of unrealistic PSs, resulting into an increase in internal precision. The bowl and bilinear interpolation case do not contain a denser distribution of PSs, but a more spread out distribution. Since the number of PSs in the Sexbierum area for both cases decreased compared to the conventional results and some errors are present in the PS sets the internal precision also decreased.

The reliability of the model is described by the Overall Model Test. In table C.11 the OMT scaled to the number of PSs for the different cases can be found. The difference between the reference case OMT and the OMT of the case of interest is presented in table C.13. A negative number indicates a more reliable fit of the PSs to the model. The increase in OMT for case 5 and 8 is caused by the larger variance in the annual velocities. These PSs do not fit the bowl properly and thus the OMT is larger then in the reference case. Also notice that the gas subtraction bowl is not modeled. Thus when more PSs are present in this area, this will also influence the OMT. This occurs in all three cases experiencing a larger OMT.

Case	Ref. Case	$Q_{\hat{x}}/Q_{\hat{x},ref}$	$Q_{\hat{y}}/Q_{\hat{y},ref}$	ΔOMT
2	1	0.99	precision increase	-589
3	1	0.81	precision increase	-488
4	3	0.90	precision increase	689
5	1	0.65	precision increase	114
6	1	2.64	precision decrease	-266
7	3	1.46	precision decrease	-534
8	4	0.89	precision decrease	592

Table C.13: Internal and external precision investigated cases of track 258.

Appendix D

Estimated Mogi parameters

This appendix contains the Mogi model estimates for the Veendam and Barradeel concession not covered in chapter 6. Three tracks covering the Veendam area are investigated throughout this thesis. These tracks are track 108, track 380 and track 487. The optimized PS results from the different tracks are combined. These results are obtained by the implemented methods as described in chapter 4. The Mogi model describes a point source with parameters x , y , depth and volume change. Estimation of unknown reservoir parameters is performed on the deformation in the optimized PS datasets. The Mogi model is applied as inverse model, as described in chapter 6. Estimated parameters for the Veendam concession are treated in the first section. Plots of the estimates per epoch and tables containing the temporal behavior are described in the same section.

The two tracks 151 and 258 cover the Barradeel concession. Mogi parameter estimates are based on optimized datasets as presented in chapter 5. Because two extraction sources are present in this area, two Mogi sources are modeled. BAS-1 and 2, Frisia salt reservoirs, are approximated by one Mogi source and the Vermilion gas reservoir is approximated by the second source. The position and depth of the Barradeel source is taken fixed throughout the estimation, see chapter 6. Section two contains estimated parameters per epoch, plots of the estimates and tables of the temporal behavior of the estimated position parameters.

D.1 Estimated Mogi parameters Veendam concession

Mogi parameters track 487

The xrd and yrd coordinates, depth and volume changes estimated by the Mogi model in track 487 are presented in table D.1. Except for the xrd coordinate, the estimates approach the estimates for track 108. The difference in xrd coordinate is introduced by the number of PS present in the centre of the bowl. In the dataset of track 487 less PS are present in the subsidence centre and more in the West of the bowl compared to track 108. This introduced a smaller xrd coordinate. A difference in the volume change in track 108 is present since the volume changes estimated for the epochs approaching the reference coordinate are not correct. This is due to the unclear deformation pattern because the the subsidence approaches the variance of the data. The slope of the volume changes in track 487 approach the slope of the volume changes in track 108, see figure 6.3. The first two and final two epochs are rejected by the w-test. Calculation of the correlation coefficients between provided volume changes and the estimated volume changes results into table D.2. Elimination of the epochs rejected by the w-test resulted into correlation coefficients as presented in the table as correlation coefficients2.

Figure D.2 presents the OMT between the calculated deformation with estimated Mogi pa-

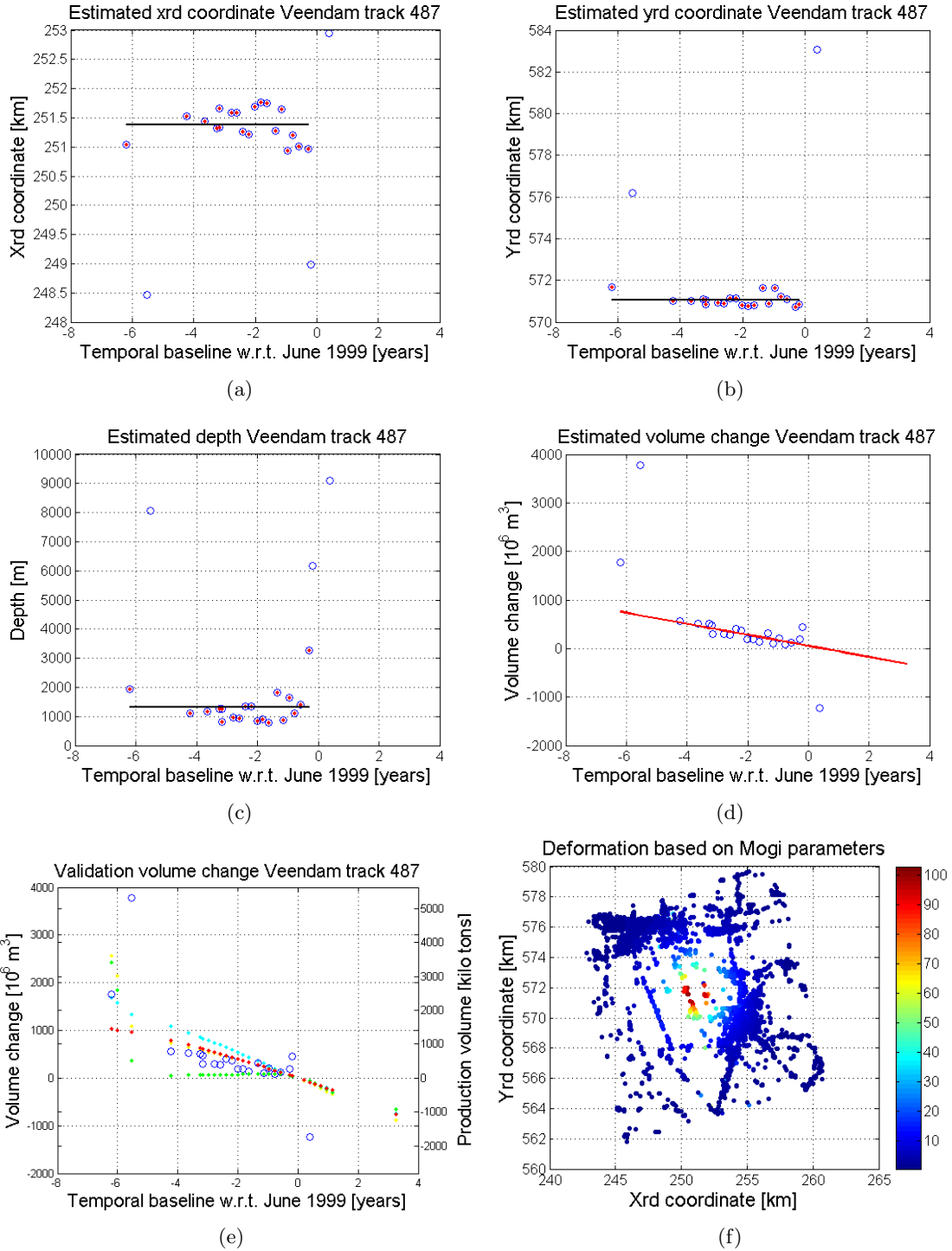


Figure D.1: Estimated source parameters Veendam track 487. The blue lines represent the estimated parameters. In subfigures (a), (b) and (c) the red points display the epochs accepted by the w-test. In (d) the red line displays the linear temporal behavior. In (e) the blue line shows the estimated volume change of track 487. The red line shows the Veendam production data. Underground volumes, squeeze volumes and the summed underground and squeeze volumes are plotted by the green, cyan and yellow line respectively. Subfigure (f) shows the deformation in mm at April 1993 w.r.t. June 1999 calculated with estimated Mogi parameters.

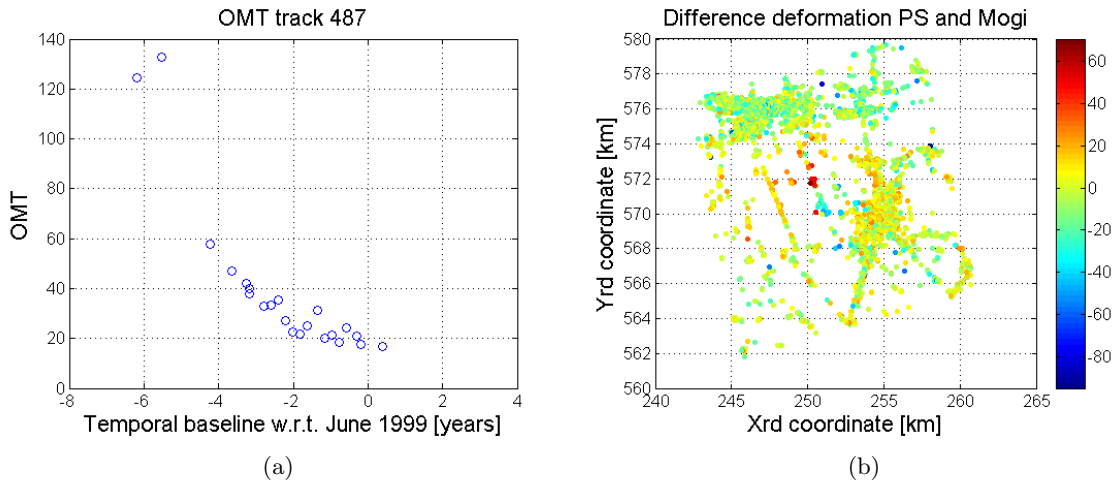


Figure D.2: The reliability of the Mogi parameter estimation track 487. Subfigure (a) displays the OMT between the PS data and the estimated data with Mogi. The difference between the estimated deformation with Mogi and the estimated deformation by the PS analysis is displayed in subfigure (b). The deformation plots visualize the deformation at April 1993 respectively to June 1999.

Parameter	Conventional model
x_s	251379 <i>m</i>
y_s	571070 <i>m</i>
d	1302 <i>m</i>
ΔV_c	$53.75 \cdot 10^3 \text{ m}^3$
ΔV_t	$-113.23 \cdot 10^3 \text{ m}^3/\text{year}$

Table D.1: Parameter estimates for Veendam concession dataset track 487

Dataset	Correlation coefficient	Correlation coefficient
Production volumes	0.668	0.826
Underground volumes	0.517	0.633
Squeeze volumes	0.673	0.822
Summed underground & squeeze volumes	0.651	0.843

Table D.2: Correlation coefficients between the estimated volume changes in track 487 with Mogi and the provided underground, squeeze and production volumes. Correlation coefficient2 is based on the epochs selected by the w-test performed on the estimated xrd, yrd coordinates and depth.

rameters and the estimated PS deformation. The deformation as found by the Mogi parameters is plotted in figure D.1(f). The error between the Mogi and PS deformation is plotted at the PS locations for the first epoch in April 1993 relative to the reference epoch at June 1999 in figure D.2. The errors present in the West of the subsidence bowl are relatively large. When deformation becomes larger, the errors become larger, hence the epochs furthest away from the reference epoch, experience the largest OMT. The large errors seem to be introduced by the xrd coordinate which is placed between the extraction location and the West of the subsidence bowl experiencing large errors.

Mogi parameters track 380

The xrd and yrd coordinates, depth and volume changes estimated by the Mogi model in track 380 are presented in table D.3 and plotted in figure D.3. The estimates approach the estimates for track 108. Calculation of the correlation coefficients between provided volume changes and the estimated volume changes results into table D.4. The correlation coefficients are large for these volume changes.

Figure D.4 presents the OMT between the calculated deformation with estimated Mogi parameters and the estimated PS deformation. The deformation as found by the Mogi parameters is plotted in figure D.3. The error between the Mogi and PS deformation is plotted at the PS locations for the first epoch in July 1992 relative to the reference epoch at July 1997 in figure D.4. Compared to track 487 the position of the source corresponds better with the PS deformation, resulting into smaller errors between the datasets.

Parameter	Conventional model
x_s	251930 <i>m</i>
y_s	571140 <i>m</i>
d	1773 <i>m</i>
ΔV_c	$132.13 \cdot 10^3 \text{ m}^3$
ΔV_t	$-248.42 \cdot 10^3 \text{ m}^3/\text{year}$

Table D.3: Parameter estimates for Veendam concession area dataset track 380

Dataset	Correlation coefficient
Production volumes	0.940
Underground volumes	0.745
Squeeze volumes	0.950
Summed underground & squeeze volumes	0.918

Table D.4: Correlation coefficients between the estimated volume changes in track 380 with Mogi and the provided underground, squeeze and production volumes.

D.2 Estimated Mogi parameters Barradeel concession

Mogi parameters track 258

The xrd and yrd coordinates, depth and volume changes estimated by the Mogi model in track 258 are presented in table D.5. Except for the xrd coordinate the estimates approach the estimates for track 151. Similar as for track 151 the xrd, yrd coordinates and depth of the Barradeel cavern are taken fixed. A difference in estimated volume changes of the first epochs of track 258 and track 151 is present. This is introduced by uncorrected data. The unwrapping errors are not eliminated in this track. The volume changes experience a larger variance in track 258 than in track 151. This is introduced by the number of available epochs. Less images are present for track 258, resulting in less constrained estimated and therefore also less constraint Mogi estimates, resulting in larger variances in the PS dataset and hence also in the Mogi estimates.

Figure D.6 presents the OMT between the calculated deformation with estimated Mogi parameters and the estimated PS deformation. The error between the Mogi and PS deformation is plotted at the PS locations for the first epoch in March 1993 relative to the reference epoch

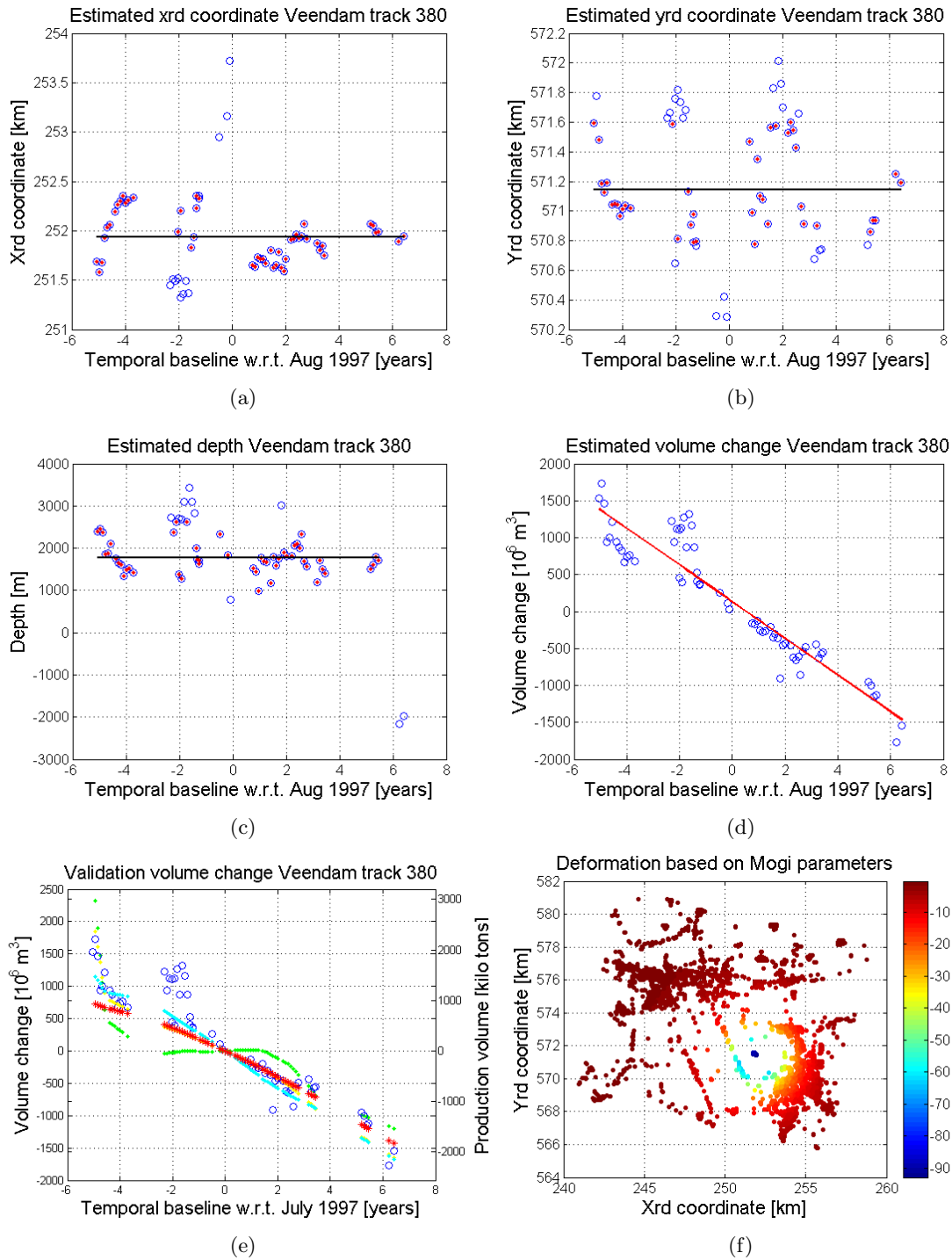


Figure D.3: Estimated source parameters Veendam track 380. The blue lines represent the estimated parameters. In (a), (b) and (c) the red points display the epochs accepted by the w-test. In subfigure (d) the red line displays the linear temporal behavior. In (e) the blue line shows the estimated volume change for track 108. The red line shows the Veendam production data. Underground volumes, squeeze volumes and the summed underground and squeeze volumes are plotted by the green, cyan and yellow line respectively. Subfigure (f) shows the deformation in mm at September 2002 w.r.t. July 1997 calculated with estimated Mogi parameters

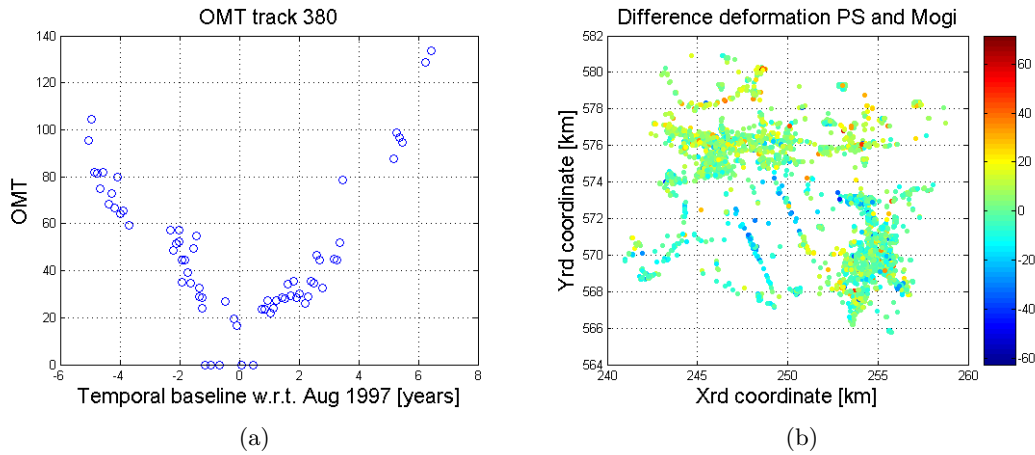


Figure D.4: The reliability of the Mogi parameter estimation for track 380. Subfigure (a) displays the OMT between the PS data and the estimated data with Mogi. The difference between the estimated deformation with Mogi and the estimated deformation by the PS analysis is displayed in subfigure (b). The deformation plots visualize the deformation at September 2002 respectively to July 1997.

at June 1997 in figure D.6. The estimation of the volume change of the Barradeel source was not correct. Larger errors between the datasets are present. Because no PS are present in the subsidence bowl, but only on the sides, the volume change is not estimated correct. This also has an influence on the volume change of the Franeker source. This sources seems to cause more deformation than in reality since the Barradeel bowl causes a part of the deformation present in the area. This problem can have caused the shift of 610 meters between track 258 and 151.

Parameter	Estimated values	Parameter	Estimated values
$\Delta V_{c1(\text{part } 1)}$	$61.02 \cdot 10^3 \text{ m}^3$	x_{s2}	162770 <i>m</i>
$\Delta V_{t1(\text{part } 1)}$	$-310.98 \cdot 10^3 \text{ m}^3/\text{year}$	y_{s2}	578490 <i>m</i>
$\Delta V_{c1(\text{part } 2)}$	$550.45 \cdot 10^3 \text{ m}^3$	d_2	1000 <i>m</i>
$\Delta V_{t1(\text{part } 2)}$	$-735.15 \cdot 10^3 \text{ m}^3/\text{year}$	ΔV_{c2}	$-26.24 \cdot 10^3 \text{ m}^3$
		ΔV_{t2}	$-43.81 \cdot 10^3 \text{ m}^3/\text{year}$

Table D.5: Parameter estimates for the Barradeel concession track 258 obtained with 2 modeled sources.

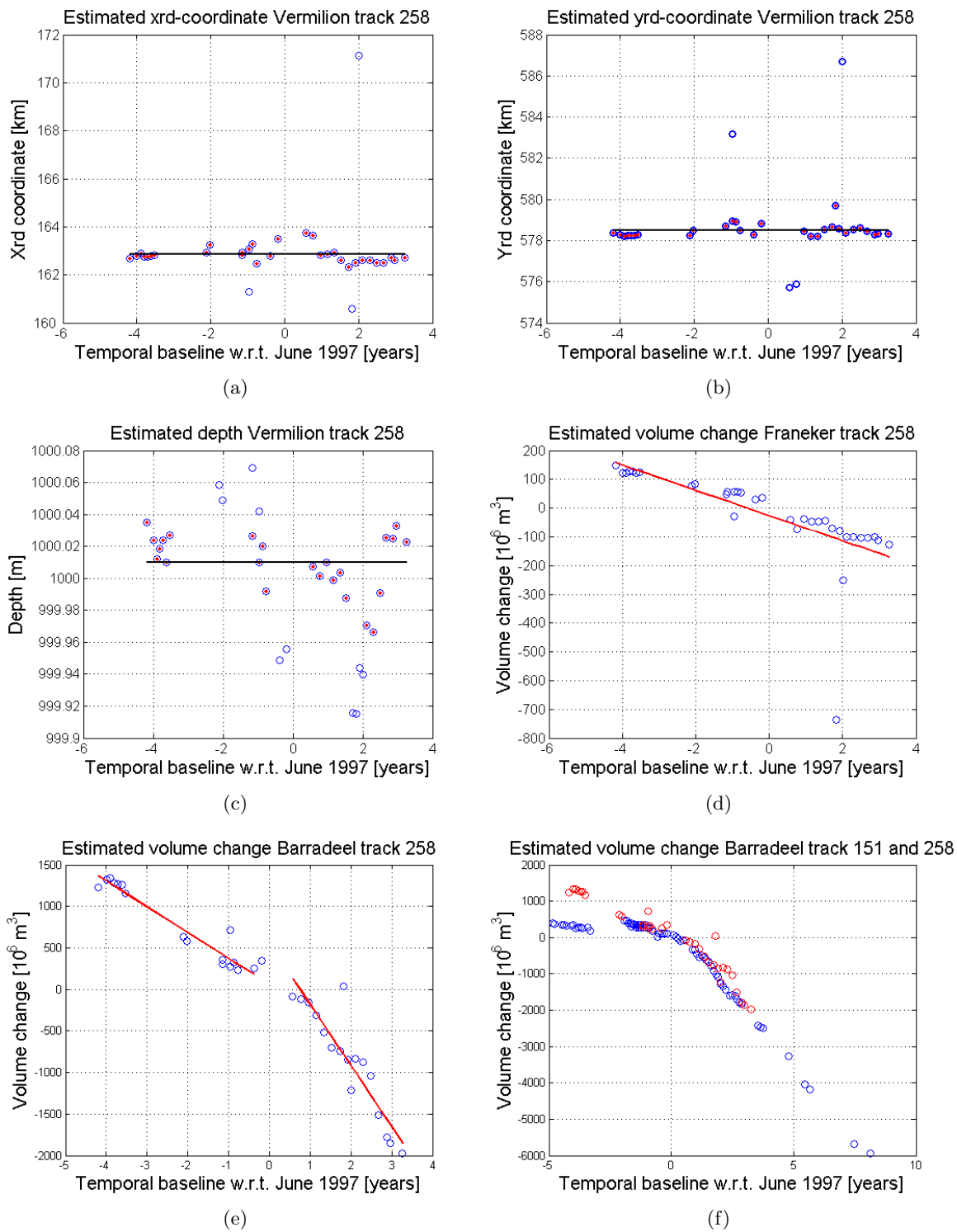


Figure D.5: Estimated source parameters of the gas subtraction near Franeker and salt extraction near Barradeel in track 258. The blue lines represent the estimated parameters. In subfigures (a), (b) and (c) the red points display the epochs accepted by the w-test. In subfigure (d) the red line displays the linear temporal behavior. Subfigure (e) presents the volume changes of the Barradeel concession and the temporal behavior of the volume change. The volume changes of track 151 (blue line) and track 258 (red line) in the Barradeel concession are plotted in subfigure (f).

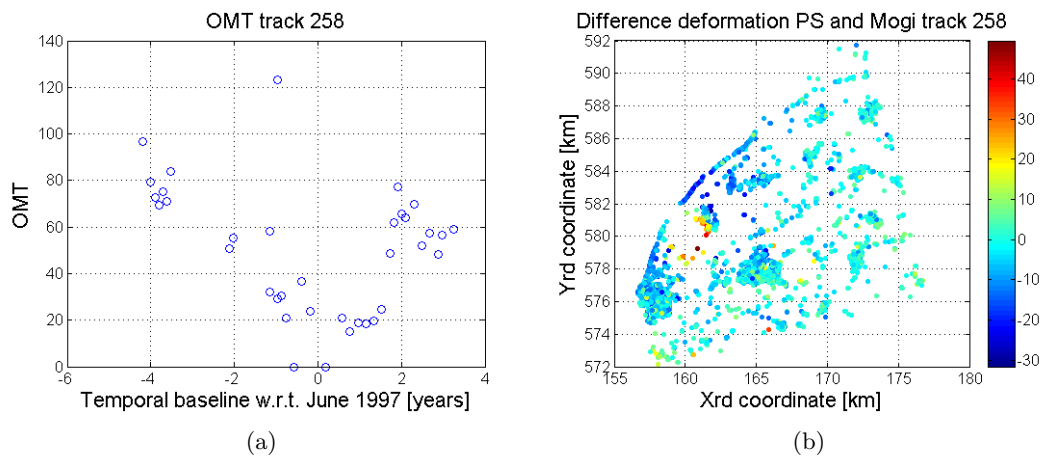


Figure D.6: The reliability of the Mogi parameter estimation for track 258. Subfigure (a) displays the OMT between the PS data and the estimated data with Mogi. The difference between the estimated deformation with Mogi and the estimated deformation by the PS analysis is displayed in mm in subfigure (b). The deformation plots visualize the deformation at March 1993 respectively to June 1997.